

UNIVERSITY OF CRETE
DEPARTMENT OF MATERIALS SCIENCE AND TECHNOLOGY

NOVEL APPROACHES FOR ROBUST
POLARITONICS

RAHUL JAYAPRAKASH



Heraklion, Greece, October 2015

NOVEL APPROACHES FOR ROBUST POLARITONICS



A DISSERTATION
SUBMITTED TO THE DEPARTMENT OF MATERIALS SCIENCE
AND TECHNOLOGY
AND THE COMMITTEE ON GRADUATE STUDIES
OF UNIVERSITY OF CRETE
IN PARTIAL FULFILLMENT OF THE REQUIREMENTS
FOR THE DEGREE OF
DOCTOR OF PHILOSOPHY

JAYAPRAKASH RAHUL

October 2015

© Copyright by JAYAPRAKASH RAHUL 2015
All Rights Reserved

NOVEL APPROACHES FOR ROBUST POLARITONICS

Thesis author : Rahul Jayaprakash

Principal advisor : Prof. Nikolaos T. Pelekanos

Committee members : Prof. Pavlos Savvidis
: Prof. Maria Vamvakaki
: Prof. Alexandros Georgakilas
: Asst. Prof. Eleftherios Iliopoulos
: Dr. Wolf von Klitzing
: Prof. Georgios Kavoulakis

Department of Materials Science and Technology, University of Crete
Heraklion, Greece

October 2015

Remembering the love and blessings she bestowed up on me,

*I dedicate this thesis to my loving mother, Kusumam
Jayaprakash*

Abstract

The possibility of having low-threshold, inversion-less lasers, making use of the macroscopic occupation, of the low density of states, at the bottom of the lower polariton branch, has intensified polariton research in the last two decades. State of the art devices based on this admixed quasiparticle have already been realized using GaAs and CdTe active layers, although the accomplishment of room temperature lasers has been limited by their relatively weak exciton binding energy. The high exciton binding energy and oscillator strength, as well as the advantageous relaxation dynamics of wide bandgap semiconductors, such as GaN, are well suited for room temperature polariton operation. The up to date demonstrations of GaN based polariton lasers have used as the active layer bulk GaN, GaN quantum wells (QW's), and GaN nanowires. In the latter approach, individual nanowires are positioned in a microcavity showing remarkable polariton characteristics, but questions remain on the scalability of the approach, as well as on how to turn these nanowire-based structures into real electrically-injected devices. The former two cases are technologically viable, but are currently limited by the relatively poor quality of the active region, due to the structural disorder introduced by the bottom GaN based Distributed Bragg Reflector (DBR) mirrors.

In this thesis, a very straightforward processing technique is used to etch away an InGaN sacrificial layer, using photo-electrochemical (PEC) etching, creating ultra-smooth membranes containing GaN/AlGaN QW's, which are then embedded between high quality dielectric DBR mirrors, on which polaritonic studies are performed. The GaN membrane or the

active region is carefully engineered, ensuring superior optical properties, both prior to and after etching. At room temperature, the QW emission is state of the art, with a linewidth of $\sim 28\text{meV}$, and a corresponding lifetime of $\sim 275\text{ps}$. The PEC lateral etching parameters are optimised in such a way, that the rms roughness of the membranes, measured by Atomic Force Microscopy (AFM), is as small as 0.65nm , very close to epitaxial quality. A temperature dependent study on the full-microcavity structure, unveils the strong coupling regime, exhibiting a robust Rabi splitting as large as 64meV at room temperature. The non-linear properties are examined, under non-resonant quasi-continuous excitation, with polariton lasing demonstrated at an ultra-low, average threshold of $\sim 4.5\text{W} / \text{cm}^2$ ($\sim 594\mu\text{J} / \text{cm}^2$), the lowest ever reported for a 2D GaN based system, accompanied by a spectacular condensation pattern in k-space. The latter is attributed to a site-specific polariton trapping mechanism, where polaritons accumulate in discrete levels within the trapping potential, helping to escalate the polariton density locally. This, along with the high optical quality of the all-dielectric microcavity (Q-factor ~ 1770), explains the obtained ultra-low threshold. It should be noted that the use of ultra-smooth GaN membranes in microcavities is fully compatible with the realisation of electrically injected GaN polariton devices.

In the direction of obtaining even more robust polaritonic devices, the basic optical properties of high quality, strain free, GaN nanowires are studied. However, to make the most out of this novel system, the absorption coefficients are extracted from as-grown GaN nanowires, on silicon $\langle 111 \rangle$ substrates, developing an all-optical method, analysing merely the reflectivity spectra, which is demonstrated for the first time. It should be noted that the absorption coefficients (directly proportional to oscil-

lator strengths) corresponding to the excitons, provide a glance into the appropriateness of the respective GaN nanowire system, as optimal candidates for hefty polaritonics. However, the nanowires studied here, failed to show an enhancement of absorption, which can be mainly attributed to the nanowire dimensions. The new method demonstrated here, can be extended to any family of nanowires, provided they are grown on a substrate having considerable difference in permittivity with the nanowire-air matrix.

Acknowledgement

I would like to express my gratitude, to my principal advisor, Prof. Nikolaos T. Pelekanos, for all his advice and support throughout my doctoral studies. Having a background in electronics engineering, it is Pelekanos who introduced me into the field of hardcore polariton physics and optoelectronics. Had it not been for him, my knowledge and experience would have been limited. I'm also thankful to him, for introducing me to many excellent researchers and institutes around Europe. Apart from being my advisor, we always shared a strong bond, more of a 'father-like' figure for me. I am thankful to Prof. Pavlos Savvidis, for allowing me to be a part of one of the biggest polaritonic research projects in Europe - 'ICARUS', through Marie Curie initial training network (ITN). I would like to express my regards to Dr. Eva Monroy, who supported us with all the necessary 2D - GaN based samples, through her excellent growth facilities in INAC, CEA, Grenoble, and moreover played an active role in all our projects, through discussions and suggestions. I would like to extend my regards to Prof. Alexandros Georgakilas, who provided us with high quality GaN nanowire samples, grown at our MBE facility in Crete. I would like to show my salutations to Dr. George Konstantinidis, for granting access to the cleanroom facilities, and of course his part in keeping the Microelectronics Research Group awake and active. Finally, I would like to compliment Asst. Prof. Eleftherios Iliopoulos, for his extensive support through the ellipsometry facilities available, here in Crete.

I would like to thank the post-doctoral researchers, who also happen to

be my very dear friends. Firstly Dr. Fotis Kalaitzakis, who has actively participated in our work, mainly through his cleanroom expertise like RIE, GaN membrane transfer to any suitable substrate and the list goes on. Secondly Dr. Symeon Tsintzos, who is more like a research associate, whom I met on my very first day in Crete. I have been lucky to utilise his extensive knowledge in the field of polaritonics, both experimentally and theoretically. Thirdly Dr. Gabriel Christmann, who arrived as a post-doctoral researcher, at the beginning of my fourth year. I feel myself extremely fortuitous, for having met a person like him. Gabriel again, who was an expert in polaritonics, especially GaN, helped me gain a lot of knowledge, through fruitful discussions we often had. His vast experience with optical characterisation techniques, helped me a lot while trying to setup my own UV-imaging setup.

I would like to express my devoirs for our technical staff, who are also more like my friends. Firstly Mrs. Maria Androulidaki, who initially showed me the lines in the lab and helped me with simple optical characterisation. Her knowledge about each and every detail in the lab has often helped me. Secondly Mrs. Katerina Tsagaraki, who was the first priority when new samples were grown, as her expertise was mainly on SEM, AFM and XRD. All the beautiful SEM and AFM images, as well as XRD measurements, reported in this work, can be owed to her. Thirdly Mrs. Maria Kayambaki, who introduced me to the photo-electrochemical (PEC) lateral etching setup. The experience I gained through initial experiments and discussions with her, has been able to shape my etching skills. Lastly Nikolaos Papadakis and Michalis Sfindourakis, with their expertise in electrical, mechanical and cryogenic systems, whose support was crucial for the operation of the entire lab.

I am extremely thankful to Dr. Savvas Germanis, for all the scientific and mental support he offered me, a friend whom I could always look forward to. His love for physics and quantum mechanics has always inspired me. The perfectionist within him, has influenced me greatly, as well as my skills in the lab. I would like to specially mention Mr. Stelios Kazazis, Ph.D. student, who offered his support for precise ellipsometry measurements and analysis. Moreover, a very good friend, who has always been on my side, whenever i needed him. I am thankful to each and everyone in the Microelectronics Research Group, and a bunch of friends whom i happened to meet, here in the group. I would like to express my regards to the big Italian / Greek community in Heraklion, with special mention to Dr. Niccolo Somaschi and Dr. Paolo Carpeggiani, through whom I met all of them. They are my ever-loving friends, who have been there with me, at moments of happiness and sorrow.

Finally I would like to thank my parents - dad, mom, sister, grandmother and my uncles. At this auspicious period of my life, I would like to remember my late grandmother - Nalini. T, who passed away during the course of my doctoral studies.

I would like to express my regards to Marie Curie initial training network (ITN), for funding the first three years of my doctoral studies, through project 'ICARUS', as part of the European Union (EU), 7th framework programme for research and technological development (FP7), and European Social Fund and National resources, for funding the last two years, through the 'THALES' programme 'NANOPHOS'.

I conclude by quoting **Aristotle** -

'Litterarum radices amarae, fructus dulces' - *'The roots of education are bitter, but the fruit is sweet'*

Contents

Abstract	xi
Acknowledgement	xv
List of Tables	xxv
List of Figures	xxvii
Introduction	1
Conventional lasers	1
What is a polariton laser ?	2
Why GaN membranes ?	5
Issues related to creating ultra-smooth GaN membranes	6
About this work	7
Bibliography	11
1 The active region	17
1.1 Introduction	17
1.2 Samples studied	17
1.3 Basic optical characterisation	20
1.3.1 Photoluminescence and Reflectivity with temper- ature	20
1.3.1.1 Low temperature results	20
1.3.1.2 Delocalisation of quantum well excitons with temperature	22

1.3.1.3	Room temperature results	24
1.3.2	Time resolved photoluminescence with temperature	26
1.3.3	Confirmation of indium percentage in the sacrificial layers based on photoluminescence	30
1.4	Conclusion	31
	Bibliography	32
2	Ultra-smooth GaN membranes by photo-electrochemical etching	35
2.1	Introduction	35
2.2	Samples studied and initial processing	36
2.3	Photo-electrochemical (PEC) etching setup	37
2.4	Optimising PEC lateral etching for ultra-smooth GaN mem- branes	39
2.5	Optical characterisation	46
2.5.1	Sample before etching	46
2.5.2	Ultra-smooth GaN membranes on sapphire	49
2.6	Conclusion	53
	Bibliography	54
3	Polaritonic studies on GaN membranes	57
3.1	Introduction	57
3.2	Design of a microcavity	58
3.2.1	Distributed Bragg Reflectors (DBR's)	59
3.2.2	The cavity layer using PEC lateral etching	66
3.2.3	The process flow for a full-microcavity structure	67
3.2.4	Half microcavity	69
3.2.4.1	Cavity mode inhomogeneities	72

3.2.4.2	Q-factor	74
3.2.4.3	Modelling the reflectivity response	75
3.2.4.4	Angular dispersion	80
3.2.5	Full microcavity	82
3.2.5.1	Electric field distribution within the structure	83
3.2.5.2	Q-factor, lifetime and Finesse	86
3.2.5.3	Altering the cavity mode properties	88
3.2.5.4	Angular dispersion and effective mass of the cavity photon	91
3.3	Demonstration of strong coupling	93
3.3.1	Feasibility of strong coupling	94
3.3.2	Membranes studied and experimental conditions	97
3.3.3	Models used	99
3.3.4	Verification of strong coupling as a function of temperature	100
3.3.5	Determination of Q-factor	105
3.4	Conclusion	107
	Bibliography	109
4	A GaN membrane based polariton laser	113
4.1	Introduction	113
4.2	Theory	113
4.3	Experimental conditions and models used	119
4.4	Experimental verification of polariton condensation aided by modelling	120
4.4.1	Estimation of exciton density / QW at threshold	125

4.5	The k-space pattern	128
4.5.1	Analysis of non-linear properties based on site-specific polariton trapping	132
4.6	Conclusion	134
	Bibliography	136
5	Study of GaN nanowires as a potential candidate for po- laritonic applications	139
5.1	Introduction	139
5.2	Samples studied and experimental methods	141
5.3	Basic optical characterisation	143
5.4	Total reflectivity measurements and modelling	147
5.4.1	Homogenising an anisotropic medium	151
5.4.2	Estimation of effective ordinary permittivity using effective medium theory (EMT)	152
5.4.3	Specular reflectivity to absorption	154
5.5	Determination of absorption coefficients	156
5.6	Conclusion	160
	Bibliography	161
	Conclusion	167
	Future perspectives	170
	Bibliography	172
A	Experimental equipments and setups	175
A.1	Building blocks	175
A.1.1	Laser's	175
A.1.2	White light source's	176

A.1.3	Sample placement and temperature dependent measurements	176
A.1.4	Spectrometer	176
A.1.5	Streak camera	177
A.2	Optical setups	177
A.2.1	Basic PL / Reflectivity setup	177
A.2.2	Time resolved photoluminescence (TRPL) setup	179
A.2.3	Simultaneous PL and Transmission setup relying on the principle of magnification	180
A.2.4	Reflectivity setup relying on the principle of magnification	182
A.2.5	Simple Reflectivity setup using optical fibres	184
A.2.6	PL Imaging setup	185
A.2.7	Reflectivity measurements using integrating sphere	187
B	Transfer matrix model	191
B.1	Matrix calculating method	191
B.2	Relation between transfer matrix and effective characteristic matrix	195
B.3	Application of the model to a microcavity system	196
	Bibliography	198
C	Linear Hamiltonian model	201
	Bibliography	206

List of Tables

- 1.1 A complete summary of the samples studied. 19
- 3.1 A table summarising the different membranes studied, which are embedded between DBR mirrors, forming a full microcavity structure. 98

List of Figures

- 1.1 The active region corresponding to the two parent samples: (a) parent ‘A’, and (b) parent ‘B’. (c) The possible structure of children samples, based on the two parent samples, separated from the template by an InGaN sacrificial layer, that ought to be etched using PEC lateral etching. 18
- 1.2 A comparison of PL (black) and Reflectivity (red) at 23K from (a) sample 1, and (b) sample 2, exhibiting various excitonic features. 21
- 1.3 Evolution of QW excitons with temperature, based on PL, for: (a) sample 1, and (b) sample 2, where the delocalisation behaviour is evident. 23
- 1.4 A comparison of PL (black) and Reflectivity (red) at 280K from (a) sample 1, and (b) sample 2, exhibiting various excitonic features. 24
- 1.5 A comparison of the integrated intensity between QW emission from sample 2 and GaN emission from bare GaN template, where the fall in intensity from LT to RT is ~ 6 times better for sample 2 as opposed to bare GaN template. . . . 26
- 1.6 (a) Lifetimes extracted as a function of temperature from the dominant QW peak of sample 2, where the excitation power density is very low. (b) TRPL response at RT, for similar experimental conditions, from which the lifetime is extracted to be ~ 275 ps. 27

1.7	Evolution of (a) radiative lifetime (τ_R), and (b) non-radiative lifetime (τ_{NR}) with temperature, for different values of $\eta(140K)$, which is varied from 0.1 to 1.0.	30
1.8	(a) PL from the $\text{In}_x\text{Ga}_{1-x}\text{N}$ sacrificial layer: (a) for samples 3, 4 and 5, at 25K, and (b) for sample 6 at 25K and 295K, where the PL peak energy shifts according to the variation in the indium concentration.	30
2.1	Mask pattern used for RIE, where the dimensions range from 45×45 to $155 \times 155 \mu\text{m}^2$	36
2.2	(a) PEC lateral etching setup, where the etching is shown to take place on a single MESA, under the application of a reverse bias, accompanied by a light source. (b) Band alignment during the etching process, under similar experimental conditions.	37
2.3	(a) IV characteristics of the electrolyte-semiconductor interface, at dark and light conditions, where the average laser power is 4mW and the electrolyte concentration is 0.0004M. The inset depicts a magnification of the positive bias regime. (b) $10 \times 10 \mu\text{m}^2$ AFM image from a GaN membrane transferred to double sided tape exhibiting very low roughness, on the bottom N-face GaN surface.	40
2.4	(a) SEM lateral view of a GaN membrane detached from substrate after PEC lateral etching. (b) Optical microscope image of an etched region clearly depicting regions with and without GaN membranes.	42

2.5	(a) Variation of photocurrent produced as etching progresses, under a constant dc bias of 4V. The dashed line through the experimental curve is a fitting with a double exponential. (b) Variation of photocurrent with etching time, under a pulsed dc bias of 4V. The inset shows the variation of photocurrent during a pulse period.	43
2.6	Optical microscope image of: (a) GaN membranes transferred to double sided tape, and (b) GaN membranes transferred to double-side polished sapphire substrate.	45
2.7	A comparison of PL and Reflectivity from bare sample 4 (blue lines), prior to PEC lateral etching, at LT, to the PL of its parent sample: sample 1 (red line), exhibiting various excitonic features.	47
2.8	(a) Comparison of PL from sample 4 membrane, transferred to a double side polished sapphire substrate, to that of bare sample 4, prior to PEC lateral etching, showing the variation in intensity as well as energy position, corresponding to different peaks at LT. (b) Comparison of PL and transmission from a GaN membrane on sapphire substrate, etched out from sample 4, at LT, showing various excitonic features.	49
2.9	Optical characterisation of a GaN membrane transferred to double-side polished sapphire substrate: (a) temperature-dependent transmission spectra, and (b) optical density at 20K and 120K.	51

3.1	Schematic of a basic planar full-microcavity structure, where the cavity layer encapsulating the active layer, is embedded between the top and bottom mirrors.	58
3.2	(a) Schematic of top DBR mirror, which consists of 10 pairs of $\text{HfO}_2 / \text{Al}_2\text{O}_3$ layers, on sapphire. (b) Experimental reflectivity response from top DBR mirror, along with its simulation, at 300K, where the angle of incidence is $\sim 6^\circ$	60
3.3	(a) Schematic of bottom DBR mirror, which consists of 11 pairs of $\text{SiO}_2 / \text{Ta}_2\text{O}_5$ layers, on sapphire. (b) Experimental reflectivity response from bottom DBR mirror, along with its simulation, at 300K, where the angle of incidence is $\sim 18^\circ$	62
3.4	The effects on maximum stopband reflectivity as well as its width are studied as a function of: (a) refractive index contrast between subsequent layers of the top DBR stack, where the number of pairs are kept constant at 10, and (b) the number of pairs of the top DBR stack, where the refractive index contrast of the corresponding subsequent layers is kept at 0.48, very similar to actual top DBR design configuration.	64
3.5	(a) Schematic of Sample 6, where the cavity layer is separated from the template by an $\text{In}_{0.115}\text{Ga}_{0.885}\text{N}$ sacrificial layer, that ought to be etched using PEC lateral etching, forming $\frac{3\lambda_0}{2n}$ thick GaN membranes. (b) $5 \times 5 \mu\text{m}^2$ AFM image from a GaN membrane transferred to double sided tape exhibiting very low roughness, on the bottom N-face GaN surface.	66

3.6	An algorithm summarising the various processing steps leading to the formation of a full-microcavity structure. . .	68
3.7	(a) Schematic of a half-microcavity structure formed by transferring the etched out GaN membranes, to the bottom DBR mirror on sapphire. (b) Reflectivity response from the half-microcavity structure, at 23K, where the angle of incidence is $\sim 22^\circ$, clearly depicting the broad cavity mode and various excitonic features. The inset shows the optical microscope image of a GaN membrane lying on the bottom DBR mirror / sapphire - half-microcavity structure.	69
3.8	Behaviour of cavity mode and excitons with temperature, based on reflectivity response from the half-microcavity structure.	71
3.9	The variation in cavity mode energy for: (a) different membranes, at 25K, where the maximum shift observed is $\sim 8\text{meV}$, denoted by pink dashed lines, and (b) a single membrane, corresponding to different positions on it, at 300K, where the maximum shift observed is $\sim 10\text{meV}$. The variation in cavity mode energy can be strongly correlated to the variation in thickness, on different membranes for the former, and at different positions on a single membrane for the latter.	72
3.10	Reflectivity response from the half-microcavity structure at 295K, where the angle of incidence is $\sim 22^\circ$ and the Q-factor is depicted to be ~ 85	74

3.11	Experimental reflectivity response (black line) from the half-microcavity structure at 300K, where the angle of incidence is $\sim 22^\circ$. The other lines correspond to simulated data, without including excitons, although a residual absorption is defined around the cavity region, varying from 0cm^{-1} to 6600cm^{-1}	75
3.12	A simulation showing the angular dispersion of the reflectivity response, of a half-microcavity structure, at 300K, from -39° to $+39^\circ$, clearly depicting the cavity and the Bragg modes. At around 28° , a splitting of the Bragg modes are visible, corresponding to their respective TE / TM modes.	80
3.13	(a) Schematic and (b) cross-sectional SEM image, of a full-microcavity structure, where the $\frac{3\lambda_o}{2n}$ thick GaN membrane ('m') is embedded between top and bottom DBR mirrors, on sapphire substrate. (c) Simulation showing the reflectivity response from a full-microcavity structure, without considering excitons, at RT, where the angle of incidence is $\sim 0^\circ$ and the cavity layer thickness is $\sim 206.35\text{nm}$	82
3.14	Standing wave electric field (black line), at resonant cavity energy ($\sim 3.4154\text{eV}$), for an angle of incidence $\sim 0^\circ$, along with refractive index variations (red line) are plotted for: (a) the entire structure, and (b) the region around the cavity layer.	84

3.15	Simulated reflectivity / absorption response around the cavity mode region, at 295K, for an angle of incidence $\sim 0^\circ$. The Q-factor is estimated to be ~ 1770	87
3.16	The effect on cavity mode properties based on simulated reflectivity response, at 295K, for an angle of incidence $\sim 0^\circ$, by varying the number of DBR stacks corresponding to: (a) bottom DBR mirror, where the number of top DBR stacks are kept constant at 10, and (b) top DBR mirror, where the number of bottom DBR stacks are kept constant at 11.	88
3.17	A simulation showing the angular dispersion of the reflectivity response, of a full-microcavity structure, at 300K, from -34° to $+34^\circ$, clearly depicting the cavity and the Bragg modes. At around 20° , a splitting of the Bragg modes are visible, corresponding to their respective TE / TM modes.	91
3.18	The essential prerequisites for an exciton in terms of linewidth (γ) and coupling constant (g), and for the cavity mode in terms of linewidth (γ_{cav}), in order for the system to be in the weak, intermediate or strong coupling regime.	94
3.19	Demonstration of strong coupling behaviour in membrane 1 at: (a) 20K, and (b) 100K, revealing the LPB dispersion, which clearly flattens out at large angles. The MPB and UPB are not visible, however the uncoupled ‘QW’ excitons are visible as a straight line.	101

3.20	Demonstration of strong coupling behaviour revealing the LPB and MPB dispersions, for: (a) membrane 1 at 230K, and (b) a less negatively detuned membrane at 80K. . . .	102
3.21	Demonstration of strong coupling behaviour in membrane 1 at RT, revealing the LPB and MPB dispersions, however UPB is not visible. The solid and dashed lines correspond to simulated data, which precisely follows the experimental data, in the case of LPB and MPB, and based on the UPB dispersion as well, an estimate is made for the Rabi splitting which is $\sim 64\text{meV}$	103
3.22	Demonstration of strong coupling behaviour at RT, revealing the LPB and MPB dispersions, for: (a) membrane 2, and (b) membrane 3. The solid and dashed lines in either figures correspond to simulated data, which precisely follows the experimental data, in the case of LPB and MPB, and based on the UPB dispersion as well, an estimate for the Rabi splitting is made for both membranes, which is not very different from 64meV	104
3.23	PL experimental data (black line) from membrane 1, at around $k_{\parallel} = 10^{\circ}$, at RT, where the narrow LPB is visible having a linewidth of $\sim 10.8\text{meV}$ and the uncoupled ‘QW’ excitons are seen as a weak shoulder. The dashed red line corresponds to simulated data, precisely following the experimental LPB curve and revealing the UPB as well, at a much higher energy.	106

4.1	A schematic for understanding polariton condensation under non-resonant excitation, for a system where the cavity is negatively detuned $\sim 10\text{meV}$, from the excitonic energy.	114
4.2	PL imaging data from membrane 4, at RT, for the following pump power densities: (a) $0.39P_{th}$ - only LPB_1 is visible, (b) $0.96P_{th}$ - just below threshold where LPB_1 and LPB_2 are visible, and (c) - (f) - polariton condensation above threshold with a k-space pattern, far below the cavity mode energies corresponding to LPB_1 and LPB_2 .	121
4.3	A PL power dependent study is made on membrane 4 at RT, using spectroscopy mode, discussing the following results: (a) spectral data from $0.28P_{th}$ - $1.04P_{th}$, clearly depicting LPB_1 and LPB_2 below threshold, and polariton condensation above threshold, (b) the integrated intensity (red) for the region around LPB_1 and LPB_2 , and the linewidth (blue), estimated from LPB_1 peak below threshold and level '1' peak above threshold, as a function of pump power density, (c) the spectral data above threshold, from $1.04P_{th}$ - $1.26P_{th}$ revealing the three levels within the energy range of LPB_1 and LPB_2 , and (d) occupation number as a function of pump power density, from $0.28P_{th}$ - $1.76P_{th}$, where the occupation shoots up far beyond unity above threshold.	123
4.4	The exciton / cavity fraction corresponding to: (a) LPB_1 , and (b) LPB_2 . (c) A plot showing the carrier density at excitation (blue) and the exciton / polariton density (red), per QW per laser pulse, at threshold.	125

4.5	An energetic picture of membrane 4, depicting the two regions corresponding to LPB ₁ and LPB ₂ , and moreover highlighting the square-like pocket trap	129
4.6	(a) PL imaging data from membrane 4 at RT, where the power density is 1.04P _{th} . The corresponding spectral data is plotted within the image, marking the levels ‘1’, ‘2’ and ‘3’. The levels ‘a’, ‘b’, ‘c’ and ‘d’ are the respective simulated levels. A plot of the real space wavefunctions corresponding to: (b) level ‘1’, (c) level ‘2’, and (d) level ‘3’. The strip within white dashed lines gives rise to the respective k-space profiles.	132
5.1	(a) Top, and (b) lateral SEM view, of GaN (0001) nanowires on Si (111).	141
5.2	Comparison of PL (blue) and reflectivity (red) from GaN NWs: (a) at LT, and (b) at RT, showing pronounced excitonic features.	143
5.3	(a) Evolution of GaN NW excitons with temperature, based on PL. (b) Comparison of PL (blue) and reflectivity (red) from GaN NWs at 100K, where the weak shoulder corresponds to C _{GaN} excitons.	145
5.4	(a) Polarisation-resolved reflectivity measurements, at a large angle of incidence of ~ 65°, where the polariser angle is varied from 0° to 90°, demonstrating the polarisation dependence of the excitons. (b) Wide range reflectivity spectrum of GaN NWs showing transmission-like characteristics.	146

5.5	Total (red), specular (blue) and diffuse (black) reflectivity spectra obtained from the GaN NW sample, at RT. . . .	148
5.6	Simulation of the total reflectivity spectrum from: (a) GaN / Si thin film, and (b) GaN NWs grown on Si, where the black and red lines correspond to experimental and simulated data respectively.	149
5.7	(a) An illustrative diagram showing how the nanowires are divided into two layers, introducing four parameters: h_1 - height of top layer, f_1 - volume fraction of top layer, h_2 - height of bottom layer and f_2 - volume fraction of bottom layer. (b) Deduced power reflectivities from the simulation, at different interfaces of the GaN NW array, such as top (blue), middle (dark cyan) and bottom (magenta) interfaces.	152
5.8	(a) Absorption spectra from GaN NWs, as a function of temperature, from 25K to 295K. (b) LT and RT absorption spectra, emphasising the exciton absorption lines, along with the phonon assisted absorption peak.	156
A.1	Basic PL setup.	177
A.2	Basic Reflectivity setup.	178
A.3	Time resolved photoluminescence setup.	179
A.4	Simultaneous PL and Transmission setup relying on the principle of magnification.	181
A.5	Reflectivity setup relying on the principle of magnification.	183
A.6	Simple Reflectivity setup using optical fibres.	184
A.7	PL Imaging setup.	186
A.8	An imaging setup on a breadboard, which allows the measurement of PL / Reflectivity, by the use of a flipping mirror.	187

A.9	Different integrating sphere configurations, used for measuring total and diffuse reflectivity.	188
B.1	A multilayer system consisting of homogeneous, isotropic layers, where the number of layers are assumed to be m , numbered from the substrate to air.	191
B.2	Relation between effective characteristic matrix (M) and the different spectral amplitudes such as reflection, transmission and absorption, which in turn are represented by the transfer matrix (C).	195
B.3	A multilayer system divided into three regions: (1) bottom DBR ₁ , (2) cavity layer, and finally (3) top DBR ₂ , collectively forming a microcavity system, where the effective characteristic matrix of the corresponding regions are M_1 , M_{cav} and M_2 respectively.	196

Conventional lasers

LASER's are one of those key devices you can find in every walks of your life, from high-speed optical local area networks to conventional DVD players at home. Semiconductor lasers based on III-V compounds are the most popular ones found in the commercial market. One of the key requirements of lasing operation is population inversion i.e. there should be more number of electrons in the conduction band as opposed to the valence band, which is achieved by optically or electrically pumping the active region. In such a scenario a single photon can create an identical second photon, by stimulating the recombination of an electron-hole pair, such that the wavelength and phase of the second photon is identical to the first one, thereby doubling the amplitude of the monochromatic wave. A series of such processes leads to strong light amplification. However, a certain number of photons are a prerequisite in the system, in order to trigger the stimulated emission. This leads to the necessity of having optical feedback and confinement, which is provided by two reflecting facets at the ends of an optical waveguide in an edge-emitting laser, whereas in a surface emitting laser the active layer is embedded between mirrors possessing very high reflectivity [1].

However, one of the fundamental limitations to conventional laser systems is that the carrier injection density required to create population inversion, at threshold, is of the order of $10^{13}/\text{cm}^2$ and $10^{20}/\text{cm}^3$, corresponding to quantum well (QW) and bulk material based active regions,

respectively (true for GaN based systems). Towards this direction, polariton lasers have a significant advantage, since the injection density required to trigger stimulated scattering accompanied by a macroscopic occupation of the final state, as will be discussed next, is at least more than two orders of magnitude lower.

What is a polariton laser ?

Before entering into the core of polariton laser, it is better to have a nice overview, how the idea of polariton lasing evolved. The long road to polariton lasers began back in 1925, when Albert Einstein proposed the idea that in the case of an ideal Bose gas, non-interacting bosons will condense in the lowest quantum state, below a critical temperature [2], referred to as Bose Einstein Condensation (BEC). This proposal however was not initially accepted by the scientific community based on Uhlenbeck's thesis, where he argued that it is impossible to observe BEC in a finite system [3]. The idea of BEC finally made a comeback with the observation of superfluidity in He-4 [4, 5], and with London proposing the theory to be related to BEC [6]. However, the highly interacting nature of He already in the liquid phase, was far from Einstein's idea of an ideal Bose gas. It should be noted that critical temperature, which is an important criterion for the observation of BEC, bears an inversely proportional relation to the effective mass. Taking into account the high effective mass of dilute atomic gases, extremely low temperatures are required for the realisation of BEC, which hindered its observation for a long time. Finally the breakthrough came in 1995, when BEC was observed in Rubidium [7] and Sodium [8] atoms, where the critical temperature was

of the order of $6\mu\text{K}$.

Meanwhile the idea of observing BEC in solids was suggested by Moskaleenko [9] and Blatt [10] in 1962, since the excitons of the system could be considered as a dilute Bose gas. The low effective mass of the excitons, of the order of m_o (electron mass), compared to that of the dilute atomic gases, of the order of $10^4 m_o$, offered significant advantage, since BEC could be observed at higher temperatures. The main limitation for excitonic systems was their short lifetimes, such that they failed to reach the lattice temperature, before recombination. Moreover, the weak binding energy resulted in a rapid loss of excitonic behavior, as the carrier density injected into the system was increased. In this field, a couple of works have been published, on different materials, where the results were positive to BEC, however failed to be conclusive [11, 12].

Exciton-polaritons are a type of polariton quasi-particles formed from the coupling of excitons to photons, usually referred to as composite bosons, since the fermionic part of the excitons, the electron and hole, do maintain their fermionic character. They are profusely found in bulk semiconductors, where they follow wavevector conservation i.e. an exciton that recombines to produce a photon, can couple strongly only to another exciton having the same wavevector, first suggested by Hopfield [13]. The attractive thing about polaritons was their extremely small effective mass, of the order of $10^{-5} m_o$, which could then help BEC realisation, at much higher temperatures. However, the lack of ways to engineer exciton polaritons remained as a barricade. The breakthrough came in 1992, when Weisbuch et al. [14] pointed out a way of engineering polaritons, by embedding an active GaAs semiconductor layer between Distributed Bragg Reflector (DBR) mirrors, forming microcavities. They

observed strong interaction between QW excitons and the cavity mode, resulting in an anti-crossing of the exciton and cavity mode dispersions [15], forming new polariton branches, corresponding to lower polariton branch (LPB) and upper polariton branch (UPB). At low wavevectors, the LPB (UPB) followed a more cavity (exciton) like behaviour, whereas at high wavevectors, the LPB (UPB) followed a more exciton (cavity) like behaviour. The newly formed, half-light half-matter quantum quasi-particles, were referred to as cavity polaritons. The cavity polaritons undergo polariton-polariton, and polariton-phonon scattering, and relax along the lower polariton branch, trying to reach the bottom of the trap. The most innovative thing in the design, was the ability to alter the properties of cavity polaritons formed, by engineering the active region, which in turn varied the cavity energy, the coupling strength and several other parameters. İmamoğlu and Ram in 1996, tried to harness this bosonic nature of polaritons, in a 2D microcavity system, in the presence of stimulated scattering, which then tends to accumulate at the bottom of the LP dispersion curve (trap), forming condensates [16]. The polaritons eventually recombine acting as a coherent source of monochromatic light, which is usually referred to as the polariton laser. However their observation for BEC was misleading, since the system was not in thermal equilibrium, and moreover they were in the weak-coupling regime – the operating regime of a vertical cavity surface emitting laser (VCSEL). Nevertheless their speculation based on the preliminary results initiated the idea of inversionless lasing, which has since then gained tremendous popularity, especially in the last two decades. It has to be noted that, since 1996, several works have been reported, successfully demonstrating polariton BEC in semiconductor microcavities [17, 18].

Why GaN membranes ?

Towards this direction, state of the art devices, based on this admixed quasiparticle has already been realised using GaAs [17, 19] and CdTe [20] active layers, although the accomplishment of room temperature polariton lasers has been limited, by their relatively weak binding energy. The high binding energy and oscillator strength, as well as the advantageous relaxation dynamics of wide bandgap semiconductors, such as GaN and ZnO, are well suited for room temperature polariton operation, demonstrated efficiently by [21–24]. Among the two materials systems, GaN is clearly more mature technologically, based on the availability of both types of doping. The current GaN based polariton lasers that rely on optical pumping use bulk GaN [21], GaN quantum wells (QW's) [22] and GaN nanowires [24], as the active layer. In the latter approach, individual nanowires positioned in a microcavity show remarkable polariton characteristics, but remains unclear how to turn them into real electrically-injected devices. The former two are currently limited by the relatively moderate quality of the active region, due to structural disorder introduced by the bottom GaN based Distributed Bragg Reflector (DBR) mirror. The relatively low quality of the DBR mirrors can be attributed to the large difference in lattice constants between III-nitride binaries, resulting in buildup of mismatch strain and cracking of the epitaxial structures [25, 26]. On the other hand, the use of lattice-matched binaries resulted in a very low stopband width comparable to the Rabi splitting of the polaritonic system [26–28]. In this context, the use of strain and structural disorder free, high quality, GaN membrane based active region, could be a very nice alternative. Moreover, GaN membranes also provide the feasibility of incorporating

high quality dielectric DBR mirrors into the microcavity system, having several advantages over semiconductor based DBR mirrors, which are as following: (1) relatively easy growth techniques like evaporation, Atomic Layer Deposition (ALD) and sputtering, rendering extremely high quality mirrors, (2) a large variety of materials to choose from, having a considerable difference in refractive indices (more the refractive index contrast between the two materials of a DBR stack, less the number of pairs of DBR stack required, to produce very high reflectivity mirrors, and (3) minimal absorption around the stopband region. These factors significantly boost up the Q-factor, as well as the β of a microcavity system. In addition, the use of ultra-smooth GaN membranes in microcavities is fully compatible with the realisation of electrically injected GaN polariton devices [29, 30].

Issues related to creating ultra-smooth GaN membranes

Ultra-smooth GaN membranes are usually prepared by conventional etching techniques. However, the fascinating robustness and chemically inert nature of the material makes processing of GaN a rather tedious task [31]. As a result, dry etching methods [32–35] are usually preferred over conventional wet etching [36], bringing along issues of ion induced damages as well as the inability to obtain very smooth side wall etches [36]. In this context, photo-electrochemical (PEC) wet etching of GaN, has recently turned out to be a very successful technique, yielding high quality surfaces [37–41]. Along this line, Trichas et al. made use of PEC etching in the lateral direction, selectively etching away an InGaN

sacrificial layer, creating very smooth GaN membranes [26], where the rms roughness was of the order of 6nm, measured by Atomic Force Microscopy (AFM).

About this work

The GaN membrane / active region containing GaN / AlGaIn quantum wells (QW's) is carefully engineered, by keeping the aluminium content ($\sim 5\%$) in the barriers very low, ensuring superior optical properties. PEC lateral etching is further optimised, etching away an InGaIn sacrificial layer that separates the membranes from the GaN template, creating ultra-smooth GaN membranes. The etched out membranes are embedded between dielectric mirrors, forming a full microcavity structure, on which polaritonic studies are performed, thereby leading to the development of a polariton laser. The work is basically divided into four chapters with an additional chapter at the end, which focuses on the study of GaN nanowires as a potential candidate for polaritonic studies.

The first chapter starts off discussing about the design and growth of samples, where the basic structure consists of the active region that is separated from the GaN template by an InGaIn sacrificial layer that ought to be etched using PEC lateral etching. Some basic optical characterisation is performed on the sample, from low temperature to room temperature, studying the various excitonic properties. The phenomenon of localisation of quantum well excitons is studied as a function of temperature. At room temperature however, the QW excitons have state of the art emission with a homogeneous linewidth of the order of 28meV and a lifetime of ~ 275 ps, quite suitable for polaritonic studies.

The second chapter initially describes the photo-electrochemical etching process, with a detailed description about the setup used. The PEC etching parameters are further optimised in the lateral direction, so as to achieve ultra-smooth 200nm-thick GaN membranes, with a ‘near-epitaxial’ rms roughness of $\sim 0.65\text{nm}$, as measured by AFM, approximately one order of magnitude lower than the previously reported values, where they used a very similar technique [26]. The evolution of photocurrent as etching progresses is analysed on the basis of oxide formation and dissolution during the process. The free-standing GaN membranes are subsequently transferred to a double-side polished sapphire substrate, on which optical characterisation is performed at cryogenic temperatures. Very sharp excitonic features are observed in both photoluminescence (PL) and transmission experiments, based on which the absorption coefficients for GaN are deduced, which turn out to be 30% higher than previously reported values [42].

The third chapter firstly discusses about the growth and properties of the subsequent top and bottom DBR mirrors that are eventually used in the full microcavity structure. The photo-electrochemical etching parameters used for creating ultra-smooth GaN membranes are then examined. The membranes are transferred to the bottom DBR / sapphire, forming a half-microcavity structure, on which optical characterisation is performed. Very sharp excitonic features are observed, along with the cavity mode, where the Q-factor is estimated to be ~ 85 . Some basic optical characterisation results from a half-microcavity structure, formed by transferring GaN membranes to the bottom DBR / sapphire is discussed, where the room temperature Q-factor is around 85. In addition, some simulations are performed as well, justifying the experimental results. The top DBR

is deposited on to the half-microcavity structure, in order to form the full-microcavity sample. Initially the full microcavity structure is studied based on simulation, where the coupling effects between the excitons and the cavity mode are not considered. This is followed by the demonstration of strong coupling, where a temperature dependent study unveils the strong coupling regime, giving a robust Rabi splitting as large as 64meV, at room temperature. The Q-factor of the system is estimated to be ~ 1770 , very close to the theoretical prediction.

The fourth chapter investigates the non-linear properties, in a GaN membrane based full-microcavity structure, under non-resonant quasi-continuous excitation. Initially the theory of polariton lasing / condensation is discussed, followed by experimental evidence, supported by modelling. Polariton lasing is confirmed, under the strong coupling regime, where the average power density at threshold is $\sim 4.5\text{W} / \text{cm}^2$ ($\sim 594\mu\text{J} / \text{cm}^2$), the lowest ever reported for 2D-GaN based systems [22]. A beautiful condensation pattern is observed in the k-space, above threshold, which is attributed to a site specific polariton trapping mechanism, in a square-like pocket. Taking into account this scenario, the non-linear properties are further analysed.

The fifth chapter is an additional work, investigating the suitability of GaN nanowires, as a potential candidate for polaritonic studies. The enhanced absorption in nanowire systems has recently gained popularity, where lots of research is being reported everyday [43–48]. Since the absorption coefficients are directly proportional to oscillator strengths, nanowires may find tremendous applications in the field of polaritonics, especially GaN nanowires, where the advantage of using GaN has already been discussed. Recently Das et al. have shown a very large Rabi split-

ting value [49] and an ultra-low threshold [24, 49] for their GaN nanowire based system, where a single nanowire is positioned at the antinode of the field distribution within the microcavity structure. In this context, a better understanding about the basic optical properties as well as absorption coefficients of GaN nanowires, might unravel its real potential. The chapter thus initially concentrates on the basic optical properties of high quality, strain free, GaN nanowires, which is followed by the demonstration of a new direct method, to extract absorption coefficients from as-grown GaN NWs grown on Si<111> substrates, using an all-optical method, merely by analysing the reflectivity spectra. This method can be extended to any family of NWs, provided they are grown on a substrate having considerable difference in permittivity with the nanowire-air matrix.

Bibliography

- [1] J. Piprek. “Edge-Emitting Laser”, *Semiconductor Optoelectronic Devices*. Elsevier, 2003, pp. 151–169.
- [2] A. Einstein. “Quantentheorie des einatomigen idealen Gases”, *Albert Einstein: Akademie-Vorträge*. Vol. 1. 3. Weinheim, FRG: Wiley-VCH Verlag GmbH & Co. KGaA, Sept. 2006, pp. 237–244.
- [3] G. E. Uhlenbeck. “Over statistische methoden in de theorie der quanta”. Gravenhage, 1927.
- [4] P. Kapitza. *Viscosity of liquid helium below the λ -point*. 1938.
- [5] J. F. Allen and A. D. Misener. *Flow of Liquid Helium II*. 1938.
- [6] F. London. “On the Bose-Einstein Condensation”, *Physical Review* 54.11 (Dec. 1938), pp. 947–954.
- [7] M. H. Anderson, J. R. Ensher, M. R. Matthews, C. E. Wieman, and E. A. Cornell. “Observation of bose-einstein condensation in a dilute atomic vapor.”, *Science (New York, N.Y.)* 269.5221 (1995), pp. 198–201.
- [8] K. Davis, M. Mewes, M. Andrews, N. van Druten, D. Durfee, D. Kurn, and W. Ketterle. “Bose-Einstein Condensation in a Gas of Sodium Atoms”, *Physical Review Letters* 75.22 (Nov. 1995), pp. 3969–3973.
- [9] S. A. Moskalenko. “Reversible optico-hydrodynamic phenomena in a nonideal exciton gas”, *Soviet Physics-Solid State* 4.1 (1962), pp. 199–204.
- [10] J. M. Blatt, K. W. Böer, and W. Brandt. “Bose-Einstein Condensation of Excitons”, *Physical Review* 126.5 (June 1962), pp. 1691–1692.
- [11] J. L. Lin and J. P. Wolfe. “Bose-Einstein condensation of paraexcitons in stressed Cu 2 O”, *Physical Review Letters* 71.8 (Aug. 1993), pp. 1222–1225.
- [12] S. Yang, A. T. Hammack, M. M. Fogler, L. V. Butov, and A. C. Gossard. “Coherence Length of Cold Exciton Gases in Coupled Quantum Wells”, *Physical Review Letters* 97.18 (Oct. 2006), p. 187402.
- [13] J. J. Hopfield. “Theory of the Contribution of Excitons to the Complex Dielectric Constant of Crystals”, *Physical Review* 112.5 (Dec. 1958), pp. 1555–1567.

-
- [14] C. Weisbuch, M. Nishioka, A. Ishikawa, and Y. Arakawa. “Observation of the coupled exciton-photon mode splitting in a semiconductor quantum microcavity”, *Physical Review Letters* 69.23 (Dec. 1992), pp. 3314–3317.
- [15] M. S. Skolnick, A. I. Tartakovskii, R. Butté, D. M. Whittaker, and R. M. Stevenson. “High-occupancy effects and stimulation phenomena in semiconductor microcavities”, *IEEE Journal on Selected Topics in Quantum Electronics* 8.5 (2002), pp. 1060–1071.
- [16] A. İmamoglu, R. J. Ram, S. Pau, and Y. Yamamoto. “Nonequilibrium condensates and lasers without inversion: Exciton-polariton lasers”, *Physical Review A* 53.6 (June 1996), pp. 4250–4253.
- [17] H. Deng, G. Weihs, D. Snoke, J. Bloch, and Y. Yamamoto. “Polariton lasing vs. photon lasing in a semiconductor microcavity”, *Proceedings of the National Academy of Sciences* 100.26 (Dec. 2003), pp. 15318–15323.
- [18] J. Kasprzak, M. Richard, S. Kundermann, A. Baas, P. Jeambrun, J. M. J. Keeling, F. M. Marchetti, M. H. Szymańska, R. André, J. L. Staehli, V. Savona, P. B. Littlewood, B. Deveaud, and L. S. Dang. “Bose-Einstein condensation of exciton polaritons.”, *Nature* 443.7110 (2006), pp. 409–414.
- [19] S. I. Tsintzos, N. T. Pelekanos, G. Konstantinidis, Z. Hatzopoulos, and P. G. Savvidis. “A GaAs polariton light-emitting diode operating near room temperature.”, *Nature* 453.7193 (May 2008), pp. 372–5.
- [20] R. Huang, Y. Yamamoto, R. Andre, J. Bleuse, M. Muller, and H. Ulmer-Tuffigo. “Exciton-polariton amplification based on exciton-exciton scattering in a CdTe quantum well”, *Technical Digest. Summaries of papers presented at the Quantum Electronics and Laser Science Conference. Postconference Technical Digest (IEEE Cat. No.01CH37172)* 65 (2001), pp. 1–7.
- [21] S. Christopoulos, G. von Högersthal, A. Grundy, P. Lagoudakis, A. Kavokin, J. Baumberg, G. Christmann, R. Butté, E. Feltin, J.-F. Carlin, and N. Grandjean. “Room-Temperature Polariton Lasing in Semiconductor Microcavities”, *Physical Review Letters* 98.12 (Mar. 2007), pp. 1–4.
- [22] G. Christmann, R. Butté, E. Feltin, J.-F. Carlin, and N. Grandjean. “Room temperature polariton lasing in a GaNAlGaN multiple quantum well microcavity”, *Applied Physics Letters* 93.5 (2008), p. 051102.

-
- [23] Y.-Y. Lai, Y.-P. Lan, and T.-C. Lu. “Strong light–matter interaction in ZnO microcavities”, *Light: Science & Applications* 2.6 (2013), e76.
- [24] A. Das, J. Heo, M. Jankowski, W. Guo, L. Zhang, H. Deng, and P. Bhattacharya. “Room temperature ultralow threshold GaN nanowire polariton laser”, *Physical Review Letters* 107.6 (2011), pp. 1–5.
- [25] J. Dorsaz, J.-F. Carlin, S. Gradecak, and M. Ilegems. “Progress in AlInN–GaN Bragg reflectors: Application to a microcavity light emitting diode”, *Journal of Applied Physics* 97.8 (Apr. 2005), p. 084505.
- [26] E. Trichas, N. T. Pelekanos, E. Iliopoulos, E. Monroy, K. Tsagaraki, A. Kostopoulos, and P. G. Savvidis. “Bragg polariton luminescence from a GaN membrane embedded in all dielectric microcavity”, *Applied Physics Letters* 98.22 (2011), p. 221101.
- [27] R. Butté, G. Christmann, E. Feltin, J.-F. Carlin, M. Mosca, M. Ilegems, and N. Grandjean. “Room-temperature polariton luminescence from a bulk GaN microcavity”, *Physical Review B* 73.3 (Jan. 2006), p. 033315.
- [28] G. Christmann, R. Butté, E. Feltin, J.-F. Carlin, and N. Grandjean. “Impact of inhomogeneous excitonic broadening on the strong exciton-photon coupling in quantum well nitride microcavities”, *Physical Review B* 73.15 (Apr. 2006), p. 153305.
- [29] T.-C. Lu, C.-C. Kao, H.-C. Kuo, G.-S. Huang, and S.-C. Wang. “CW lasing of current injection blue GaN-based vertical cavity surface emitting laser”, *Applied Physics Letters* 92.14 (Apr. 2008), p. 141102.
- [30] K. S. Daskalakis, P. S. Eldridge, G. Christmann, E. Trichas, R. Murray, E. Iliopoulos, E. Monroy, N. T. Pelekanos, J. J. Baumberg, and P. G. Savvidis. “All-dielectric GaN microcavity: Strong coupling and lasing at room temperature”, *Applied Physics Letters* 102.10 (2013).
- [31] W. C. Johnson, J. B. Parson, and M. C. Crew. “Nitrogen Compounds of Gallium. III”, *The Journal of Physical Chemistry* 36.10 (Jan. 1931), pp. 2651–2654.
- [32] I. Adesida, A. Mahajan, E. Andideh, M. A. Khan, D. T. Olsen, and J. N. Kuznia. “Reactive ion etching of gallium nitride in silicon tetrachloride plasmata”, *Applied Physics Letters* 63.20 (1993), p. 2777.

-
- [33] S. J. Pearton. “Dry and wet etching characteristics of InN, AlN, and GaN deposited by electron cyclotron resonance metalorganic molecular beam epitaxy”, *Journal of Vacuum Science & Technology A: Vacuum, Surfaces, and Films* 11.4 (July 1993), p. 1772.
- [34] A. T. Ping, I. Adesida, and M. Asif Khan. “Study of chemically assisted ion beam etching of GaN using HCl gas”, *Applied Physics Letters* 67.9 (1995), p. 1250.
- [35] R. J. Shul, G. B. McClellan, S. A. Casalnuovo, D. J. Rieger, S. J. Pearton, C. Constantine, C. Barratt, R. F. Karlicek, C. Tran, and M. Schurman. “Inductively coupled plasma etching of GaN”, *Applied Physics Letters* 69.8 (1996), p. 1119.
- [36] C. Youtsey, I. Adesida, and G. Bulman. “Highly anisotropic photoenhanced wet etching of n-type GaN”, *Applied Physics Letters* 71.15 (1997), p. 2151.
- [37] M. S. Minsky, M. White, and E. L. Hu. “Room-temperature photoenhanced wet etching of GaN”, *Applied Physics Letters* 68.11 (1996), p. 1531.
- [38] E. D. Haberer, R. Sharma, C. Meier, A. R. Stonas, S. Nakamura, S. P. DenBaars, and E. L. Hu. “Free-standing, optically pumped, GaMnGaN microdisk lasers fabricated by photoelectrochemical etching”, *Applied Physics Letters* 85.22 (2004), p. 5179.
- [39] L.-H. Peng, C.-W. Chuang, J.-K. Ho, C.-N. Huang, and C.-Y. Chen. “Deep ultraviolet enhanced wet chemical etching of gallium nitride”, *Applied Physics Letters* 72.8 (1998), p. 939.
- [40] E. Trichas, M. Kayambaki, E. Iliopoulos, N. T. Pelekanos, and P. G. Savvidis. “Resonantly enhanced selective photochemical etching of GaN”, *Applied Physics Letters* 94.17 (2009), p. 173505.
- [41] C. Youtsey, I. Adesida, L. T. Romano, and G. Bulman. “Smooth n-type GaN surfaces by photoenhanced wet etching”, *Applied Physics Letters* 72.5 (1998), p. 560.
- [42] J. F. Muth, J. H. Lee, I. K. Shmagin, R. M. Kolbas, H. C. Casey, B. P. Keller, U. K. Mishra, and S. P. DenBaars. “Absorption coefficient, energy gap, exciton binding energy, and recombination lifetime of GaN obtained from transmission measurements”, *Applied Physics Letters* 71.18 (1997), p. 2572.
- [43] L. Hu and G. Chen. “Analysis of optical absorption in silicon nanowire arrays for photovoltaic applications.”, *Nano letters* 7.11 (Nov. 2007), pp. 3249–52.

- [44] L. Tsakalacos, J. Balch, J. Fronheiser, M.-Y. Shih, S. F. LeBoeuf, M. Pietrzykowski, P. J. Codella, B. A. Korevaar, O. V. Sulima, J. Rand, A. Davuluru, and U. Rapol. “Strong broadband optical absorption in silicon nanowire films”, *Journal of Nanophotonics* 1.1 (2007), p. 013552.
- [45] Y. Lu and A. Lal. “High-Efficiency Ordered Silicon Nano-Conical-Frustum Array Solar Cells by Self-Powered Parallel Electron Lithography”, *Nano Letters* 10.11 (Nov. 2010), pp. 4651–4656.
- [46] L. Cao, J. S. White, J.-S. Park, J. A. Schuller, B. M. Clemens, and M. L. Brongersma. “Engineering light absorption in semiconductor nanowire devices.”, *Nature materials* 8.8 (Aug. 2009), pp. 643–7.
- [47] J. Kupec, R. L. Stoop, and B. Witzigmann. “Light absorption and emission in nanowire array solar cells.”, *Optics Express* 18 (2010), pp. 27589–27605.
- [48] P. Kailuweit, M. Peters, J. Leene, K. Mergenthaler, F. Dimroth, and A. W. Bett. “Numerical simulations of absorption properties of InP nanowires for solar cell applications”, *Progress in Photovoltaics: Research and Applications* 20.8 (Dec. 2012), pp. 945–953.
- [49] A. Das, P. Bhattacharya, J. Heo, A. Banerjee, and W. Guo. “Polariton Bose-Einstein condensate at room temperature in an Al(Ga)N nanowire-dielectric microcavity with a spatial potential trap.”, *Proceedings of the National Academy of Sciences of the United States of America* 110.8 (2013), pp. 2735–40.

This page is intentionally left blank

1.1 Introduction

The growth of the samples, consisting of GaN / AlGaN quantum wells (QW's) in the active region is initially discussed, where the aluminium content ($\sim 5\%$) of the barriers is carefully selected, so as to ensure enhanced optical properties, which is confirmed by performing basic optical characterisation of the samples using photoluminescence (PL) and reflectivity measurements. Very sharp excitonic features are observed at low temperature, with superior QW excitonic emission up to room temperature (RT), where the homogeneous linewidth is $\sim 28\text{meV}$. The phenomenon of localisation of QW excitons is studied as a function of temperature. A further understanding of the quality of the samples is obtained by performing some time resolved photoluminescence measurements, where the RT lifetime of the dominant QW excitonic peak is $\sim 275\text{ps}$.

1.2 Samples studied

The GaN layers are grown along the [0001] direction by plasma-assisted molecular beam epitaxy (MBE), on a c-axis n-doped GaN template, $\sim 9\mu\text{m}$ thick, which in turn is grown on sapphire by metal organic chemical vapour deposition (MOCVD), as shown in Figure 1.1. All the samples studied in this work are based on two main samples, named as parent 'A'

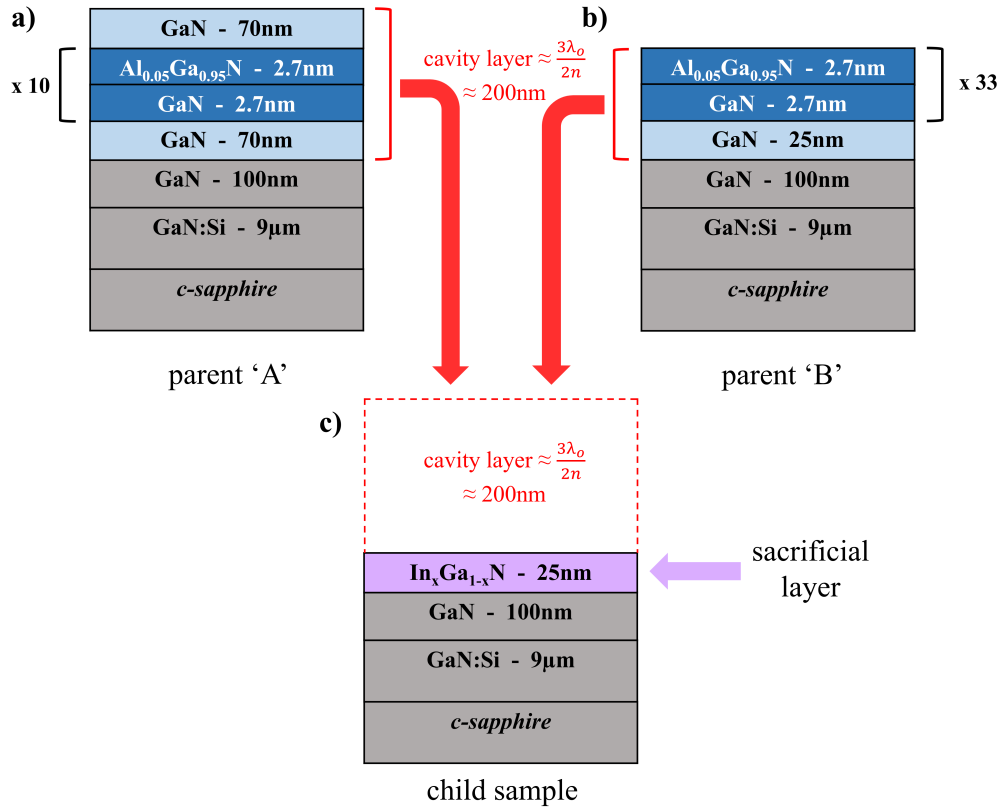


Figure 1.1: The active region corresponding to the two parent samples: (a) parent 'A', and (b) parent 'B'. (c) The possible structure of children samples, based on the two parent samples, separated from the template by an InGa_N sacrificial layer, that ought to be etched using PEC lateral etching.

and parent 'B', where the active region is 200-nm thick, as shown by red brackets in Figure 1.1 (a and b). Parent 'A' consists of 10 pairs of 2.7nm thick GaN/Al_{0.05}Ga_{0.95}N quantum wells (QW's), with 2.7nm thick barrier layers, embedded between 70nm thick layers of GaN, whereas parent 'B' has 33 pairs of similar QW's and barrier layers, with a 25nm thick GaN spacer layer in the bottom. The child sample has a similar active region like parent 'A' or parent 'B', the only difference being that the active region is separated from the template by a 25nm thick InGa_N sacrificial layer as shown in Figure 1.1 (c), that ought to be etched using photo-electrochemical (PEC) etching, creating ~ 200nm thick GaN membranes,

which will be described later in chapter 2. A number of such samples are grown, based on the active region from each parent, with different indium content in the sacrificial layer, hereby referred to as children samples. A complete summary of the samples studied are tabulated in the following table.

sample name	sample number	GaN template series	active region from	presence of InGaN sacrificial layer	In content (%)	area of investigation
sample 1	E2557	A	Parent 'A'	-	-	• basic optical characterisation
sample 2	E2794	C	Parent 'B'	-	-	• basic optical characterisation
sample 3	E2657	B	Parent 'A'	Yes	9	• optimising PEC etching
sample 4	E2662	B	Parent 'A'	Yes	12	• optimising PEC etching • all results under fabrication of ultra-smooth membranes • optical characterisation of GaN membranes on sapphire
sample 5	E2659	B	Parent 'A'	Yes	14.4	• optimising PEC etching
sample 6	E2796	C	Parent 'B'	Yes	11.5	• polaritonic studies on GaN membranes

Table 1.1: A complete summary of the samples studied.

The aluminium content in the QW barriers ($\sim 5\%$) is carefully chosen such that, confinement as well as a reduction in the strain and piezoelectric field, within the active layer can be achieved. The aluminium composition in the active regions as well as the indium content in the sacrificial layers, of the subsequent samples, are accurately determined by X-ray diffraction measurements, which very well adheres to the growth condition values. Moreover, the measurements also confirm that the full structure in all samples, is coherently strained on the GaN template. Samples 3,4 and 5, where the indium content varies from 9 to 14.4%, are used to optimise PEC etching conditions whereas, Sample 6 having an indium percentage of $\sim 11.5\%$, tailored to suit the optimised etching conditions,

is used for creating ultra-smooth GaN membranes, which are then embedded between dielectric mirrors, forming full microcavity structures, on which polaritonic studies are performed.

1.3 Basic optical characterisation

This section discusses some basic characteristics of the samples, indicative of its quality, by analysing PL / reflectivity data. Most of the results presented here are based on the parent samples: sample 1 and sample 2, since they are very identical to the data from the children samples (See Table 1.1).

1.3.1 Photoluminescence and Reflectivity with temperature

The PL/reflectivity measurements are made using the setup described under subsection A.2.1. He-Cd laser laser, at 325nm is used as a source for PL excitation whereas Xenon lamp is used for reflectivity. The grating used is the 2400 grooves/mm, for high resolution. See section A.1 for more information.

1.3.1.1 Low temperature results

The PL (black) and reflectivity (red) from sample 1 (left) and sample 2 (right), at 23K, are shown in Figure 1.2. The ‘A’, ‘B’ and ‘C’ excitons of GaN substrate are denoted as A_{GaN} , B_{GaN} and C_{GaN} respectively whereas those of QW are denoted as A_{QW} , B_{QW} and C_{QW} . In Figure 1.2 (a), the three excitons of GaN can be easily identified in the reflectivity spectrum, based on the energy difference between the corresponding peaks, which is well know for MBE grown GaN layers on sapphire. Moreover their po-

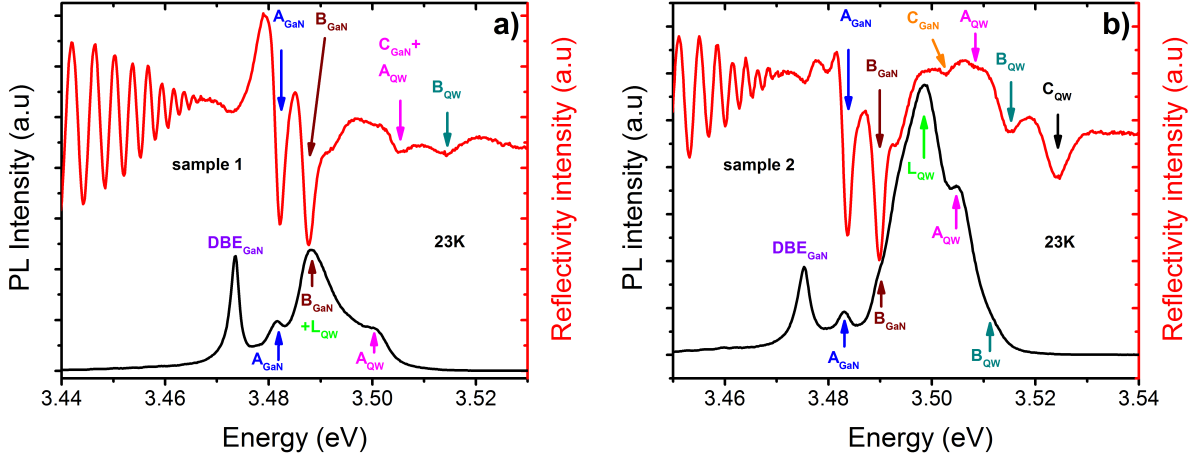


Figure 1.2: A comparison of PL (black) and Reflectivity (red) at 23K from (a) sample 1, and (b) sample 2, exhibiting various excitonic features.

sitions are confirmed by comparing with the reflectivity data of the sole GaN template. In the PL, A_{GaN} is clearly visible although the emission corresponding to B_{GaN} appears to be strangely superior than A_{GaN} . This dominance in emission thus leads to the attribution of the respective peak to localised QW emission (L_{QW}) apart from B_{GaN} , thereby naming the peak as $B_{GaN} + L_{QW}$. This assignment is further supported by temperature dependent PL measurements which will be discussed later. On the higher energy side of this peak, we see another dominant emission peak in the PL, close to the energy position of C_{GaN} , as seen in reflectivity. The peak has an intensity similar to A_{GaN} , ruling out the possibility of having decisive contributions from C_{GaN} , instead this peak is attributed to A_{QW} . The C_{GaN} peak in reflectivity is therefore named as $C_{GaN} + A_{QW}$. B_{QW} is visible in the reflectivity at a higher energy, though at low temperature (LT), is not visible in the PL. C_{QW} is relatively very weak in the PL as well as reflectivity.

In Figure 1.2 (b), similar to sample 1, the three GaN excitons are located on the reflectivity spectrum. A_{GaN} and B_{GaN} can be uniquely

identified on the PL, although C_{GaN} is hardly visible. The dominant PL peak can be attributed to localised QW emission (L_{QW}), similar to sample 1. At a higher energy from L_{QW} , two other peaks are visible in the PL, named as A_{QW} and B_{QW} , with corresponding peaks in the reflectivity as well. C_{QW} is visible in reflectivity, though not very clear in PL, at LT. In both samples, the PL from the QW is quite superior to that of GaN, with a line-width of ~ 5.5 meV and 6.5 meV, in sample 1 and sample 2 respectively, estimated from the dominant peak (L_{QW}). They compare very closely to 2.3 meV and 3.4 meV, which are the linewidths of the corresponding GaN donor bound excitonic (DBE) peaks, confirming the high quality of the QW's and the minimal inhomogeneous broadening, attributed to the low aluminium content in the QW barriers of $\sim 5\%$. Although the QW's in both samples are very identical, the difference in the number of QW's, causes a shift in the QW peak emission energies, confirming the fact that quantum confined stark effect (QCSE) cannot be neglected even in shallow QW's or to say that the internal field profile in the two samples is different. The GaN emission peak energies as well as line-widths from the two samples, as seen in Figure 1.2, are slightly different, originating from the two different GaN template series used (see Table 1.1).

1.3.1.2 Delocalisation of quantum well excitons with temperature

The localisation of excitons in GaN QW's is a quite well known phenomenon [1–4]. The fluctuations in the well or barrier width as well as the variation of aluminium content in the barriers, in the subsequent MBE grown QW layers, are the main cause of in-plane disorders in GaN/AlGaIn QW's, causing localisation of excitons resulting in large inhomogeneous

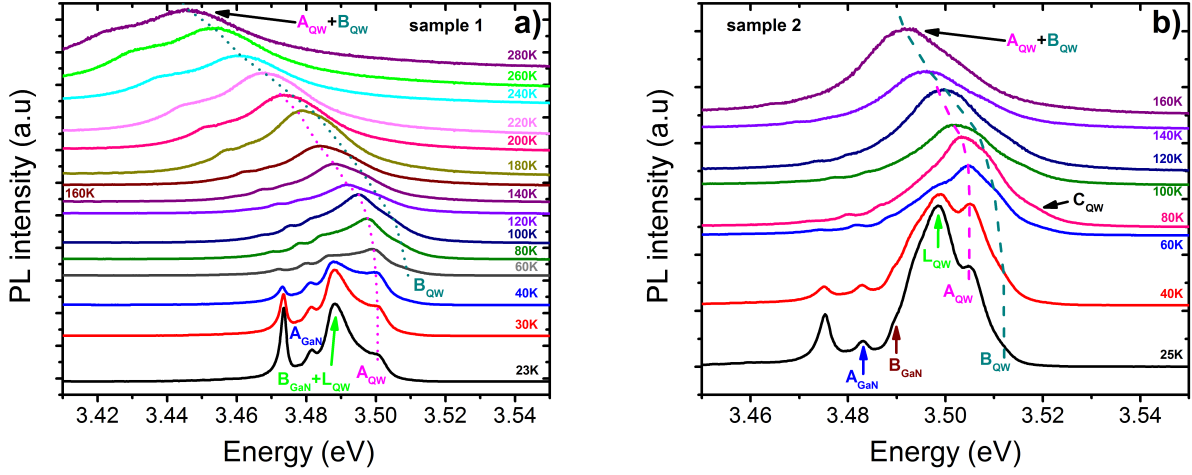


Figure 1.3: Evolution of QW excitons with temperature, based on PL, for: (a) sample 1, and (b) sample 2, where the delocalisation behaviour is evident.

broadening of the QW peaks [1, 3, 4]. In the samples studied here, the effect seems to be minimal although cannot be neglected completely. As the temperature is increased, the excitons are seen to red-shift and broaden, in line with excitonic behavior, as shown in Figure 1.3. A very quick reduction in intensity of the $B_{GaN} + L_{QW}$ peak is seen in Sample 1, as shown in Figure 1.3 (a), with A_{QW} excitons getting dominant already at 60K. Considering the high binding energy and oscillator strength of B_{GaN} excitons, the strong reduction in intensity can only be correlated to delocalisation of QW excitons. Moreover B_{QW} excitons also start getting visible around 80K. With further increase in temperature, both A_{QW} and B_{QW} red-shift, with B_{QW} slowly gaining importance, which can be attributed to the stronger oscillator strength and the relatively smaller broadening of B_{QW} , as opposed to A_{QW} . At around 240K, A_{QW} and B_{QW} merge together and continue to red shift and broaden, up to room temperature. The dotted lines in Figure 1.3 (a) guide the eye to follow the evolution of A_{QW} and B_{QW} , with temperature.

The behaviour of sample 2, with temperature, as shown in Figure 1.3 (b),

is again similar to sample 1, with a subsequent red-shift and broadening of excitons. The localised peak L_{QW} quickly loses its prominence, already at 40K, with A_{QW} gaining dominance at around 60K. B_{QW} follows a red-shift along with A_{QW} , right from 23K, achieving a relative gain in intensity with temperature, which can again be attributed to the stronger oscillator strength and broadening effects, as explained earlier. C_{QW} starts to be visible around 80K, after which it starts to follow a red-shift similar to A_{QW} and B_{QW} . At around 140K, A_{QW} and B_{QW} completely merge with each other, with C_{QW} seen as a weak shoulder on the higher energy side. With further increase in temperature, the merged A_{QW} and B_{QW} , dominantly continue to red-shift along with C_{QW} up to room temperature, although it is very hard to distinguish the C_{QW} line. Figure 1.3 (b) shows the temperature dependence only up to 160K, for a better dynamic view of the QW excitonic behavior at lower temperatures. The dotted lines guide the eye to follow the evolution with temperature, of mainly A_{QW} and B_{QW} peaks, with C_{QW} seen as a very weak shoulder.

1.3.1.3 Room temperature results

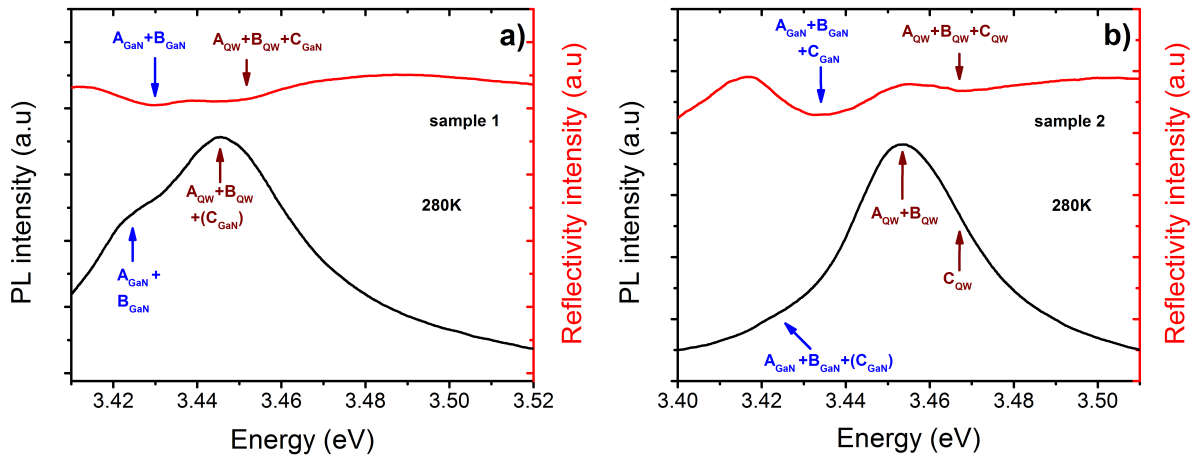


Figure 1.4: A comparison of PL (black) and Reflectivity (red) at 280K from (a) sample 1, and (b) sample 2, exhibiting various excitonic features.

Figure 1.4 shows the PL (black line) and reflectivity (red line), of sample 1 (left) and sample 2 (right), at RT. In Figure 1.4 (a), two peaks are visible in the PL as well as reflectivity. The dominant peak in PL, corresponds to a peak in reflectivity that has contributions from A_{QW} , B_{QW} and C_{GaN} . The relative intensity of C_{GaN} in comparison to the merged $A_{QW} + B_{QW}$ peak, as mentioned in the previous subsection, should be very weak, due to which the dominant PL peak is named at $A_{QW} + B_{QW} + (C_{QW})$. The weak shoulder in the PL, corresponds to merged $A_{GaN} + B_{GaN}$ peak, with a clear signature in the reflectivity as well. In line with the discussion under subsection 1.3.1.2, at around 220K, as seen in Figure 1.3 (a), A_{GaN} merges with B_{GaN} , clearly visible up to RT.

In Figure 1.4 (b), a dominant PL peak with a hardly distinguishable shoulder on the higher energy side is the merged $A_{QW} + B_{QW}$ peak and C_{QW} peak respectively, as described in the previous subsection. In reflectivity, corresponding to the position of C_{QW} , a peak is visible though it also has contributions from A_{QW} and B_{QW} , due to which it is named as $A_{QW} + B_{QW} + C_{QW}$. The peak in reflectivity on the lower energy side has contributions from A_{GaN} , B_{GaN} and C_{GaN} . The corresponding peak in PL, is due to merging of individual A_{GaN} and B_{GaN} peaks as seen in the LT spectrum of Figure 1.2 (b), The C_{GaN} is not observable in the PL even at high temperatures (See Figure 1.3 (b)), although their contribution to the merged $A_{GaN} + B_{GaN}$ peak at RT cannot be completely neglected, due to which the PL peak is named as $A_{GaN} + B_{GaN} + (C_{GaN})$ as shown in Figure 1.4 (b). The linewidth of the dominant QW peak from both samples, at RT, is around 28 to 30 meV, comparing very closely to GaN linewidths at RT, and much larger than their respective LT linewidths. In other words, the QW emission at RT can be safely assumed to be

homogeneous.

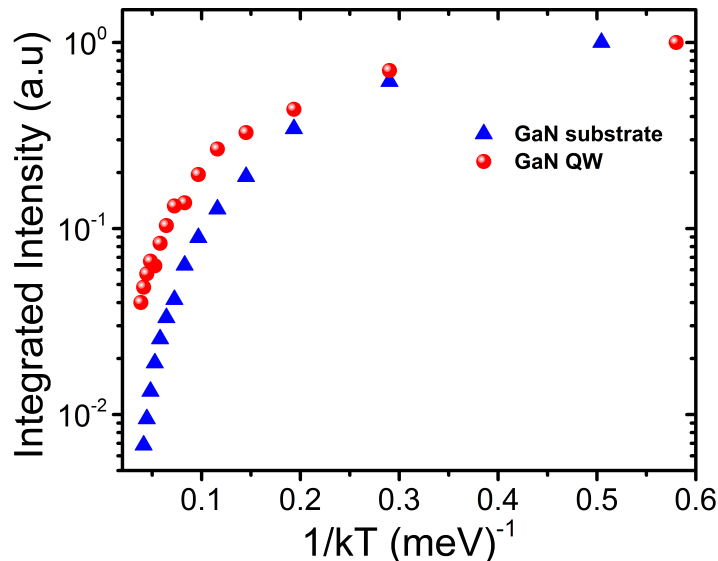


Figure 1.5: A comparison of the integrated intensity between QW emission from sample 2 and GaN emission from bare GaN template, where the fall in intensity from LT to RT is ~ 6 times better for sample 2 as opposed to bare GaN template.

Figure 1.5 shows the integrated intensity as a function of temperature. A comparison is made between QW emission from sample 2 and the GaN emission from the bare GaN template used to grow sample 2. The fall in QW intensity from LT to RT is around 25 times as opposed to GaN, which is like 146 times, clearly confirming the superior temperature behaviour of the QW's, making them excellent candidates for polaritonic studies.

1.3.2 Time resolved photoluminescence with temperature

All TRPL measurements are made on sample 2, from 5K to 300K, using the setup described under subsection A.2.2, where the excitation power density is very low i.e. a regime where the exciton-exciton interaction can be neglected. At 5K, being limited by the grating used, only one dominant QW peak is resolved, unlike the three shown in Figure 1.2 (b), which is the peak studied up to RT, in order to extract the QW lifetimes

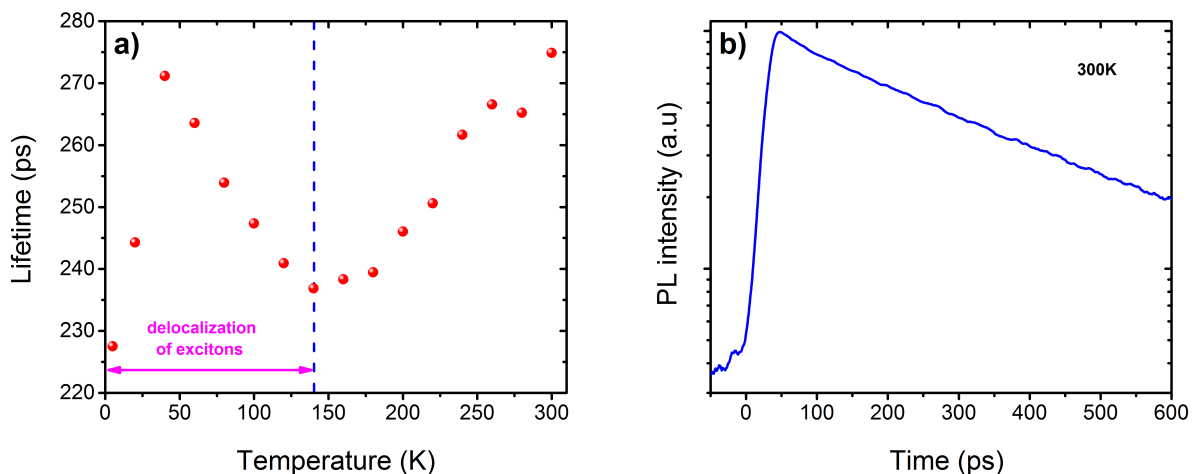


Figure 1.6: (a) Lifetimes extracted as a function of temperature from the dominant QW peak of sample 2, where the excitation power density is very low. (b) TRPL response at RT, for similar experimental conditions, from which the lifetime is extracted to be ~ 275 ps.

as shown in Figure 1.6 (a). At 5K, the lifetime is around 230ps, which gradually increases up to 40K, after which it shows a decreasing tendency up to 140K, before increasing again and turning out to be more or less stable after 265K. The lifetime of an exciton τ_{exc} is given by the relation:

$$\frac{1}{\tau_{exc}} = \frac{1}{\tau_R} + \frac{1}{\tau_{NR}} \quad (1.1)$$

where τ_R is the radiative lifetime and τ_{NR} is the non-radiative lifetime of the exciton. Usually in QW's, τ_R increases with temperature whereas τ_{NR} decreases. The effective lifetime (τ_{exc}) as a function of temperature thereby shows the following behaviour: first, an increase in the lifetimes, which is usually seen at LT's followed by a more or less constant lifetime regime, and finally a decrease in the lifetimes. The temperatures at which these different regimes are observed depend strongly on the material system under study along with its optical and structural quality. In good quality GaAs/AlGaAs QW's, the stabilised regime is usually around 150K. The behaviour in our sample is very much in line with this explana-

tion after 140K, where the lifetimes show a gradual increase up to $\sim 265\text{K}$, after which they seem to stabilise up to RT. At even high temperatures most probably a fall in lifetimes will follow. However the erratic behaviour up to 140K could only be attributed to the delocalisation of L_{QW} excitons as presented in subsection 1.3.1.2. As shown in Figure 1.3 (b), the L_{QW} line can be probed only up to $\sim 80\text{K}$, though complete delocalisation might be occurring at $\sim 140\text{K}$. The ‘inconsistent’ region is marked in Figure 1.6 (a), as the region towards the left of 140K - blue dotted line. Figure 1.6 (b) shows the very long QW lifetime at RT $\sim 275\text{ps}$, once again confirming its high optical quality and suitability as an active layer, for polaritonic studies.

Now in order to estimate τ_R and τ_{NR} from τ_{exc} , at RT, a procedure described in detail in [5], is followed. The time integrated photoluminescence intensity (I_{PL}) as a function of temperature is given by the relation:

$$I_{PL}(T) = \frac{I_o \tau_{exc}(T)}{\eta_o \tau_R(T)} = \frac{I_o}{\eta_o} \eta(T) \quad (1.2)$$

where $\eta(T)$ is the radiative efficiency as a function of temperature, I_o is a normalisation factor depending on the number of photoexcited carriers and η_o is the radiative efficiency associated with I_o . Usually I_{PL} measured at very low temperatures (*low T*) like 2K or 5K, can be safely assumed to be completely radiative (proportional to the number of photoexcited carriers) in a good quality sample, considering the fact that the thermal energy is too small for the formed excitons, to move around and find a non-radiative trap. In such a scenario $I_o = I_{PL}(\text{low } T)$. At this particular temperature used to estimate I_o , although assumed to be completely radiative, the situation might differ based on the quality of the sample. To account for this uncertainty in the radiative efficiency, η_o ($\eta(\text{low } T)$)

is varied from 0.1 to 1. These values are used in equation 1.2 to calculate $\eta(T)$ for different values of η_0 , which in turn is used in equations 1.3 and 1.4 to estimate $\tau_R(T)$ and $\tau_{NR}(T)$ for different values of η_0 .

$$\tau_R(T) = \frac{I_o \tau_{exc}(T)}{\eta_o I_{PL}(T)} = \frac{\tau_{exc}(T)}{\eta(T)} \quad (1.3)$$

$$\tau_{NR}(T) = \tau_{exc}(T) \left(\frac{1}{1 - \frac{\eta_o I_{PL}(T)}{I_o}} \right) = \tau_{exc}(T) \left(\frac{1}{1 - \eta(T)} \right) \quad (1.4)$$

Generally $\tau_{NR}(T)$, estimated for different values of η_0 tends to converge towards RT, giving a proper estimate for $\tau_{NR}(300K)$, which is used in equation 1.1 to calculate $\tau_R(300K)$. This approach is now applied to analyse the lifetimes from sample 2, by initialising $I_0 = I_{PL}(5K)$ and by varying η_0 ($\eta(5K)$) from 0.1 to 1. However $\tau_{NR}(T)$ estimated for different η_0 , shows a converging behaviour already around 160K, rather than towards RT, quite contrary to what is expected. This can be attributed to the erratic behaviour in the lifetimes up to 140K, as visible in Figure 1.6(a). In order to correlate free excitonic behaviour to lifetime rather than localisation effects, I_0 is considered equal to $I_{PL}(140K)$, with η_0 ($\eta(140K)$) varied from 0.1 to 1. Now using equations 1.2, 1.3 and 1.4, $\tau_R(T)$ and $\tau_{NR}(T)$ are estimated for different values of η_0 , as shown in Figure 1.7. It is evident from Figure 1.7 that τ_R increases with temperature whereas as τ_{NR} follows a decrease, in line with the usual quantum well behavior. Moreover from Figure 1.7 (b), τ_{NR} converges towards RT, for all the values of η_0 ($\eta(140K)$) from 0.1 to 1, returning an estimate of around 333ps at RT. Putting this value in equation 1.1, gives a radiative lifetime τ_R of ≈ 1.6 ns, at RT.

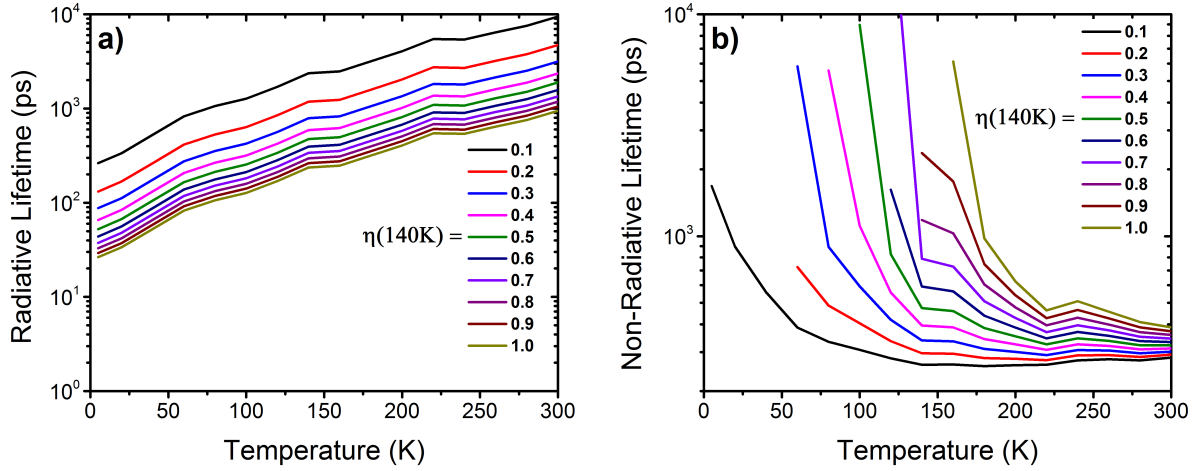


Figure 1.7: Evolution of (a) radiative lifetime (τ_R), and (b) non-radiative lifetime (τ_{NR}) with temperature, for different values of $\eta(140K)$, which is varied from 0.1 to 1.0.

1.3.3 Confirmation of indium percentage in the sacrificial layers based on photoluminescence

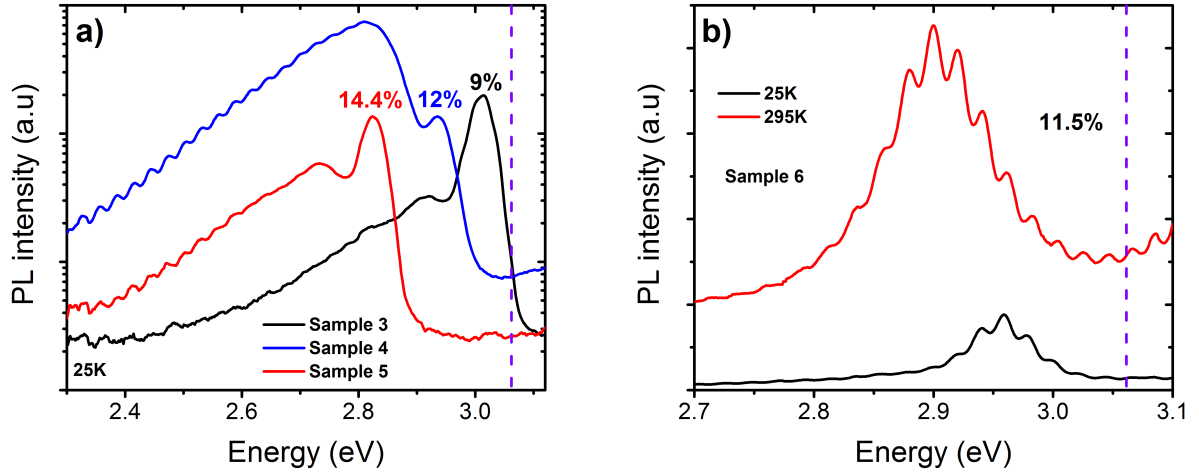


Figure 1.8: (a) PL from the $\text{In}_x\text{Ga}_{1-x}\text{N}$ sacrificial layer: (a) for samples 3, 4 and 5, at 25K, and (b) for sample 6 at 25K and 295K, where the PL peak energy shifts according to the variation in the indium concentration.

This section confirms the indium percentage in the $\text{In}_x\text{Ga}_{1-x}\text{N}$ sacrificial layer of the children samples, estimated from XRD, based on PL from the corresponding layer. The measurements are made on sample 3, sample 4, sample 5 and sample 6, using the setup described under the

subsection A.2.1. See Table 1.1 for further information on the samples studied. For the first three samples, He-Cd laser, at 325nm is used as a source for excitation whereas for the last sample, considering the high absorption in the 33 pairs of GaN/AlGaN QW's, the pulsed Nd-YAG laser, at 266nm is used. See section A.1 for further information on the lasers used. Figure 1.8 (a) shows the PL from the $\text{In}_x\text{Ga}_{1-x}\text{N}$ sacrificial layers, for samples 3, 4 and 5, at 25K whereas Figure 1.8 (b) shows the PL from sample 6, at 25K and 295K. The energy position of the PL peaks, in all 4 samples, are exactly in line with the In % determined from XRD i.e. the PL peak with the highest energy corresponds to the least In %.

1.4 Conclusion

A clear understanding of the quality of the samples is obtained, based on optical characterisation results. The aluminium content ($\sim 5\%$) in the barriers is found to be optimal, resulting in state of the art QW emission at RT, where the homogeneous linewidth is estimated to be $\sim 28\text{meV}$, confirming the suitability of the samples for polaritonic studies. The delocalisation of QW excitons is understood as a function of temperature, where most of the delocalisation occurs below 100K, in line with the low linewidth of the dominant QW peak, at RT. Moreover the lifetime of the respective peak is estimated to be $\sim 275\text{ps}$, further confirming the quality.

Bibliography

- [1] B. Chwalisz, A. Wyszomolek, R. Bozek, K. Korona, R. Stepniewski, W. Knap, K. Pakula, J. Baranowski, N. Grandjean, J. Massies, P. Prystawko, and I. Grzegory. “Localization effects in GaN/AlGa_N quantum well - Photoluminescence studies”, *Acta Physica Polonica A* 103.6 (2003), pp. 573–578.
- [2] J. A. Davidson, P. Dawson, T. Wang, T. Sugahara, J. W. Orton, and S. Sakai. “Photoluminescence studies of InGa_N / Ga_N multi-quantum wells”, *Semiconductor Science and Technology* 15.6 (2000), pp. 497–505.
- [3] J. Harris, T. Someya, K. Hoshino, S. Kako, and Y. Arakawa. “Photoluminescence of Ga_N Quantum Wells with AlGa_N Barriers of High Aluminium Content”, *physica status solidi (a)* 180.1 (July 2000), pp. 339–343.
- [4] E. Shevchenko, A. Toropov, D. Nechaev, V. Jmerik, T. Shubina, S. Ivanov, M. Yagovkina, G. Pozina, J. Bergman, and B. Monemar. “AlGa_N Quantum Well Heterostructures for Mid-Ultraviolet Emitters with Improved Room Temperature Quantum Efficiency”, *Acta Physica Polonica A* 126.5 (Nov. 2014), pp. 1140–1142.
- [5] M. Gurioli, A. Vinattieri, M. Colocci, C. Deparis, J. Massies, G. Neu, A. Bosacchi, and S. Franchi. “Temperature dependence of the radiative and nonradiative recombination time in GaAs/Al_xGa_{1-x}As quantum-well structures”, *Physical Review B* 44.7 (Aug. 1991), pp. 3115–3124.



This page is intentionally left blank



This page is intentionally left blank

Ultra-smooth GaN membranes by photo-electrochemical etching

2.1 Introduction

The principles of photo-electrochemical (PEC) etching are examined along with a detailed description about the setup used. The PEC lateral etching parameters are further optimised, to achieve ultra-smooth 200nm-thick GaN membranes, with a “near-epitaxial” rms roughness of $\sim 0.65\text{nm}$, as measured by Atomic Force Microscopy (AFM), approximately one order of magnitude lower than the previously reported values, where they used a very similar technique [1]. The evolution of photocurrent as etching progresses is analysed on the basis of oxide formation and dissolution during the process. The free-standing GaN membranes are subsequently transferred to a double-side polished sapphire substrate, on which optical characterisation is performed at cryogenic temperatures. Very sharp excitonic features are observed in both photoluminescence (PL) and transmission experiments. Moreover, absorption coefficients are deduced from the transmission spectra, based on which absorption coefficients of GaN excitons, turned out to be at least 30% higher than previously reported values [2].

2.2 Samples studied and initial processing

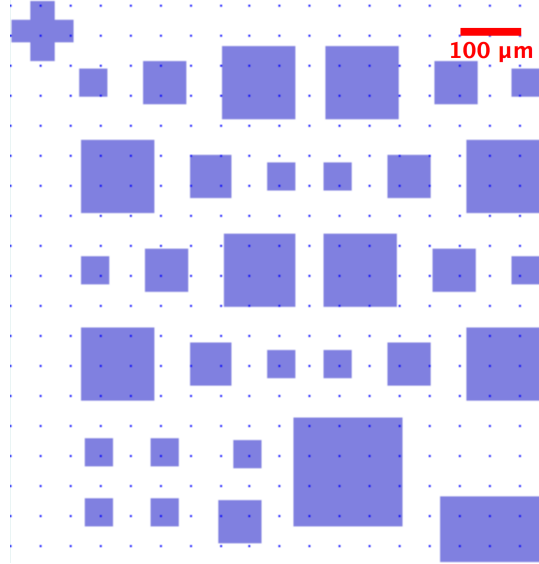


Figure 2.1: Mask pattern used for RIE, where the dimensions range from 45×45 to $155 \times 155 \mu\text{m}^2$.

The samples on which PEC lateral etching is undergone, to create ultra-smooth membranes are tabulated in Table 1.1, although sample 3, 4 and 5 are used for optimising the etching conditions. The three samples have the same active region, separated from the GaN template, by an InGaN sacrificial layer, although the indium content in the sacrificial layers corresponding to the three samples are different (Refer section 1.2 and subsection 1.3.3 for more details). The samples are initially patterned into $1 \mu\text{m}$ -high square mesas of various dimensions ranging from 45×45 to $155 \times 155 \mu\text{m}^2$, using Reactive Ion Etching (RIE), so as to expose laterally the InGaN sacrificial layer, for selective PEC etching. The mask pattern used for RIE, is depicted in Figure 2.1. The 200nm GaN membranes etched out from sample 5 are used for optical characterisation.

2.3 Photo-electrochemical (PEC) etching setup

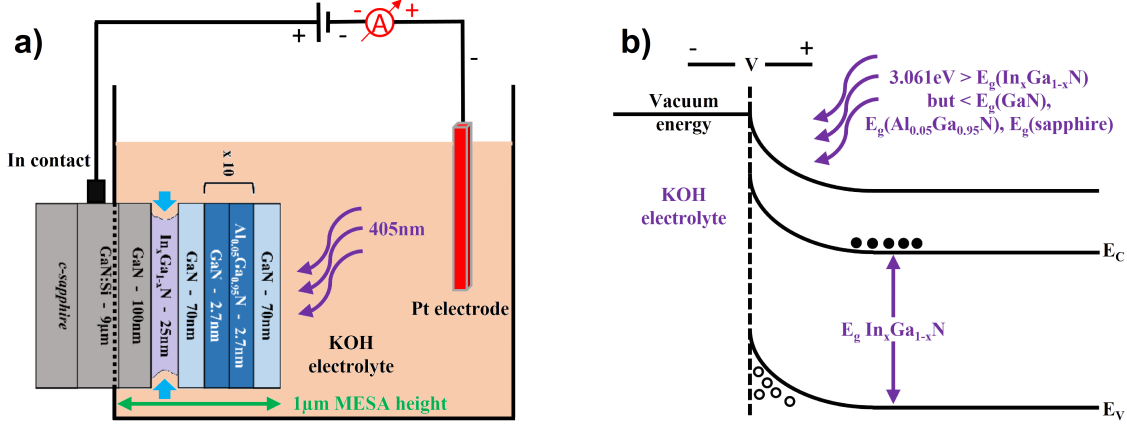
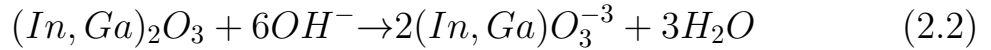


Figure 2.2: (a) PEC lateral etching setup, where the etching is shown to take place on a single MESA, under the application of a reverse bias, accompanied by a light source. (b) Band alignment during the etching process, under similar experimental conditions.

PEC lateral etching is carried out in an electrochemical cell at room temperature, using KOH electrolyte with the sample acting as cathode and a platinum electrode as anode, as shown in Figure 2.2 (a). The sample shown here is just a single mesa, for simplicity, whereas in reality a large number of mesa's can be etched simultaneously, limited by the illuminated / wetted area on the sample, which is $\sim 0.0078 \text{ cm}^2$. The structure of the sample shown here is a replica of the samples used for PEC lateral etching optimisation (See Table 1.1). The $1\mu\text{m}$ deep mesa's enable the bias to be applied on to the n-type GaN template (n-type) layer, on which the active region consisting of QW's is grown, using an ohmic indium contact as shown in Figure 2.2 (a). The electrolyte-semiconductor interface behaves like a metal-semiconductor (n-type) Schottky junction [3], resulting in band bending at the interface, where the holes are held towards the surface whereas the electrons are drawn inside, similar to Figure 2.2 (b). The etching is initiated by applying a reverse bias on the sample accompanied

by a light source having an energy greater than the bandgap of InGaN whereas less than the bandgap of the other subsequent layers. The n-type GaN template further favours the application of field in the structure with the reverse bias intensifying the Schottky band bending at the interface as shown in Figure 2.2 (b), confining the holes more towards the surface [3]. The lateral etching process can be described by the following chemical reactions:



The first equation describes the oxidation procedure of *InGaN* where the dissociated OH^- ions from the electrolyte react with the holes held towards the sample surface forming oxides with water and nitrogen as the by-products. The oxides formed further undergo a dissolution process as described by equation 2.2.

The etching quality is determined by several factors such as the energy of light source used, the bias voltage applied and finally the molarity of electrolyte which are referred to as etching parameters. A 405nm diode laser is used to excite the InGaN sacrificial layer, close to resonance, below the bandgap of GaN, which was shown to have enhanced etching rates by Trichas et al. [1, 4]. A Keithley 6517A electrometer is used as a voltage source and electrometer simultaneously where the voltage is varied from -10V to +10V. The in-situ measurement of current as a function of time provides an insight into the etching quality as well as

the progress of etching. All current measurements under reverse bias condition are positive due to the configuration of electrometer as shown in Figure 2.2 (a).

2.4 Optimising PEC lateral etching for ultra-smooth GaN membranes

In order to study the correlation of various etching parameters with the smoothness of GaN membranes, two sets of experiments with the following conditions are performed: (1) constant dc bias of 4V, average laser power of 4mW, and various concentrations of electrolyte from 0.1M down to 0.0004M, and (2) pulsed dc bias of 4V, average laser power of 4mW, and a fixed concentration of electrolyte at 0.0004M. Figure 2.3 (a) shows the IV characteristics of the electrolyte-semiconductor interface, where the voltage is varied from -10V to +10V, measuring both the dark and light currents, for an average laser power of 4mW and an electrolyte concentration of 0.0004M. The inset of the figure, depicts a magnification of the positive bias regime. The general response is quite indicative of a Schottky behaviour with the magnitude of light current being higher than that of dark current. In the region of interest i.e, the positive bias (reverse bias) regime, the dark currents are almost zero as visible in the inset of Figure 2.3(a), confirming that etching rate is minimal in the absence of light. However, in the presence of light, it is evident from the figure that using higher bias voltages, of the order of 8V or 10V, can help in achieving higher etching currents and thereby reducing the overall etch time. But nevertheless, higher bias voltages do create excessive bubbling as etching proceeds, inhibiting the uniform exposure of the sample surface, resulting

in bad etching. Low voltages in turn, of the order of 2V, result in a very low etch current, increasing the etching time to large extents, like hours, although extremely smooth membranes could be achieved. Thus a bias voltage of 4V is a trade-off between etching times and smoothness. The laser power chosen is the maximum output of the laser at hand, as the higher is the excitation, the more numerous are the photo-carriers which can actively participate in the etching process, thus increasing the etch current and reducing the overall etch time.

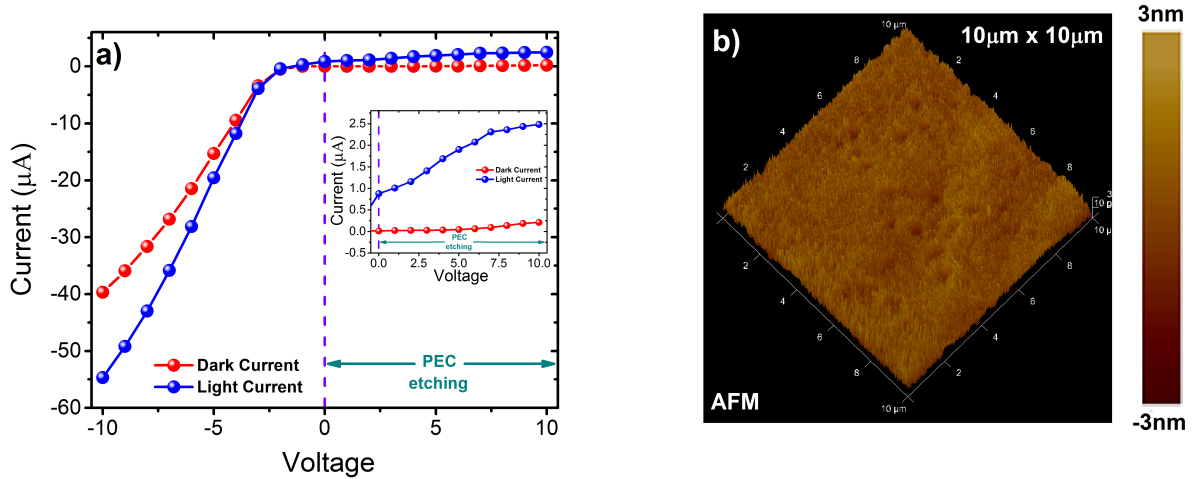


Figure 2.3: (a) IV characteristics of the electrolyte-semiconductor interface, at dark and light conditions, where the average laser power is 4mW and the electrolyte concentration is 0.0004M. The inset depicts a magnification of the positive bias regime. (b) 10x10 μm^2 AFM image from a GaN membrane transferred to double sided tape exhibiting very low roughness, on the bottom N-face GaN surface.

Firstly PEC is carried out according to the etching conditions described in the first set of experiments, by varying the concentration of KOH from 0.1M down to 0.0004M, on sample 4 having a moderate indium content as compared to samples 3 and 5, which is $\sim 12\%$. At higher concentrations, the etch currents are higher with lower overall etching time, and vice versa at lower concentrations. The overall etching time varies between 30 minutes for 0.1M to 150 minutes for 0.0004M. Inspection of the corresponding spots on the sample after etching, with an optical microscope,

clearly reflects the much better quality of membranes etched with the lowest concentration of electrolyte, i.e. 0.0004M, which required further confirmation through AFM measurements. In order to facilitate this, the membranes are transferred to a double sided tape and AFM measurements are undergone on the bottom N-face GaN surface. The measurements returned an rms roughness of $\sim 0.65\text{nm}$, as shown in Figure 2.3 (b) for the lowest electrolyte concentration used, over an area of $10 \times 10 \mu\text{m}^2$. This is approximately one order of magnitude lower than the 6nm reported by Trichas et al. [1], using electrolyte concentrations of the order of 0.01M. The very high quality of our membranes can be attributed to the very low etching rates, made possible by using 0.0004M, KOH electrolyte. The same experimental conditions along with a KOH molarity of 0.0004M are further used to perform PEC lateral etching on samples 3 and 5, having an indium content of 9 and 14.4% respectively. In the former, the excitation of the InGaN sacrificial layer is very resonant whereas, it is a bit off-resonant in the latter, as visible in Figure 1.8 (a), where the excitation energy is denoted by violet dashed lines. In sample 5, the same quality of extremely smooth membranes, with a similar AFM rms roughness of $\sim 0.65\text{nm}$, is achieved for an overall etching time of just 30 minutes, as opposed to 150 minutes taken by sample 4. However, in the case of sample 3, even after an etching period of ~ 180 minutes, the sample still remained unetched. This variation in etching times can directly be attributed to the different absorptions in the InGaN layer of the three samples, at 405nm, which in turn corresponds to their respective indium content i.e. high indium content sacrificial layer sample, more absorption at 405nm, less etching time, and vice versa. All further experiments and results, will be based on sample 4, etched using 0.0004M KOH solution, which produces

ultra-smooth membranes with etching times of ~ 150 minutes.

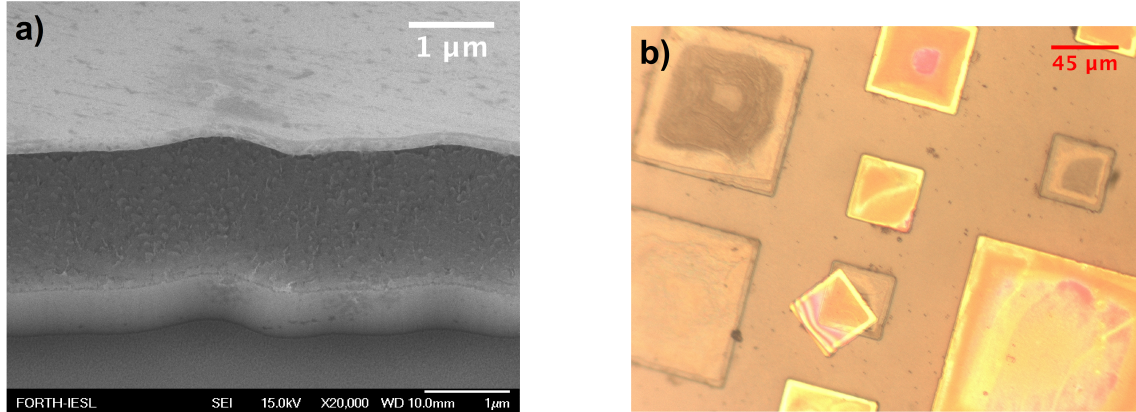


Figure 2.4: (a) SEM lateral view of a GaN membrane detached from substrate after PEC lateral etching. (b) Optical microscope image of an etched region clearly depicting regions with and without GaN membranes.

A SEM analysis is undergone on such a spot, with Figure 2.4 (a) showing the SEM lateral view of a GaN membrane, detached from the substrate. The InGaN sacrificial layer has been ‘eaten’ away by PEC. The wavy membrane edges cannot be attributed to the etching process, as they are also visible on the underneath mesa, where effectively etching does not take place. Instead, they are rather produced during the lithographic process, either by mask roughness or by RIE. Figure 2.4 (b) shows the optical microscope image of the etched spot, which clearly depicts regions with etched membranes lying on the substrate, as well as regions, where the membranes are completely removed, leaving an uncapped mesa behind. In the bottom-middle region, a membrane can be seen to be clearly displaced from its position, giving us a view of the mesa below as well. The black spots that are visible around the etched membranes are indium/gallium oxides formed as PEC etching progresses according to equation 2.1. Most of the oxide gets removed according to equation 2.2, as replenishment of hydroxyl ions to the sample surface takes place, although, a small portion

of it accumulates on the sample surface. Optical microscope image of the etched region, without cleaning the sample with deionised (DI) water, evidently indicates black oxide traces all around the etched region in contrary to the few spots seen in Figure 2.4 (b). Thus, cleaning of the sample with DI water is essential after etching, which however may result in the loss of few membranes. Moreover, a few membranes could also be seen sticking to the Teflon ring, which isolates the etching area from the rest of the sample. This may be due to the high tendency of Teflon to gather electrons on its surface and become negatively charged, thereby attracting the etched membranes to it.

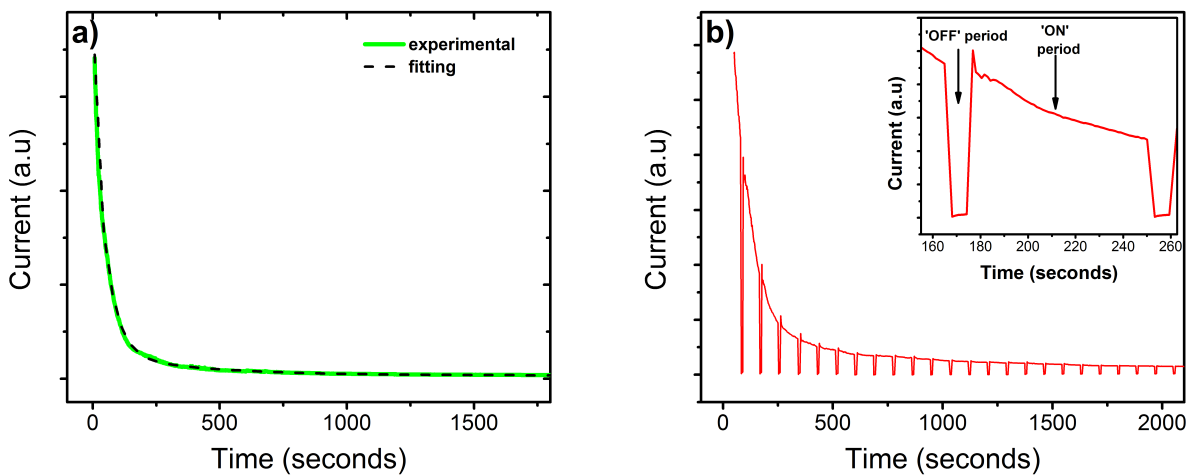


Figure 2.5: (a) Variation of photocurrent produced as etching progresses, under a constant dc bias of 4V. The dashed line through the experimental curve is a fitting with a double exponential. (b) Variation of photocurrent with etching time, under a pulsed dc bias of 4V. The inset shows the variation of photocurrent during a pulse period.

Figure 2.5 (a) shows the etching current (green line) as a function of time, at a constant dc bias of 4V, along with its fitting (black dashed line). The evolution of current follows a double exponential decay, with a very quick decay at the beginning of the order of 44 seconds, followed by a slow decay, of the order of 300 seconds. Initially, fresh electrolyte attacks the sample surface, where there are no oxides at all. Etching

takes place very efficiently, quickly forming oxides on the attacked surface, which gradually slow down the etching process, visible as a steep decay of the etching current. In parallel, the oxides also undergo a removal procedure according to equation 2.2, as replenishment of hydroxyl ions to the sample surface takes places. In short, the overall etching rate critically depends on the interplay between oxide formation and removal, processes that we define as internal etching parameters, to distinguish from the external parameters such as bias voltage, laser power and electrolyte concentration. As PEC commences, rapid oxide formation on the unexposed surface reduces swiftly the available sites, bringing the oxide formation and removal rates into an equilibrium, and leading to the slow decay regime of the etching current in Figure 2.5 (a). The slow decay regime reflects the gradual decrease of the amount of material to be etched, as the etching progresses.

To study this further, PEC etching is performed on sample 5, as per the etching parameters described in the second set of experiments. According to this setup, instead of 4V constant dc bias, a pulsed 4V dc bias is applied with an OFF period of around 10.9 seconds per pulse, providing some time for the additional replenishment of hydroxyl ions to the sample surface apart from the usual supply under PEC etching conditions, which also results in a simultaneous removal of formed oxides according to equation 2.2, after PEC etching takes place for a certain ON period. The overall current pattern, for pulsed 4V dc bias, as shown in Figure 2.5 (b), is almost similar to its constant counterpart. The inset of Figure 2.5 (b) zooms at the etching current variations during an OFF and ON period of a single 4V dc pulse. As soon as the voltage turns 0V during the OFF period, there is a steep fall in the etch current, followed

by a small exponential increase. The latter can be interpreted as due to removal of oxides, as replenishment of hydroxyl ions to the sample surface takes place. As soon as the voltage becomes 4V during the ON period, there is a small overshooting of current, followed by a sharp decrease corresponding to the rapid re-establishment of equilibrium, following which the etch current converges to values as if the OFF period never occurred. This characteristic seems to repeat during every pulse, although at longer times, it is gradually suppressed due to less available InGaN material. Overall, providing an OFF period does not make much of an impact on the etching quality and effective etching time, since similar RMS roughness with the same etching time of 30 minutes could be achieved in both cases.

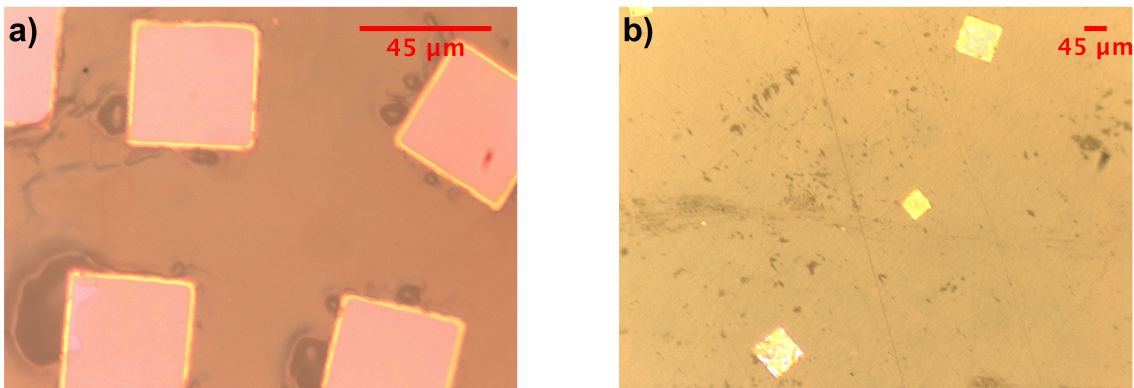


Figure 2.6: Optical microscope image of: (a) GaN membranes transferred to double sided tape, and (b) GaN membranes transferred to double-side polished sapphire substrate.

Figure 2.6 (a) shows an optical microscope image of the ultra-smooth membranes, transferred to a double-sided tape. The uniform colouration of the membranes with well-defined edges, further confirms the quality of etching in addition to the AFM measurements. Transferring the GaN membranes on double-sided tape has several drawbacks, such as the inability of performing optical characterisation at low temperatures, as paper

is a very bad thermal conductor, as well as transmission experiments, as paper is opaque in the UV region. Other possibilities such as carbon tape, used by Trichas et al. [1], also face similar issues. To solve this, we have developed a procedure to transfer the ultra-smooth membranes to a suitable substrate like double-side polished sapphire, as shown in Figure 2.6 (b). The GaN membranes are clearly visible, with uniform colouration and well-defined edges. AFM measurements further confirmed that the transfer process did not alter the quality of the membranes, as they returned similar RMS roughness of 0.65nm.

2.5 Optical characterisation

The PL/Reflectivity measurements on the sample before etching are made using the setup described under subsection A.2.1. The PL/transmission measurements on the membranes transferred to sapphire are made using the setup described under subsection A.2.3, which allows simultaneous measurement of PL and transmission from the same membrane. He-Cd laser, at 325nm is used as a source for PL excitation whereas Xenon lamp is used for transmission and reflectivity. The spectrometer grating used is the 2400 grooves/mm, to facilitate high resolution measurements. See section A.1 for more information.

2.5.1 Sample before etching

Before discussing the optical properties of membranes from sample 4 transferred to sapphire, PL and Reflectivity from bare sample 4 (blue lines), prior to processing, at LT, is compared with the PL of its parent sample: sample 1 (red line), as shown in Figure 2.7 (refer to Table 1.1 for

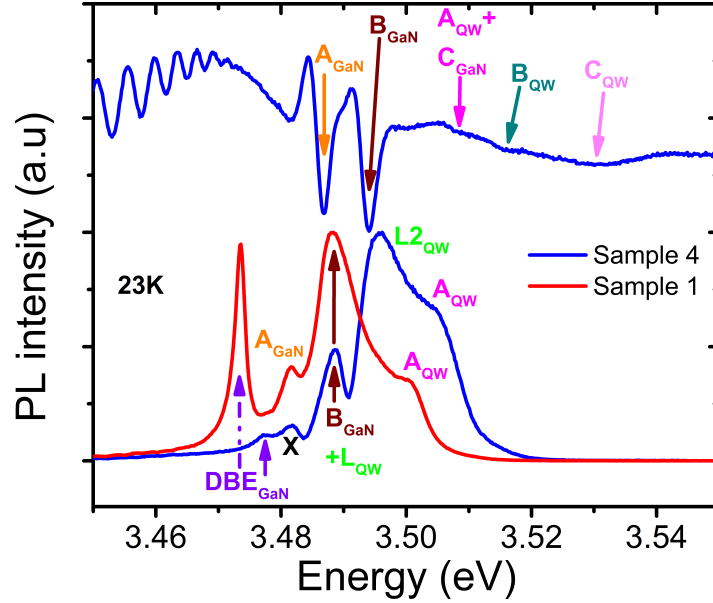


Figure 2.7: A comparison of PL and Reflectivity from bare sample 4 (blue lines), prior to PEC lateral etching, at LT, to the PL of its parent sample: sample 1 (red line), exhibiting various excitonic features.

more details on the samples). The basic PL from sample 4 is expected to be very similar to sample 1, considering the fact that the only difference in the structure being an additional InGaN sacrificial layer, in sample 4. However a small shift between the PL spectra, at least in terms of GaN excitonic positions, corresponding to the two samples is expected, taking into account the fact that the GaN template series used for either samples are different (see Table 1.1). The origin of the different peaks, in the PL from sample 1, has already been discussed under subsection 1.3.1, and so has been named accordingly. The ‘A’, ‘B’ and ‘C’ excitons of GaN can be easily located on the reflectivity spectrum based on the energy difference between the corresponding excitons which is well known for GaN grown on sapphire, being named as A_{GaN} , B_{GaN} and C_{GaN} respectively, as shown in Figure 2.7. The A_{GaN} peak seems to be a bit blue-shifted as opposed to parent sample 1, in line with the previous discussion. However corresponding to its position, in the PL of sample 4, no evident peak is visible.

Taking into account the blue shift, and by comparing the respective PL of sample 4 to that of sample 1, a few peaks like DBE_{GaN} and A_{QW} , can be easily identified, and thereby named accordingly. Approximately 4meV on the lower energy side of A_{GaN} reflectivity peak, in the corresponding PL a peak can be observed whose origin is unknown, which is thereby denoted as X. Corresponding to A_{QW} PL peak of sample 4, a weak peak is observed in the reflectivity at a position similar to C_{GaN} excitons, thereby renaming it as $\text{C}_{\text{GaN}}+\text{A}_{\text{QW}}$. On the higher energy side of this peak, in the reflectivity, two more peaks are observed, which are named as B_{QW} and C_{QW} respectively. B_{QW} is also observable in the reflectivity spectrum of sample 1 (see Figure 1.2 (a)) whereas C_{QW} is hardly visible. In between X and A_{QW} peaks in the PL from sample 4, two relatively strong peaks are visible, which can be attributed to localised QW emission. The peak around 3.49eV might have minimal contributions, from GaN ‘B’ excitons as well, based on the corresponding B_{GaN} peak in the reflectivity, thereby renaming it as $\text{B}_{\text{GaN}}+\text{L}_{\text{QW}}$. However, the B_{GaN} peak in the reflectivity is not renamed since the contribution of localised QW excitons is expected to be small. The peak around 3.495eV in the PL of sample 4 is named as L2_{QW} . Considering the blue-shift of GaN as well as GaN QW excitons in sample 4, as opposed to sample 1, it is not clear why the energy of $\text{B}_{\text{GaN}}+\text{L}_{\text{QW}}$ alone remains unchanged. Moreover an additional localised QW emission is visible as well, which has absolutely no traces in sample 1. To conclude, the general behaviour of sample 4 is very similar to its parent: sample 1, although the quality might be slightly compromised by the 25nm thick InGaN sacrificial layer, which is reflected by the presence of an additional localised QW emission peak. However the evolution of PL from sample 4, as well as the fall in QW emission intensity with tem-

perature is very similar to sample 1, assuring its suitability for polaritonic studies.

2.5.2 Ultra-smooth GaN membranes on sapphire

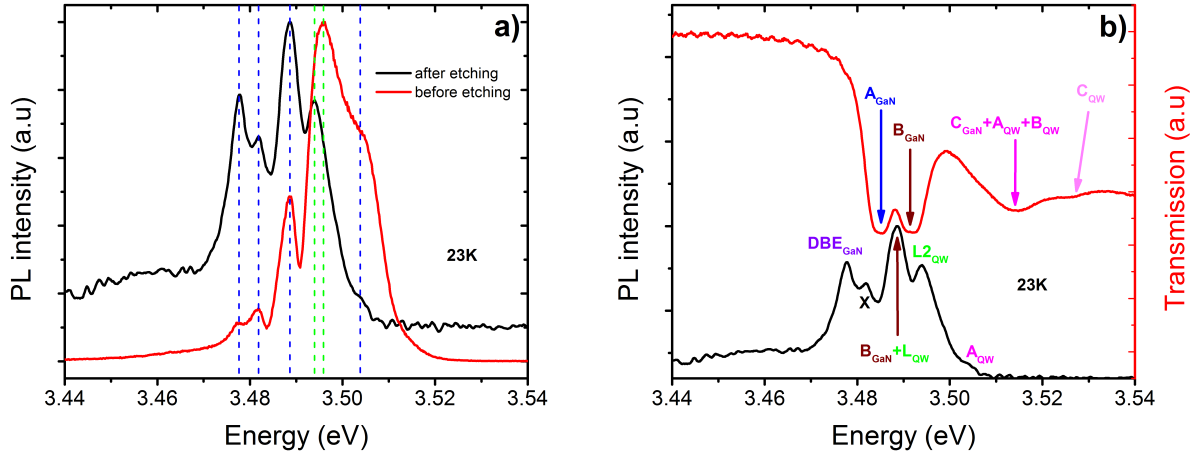


Figure 2.8: (a) Comparison of PL from sample 4 membrane, transferred to a double side polished sapphire substrate, to that of bare sample 4, prior to PEC lateral etching, showing the variation in intensity as well as energy position, corresponding to different peaks at LT. (b) Comparison of PL and transmission from a GaN membrane on sapphire substrate, etched out from sample 4, at LT, showing various excitonic features.

The high quality of the extremely smooth GaN membranes, on sapphire substrate is further testified through optical characterisation. Figure 2.8 (a) shows the PL from a sample 4 membrane (black line), compared to the PL from bare sample 4 (red line) before processing. The peaks in both spectra have a one to one correspondence, marked with blue dashed lines, except for a single peak which is denoted by a green dashed line on either spectra. The agreement in the peak positions of the main excitonic peaks like DBE_{GaN} , $B_{GaN} + L_{QW}$ and A_{QW} , prior to and after etching once again confirms that the whole structure including the InGaN sacrificial layer are coherently strained on the GaN template and rules out the possibility of any kind of strain induced in the structure by the InGaN sacrificial layer. Figure 2.8 (b) shows the PL and transmis-

sion spectra from membranes on sapphire, at LT. Basically four peaks are visible in the transmission spectrum from the lower energy side towards the higher energy. The first peak around 3.4850 ± 0.0002 eV has a very similar energy position to A_{GaN} excitons of sample 4, visible in the reflectivity spectrum of Figure 2.7, thereby naming the peak as A_{GaN} . The second peak corresponds to $B_{GaN}+L_{QW}$ peak in the PL, although it is named as just B_{GaN} , since the contribution of localised QW excitons to oscillator strength is small. Moreover its position is very similar to B_{GaN} peak, visible in the reflectivity spectrum from sample 4, in Figure 2.7. The third peak seems to be relatively broadened with an energy position lying in between $C_{GaN}+A_{QW}$ and B_{QW} peaks, as visible in the reflectivity spectrum of Figure 2.7. The peak can therefore be safely assumed to be a convolution of two peaks, naming it as $C_{GaN}+A_{QW}+B_{QW}$. The fourth peak can be attributed to C excitons of QW, thereby naming it as C_{QW} , having an energy position very similar to C_{QW} peak, visible in the reflectivity spectrum of Figure 2.7. Slight variations in the QW excitonic positions in Figure 2.7 and Figure 2.8 (b) are acceptable considering the fact that the signal is probed from different areas of sample 4. An initial PL mapping of all the samples, consisting of QW's, tabulated in Table 1.1, showed a maximum energy difference up to 7meV for the same QW peak, on different areas of the sample, being more uniform in the centre as opposed to the periphery.

The depth of the three peaks in the transmission spectrum clearly reflects the high oscillator strength of the related excitonic transitions, which is quite typical of GaN. In Figure 2.9 (a), temperature dependent transmission spectra are depicted up to 160K. The exciton lines clearly follow a red shift with temperature, along with a reduction in the oscillator

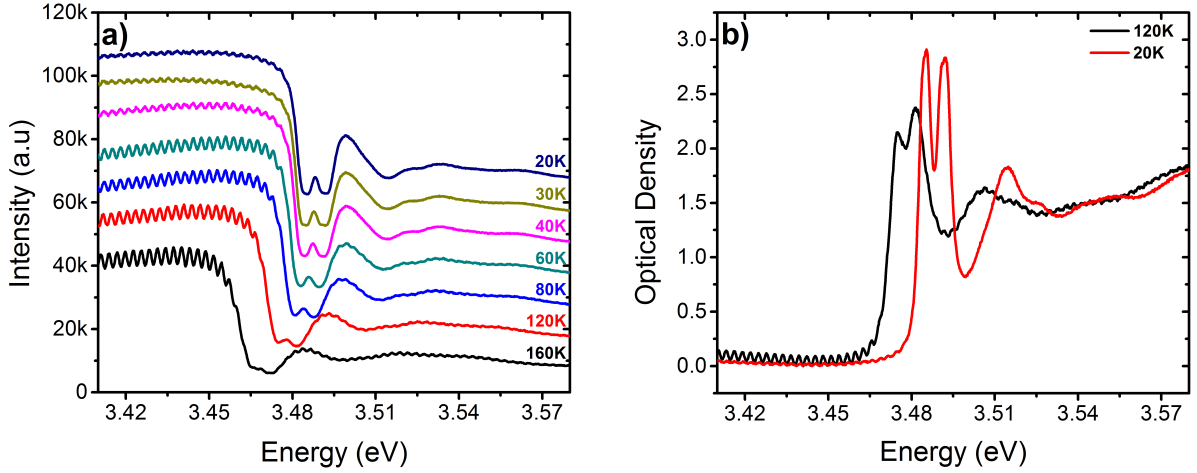


Figure 2.9: Optical characterisation of a GaN membrane transferred to double-side polished sapphire substrate: (a) temperature-dependent transmission spectra, and (b) optical density at 20K and 120K.

strength due to broadening, in line with previous reports for GaN [5]. The first two peaks, A_{GaN} and B_{GaN} , start merging with each other, due to broadening, at around 160K. The optical density of the membranes can be easily derived from the transmission spectrum using Beer Lambert’s law as follows:

$$I = I_0 e^{-OD} \quad (2.3)$$

where I is the intensity of transmitted light, I_0 is the reference intensity including the various reflections at the air/GaN, GaN/sapphire and sapphire/air interfaces, and OD the optical density. Assuming that the various reflections do not vary much around the GaN energy gap, we can estimate I_0 from the transmittance signal just below the band gap of GaN. The derived optical density spectra for the GaN membrane at 20K and 120K are shown in Figure 2.9 (b). At 20K, the first peak A_{GaN} , which is interpreted as GaN ‘A’ excitons, has an optical density of around 2.9, whereas the second peak B_{GaN} , which is attributed to GaN B excitons, has an optical density of 2.8. With temperature, the B_{GaN} line seems

to persist better having an OD of 2.4 at 120K, compared to 2.2 for the A_{GaN} line. Usually B excitons of GaN have a faster broadening than A excitons [5], which would have resulted in a quicker fall of the OD correlated to B_{GaN} , quite contrary to the observation here. This can only be explained by an additional contribution to the B_{GaN} oscillator strength from localised QW excitons, as depicted by $B_{GaN}+L_{QW}$ peak, in the PL of Figure 2.8 (b). The optical density can be correlated to the absorption coefficient according to the following relation:

$$OD = \alpha d \tag{2.4}$$

where α is the absorption coefficient and d the thickness of the layer. Assuming the thickness of GaN in the sample 4 membrane to be $\leq 140\text{nm}$ (Refer Table 1.1), the absorption coefficient corresponding to the A excitons turns out to be higher than $207,000\text{cm}^{-1}$ at 20K. This is about 30% higher than the α value reported by Muth et al. [2], which is around $95,000\text{cm}^{-1}$ at 295K and about $150,000\text{cm}^{-1}$ at 77K, for bulk GaN. Please note that this increase cannot be attributed to some error in estimating the GaN thickness, considering that the MBE nominal thicknesses are accurate to within $\pm 5\%$, and more importantly that the thickness of this particular membrane was independently confirmed using a Veeco Dektak 150 profilometer, which returned a value of around 190nm. Even assuming an uncertainty of 10% in the measured thickness by the profilometer, the estimated absorption coefficients of GaN A excitons would be still 20-25% higher than those reported by Muth et al. [2], further supporting our results. A possible explanation for this increase could be the ultra-smooth PEC lateral etching technique used to prepare the membrane in our case, where the sacrificial InGaN layer is selectively etched away, isolating the

GaN membrane from the template in such a way, that the GaN surface above the sacrificial layer is completely intact, unlike the chemical and mechanical methods used by Muth et al., in their sample preparation. The rms roughness of 0.65nm, measured on the bottom N-face of GaN surface, clearly reflects the high quality of the intact GaN surface, after etching.

2.6 Conclusion

To conclude, by optimising the PEC etching parameters, the quality of freestanding GaN membranes produced by selectively ‘eating’ away the InGaN sacrificial layer, can be improved substantially. Extremely smooth membranes are produced by using very low concentration of KOH, as low as 0.0004M, along with constant excitation power and a constant / pulsed dc bias voltage. The AFM rms roughness of the membranes is estimated to be $\sim 0.65\text{nm}$, over an area of $100\ \mu\text{m}^2$, which can be termed as “near-epitaxial”. The behaviour of etching current as PEC progresses is carefully studied and interpreted taking into account the dynamics of oxide formation and dissolution during the process. Absorption coefficients have been deduced from low temperature transmission experiments, performed on these amazingly planate membranes transferred to a sapphire substrate, based on which absorption coefficients of GaN excitons, turned out to be at least 30% higher, compared to previous reports in the literature [2].

Bibliography

- [1] E. Trichas, N. T. Pelekanos, E. Iliopoulos, E. Monroy, K. Tsagaraki, A. Kostopoulos, and P. G. Savvidis. “Bragg polariton luminescence from a GaN membrane embedded in all dielectric microcavity”, *Applied Physics Letters* 98.22 (2011), p. 221101.
- [2] J. F. Muth, J. H. Lee, I. K. Shmagin, R. M. Kolbas, H. C. Casey, B. P. Keller, U. K. Mishra, and S. P. DenBaars. “Absorption coefficient, energy gap, exciton binding energy, and recombination lifetime of GaN obtained from transmission measurements”, *Applied Physics Letters* 71.18 (1997), p. 2572.
- [3] D. Wei. “Photoelectrochemical cell and its applications in optoelectronics”, *Int. J. Electrochem. Sci* 2 (2007), pp. 897–912.
- [4] E. Trichas, M. Kayambaki, E. Iliopoulos, N. T. Pelekanos, and P. G. Savvidis. “Resonantly enhanced selective photochemical etching of GaN”, *Applied Physics Letters* 94.17 (2009), p. 173505.
- [5] C. F. Li, Y. S. Huang, L. Malikova, and F. H. Pollak. “Temperature dependence of the energies and broadening parameters of the interband excitonic transitions in wurtzite GaN”, *Physical Review B* 55.15 (Apr. 1997), pp. 9251–9254.



This page is intentionally left blank



This page is intentionally left blank

Polaritonic studies on GaN membranes

3.1 Introduction

The various design procedures, eventually leading to a GaN membrane (GaN / AlGaN QW's) based full-microcavity structure, that demonstrates strong coupling, are discussed in this chapter. The design of top and bottom DBR mirrors are initially examined, with the aid of modelling. This is followed by the discussion of some important PEC lateral etching parameters, used to create ultra-smooth GaN membranes, by etching away the InGaN sacrificial layer. The etched membranes are transferred to the bottom DBR / sapphire, thereby creating a half-microcavity structure, on which optical characterisation is performed. Very sharp excitonic features are observed, along with a relatively broad cavity mode, where the Q-factor is estimated to be ~ 85 , at RT. Moreover the reflectivity response from the structure is carefully analysed, with the help of simulations. A full-microcavity structure is formed by depositing the top DBR mirror on to the half-microcavity structure. Initially the structure is studied based on simulation, without considering the coupling effects of excitons to the cavity mode. This is followed by the experimental verification of strong coupling, which is further confirmed by fitting the dispersion curves. The Q-factor of the system is estimated to be ~ 1770 , very close to the theoretical prediction. The various polariton branches are carefully studied, understanding the contributions of spacer GaN as well as GaN QW ex-

citons, with the derived Rabi splitting of the system being $\sim 64\text{meV}$.

3.2 Design of a microcavity

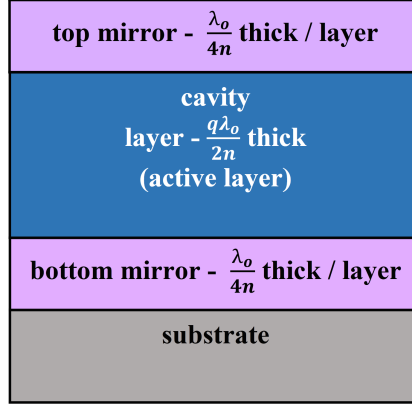


Figure 3.1: Schematic of a basic planar full-microcavity structure, where the cavity layer encapsulating the active layer, is embedded between the top and bottom mirrors.

A basic planar full-microcavity can be divided into two main regions: (1) the cavity layer which encapsulates the active layer and (2) the mirrors which comprise both the top and bottom mirrors, as shown in Figure 3.1. A microcavity which just consists of the cavity layer and the bottom mirror can be referred to as a half-microcavity. The active layer is usually a light emitting semiconductor which can either be 3D, 2D, 1D or a 0D structure. The mirrors can be either metallic, spherical or stacks of Distributed Bragg Reflectors (DBR's). According to design principles the thickness of the cavity layer (d_{cav}) is given by the following relation:

$$d_{cav} = \frac{q\lambda_o}{2n_{cav}} \quad (3.1)$$

where λ_o is the resonant cavity wavelength, at a certain angle, n_{cav} is the effective refractive index of the cavity layer at the resonant cavity wavelength for a certain angle, and q is the cavity order, which takes

values - 1, 2, 3, 4, ... etc. The thickness (d_{mirror}) of each layer in the mirror is given by:

$$d_{mirror} = \frac{\lambda_o}{4n_{mirror}} \quad (3.2)$$

where n_{mirror} is the refractive index of the specific layer in the mirror, at the resonant cavity wavelength for a certain angle. In this work the cavity layer is made of $\frac{3\lambda_o}{2n}$ thick GaN membranes, where $\lambda_o \sim 360\text{nm}$, created by PEC etching of the InGaN sacrificial layer separating the membranes from the thick GaN buffer on sapphire. The top and bottom mirrors are based on dielectric materials, again designed for $\lambda_o \sim 360\text{nm}$. A detailed description and design principles would be discussed in the next subsections.

3.2.1 Distributed Bragg Reflectors (DBR's)

A DBR stack is composed of two different materials having a relative difference in their refractive index, where the thickness of each layer corresponds to $\frac{\lambda_o}{4n}$ (see equation 3.2). A number of such stacks/pairs can be referred to as a DBR mirror. The reflectivity (R_{DBR}) from a DBR mirror at the stopband centre is given by [1]:

$$R_{DBR} = \left(\frac{1 - \frac{n_o}{n_i} \left(\frac{n_{low}}{n_{high}} \right)^{2N}}{1 + \frac{n_o}{n_i} \left(\frac{n_{low}}{n_{high}} \right)^{2N}} \right)^2 \quad (3.3)$$

where n_i and n_o are the refractive index's of the incident and transmitted media, n_{low} and n_{high} are refractive indices of the two materials that form a single DBR stack and finally N is the number of stacks/pairs that form the DBR mirror. It is very clear from the equation that a higher refractive

index contrast is required to achieve maximum reflectivity with minimal number of pairs. The stopband width ($\Delta\lambda$) is also highly dependent on the refractive index contrast, which is given by:

$$\Delta\lambda = \frac{4\lambda_o}{\pi} \sin^{-1} \left(\frac{n_{high} - n_{low}}{n_{high} + n_{low}} \right) \quad (3.4)$$

where n_{high} and n_{low} are the refractive index of the respective materials at λ_o . The equation precisely depicts that, higher the refractive index contrast, more is the stopband width and vice versa. For the realisation of high-Q microcavities, it is very important for the stopband of the DBR mirror to have a very high reflectivity ($\sim 98\%$) with a width greater than the Rabi splitting of the system, which is usually of the order of 50-100meV in GaN based microcavities. Moreover, high quality, crack-free individual layers, with minimal interface losses and negligible absorption around the stopband region are also crucial for achieving very high Q-factor's. The choice of dielectric DBR stacks in this work very well adheres to all the prerequisites of a high quality mirror suitable for polaritonic studies.

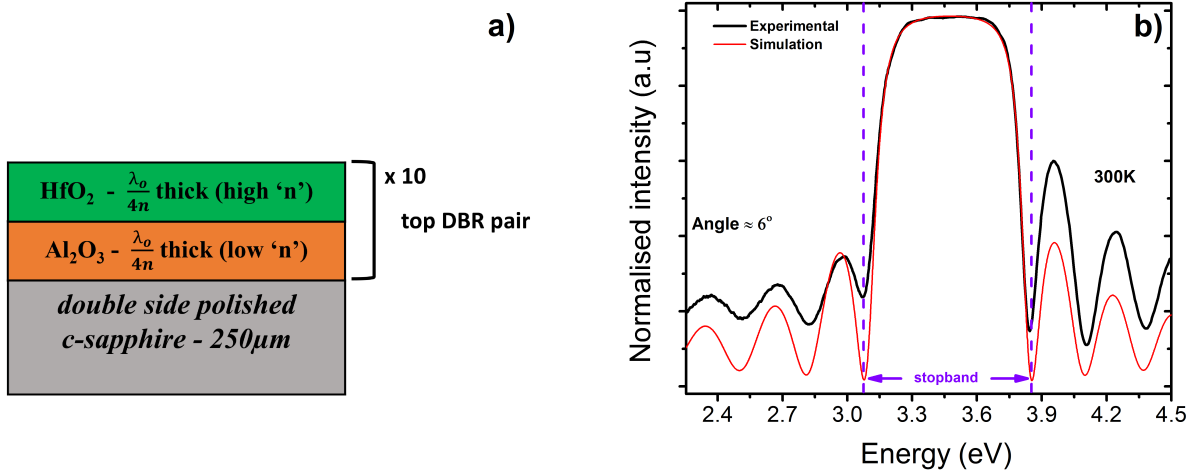


Figure 3.2: (a) Schematic of top DBR mirror, which consists of 10 pairs of HfO₂ / Al₂O₃ layers, on sapphire. (b) Experimental reflectivity response from top DBR mirror, along with its simulation, at 300K, where the angle of incidence is $\sim 6^\circ$.

Figure 3.2 (a) shows the structure of the top DBR mirror used in the full-microcavity structure. It consists of 10 pairs of $\text{HfO}_2 / \text{Al}_2\text{O}_3$ DBR stacks on sapphire, where each individual layer is $\frac{\lambda_o}{4n}$ thick (see equation 3.2), forming the top dielectric DBR mirror. To ensure the quality of the mirrors, they are grown at an extremely slow rate using atomic layer deposition (ALD), taking an overall time of around 24 hours. The order of the individual layers is such that the lower refractive index material- Al_2O_3 , as opposed to HfO_2 is just above the high refractive index GaN cavity layer, in the full-microcavity structure, in order to ensure phase matching. The same holds for the bottom DBR mirror. Figure 3.2(b) shows the experimental reflectivity response (black line) from the top DBR using the setup described in subsection A.2.5, at 300K, where the angle of incidence is $\sim 6^\circ$. Deuterium / halogen lamp is used as a source of excitation and the spectrometer grating used is 150grooves/mm. See section A.1 for more details. The violet dashed lines denote the stopband width which is around 0.773eV, centred $\sim 3.4573\text{eV}$. However at an angle of incidence $\sim 0^\circ$, the stopband is centred $\sim 3.4695\text{eV}$, a bit blue-shifted in comparison to the energy corresponding to the design wavelength (360nm) $\sim 3.44\text{eV}$. This shift can be attributed to an error of around -0.75% in the thickness of the individual layers. The experimental data is simulated using transfer matrix model as described in detail in appendix B. The refractive index of $\text{HfO}_2 / \text{Al}_2\text{O}_3$, as a function of incident wavelength, is estimated from ellipsometry measurements, made on a 200nm thick, bare $\text{HfO}_2 / \text{Al}_2\text{O}_3$ film on silicon, where the individual thickness of either layers are further confirmed from cross-sectional SEM images. However, the refractive index of sapphire, as a function of incident wavelength, is calculated using Sellmeier equation, where the Sellmeier coefficients are

taken from [2]. At the design wavelength of 360nm (3.44eV), the refractive index of the materials constituting the DBR stacks, is thus estimated to be: $n_{\text{HfO}_2} = 2.1283$ and $n_{\text{Al}_2\text{O}_3} = 1.6516$ respectively. The simulation (red line) as seen in Figure 3.2 (b), precisely follows the experimental data in terms of the energy position of the stopband, as well as the other interference fringes, for an individual thickness very close to $\frac{\lambda_o}{4n} - 0.75\%$, corresponding to the respective $\text{HfO}_2/\text{Al}_2\text{O}_3$ layers. The deviation in intensity between the experimental and simulated data can be attributed to the fact that the reflectivity measurements are not absolute and suffers from scattering losses, in addition to fibre coupling losses (see subsection A.2.5 for more details). However the overall reflectivity at the stopband centre, estimated from simulation is $\sim 98.5\%$, very close to the experimental value.

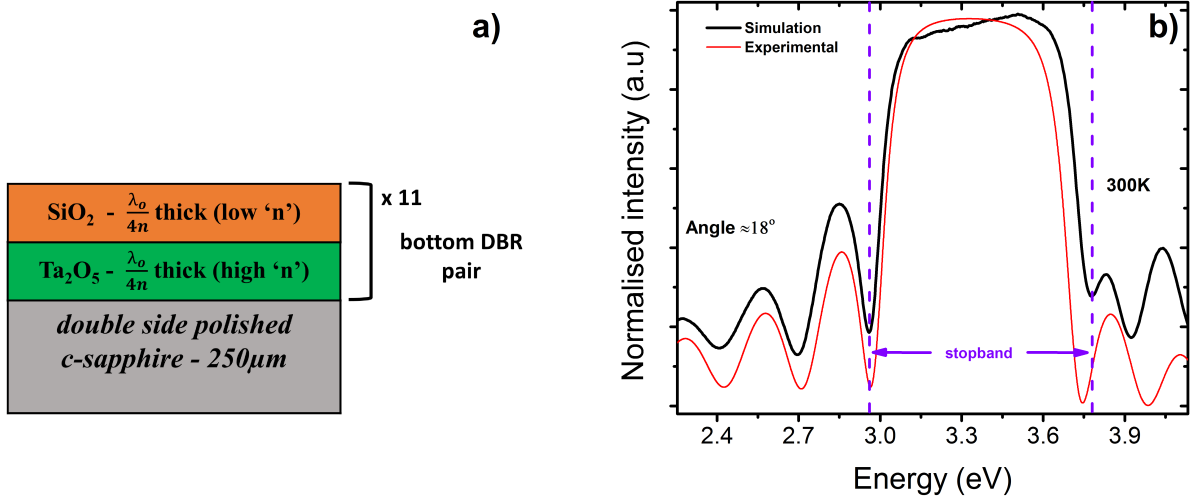


Figure 3.3: (a) Schematic of bottom DBR mirror, which consists of 11 pairs of $\text{SiO}_2 / \text{Ta}_2\text{O}_5$ layers, on sapphire. (b) Experimental reflectivity response from bottom DBR mirror, along with its simulation, at 300K, where the angle of incidence is $\sim 18^\circ$.

Figure 3.3 (a) shows the structure of the bottom DBR used in the microcavity system. It consists of 11 pairs of $\text{SiO}_2/\text{Ta}_2\text{O}_5$ DBR stacks, on sapphire, where the individual thickness of the layers correspond to $\frac{\lambda_o}{4n}$

(see equation 3.2), forming the bottom dielectric DBR mirror. The DBR stacks are industry grown by Helia photonics using a relatively fast deposition technique such as evaporation, without compromising the overall quality of the mirror, confirmed by the optical quality of the mirror. In line with the discussion above, the order of the layers forming the DBR mirror is such that the lower refractive index material-SiO₂, as opposed to Ta₂O₅, is just beneath the higher refractive index GaN cavity layer, in the full microcavity structure. Figure 3.3 (b) shows the experimental reflectivity response (black line) from the bottom dielectric mirror using the setup defined in subsection A.2.1, at 300K, where the angle of incidence is $\sim 18^\circ$. Xenon lamp is used as the source of excitation and the spectrometer grating used is 150 grooves/mm. See section A.1 for more details. The dashed violet lines correspond to the width of the stopband which is around 0.819eV, centred ~ 3.371 eV. However at an angle of incidence $\sim 0^\circ$, the stopband is centred around 3.267eV, quite red shifted in comparison to 3.44eV, which is the energy corresponding to the design wavelength of 360nm. This shift can be attributed to an error of around +5% in the thickness of the individual layers, as reported by Helia photonics. The experimental data is simulated using transfer matrix model as described in detail in appendix B. The refractive indices of SiO₂, Ta₂O₅ and sapphire, as a function of incident wavelength, are calculated using Sellmeier equation, where the Sellmeier coefficients are taken from [2–4] respectively. The estimated refractive index values of the materials constituting the DBR stacks, are further corrected based on the calibration data provided by Helia photonics. At the design wavelength of 360nm (3.44eV), the refractive index of the respective materials is thus given by: $n_{SiO_2} = 1.5099$ and $n_{Ta_2O_5} = 2.0442$. The red line in Figure 3.3 (b), precisely simulates

the experimental data below 3.542eV in terms of the energy position of the stopband as well as the other interference fringes. The discrepancy above 3.542eV can be attributed to the lack of accurate refractive index values of Ta₂O₅ in that range. However the values used in the simulation above 3.542eV is just a mere approximation derived from an extended version of the initial Sellmeier equation used for Ta₂O₅. The individual thickness of SiO₂ / Ta₂O₅ layers forming the DBR stacks, derived from simulation is very close to $\frac{\lambda_o}{4n} + 5\%$, in line with the shift observed in the stopband centre. The deviation in intensity between experimental and simulated data can be attributed to the fact that the reflectivity measurements are again not absolute and suffer scattering losses. However the overall reflectivity at the stopband centre, estimated from simulation is $\sim 98\%$, again very close to the experimental value.

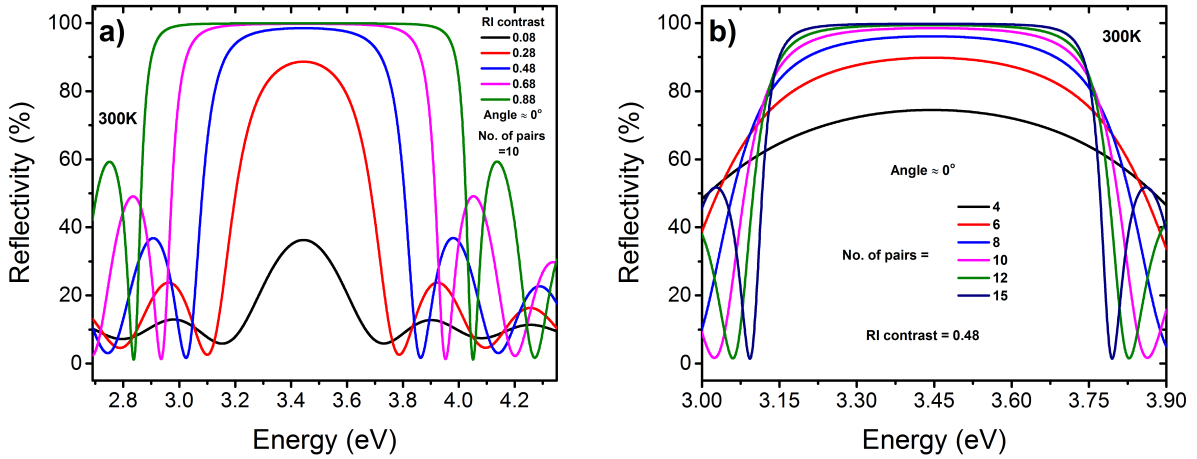


Figure 3.4: The effects on maximum stopband reflectivity as well as its width are studied as a function of: (a) refractive index contrast between subsequent layers of the top DBR stack, where the number of pairs are kept constant at 10, and (b) the number of pairs of the top DBR stack, where the refractive index contrast of the corresponding subsequent layers is kept at 0.48, very similar to actual top DBR design configuration.

In order to verify the adequacy of the dielectric mirrors in high-Q microcavities, a few simulations are performed based on the top dielectric DBR configuration as shown in Figure 3.4, studying the effects on the

maximum stopband reflectivity as well as its width. 3.4 (a) studies the effect of the refractive index contrast between the subsequent layers of a DBR stack. In order to keep the picture simple, the dispersion of the refractive index as a function of incident wavelength is ignored using the value at the design wavelength. Moreover the error in thickness (-0.5%), as mentioned earlier for the subsequent layers, has also been ignored. The number of pairs is kept constant at 10 and the angle of incidence is assumed to be 0° . The refractive index of each subsequent layer of a DBR stack is varied, in order to produce a contrast between the layers, accompanied by a change in thickness as well corresponding to $\frac{\lambda_0}{4n}$. The simulation precisely shows an increase in the overall reflectivity as well as the width of the stopband, as the refractive index contrast increases. The choice of dielectric materials for the DBR mirrors in this work is thus very well justified as they have the highest refractive index contrast compared to semiconductor based DBR mirrors, which is limited by the requirement of lattice matched binaries or ternaries. However the refractive index contrast even among dielectric materials is restrained by the choice of materials available, that can be combined to form a DBR stack. A fine tuning of the overall reflectivity response can be further achieved by varying the number of DBR stacks as shown in Figure 3.4 (b), where the refractive index contrast is kept constant at 0.48, very similar to the actual top DBR mirror design. It is very clear from the figure that as the number of pairs increases from 4 to 15, the stopband reflectivity increases although the width reduces to a certain extent, or to say that the response becomes more box-like with sharper cut-off's. Moreover higher stopband reflectivity also adds to the Q-factor of the cavity mode, when incorporated in a microcavity system. Much care is not required in terms

of stopband width, when selecting the number of pairs, as it is very large compared to the Rabi splitting of GaN based systems, as visible in Figure 3.2 (b) and Figure 3.3 (b). The number of DBR stacks in the top should be chosen in such a way that the overall reflectivity should be less than 100%, considering the fact that light has to come out of the microcavity system. This is justified by using 10 pairs in the top giving an overall stopband reflectivity of 98.5%, as seen in Figure 3.4 (b) and Figure 3.2 (b). The bottom dielectric DBR mirror can have a reflectivity $\sim 100\%$, by using an infinitely large number of pairs, which will also enhance the Q-factor of the system, although the improvement in Q factor is limited, more like getting saturated, after a certain number of pairs. Moreover a multitude of pairs also reduces the overall cost efficiency. As a trade off, 11 pairs is chosen for the bottom DBR mirror which gives an overall stopband reflectivity of around 98%, as seen in Figure 3.3 (b).

3.2.2 The cavity layer using PEC lateral etching

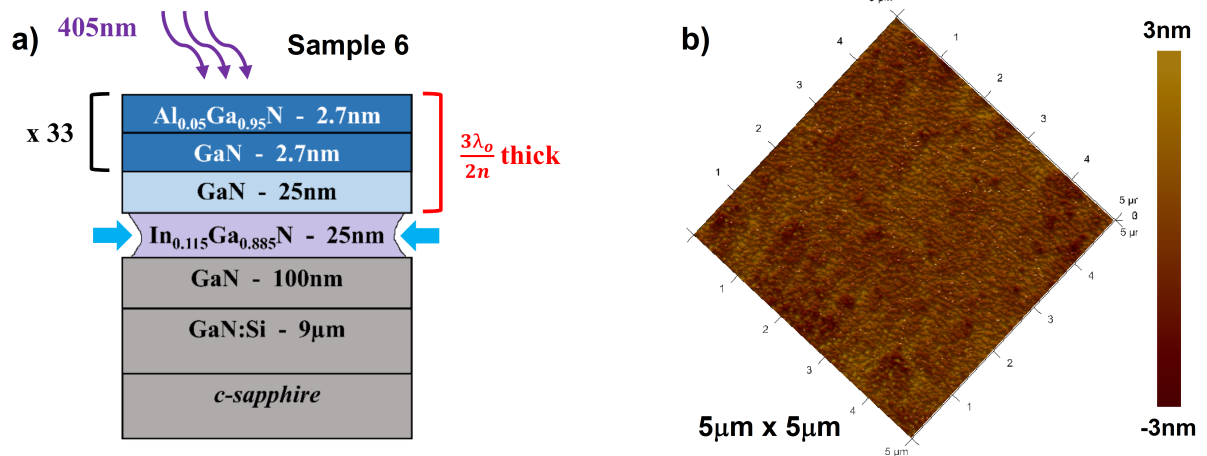


Figure 3.5: (a) Schematic of Sample 6, where the cavity layer is separated from the template by an $\text{In}_{0.115}\text{Ga}_{0.885}\text{N}$ sacrificial layer, that ought to be etched using PEC lateral etching, forming $\frac{3\lambda_0}{2n}$ thick GaN membranes. (b) 5x5 μm^2 AFM image from a GaN membrane transferred to double sided tape exhibiting very low roughness, on the bottom N-face GaN surface.

The cavity layer is $\frac{3\lambda_o}{2n}$ thick, where λ_o is 360nm, consisting of 33 pairs of 2.7nm thick GaN / Al_{0.05}Ga_{0.95}N QW's, with 2.7nm thick barrier layers and a 25nm spacer layer in the bottom, separated from the thick GaN template by a 25nm thick InGaN sacrificial layer (Sample 6), that ought to be etched using PEC lateral etching, forming $\frac{3\lambda_o}{2n}$ thick GaN membranes. The structure of the sample is as shown in Figure 3.5 (a), with additional details described under section 1.2. The optical properties of the sample are very similar to its parent sample - sample 2, taking into account the fact that the only difference in the structure being an additional InGaN sacrificial layer, in sample 6. Moreover both samples use the same GaN template series (see Table 1.1).

The sample requires initial processing as described in section 2.2, after which can be subjected to PEC lateral etching. The PEC etching parameters are as follows: (1) constant dc bias of 4V (2) average laser power of 4mW at 405nm (3.061eV) and (3) KOH concentration of 0.0004M. The whole procedure takes place in an electrochemical cell, where the etching is governed by a couple of chemical reactions, which are clearly outlined in section 2.3. The etching takes around 30 minutes, very similar to Sample 5, producing extremely smooth membranes. See section 2.4 for more details. A few membranes are then transferred to double sided tape, to facilitate AFM characterisation, returning an rms roughness of 0.65nm as shown in Figure 3.5 (b), on bottom N-face GaN surface, very similar to the other etched samples described under section 2.4.

3.2.3 The process flow for a full-microcavity structure

The basic processing steps leading to the formation of half and full microcavity structures are discussed here, with the help of an algorithm, as

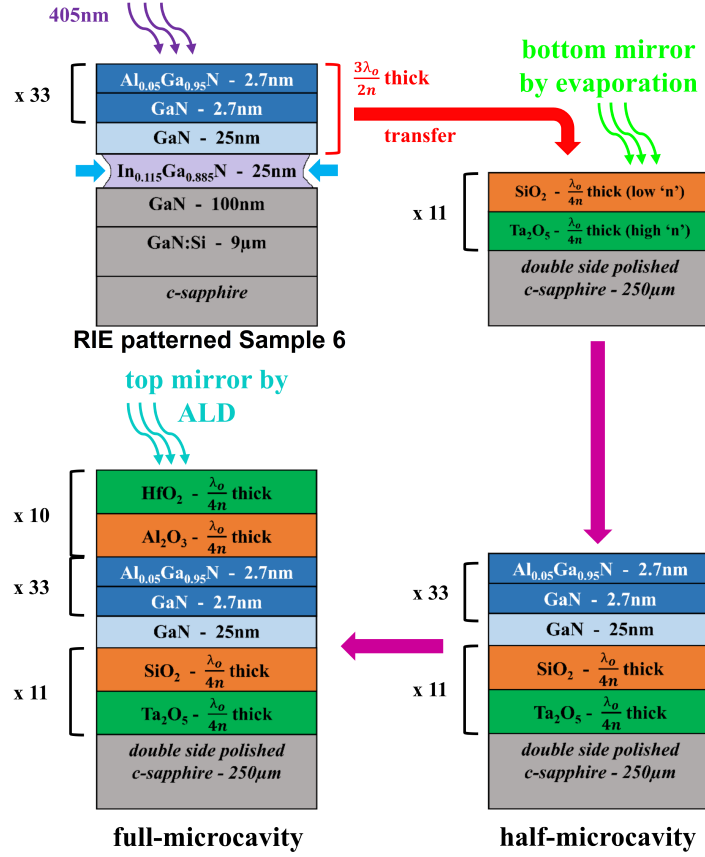


Figure 3.6: An algorithm summarising the various processing steps leading to the formation of a full-microcavity structure.

shown in Figure 3.6. Firstly PEC lateral etching is performed on RIE patterned sample 6, according to the conditions described under subsection 3.2.2, in an electrochemical cell, creating ultra-smooth GaN membranes $\sim \frac{3\lambda_0}{2n}$ thick. A couple of these membranes are transferred to the bottom DBR mirror, consisting of 11 pairs of SiO₂ / Ta₂O₅ layers, grown by evaporation on sapphire, forming a half-microcavity structure. The transferred membranes have an orientation such that the etched bottom N-face GaN, lies on the bottom DBR mirror. This is followed by the deposition of another 10 pairs of HfO₂ / Al₂O₃ layers, using ALD technique, forming the full-microcavity structure.

3.2.4 Half microcavity

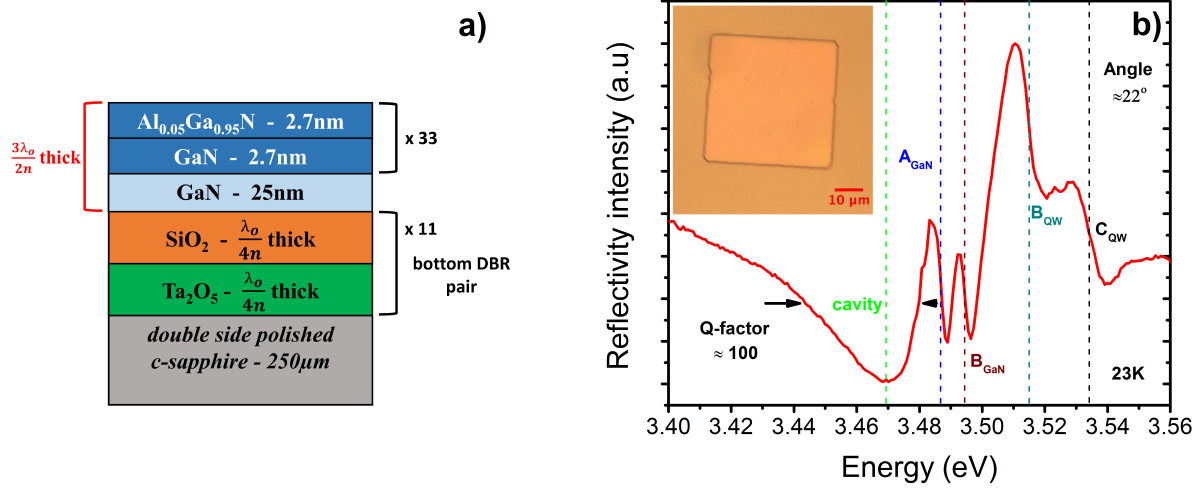


Figure 3.7: (a) Schematic of a half-microcavity structure formed by transferring the etched out GaN membranes, to the bottom DBR mirror on sapphire. (b) Reflectivity response from the half-microcavity structure, at 23K, where the angle of incidence is $\sim 22^\circ$, clearly depicting the broad cavity mode and various excitonic features. The inset shows the optical microscope image of a GaN membrane lying on the bottom DBR mirror / sapphire - half-microcavity structure.

The structure of the half-microcavity is as shown in Figure 3.7 (a), where the $\frac{3\lambda_o}{2n}$ thick GaN membrane lies on the bottom DBR mirror, comprising 11 pairs of $\text{SiO}_2/\text{Ta}_2\text{O}_5$ layers, on sapphire. An optical microscope image of a membrane lying on the bottom DBR mirror is shown in the inset of Figure 3.7 (b). All optical characterisation results are based on reflectivity measurements made using the setup described in subsection A.2.4. A Xenon lamp is used as the source of excitation and the spectrometer grating used is 600 grooves/mm, unless specified elsewhere. See section A.1 for more details. The reflectivity response of the half microcavity structure is depicted in Figure 3.7 (b), at 23K, where the angle of incidence is $\sim 22^\circ$. Comparing with the reflectivity (see Figure 1.2 (b)) of sample 2 (parent sample of sample 6), the various peaks can be easily identified, although the reflectivity peaks from the half microcavity seems to be a bit blue-shifted. In line with the discussion in subsection 2.5.2,

strain relaxation due to the removal of InGaN sacrificial layer, by PEC lateral etching is firstly ruled out here. The A and B excitons of GaN are visible around 3.487eV and 3.495eV respectively, named as A_{GaN} and B_{GaN} , approximately 4meV and 6meV blue-shifted as compared to the parent sample 2. The blue-shift of GaN excitons after etching, can be attributed to compressive stress on the GaN layers [5], caused by the AlGaN layers which form 45% of the total membrane thickness. In keeping with this explanation, a similar shift is not seen in the case of sample 4 after etching, as per the discussion under subsection 2.5.2, since the AlGaN layers there, form only 14% of the total membrane thickness, as opposed to the 45% in the case of sample 6. The C excitons of GaN named as C_{GaN} , as well as the A excitons of the QW - A_{QW} are hardly visible in Figure 3.7 (b), although B and C excitons from the QW, named as B_{QW} and C_{QW} respectively, are observed around 3.515eV and 3.534eV. B_{QW} and C_{QW} are blue-shifted as well, around 2meV and 12meV respectively, as opposed to parent sample 2. The difference in blue shift between B_{QW} and C_{QW} is quite large, around 10meV, which cannot be simply explained on the basis of strain [5] but involves a more complex scenario, that can be attributed to piezoelectric strain [6]. At around 3.469 eV in Figure 3.7 (b), the cavity mode denoted by ‘cavity’ is visible, having a linewidth ~ 0.039 eV.

To understand the behaviour of the cavity mode and the excitons with temperature, a study is made from 23K up to 295K as shown in Figure 3.8. The excitons follow a red shift with temperature in line with the usual excitonic behaviour. On the other hand, the red shift of the cavity mode is slower compared to excitons and the shift can be attributed to the increasing effective refractive index of the cavity layer, with temperature.

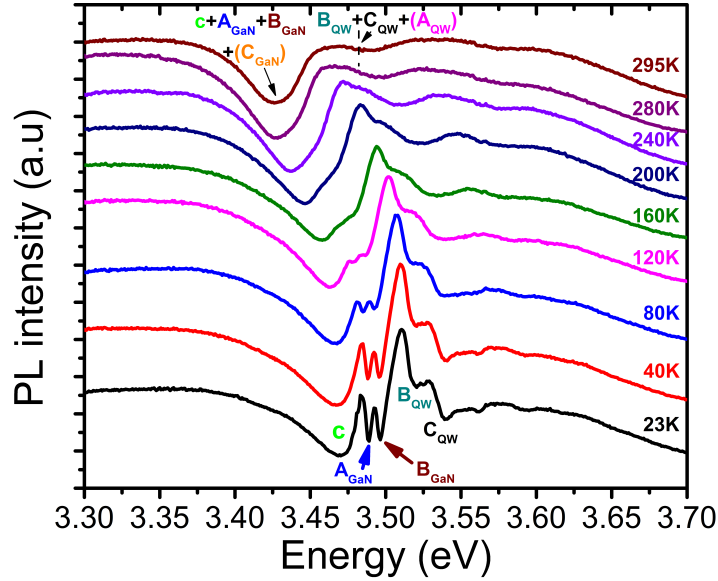


Figure 3.8: Behaviour of cavity mode and excitons with temperature, based on reflectivity response from the half-microcavity structure.

Moreover, as the temperature increases, excitons start interacting with LO phonons, resulting in broadening which weakens the excitonic peaks, precisely depicted in Figure 3.8. The LO phonon interaction of B_{GaN} is greater than that of A_{GaN} [7], which results in a more rapid weakening of B_{GaN} , visible already at 80K. Around 160K, A_{GaN} and B_{GaN} completely merge with each other, and the new entity merges with the cavity mode, at around 295K. The QW excitons on the other hand are relatively stronger with temperature than the GaN excitons. At LT, B_{QW} seems to have a higher oscillator strength than C_{QW} , although with temperature, B_{QW} broadens much faster than C_{QW} , merging with C_{QW} at around 240K. At RT, two main peaks are observed, around 3.426eV and 3.482eV. The former peak, in addition to the contributions, from the cavity mode, A_{GaN} and B_{GaN} , might also be supplemented from C_{GaN} (mentioned in brackets in Figure 3.8), as per the discussion about sample 2 in subsection 1.3.1.3. Similarly the latter peak might also have contributions from A_{QW} , in

addition to B_{QW} and C_{QW} .

3.2.4.1 Cavity mode inhomogeneities

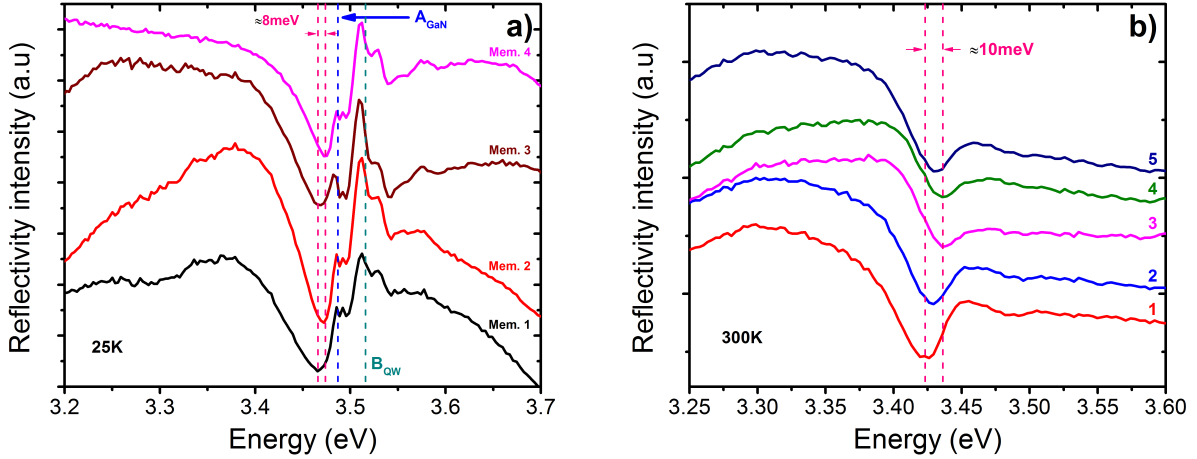


Figure 3.9: The variation in cavity mode energy for: (a) different membranes, at 25K, where the maximum shift observed is ~ 8 meV, denoted by pink dashed lines, and (b) a single membrane, corresponding to different positions on it, at 300K, where the maximum shift observed is ~ 10 meV. The variation in cavity mode energy can be strongly correlated to the variation in thickness, on different membranes for the former, and at different positions on a single membrane for the latter.

The fluctuations in the cavity mode energy along the sample surface, can be directly correlated to thickness variations on the sample, which in turn is attributed to the following factors: (1) the effect of in-plane disorders (see subsection 1.3.1.2 for more details), (2) a gradient in the MBE fluxes, leading to a thickness variation of ~ 1 -2%, and (3) the effect of PEC lateral etching. All measurements reported here are based on the same setup described above, except for mapping of a single membrane, where an additional magnifying lens is used in the collection path. The spectrometer grating used is 150 grooves/mm and the angle of incidence is kept constant for each set of measurements. Figure 3.9 (a) shows the variations in the cavity mode position for different membranes, at 25K, where the maximum shift observed is ~ 8 meV, denoted by pink dashed lines. The position of A_{GaN} and B_{QW} transitions is denoted by dashed

lines to compare the GaN as well as QW excitonic positions in different membranes, which are very identical clearly stating that the strain state, after etching is quite similar in different membranes. 3.9b, shows the effect of thickness variations on a single membrane, on the cavity mode, at 300K. The different regions on the membrane are numbered from 1 to 5, showing a shift in the cavity mode position, where the maximum shift observed is $\sim 10\text{meV}$, denoted by pink dashed lines again. In other words, a shift of 10meV in a single membrane points out to the fact that the cavity mode of each membrane in Figure 3.9 (a), is a convolution of different cavity modes corresponding to different regions of that membrane, resulting in an averaged cavity mode position as well as an increase in linewidth. In a half-microcavity structure, this may not effect the Q-factor to a large extent although might be critical in full microcavity structures, where the homogeneous linewidth of a cavity mode is of the order of a few meV. Taking into account the necessity of having high-Q microcavities for polaritonic studies, one of the ways to achieve very high Q-factor's, for a cavity layer involving GaN, would be by the use of extremely small spot sizes. In line with this discussion, Christmann et al. [8] have shown a considerable increase in Q-factor, with a reduction in spot size, reporting a Q-factor as high as 2800 for a spot size having a diameter as small as $8\mu\text{m}$, in GaN based microcavity systems.

It could be surprising to the reader that in-plane disorders (see subsection 1.3.1.2 for more information), which is cited as one of the reasons leading to a thickness gradient on the membrane surface, thereby shifting the cavity mode from one region of the membrane to another, does not seem to have any effect on the excitons. The extend of the effect of in-plane disorders on excitons is usually in the range of $\sim 100\text{nm}$ [9], whereas

the subsequent cavity mode inhomogeneities scales a few microns. Considering the area probed here, to collect the reflectivity response, which is a few tens of microns, it is obvious that the effect on excitons could be averaged out, returning a single excitonic position as opposed to the cavity mode, which shows fluctuations along the membrane surface. This explanation holds in the case of different membranes as well.

3.2.4.2 Q-factor

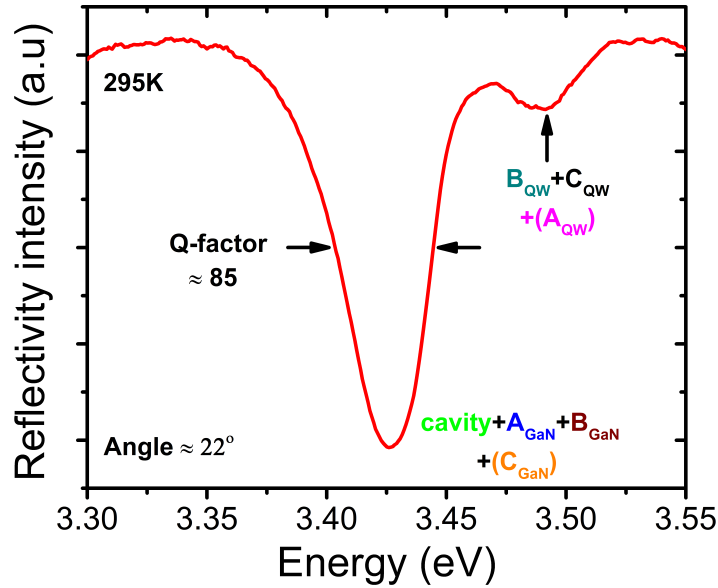


Figure 3.10: Reflectivity response from the half-microcavity structure at 295K, where the angle of incidence is $\sim 22^\circ$ and the Q-factor is depicted to be ~ 85 .

The Q-factor (Q) of a system is simply defined as the ratio of resonant cavity energy (E_o) to the linewidth (ΔE_o) of the cavity mode, given by the relation:

$$Q = \frac{E_o}{\Delta E_o} \quad (3.5)$$

The Q-factor of the half microcavity system at 295K is estimated to be ~ 85 , as shown in Figure 3.10, in comparison to a 95, observed at LT in

Figure 3.7 (b). Usually a variation in Q-factor is not expected from LT to RT, although the slight variation over here can be attributed to the effect of GaN excitons that have merged with the cavity mode, adding to the linewidth, as depicted in Figure 3.8.

3.2.4.3 Modelling the reflectivity response

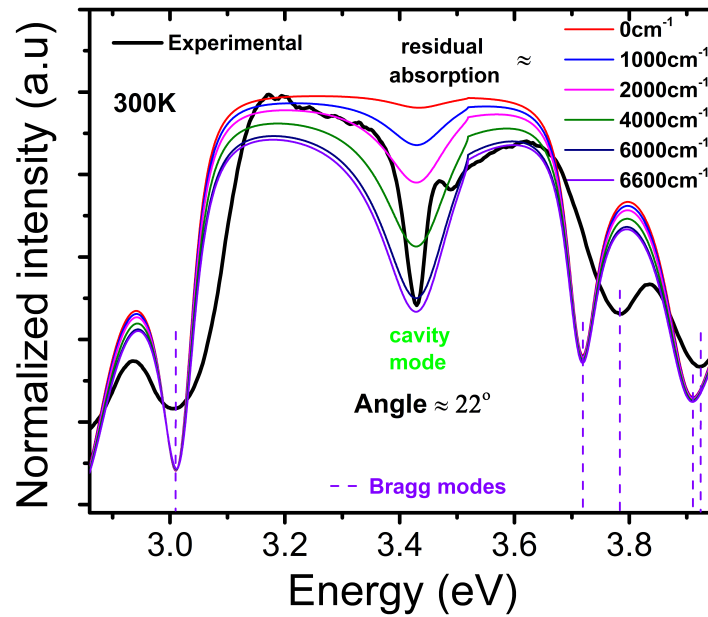


Figure 3.11: Experimental reflectivity response (black line) from the half-microcavity structure at 300K, where the angle of incidence is $\sim 22^\circ$. The other lines correspond to simulated data, without including excitons, although a residual absorption is defined around the cavity region, varying from 0cm^{-1} to 6600cm^{-1} .

In order to model the half-microcavity response, transfer matrix model, as described in detail in Appendix B is used. The excitons are included in the model by defining the imaginary part of the refractive index of the active layer, which is done by estimating the relative dielectric constant of the medium as a function of incident energy ($\epsilon_r^{E_{exc,o}}(E)$), which in turn is proportional to the oscillator strength and takes a Lorentzian shape, given by:

$$\varepsilon_r^{E_{exc,o}}(E) = \varepsilon(E) + \frac{\frac{f_{osc}^{QW}}{S} e^2 \hbar^2}{L_{QW} \varepsilon_o M} \left(\frac{1}{E_{exc,o}^2 - E^2 + i\gamma E} \right) \quad (3.6)$$

$$\varepsilon_r^{E_{exc,o}}(E) = \varepsilon(E) + \frac{\frac{f_{osc}^{bulk}}{V} e^2 \hbar^2}{\varepsilon_o M} \left(\frac{1}{E_{exc,o}^2 - E^2 + i\gamma E} \right) \quad (3.7)$$

for QW and the bulk case respectively, where ε is the background dielectric constant, related to the real part of the refractive index, as a function of incident energy, given by $\varepsilon(E) = n(E)^2$, $\frac{f_{osc}^{QW}}{S}$ is the QW oscillator strength per unit area, $\frac{f_{osc}^{bulk}}{V}$ is the bulk oscillator strength per unit volume, e is the charge of an electron, \hbar is the reduced Planck's constant, ε_o is the vacuum dielectric constant, M is the total effective mass of the exciton ($M = m_e^* + m_h^*$, where $m_e^* = 0.2m_o$ and $m_h^* = m_o$ are the electron and hole effective mass), $E_{exc,o}$ is the exciton resonance energy and finally γ is the linewidth (FWHM) of the exciton. The in-plane disorders in GaN/AlGaN QW's of a microcavity system affects mainly the excitons, causing localisation and thereby resulting in inhomogeneous broadening of the excitons. In simple words, it can be picturised as a distribution of exciton energies around a central value. Using a normal distribution, the relative dielectric constant of the inhomogeneous medium as a function of incident energy ($\varepsilon_r^{inhom}(E)$) can be estimated as follows:

$$\varepsilon_r^{inhom}(E) = \frac{1}{\sigma\sqrt{2\pi}} \int_{-\infty}^{+\infty} e^{-\frac{(E'_{exc,o} - E_{exc,o})^2}{2\sigma^2}} \varepsilon_r^{E'_{exc,o}}(E) dE' \quad (3.8)$$

where σ is the standard deviation linked to the inhomogeneous linewidth through $\gamma_{inhom} = 2\sqrt{2\ln 2}\sigma$, E' is the excitonic resonance energy around the central value $E_{exc,o}$ and $\varepsilon_r^{E'_{exc,o}}$ is the homogeneous relative dielectric constant, as a function of incident energy, given by equation 3.4, estimated

for the excitonic resonance energy E' . The response takes the shape of a Voigt line. The relative dielectric constant of the medium is related to the complex refractive index, through the relation $\tilde{n}(E) = \sqrt{\varepsilon_r(E)}$.

According to the discussion under subsection 1.3.1.2, localised excitonic peaks are visible at LT, for sample 2 (parent sample of sample 6), confirming the presence of in-plane disorders at LT. With an increase in temperature a quick delocalisation of these excitons takes place. At RT however the dominating QW emission peak has a linewidth around 28meV, quite similar to GaN linewidth, and much larger than its corresponding LT linewidth of ~ 6.5 meV (See Figure 1.4 (b)). In other words, the inhomogeneous broadening or the effect of in-plane disorders on excitons, at RT, can be ruled out in this work. In GaN / AlGa_N QW's with higher aluminium concentration or in GaN / InGa_N based QW systems, the effect of in-plane disorders seem to persist even at RT, reflected by the very high linewidth of the QW excitons.

The various parameters for the bottom DBR mirror and the sapphire substrate, used in the model, are similar to what is described under subsection 3.2.1. The Sellmeier coefficients for GaN as well as AlGa_N as a function of incident wavelength, at RT, are taken from [10, 11] respectively. The angle of incidence is set to $\sim 22^\circ$, similar to experimental reflectivity data at RT, as visible in Figure 3.11. In order to define excitons into the transfer matrix model, a knowledge of the excitonic emission peaks, from the membranes, at RT is required. The room temperature PL emission from sample 2 (parent sample of sample 6), as visible in Figure 1.4 (b) is dominated mainly by two peaks, corresponding to 3.422eV and 3.453eV respectively. The former is attributed to $A_{GaN} + B_{GaN}$, with some contributions from C_{GaN} , whereas the latter corresponds to $A_{QW} +$

B_{QW} . This scenario also applies to membranes etched out from sample 6, although as visible from Figure 3.8, the GaN excitons merge with the cavity whereas A_{QW} and B_{QW} merges with C_{QW} , making it impossible to exactly estimate its excitonic position at RT. However at LT, the excitonic positions of A_{GaN} as well as B_{QW} , as visible from Figure 3.7 (b), are not very different from their corresponding excitonic positions, in the case of sample 2 (see Figure 1.2 (b)). Taking this into account, the excitonic positions of $A_{GaN} + B_{GaN}$ as well as $A_{QW} + B_{QW}$, for the membranes, are derived from their corresponding PL positions in the case of sample 2, which are $\sim 3.422\text{eV}$ and $\sim 3.453\text{eV}$ respectively, at RT (see Figure 1.4 (b)). Thus two excitonic peaks are initially described in the model, where the oscillator strengths are kept varying. The linewidth of both excitonic peaks are considered to be homogeneous and is fixed at 28meV , which in turn is derived from the PL linewidth at RT, corresponding to the two excitonic peaks, from sample 2 (parent sample of sample 6), as depicted in Figure 1.4 (b). It should be noted that in the case of QW excitonic peak, the RT linewidth which is $\sim 28\text{meV}$ is considered to be homogeneous, since it is much larger than the LT linewidth of $\sim 6.5\text{meV}$ (see subsection 1.3.1.3 for more details). The cavity layer thickness is kept varying as well in order to account for the thickness variations arising from in-plane disorders, a gradient in the MBE fluxes and finally PEC lateral etching (see subsection 3.2.4.1 for more discussion).

The initial simulation trial of the reflectivity response returned a spectrum highly dominated by the excitons, having a convolution with the weak and broad cavity mode, although the cavity mode position precisely matched the experimental data for a cavity layer thickness of $\sim 208.5\text{nm}$, very close to the optimal $\frac{3\lambda_0}{2n}$ thickness. The results are reasonable con-

sidering the fact that the cavity mode is just $\sim 4\text{meV}$ away from the GaN excitonic (linewidth of 28meV) peak position, on the lower energy side, and moreover the oscillator strength of the excitonic peaks are not well known. In order to have a better understanding about the cavity mode, the reflectivity response is simulated again after the removal of excitonic peaks completely, which is indicated by red line in Figure 3.11, where the cavity mode is broad and very weak as compared to the experimental data, and has a Q-factor of ~ 35 . However the Bragg modes, denoted by dashed violet lines, on the lower energy side match very well with the experimental data, although the ones on the higher energy side are a bit off, owing to the lack of accurate refractive index data for Ta_2O_5 , which is one of the layers of the bottom DBR stack, above 3.542eV . A tiny discontinuity in the simulated response can also be seen around 3.519eV , corresponding to an undesirable halt in the estimated AlGaIn refractive index. The very weak and broad cavity mode can be completely correlated to the absence of a highly reflective top mirror, which in turn reduces the number of cycles that the incident light makes around the cavity, or to say that the air / cavity layer interface determines the top reflectivity. In such a scenario, a further modulation of the cavity mode can only be achieved by including losses in the cavity layer. This is done by adding some residual absorption, typically a flat response as a function of energy, which is varied from 1000cm^{-1} to 6600cm^{-1} , as depicted in Figure 3.11, which is well justified considering that the cavity mode is just $\sim 4\text{meV}$ away from the GaN excitonic peak having a linewidth of $\sim 28\text{meV}$, on the lower energy side. It is clear from the figure that as residual absorption increases, an increase in the cavity mode depth is observed accompanied by a decrease in Q-factor. For a residual absorption of $\sim 6600\text{cm}^{-1}$, the

depth of the cavity mode becomes very similar to the experimental data although the Q-factor falls further to ~ 26 , very different from the experimental data. The reason for this is not very well understood at the moment, but is likely to be related to the fact that the model applied here is rather simple, neglecting possible coupling effects with the exciton lines. However in a full microcavity structure, the presence of a highly reflective top DBR mirror, makes the cavity mode more pronounced with higher Q-factor's, and less dependent on the losses in the cavity layer, making the modelling procedure simpler, allowing for precise polaritonic simulations.

3.2.4.4 Angular dispersion

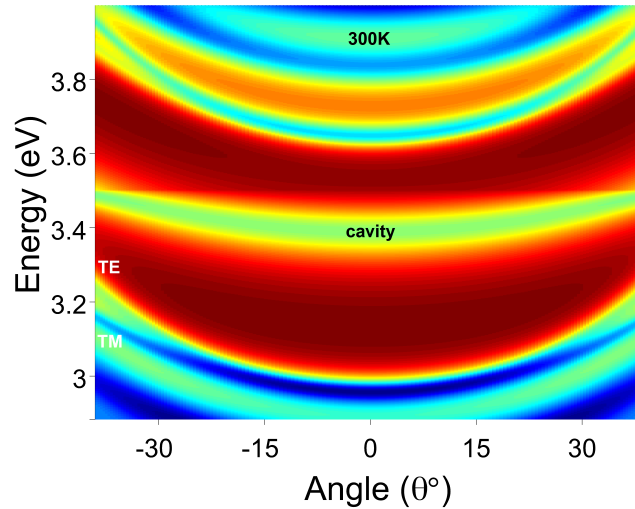


Figure 3.12: A simulation showing the angular dispersion of the reflectivity response, of a half-microcavity structure, at 300K, from -39° to $+39^\circ$, clearly depicting the cavity and the Bragg modes. At around 28° , a splitting of the Bragg modes are visible, corresponding to their respective TE / TM modes.

Figure 3.12 shows the angular dispersion of the reflectivity response (simulation), of a half-microcavity structure, from -39° to $+39^\circ$. The excitonic peaks are excluded in the model although a residual absorption

of $\sim 6600\text{cm}^{-1}$, which mimics the depth of the experimental cavity mode, as visible in Figure 3.11, is included despite the Q-factor being off. The cavity mode angular dispersion which is more dependent on the GaN based cavity layer thickness and refractive index, is seen to have a slower dependence with angle as compared to the Bragg modes, whose dispersion is more dependent on the bottom DBR mirror specifications. According to transfer matrix model, as described in detail in appendix B, the angular phase thickness inside the j_{th} layer of a microcavity structure is given by:

$$\beta_j = \frac{2}{\lambda} \tilde{n}_j d_j \cos\theta_j \quad (3.9)$$

where \tilde{n}_j is the complex refractive index of the j_{th} layer, d_j is the thickness of the j_{th} layer, and θ_j is the angle of incidence to the j_{th} layer, which can be estimated from Snell's law as follows:

$$\tilde{n}_j \sin\theta_j = n_a \sin\theta_a \quad (3.10)$$

where n_a is the refractive index of air and θ_a is the external angle of incidence from air. In accordance with equation 3.10, the angle of incidence to the j_{th} layer (θ_j) remains relatively smaller for a higher refractive index (n_j) material rather than a lower refractive index material, especially at larger external angles of incidence (θ_a). The change in phase difference as a function of angle thus remains lower for the higher refractive index material (GaN cavity layers), according to equation 3.9, which in turn produces a slower dispersion rate with angle, for the cavity mode as opposed to the Bragg modes. Even in the presence of excitons, a similar behaviour should not be confused for strong coupling.

Moreover at around 28° , a splitting of the Bragg modes is observed,

as visible in Figure 3.12, corresponding to TE and TM modes respectively, although this splitting is not observed for the cavity mode. The only difference between TE and TM modes, in line with the discussion in appendix B, is that $q = \tilde{n}_j \cdot \cos\theta_j$ for TM mode and $q = \frac{\tilde{n}_j}{\cos\theta_j}$ for TE mode. Since $\cos\theta_j$ is not very different from $\frac{1}{\cos\theta_j}$ for small angles, q starts to get affected at relatively large angles of incidence (θ_j) to the j th layer, which is true for the Bragg modes, for an external angle of incidence (θ_a) $\sim 28^\circ$, as per the discussion above, based on equation 3.10. At the same time, for the GaN cavity layer, this splitting occurs at a much larger external angle of incidence (θ_a), which is beyond the scale of this graph.

3.2.5 Full microcavity

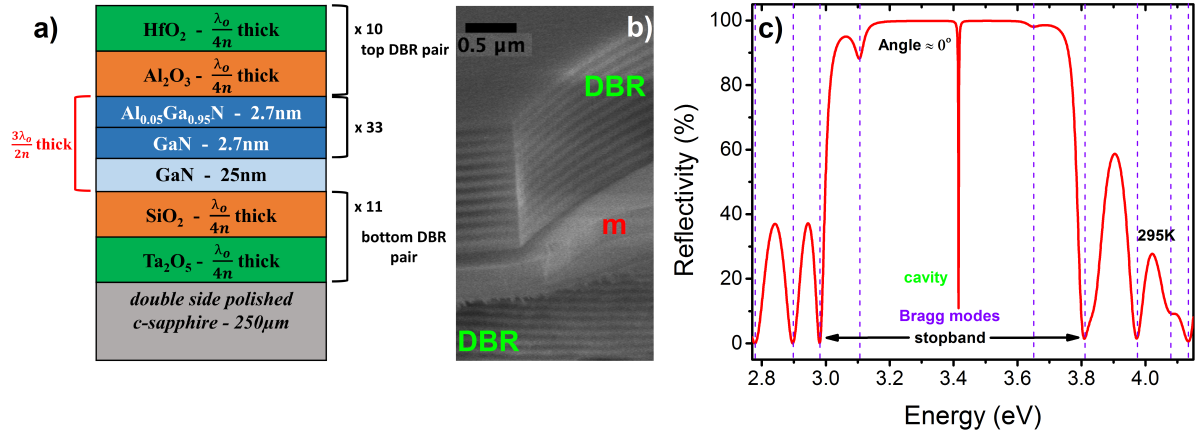


Figure 3.13: (a) Schematic and (b) cross-sectional SEM image, of a full-microcavity structure, where the $\frac{3\lambda_0}{2n}$ thick GaN membrane ('m') is embedded between top and bottom DBR mirrors, on sapphire substrate. (c) Simulation showing the reflectivity response from a full-microcavity structure, without considering excitons, at RT, where the angle of incidence is $\sim 0^\circ$ and the cavity layer thickness is ~ 206.35 nm.

The structure of the full microcavity is as shown in Figure 3.13 (a), where the $\frac{3\lambda_0}{2n}$ thick GaN membrane etched out of sample 6, is embedded between the top and bottom DBR mirrors, on sapphire substrate. A cross-sectional SEM image of the corresponding structure is visible in Figure

3.13 (b), where the GaN membrane is denoted by ‘m’. This subsection mainly discusses the important properties of a full microcavity structure based on simulation, using transfer matrix model, as described in detail in appendix B. The various parameters for the top and bottom DBR mirrors, and sapphire substrate, used in the model, are similar to what is described under subsection 3.2.1. The Sellmeier coefficients for GaN as well as AlGaIn as a function of incident wavelength, at RT, are taken from [10, 11] respectively. The excitonic peaks are not included in the model as the strong coupling regime would be studied in detail in the next section, including its experimental verification. All simulations in this subsection are performed at RT, for a cavity layer thickness $\sim 206.35\text{nm}$, which in turn positions the cavity mode at $\sim 3.4154\text{eV}$ (363.02nm). Figure 3.13 (c) shows reflectivity response from a full microcavity structure, at an angle of incidence $\sim 0^\circ$, where the actual stopband width is $\sim 0.828\text{eV}$, which can be considered as a convolution of the top and bottom DBR response, discussed independently under subsection 3.2.1. Since the stopband from the individual DBR mirrors are centred differently, the convolution results in two additional weak modes within the stopband, on either side of the cavity mode. These modes along with the other modes formed as a result of interference can be referred to as Bragg modes, marked by violet dashed lines.

3.2.5.1 Electric field distribution within the structure

The round trip of the incident light around the cavity layer, results in the formation of a standing electric field (black line), at the resonant cavity energy ($\sim 3.4154\text{eV}$), for an angle of incidence $\sim 0^\circ$, within the structure as shown in Figure 3.14 (a), along with the refractive index vari-

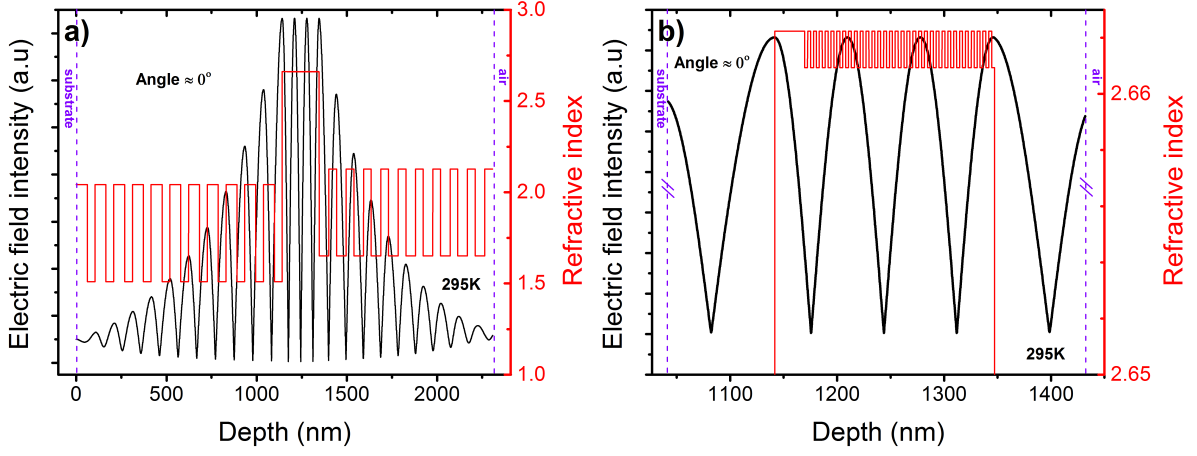


Figure 3.14: Standing wave electric field (black line), at resonant cavity energy ($\sim 3.4154\text{eV}$), for an angle of incidence $\sim 0^\circ$, along with refractive index variations (red line) are plotted for: (a) the entire structure, and (b) the region around the cavity layer.

ations, denoted by the red line. The violet dashed lines on the right side denote the top interface - air/top DBR mirror, whereas the one on the left side denotes the bottom interface - bottom DBR mirror/substrate. Figure 3.14 (b) is just a magnification of the region around the cavity layer, from Figure 3.14 (a), where the electric field is adjusted in a way that it overlaps with the refractive index variations. The procedure for determining the electric field is discussed in detail in Appendix B. It is very evident from the figure that interference peaks called antinodes are formed inside the cavity layer, at specific positions, where the enhancement is maximised. For a high refractive index cavity layer, as opposed to the DBR mirror constituents, the number of antinodes in a $\frac{q\lambda_o}{2n}$ thick cavity layer is $q - 1$, along with one each at the interface, thus making the number $q + 1$, where the interface is considered as the origin. The spacing between the respective antinodes is $\frac{\lambda_o}{2n}$. Similarly in a lower refractive index cavity layer, as opposed to the DBR mirror constituents, the number of antinodes in a $\frac{q\lambda_o}{2n}$ thick cavity layer is q , where the first antinode is at a distance of $\frac{\lambda_o}{4n}$ from the interface, which is considered as

the origin, with the spacing between the antinodes being $\frac{\lambda_o}{2n}$ again. In the microcavity structure discussed here, the $\frac{3\lambda_o}{2n}$ thick GaN cavity layer being the higher refractive index material, has thus 4 antinodes as shown in Figure 3.14 (b), which are positioned in line with the discussion above. In a well designed structure, the QW's are placed only at the antinodes, where maximum coupling between the excitons and the cavity mode takes place, maximising the efficiency of the system. However in this work the QW's are distributed along the length of the cavity except for the bottom GaN spacer layer, which facilitates things considering the fact that the overall thickness of the membranes, as per the discussion under subsection 3.2.4.1, can possibly be affected by PEC lateral etching and in-plane disorders, in addition to a gradient in the MBE fluxes, which in turn is not suitable for QW's specifically positioned at antinodes. In monolithic GaAs QW based systems, where the thickness of individual layers are only affected by a gradient in the MBE fluxes, realisation of such well designed cavity layers are comparatively easier. It should be noted that an antinode is exactly positioned around the GaN spacer layer region, confirming strong interaction of the GaN excitons with the photonic mode. This justifies the necessity of considering the contribution of GaN excitons, under strong coupling regime, which will be discussed in the next section.

The negligible absorption in the dielectric DBR mirrors, results in more penetration of light into them, depicted from the distribution of field into the DBR mirrors, as shown in Figure 3.14 (a). The penetration length into a DBR mirror (L_{DBR}), having an infinite number of pairs is given by [1]:

$$L_{DBR} = \frac{\lambda_o}{2} \frac{n_{low}}{(n_{high} + n_{low}) \cdot (n_{high} - n_{low})} \quad (3.11)$$

where λ_o is the resonant cavity wavelength at a certain angle, n_{high} and n_{low} are the higher and lower refractive index of the respective materials, of the DBR mirror, at λ_o for a certain angle. The penetration into the mirrors further adds to the effective cavity length as well as the volume of the cavity. The effective cavity length (d_{cav}^*) is thus given by:

$$d_{cav}^* = L_{topDBR} + L_{botDBR} + d_{cav} \quad (3.12)$$

where L_{topDBR} and L_{botDBR} are estimated from equation 3.11, and d_{cav} is determined from equation 3.1. For a resonant cavity energy of $\sim 3.4154\text{eV}$ ($\lambda_o \sim 363.02\text{nm}$), at 0° , as shown in Figure 3.13 (c), $L_{topDBR} \sim 166.99\text{nm}$, $L_{botDBR} \sim 145.03\text{nm}$ and finally the effective cavity length $d_{cav}^* \sim 518.37\text{nm}$, which is a reasonable value compared to the field distribution within the structure, as visible in Figure 3.14 (a). The variation in the cavity length from $\frac{q\lambda_o}{2n}$ results in a deviation of the cavity order (q) as well, which gives rise to an effective cavity order (q^*), given by the relation:

$$q^* = q + \left(\frac{n_{low}n_{high}}{(n_{high} + n_{low})(n_{high} - n_{low})} \right)_{topDBR} + \left(\frac{n_{low}n_{high}}{(n_{high} + n_{low})(n_{high} - n_{low})} \right)_{botDBR} \quad (3.13)$$

where n_{low} and n_{high} are the lower and higher refractive index of the subsequent materials, of the respective top or bottom DBR mirror. The effective cavity order q^* , for a resonant cavity energy $\sim 3.4154\text{eV}$ ($\lambda_o \sim 363.02\text{nm}$) at 0° , is ~ 6.59 .

3.2.5.2 Q-factor, lifetime and Finesse

The reflectivity/absorption response around the cavity mode region, at an angle of incidence $\sim 0^\circ$, is depicted in Figure 3.15. The absorption

visible here just relies on some residual absorption within the structure, which is as low as 50cm^{-1} in the mirrors and 100cm^{-1} in the cavity layer. It has been included in the model to account for the unavoidable interface losses. The Q-factor is determined using equation 3.5, which is around ~ 1770 . The lifetime of the incident light (τ_{cav}), before it decays away from within the cavity, is related to the Q-factor (Q) as follows:

$$\tau_{cav} = \frac{Q\lambda_o}{2\pi c} \quad (3.14)$$

where λ_o is the cavity resonance wavelength and c is the velocity of light in air. Considering $\lambda_o \sim 363.02\text{nm}$ (3.4154eV), corresponding to a cavity layer thickness of $\sim 206.35\text{nm}$, the estimated lifetime τ_{cav} is $\sim 0.34\text{ps}$. The finesse (F) of a microcavity is defined as the ratio of the difference in energy (δE_o) between successive longitudinal cavity modes to the linewidth (ΔE_0) of a cavity mode, given by the relation [1]:

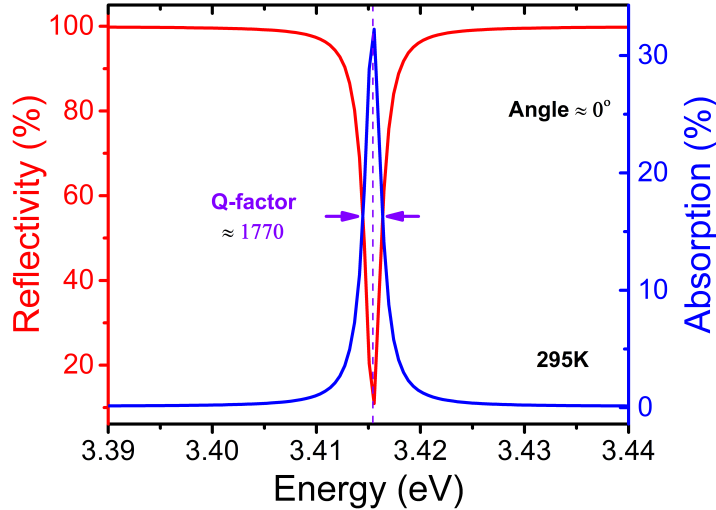


Figure 3.15: Simulated reflectivity / absorption response around the cavity mode region, at 295K, for an angle of incidence $\sim 0^\circ$. The Q-factor is estimated to be ~ 1770 .

$$F = \frac{\delta E_o}{\Delta E_0} = \frac{\pi \sqrt[4]{R_{top}R_{bot}}}{1 - \sqrt{R_{top}R_{bot}}} \quad (3.15)$$

where R_{top} and R_{bot} are the reflectivity from the top and bottom interfaces of the cavity layer, calculated in such a way that the cavity layer is considered to be the incident medium. In the case of the microcavity structure discussed here, the finesse is estimated to be ~ 249 . The Q-factor and finesse of a microcavity system are related by the following equation:

$$Q = q^* F \quad (3.16)$$

Using the finesse value (~ 249) and the effective cavity order (~ 6.59) in this equation, gives a Q-factor ~ 1640 , very close to the value estimated from the linewidth of the cavity mode.

3.2.5.3 Altering the cavity mode properties

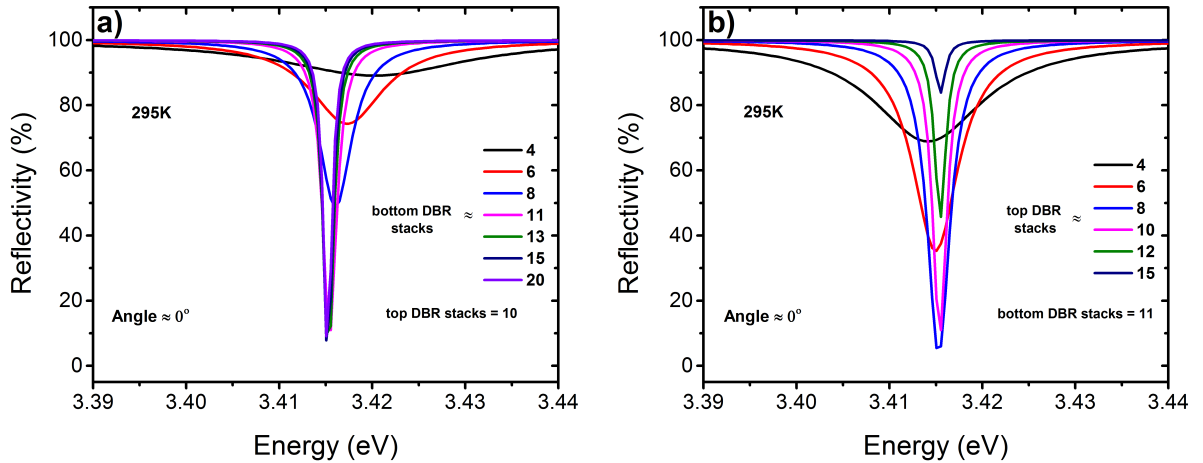


Figure 3.16: The effect on cavity mode properties based on simulated reflectivity response, at 295K, for an angle of incidence $\sim 0^\circ$, by varying the number of DBR stacks corresponding to: (a) bottom DBR mirror, where the number of top DBR stacks are kept constant at 10, and (b) top DBR mirror, where the number of bottom DBR stacks are kept constant at 11.

The properties of the cavity mode are determined mainly by the depth of the mode as well as the linewidth, which in turn is inversely proportional to the Q-factor. In order to have a further understanding, a study is made on how the cavity mode properties are affected by the number of DBR stacks, of the respective bottom (Figure 3.16 (a)) and top DBR mirrors, at an angle of incidence $\sim 0^\circ$. When the number of the bottom/top DBR stacks are varied, the respective number of top/bottom DBR stacks are kept constant, with the number of stacks being according to principal design, 10 and 11 respectively. It can be precisely depicted from Figure 3.16 (a), that there is an improvement in Q-factor, along with an increase in the depth of the cavity mode, as the number of DBR stacks increases, which can be attributed to an increase in the overall reflectivity of the bottom DBR mirror. However when the number of stacks are very high, like 13, 15 or 20, as shown in Figure 3.16 (a), the improvement in Q-factor becomes minimal, with the depth of the cavity mode becoming more or less constant. In other words, by using an infinitely large number of bottom DBR stacks, the Q-factor can be improved further, although this reduces the overall cost efficiency. Thus as a trade-off, 11 pairs are used for the bottom DBR mirror, incorporated in the microcavity structure, discussed here. A similar behaviour of the Q-factor is also seen in the case of top DBR mirror, as the number of stacks are increased, visible in Figure 3.16 (b), again attributed to an increase in the overall reflectivity of the top DBR mirror. However the depth of the cavity mode has a different behaviour, which tends to increase first and then decreases, with an increase in the number of top DBR stacks. The top DBR mirror, unlike the bottom DBR mirror, serves an additional function of allowing the light to come out of the system, at each round trip. So initially as

the number of stacks are increased, the increase in the overall reflectivity improves the depth of the cavity mode, but as the reflectivity is increased beyond a certain limit, by using a larger number of stacks, like greater than 8, as shown in Figure 3.16 (b), the overall reflectivity tends to decrease the amount of light that decays away from the cavity, at each round trip, causing a reduction in the depth of the cavity mode, although the Q-factor tends to improve. Therefore the number of stacks that can be used for the top DBR mirror, incorporated in the microcavity structure discussed here, is limited, and as a trade-off is chosen to be 10. Refer to the discussion of Figure 3.4, for a better picture. An interesting fact however that can be deduced from both graphs is a red shift of the cavity mode in Figure 3.16(a) and a blue shift in Figure 3.16 (b). This is an effect of the stopband centre of either DBR mirrors on the cavity mode. When the number of bottom DBR stacks are minimum, lets say 4 as in Figure 3.16 (a), the cavity mode position is $\sim 3.42\text{eV}$, whereas the centre of the bottom DBR mirror stopband is $\sim 3.267\text{eV}$ (see Figure 3.3 (b)). Thus as the number of bottom DBR stacks is increased, the cavity mode tends to red shift to lower energies, towards 3.267eV , although since the cavity mode position is influenced by other factors like the stopband centre of the top DBR mirror and the cavity layer thickness, the red shift is very small and moreover gets saturated, when the number of stacks are increased beyond 10. Similarly in Figure 3.16 (b), when the number of top DBR stacks are minimum, lets say 4 again, the cavity mode position is $\sim 3.414\text{eV}$, which tends to blue shift to higher energies, towards 3.4695eV , which is the stopband centre of the top DBR mirror (see Figure 3.2 (b)). But again the shift is minimal and tends to saturate as the number of stacks are increased beyond 10. However, while designing microcavities,

this influence of the DBR mirrors on the cavity mode position, which is limited to a few meV's can be neglected, in comparison to the thickness of the cavity layer that is directly proportional to the cavity mode position.

3.2.5.4 Angular dispersion and effective mass of the cavity photon

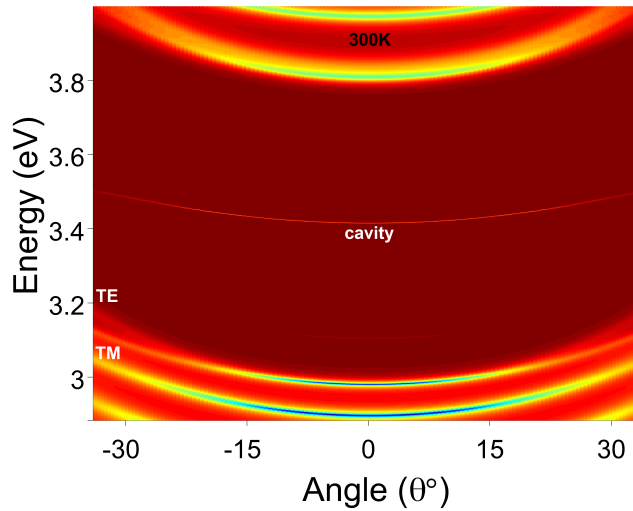


Figure 3.17: A simulation showing the angular dispersion of the reflectivity response, of a full-microcavity structure, at 300K, from -34° to $+34^\circ$, clearly depicting the cavity and the Bragg modes. At around 20° , a splitting of the Bragg modes are visible, corresponding to their respective TE / TM modes.

Figure 3.17 shows the angular dispersion of the reflectivity response, from -34° to $+34^\circ$. The high Q-factor cavity mode has a reduced dispersion rate with angle, as compared to the Bragg modes, in line with the discussion about Figure 3.12. The TE / TM mode splitting of the Bragg modes can be clearly depicted as well, at $\sim 20^\circ$, as compared to $\sim 28^\circ$, in the case of half-microcavity structure, visible in Figure 3.12. This can be attributed to the high Q-factor of the full microcavity structure, which not only explains the low linewidth of the cavity mode but also the Bragg modes, making it easier to observe the TE / TM mode splitting, at much lower angles. However, in the case of cavity mode, even at large angles,

no TE / TM mode splitting is observed, very similar to the behaviour of the half microcavity structure.

The cavity mode angular dispersion ($E_o(k_{\parallel})$), without considering the dispersion of refractive index with wavelength, can be given by a relatively simple relation as follows [12]:

$$E_o(k_{\parallel}) = \frac{\hbar c}{n_{cav}} \frac{q\pi}{d_{cav}} \sqrt{1 + \left(\frac{d_{cav}k_{\parallel}}{q\pi}\right)^2} \quad (3.17)$$

where n_{cav} is the effective refractive index of the cavity layer, at resonant cavity energy $E_o(0)$, d_{cav} is the length (thickness) of the cavity layer, q is the cavity order and finally k_{\parallel} is the in-plane wavevector given by:

$$k_{\parallel} = \frac{2\pi}{\lambda_o} n_{cav} \sin\theta_a \quad (3.18)$$

where λ_o is the resonant cavity wavelength at 0° . Based on the approximation $k_{\parallel} \ll \frac{q\pi}{n_{cav}d_{cav}}$, equation 3.17 can be further reduced to the following form:

$$E_o(k_{\parallel}) = \frac{q\pi\hbar c}{n_{cav}d_{cav}} \left(1 + \frac{1}{2} \left(\frac{d_{cav}k_{\parallel}}{q\pi}\right)^2\right) = E_o(0) + \frac{\hbar^2 k_{\parallel}^2}{2m_{cav}^*} \quad (3.19)$$

$$E_o(0) = \frac{q\pi\hbar c}{n_{cav}d_{cav}} \quad (3.20)$$

$$m_{cav}^* = \frac{q\pi\hbar n_{cav}}{cd_{cav}} \quad (3.21)$$

where m_{cav}^* is the effective mass of the cavity photon. According to the microcavity structure discussed here, the resonant cavity energy is $\sim 3.4154\text{eV}$, at 0° , based on which n_{cav} is estimated to be ~ 2.659 . Us-

ing these values in equation 3.21, the effective mass of the cavity photon (m_{cav}^*) is determined to be $\sim 4.69 \times 10^{-5} m_o$.

3.3 Demonstration of strong coupling

A system in strong coupling is usually characterised by a pronounced interaction between the corresponding excitons and the cavity mode, resulting in an anti-crossing of their respective dispersions, leading to the formation of new polariton branches, with dispersion relations possessed neither by photons nor excitons alone. The newly formed quasi-particles can be referred to as cavity polaritons. In the strong coupling regime, if the number of excitonic peaks of the system is given by n , then the resulting number of polariton states are given by $n + 1$, where the lower most and upper most polariton states are referred to as lower polariton branch (LPB) and upper polariton branch (UPB) respectively. The energy splitting between LPB and UPB at the anti-crossing point, is referred to as Rabi splitting of the system. It should be noted that the LPB (UPB) exhibits a dispersion, which is more photon-like (exciton-like) at small wavevectors and exciton-like (photon-like) at large wavevectors [13, 14].

This section mainly deals with the experimental verification of the strong coupling regime, in the full microcavity structure, supported by simulations performed using the transfer matrix model (appendix B) as well as the linear Hamiltonian model (appendix C). The previous sections in this chapter describe the various steps involved in the realisation of high-Q microcavities, the feasibility of which is confirmed by the extremely high quality, of the DBR mirrors and the ultra smooth GaN membranes. However the large linewidths of the QW excitons as com-

pared to the cavity mode, might reduce the likeliness of strong coupling or induce erroneous identification of strong coupling. Thus before entering into the further details, a brief study is made, going through the effects of broadening, that has to be considered in the strong coupling regime.

3.3.1 Feasibility of strong coupling

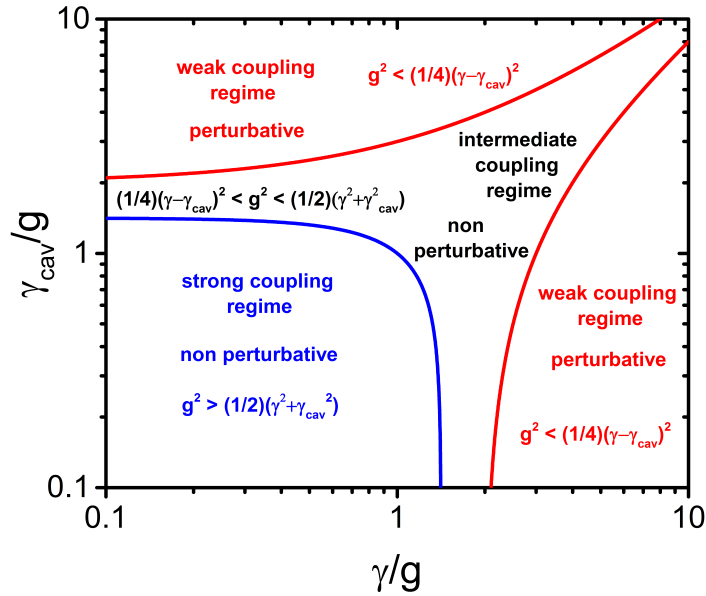


Figure 3.18: The essential prerequisites for an exciton in terms of linewidth (γ) and coupling constant (g), and for the cavity mode in terms of linewidth (γ_{cav}), in order for the system to be in the weak, intermediate or strong coupling regime.

As per the discussion in appendix C, one of the requirements for the system to be in strong coupling regime is that $4g^2 > \Delta\gamma^2$, where g is the coupling constant and $\Delta\gamma = \gamma - \gamma_{cav}$, γ being the homogeneous linewidth of the exciton and γ_{cav} is the homogeneous linewidth of the cavity mode. But the limitation of this condition is that, it does not state the maximum allowable linewidth for either the cavity mode or the excitons, so that the splitting between the lower polariton and upper polariton states is visible. However Savona et al. [15], have obtained a new expression for absorption

band splitting, based on coupled damped oscillator model, given by:

$$\Omega_{VRS}^{abs} = 2\sqrt{g^2 - \frac{1}{2}(\gamma^2 + \gamma_{cav}^2)} \quad (3.22)$$

According to this equation when $2g^2 < (\gamma^2 + \gamma_{cav}^2)$, the absorption band splitting vanishes, although it satisfies the condition $4g^2 > \Delta\gamma^2$, which is then referred to as the intermediate coupling regime, as visible in Figure 3.18. The region within the blue line corresponds to strong coupling regime whereas the region bound by the red lines correspond to weak coupling regime. The expressions for the respective coupling regimes are mentioned in Figure 3.18. Moreover, it can be clearly depicted from the figure that the maximum allowable homogeneous linewidth, of the exciton or the cavity mode, should be less than $g\sqrt{2}$, in the strong coupling regime.

In relatively low-Q microcavities Savona et al. [15] and Houdre et al. [16] have shown that there is a difference in the splitting, between reflectivity, transmission, absorption and PL or even an absence of the absorption band splitting, when the homogeneous cavity mode linewidth and homogeneous exciton mode linewidth becomes comparable to the Rabi splitting of the system. It is very possible in such cases to have a wrong interpretation about the strong coupling regime. Nevertheless they showed that for a similar coupling constant, in high-Q microcavities where the cavity mode homogeneous linewidth is far less than the homogeneous exciton linewidth and the Rabi splitting, the splitting in absorption and reflectivity, are more or less similar. Thus the former scenario can be completely ignored, considering that the full microcavity structure discussed here possess very high Q-factor. Another important parameter related to GaN

based systems, that has to be considered in the strong coupling regime is the inhomogeneous broadening of excitons. When the inhomogeneous linewidth is much smaller than the Rabi splitting, it does not influence the polariton linewidth [17], but instead the width is just governed by the homogeneous linewidths of the exciton and the cavity mode. However when this inhomogeneous linewidth of the exciton becomes comparable to the Rabi splitting, it adds to the polariton linewidth, which then has to be carefully considered under the strong coupling regime. In the case of the microcavity structure studied here, as per the discussion under subsection 3.2.4.3, the RT linewidth of the dominant QW excitonic peak is $\sim 28\text{meV}$, which is much larger than its corresponding LT linewidth of $\sim 6.5\text{meV}$, hence being considered as homogeneous ruling out the effects of inhomogeneous broadening to the polariton linewidths.

Having looked into the different broadening scenarios, in the absence of inhomogeneous broadening, the validity of the microcavity system discussed here can be checked for the strong coupling regime, based on equation C.18, described in detail in appendix C. The homogeneous linewidth of the QW excitonic peak is assumed to be $\sim 28\text{meV}$ at RT, and that of the cavity photon to be $\sim 1.93\text{meV}$ at RT, based on the simulation results under subsection 3.2.5.2, which should not be very different from the actual value, considering the high quality of the DBR mirrors and the membranes. The vacuum Rabi splitting is considered to be $\sim 50\text{meV}$, which is usually the expected value from strongly coupled GaN microcavities [18, 19]. Substituting these values into equation C.18, gives an estimate for the coupling constant, which is $\sim 28.18\text{meV}$. This number also satisfies the relation $2g^2 > (\gamma^2 + \gamma_{cav}^2)$, which is the essential condition for perceiving an absorption band splitting, clearly putting the system

into the strong coupling regime. However such easy estimations are valid only for a system that is governed by a single excitonic behaviour or multiple excitons represented by a single lorentzian peak. When there are more than one such peaks, corresponding to different excitons, the scenario becomes more complex, which then requires accurate simulations using Linear Hamiltonian model (see appendix C). This applies to the microcavity structure discussed here as well, where the two excitonic peaks corresponding to $A_{QW} + B_{QW}$, and $A_{GaN} + B_{GaN}$ play their role at RT, as per the discussion under subsection 3.2.4.3. Nevertheless, since the major part of the membrane is composed of QW's, it can be safely assumed that the role of GaN excitons would be minimal as opposed to QW excitons, thereby confirming the system to be in the strong coupling regime, based on the above discussion regarding the derived coupling constant, corresponding to the QW excitonic peak.

3.3.2 Membranes studied and experimental conditions

The full microcavity sample consists of several membranes, etched out from Sample 6 (see section 1.2), using PEC lateral etching, of varying dimensions, embedded between the two DBR mirrors. The length and breadth of the individual membranes are determined by their respective RIE pattern (see section 2.2), whereas the variation in thickness is attributed to in-plane disorders, a gradient in the MBE fluxes and PEC lateral etching (see subsection 3.2.4.1 for more discussion). All the results in this section are based on three specific membranes, which are tabulated as follows:

Throughout the text, depending on the usage, 'membrane 1', 'membrane 2' and 'membrane 3' may also refer to the full microcavity structure

membrane name	membrane thickness (nm)	detuning wrt to QW excitonic peak (meV)	area of investigation
Membrane 1	≈ 206	≈ -38	all basic optical characterisation, including temperature dependence and estimation of Rabi splitting
Membrane 2	≈ 201	≈ -10	confirmation of the determined Rabi splitting
Membrane 3	≈ 213	≈ -100	confirmation of the determined Rabi splitting

Table 3.1: A table summarising the different membranes studied, which are embedded between DBR mirrors, forming a full microcavity structure.

based on these three membranes.

All PL measurements are performed using the setup described under subsection A.2.6. A continuous wave He-Cd laser, at 325nm (see subsection A.1.1), is used as a source for all PL measurements including k-space imaging. The excitation power densities are kept low, in order to avoid the non-linear behaviour of excitons. The whole setup including the aspherical lens is aligned for the main emission wavelength, around 360nm, as a result of which, the 325nm laser is focused down to a diameter of only $\sim 9\mu\text{m}$. The spectrometer grating used is 600 grooves/mm (see subsection A.1.4). Availing the two operational possibilities provided by the spectrometer, the setup can be operated in two modes: 1) spectroscopy mode, where signal from only a few angles are probed and averaged, giving a single spectrum 2) imaging mode, where the entire k-space as a function of angle, limited by the numerical aperture (NA) of the system, is recorded in a single shot, giving an image.

3.3.3 Models used

Two models are mainly used for simulating all the experimental data at RT: transfer matrix model and linear Hamiltonian model, as described in detail in appendix B and C respectively. The transfer matrix model is more accurate as it takes into account the entire structure, in order to estimate the reflectivity, transmission or absorption response. Moreover in addition to the homogeneous broadening of excitons, also facilitates the inclusion of inhomogeneous broadening. The only drawback of the model being the computational time. It should be noted that the PL based, experimental polariton dispersion curves at RT, are simulated using absorption response, estimated from the model, assuming direct proportionality between absorption and spontaneous emission. The linear Hamiltonian model on the other hand is much quicker although it does not take into account the structure precisely (limitation 1). The cavity dispersion ($E_o(k_{\parallel})$), used in the equation C.13, which in turn is used to determine the polariton energies, is estimated from equation 3.17. However in order to estimate $E_o(k_{\parallel})$, the value of n_{cav} used is usually an approximation and moreover equation 3.18, does not take into consideration the dispersion of the refractive index, with wavelength (limitation 2). The model also does not facilitate the inclusion of inhomogeneous broadening of the excitons (limitation 3).

The last limitation can be easily ruled out, considering the fact that the excitons studied here, have negligible inhomogeneous broadening (see subsection 3.2.4.3). The second limitation can also be easily bypassed by estimating $E_o(k_{\parallel})$, directly from the transfer matrix model, which then takes into consideration the dispersion of the refractive index with wavelength and also the structure to an extent, thereby making the model

suitable for the simulation of the experimental data, observed from the full microcavity structure, discussed here.

The initial parameters defined in the models are as follows: (1) two excitonic peaks are defined around $\sim 3.422\text{eV}$ and $\sim 3.453\text{eV}$, corresponding to bulk GaN ($A_{\text{GaN}} + B_{\text{GaN}}$) and GaN QW ($A_{\text{QW}} + B_{\text{QW}}$) excitons respectively, (2) the linewidth of both excitonic peaks are considered to be homogeneous and is fixed at 28meV (see subsection 3.2.4.3 for more details), (3) the coupling constant (oscillator strength) of both excitonic peaks are kept varying, and (4) the cavity length is kept varying. See subsection 3.2.4.3, for more details on how the initial values are chosen. Moreover both models, do not take into account exciton-exciton interaction, due to which they can only be used to simulate PL experimental data, measured at low excitation power densities. The thicknesses of the membranes, in Table 3.1, are estimated by fitting the polariton dispersion curves (will be discussed in the next subsection), corresponding to the three membranes, having fixed the coupling constants (oscillator strengths) for the respective bulk GaN and GaN QW excitonic peaks. It should be noted that most of the simulation, presented in this section are based on linear Hamiltonian model, however care has been taken to verify the results, by comparing it with the output obtained from the transfer matrix model, for the same initial parameters.

3.3.4 Verification of strong coupling as a function of temperature

A PL temperature dependent study is performed on membrane 1, with the setup operated in imaging mode. Figure 3.19 (a) shows the LPB dispersion at 20K , where the strong coupling behaviour is clearly evident.

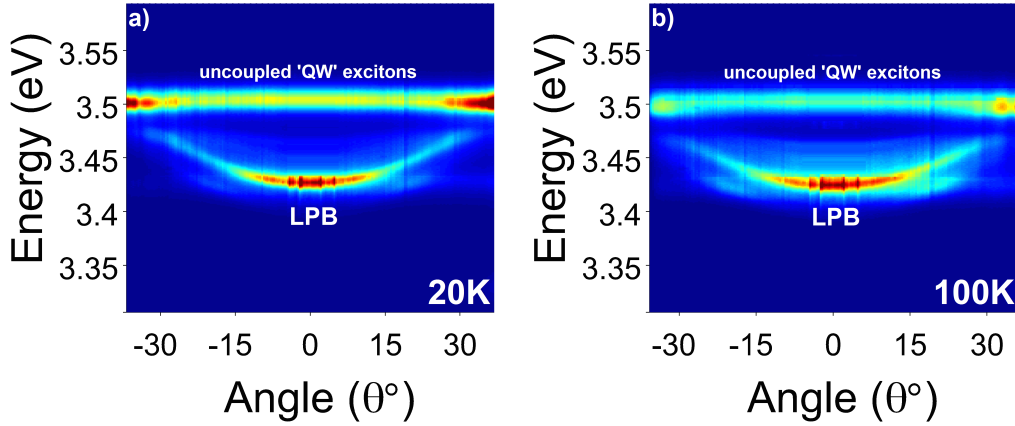


Figure 3.19: Demonstration of strong coupling behaviour in membrane 1 at: (a) 20K, and (b) 100K, revealing the LPB dispersion, which clearly flattens out at large angles. The MPB and UPB are not visible, however the uncoupled ‘QW’ excitons are visible as a straight line.

At large angles the LPB flattens out as the cavity mode interacts with at least two excitons, corresponding to bulk GaN and GaN QW’s respectively. The middle polariton branch (MPB) and the UPB, which correspond mainly to spacer GaN excitons and GaN QW excitons are not visible. It is very common in nitride based microcavity (MC) systems, that the UPB features are either weak [20] or not visible at all [21]. The straight line around 3.5eV, corresponds to “uncoupled” QW excitons, which should be localised at 20K. However the visibility of this line is quite prominent in the case of the full microcavity structure discussed here, considering the fact that the QW’s extend along, almost the full length of the cavity layer, with the exception of the 25nm GaN spacer layer in the bottom. The QW’s, which are not at the antinodes of the standing wave, are likely to couple weakly. See subsection 3.2.5.1 for a more detailed discussion. In Figure 3.19 (b), a slight red-shift can be seen in the excitonic as well as the LPB positions with temperature (100K), in keeping with GaN excitonic behaviour as a function of temperature [22]. As temperature increases, the exciton approaches the cavity, resulting in

an even flatter LPB dispersion curve that is red-shifted, following an LPB to exciton red-shift ratio of around 2:3.

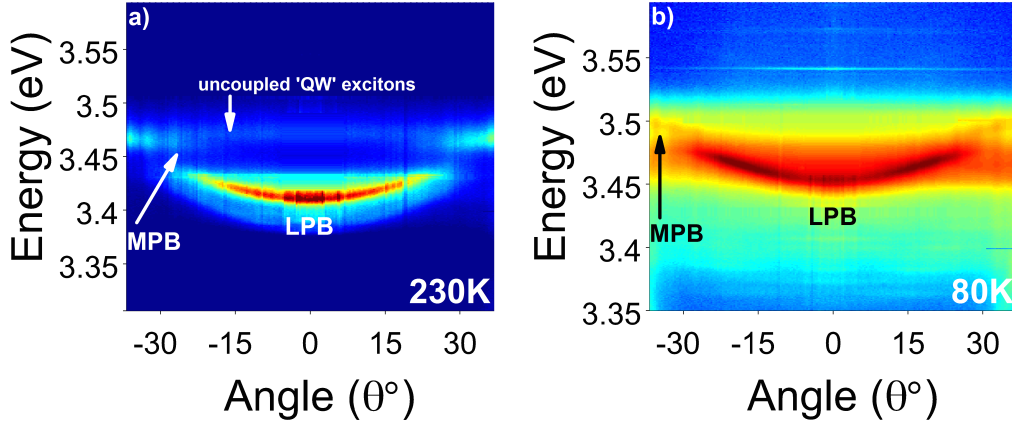


Figure 3.20: Demonstration of strong coupling behaviour revealing the LPB and MPB dispersions, for: (a) membrane 1 at 230K, and (b) a less negatively detuned membrane at 80K.

Figure 3.20 (a) corresponds to 230K, where in addition to the red-shifting LPB and uncoupled QW excitons with temperature, a new branch is observed with angular dispersive characteristic, attributed to MPB. However in order to confirm this dispersive behaviour, similar measurements are performed on a less negatively detuned membrane, which clearly shows the MPB at even lower temperatures, at $\sim 80\text{K}$, as visible in Figure 3.20 (b). Moreover the cavity like behaviour attained by the MPB after anti-crossing with the LPB, soon flattens out as it approaches the uncoupled QW excitons. At RT, the uncoupled excitons lose intensity while the dispersive nature of MPB and its anti-crossing with the LPB becomes more obvious, although the splitting is hardly distinguishable, as depicted in Figure 3.21. Moreover, the MPB flattens out as it approaches the GaN QW excitons. An increase in the LPB linewidth is also observed with temperature, in line with phonon-related broadening of excitons, as temperature goes up [22].

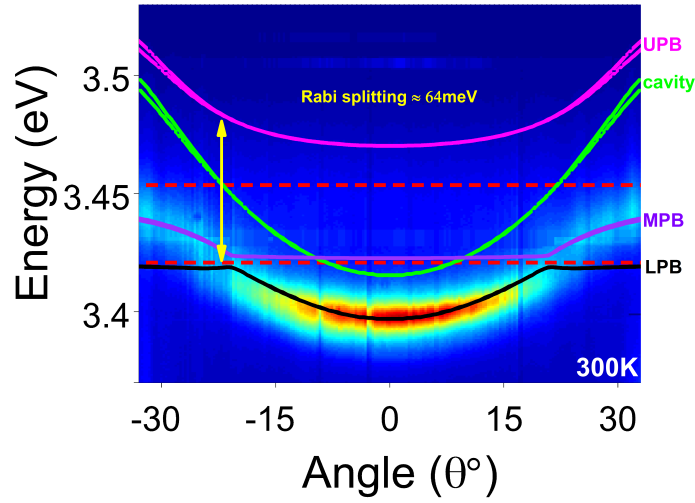


Figure 3.21: Demonstration of strong coupling behaviour in membrane 1 at RT, revealing the LPB and MPB dispersions, however UPB is not visible. The solid and dashed lines correspond to simulated data, which precisely follows the experimental data, in the case of LPB and MPB, and based on the UPB dispersion as well, an estimate is made for the Rabi splitting which is $\sim 64\text{meV}$.

To account for the observed polariton branches and to estimate the Rabi splitting of the system, the linear Hamiltonian model, as described in detail in appendix C, is used to simulate the angle dependent PL data at RT. The two excitonic peaks corresponding to bulk GaN and GaN QW excitons, as defined in the model, are seen as dashed red lines, whereas the green line represents the cavity mode, as depicted in Figure 3.21. Both the excitonic lines interact with the cavity according to their respective coupling constants, at different k_{\parallel} 's, forming three polariton states: the black line represents LPB, the magenta line corresponds to UPB, having most of its contribution from the GaN QW excitons due to their high oscillator strength as compared to GaN, and the violet line corresponds to MPB having contributions mainly from the GaN excitons. An anti-crossing behaviour can be observed around 21° , after which the LPB clearly flattens out gaining a more excitonic behaviour, whereas the MPB as well as the UPB gain a more cavity like behaviour, as visible in Figure 3.21. However

the MPB flattens out as it approaches the uncoupled GaN QW excitons, gaining a more excitonic behaviour. The LPB and MPB are clearly visible in the experimental data, though not the UPB [20, 21]. At very large angles, a splitting of the dispersion lines is seen corresponding to their respective TE/TM modes. The coupling strengths of the GaN QW and spacer GaN excitonic peaks are around 31.6 meV and 10meV respectively, for a cavity layer thickness of $\sim 206.35\text{nm}$, all the values being estimated from the model. The Rabi splitting of the system is estimated graphically from Figure 3.21, which is $\sim 64\text{meV}$, rather than using the simple equation C.18, described in detail in appendix C. The equation can be used to estimate the Rabi splitting based on the coupling constant of GaN QW excitonic peak, under the assumption that the bulk of the membrane is composed of GaN QW's, which then does not take into account the influence of the spacer GaN excitonic peak, thereby reducing the accuracy of the estimated Rabi splitting value.

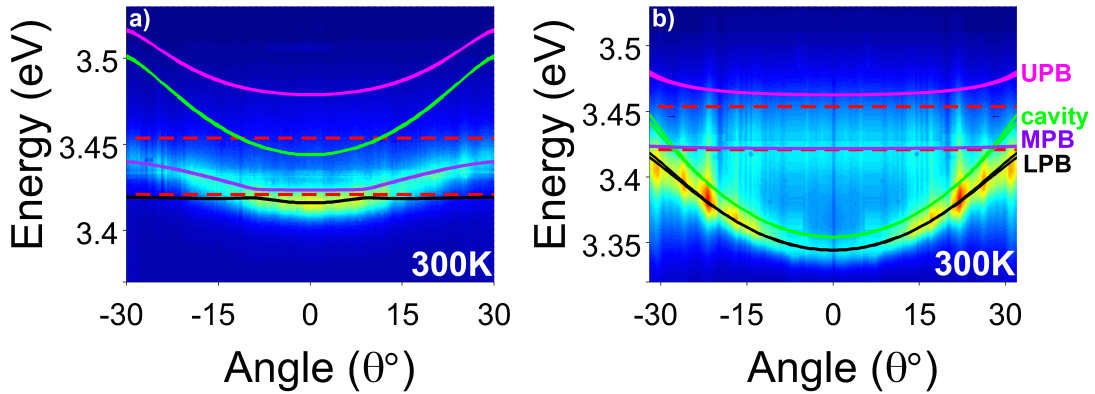


Figure 3.22: Demonstration of strong coupling behaviour at RT, revealing the LPB and MPB dispersions, for: (a) membrane 2, and (b) membrane 3. The solid and dashed lines in either figures correspond to simulated data, which precisely follows the experimental data, in the case of LPB and MPB, and based on the UPB dispersion as well, an estimate for the Rabi splitting is made for both membranes, which is not very different from 64meV.

It should be noted that basically three parameters, the two coupling

constants and the cavity length, are derived from the model, whose precision then can be questioned. However, in order to ensure the accuracy, two other membranes, membrane 2 and membrane 3, with different detunings as compared to membrane 1 (see Table 3.1), are simulated using the same coupling constants, corresponding to their respective excitonic peaks, having only the cavity layer thickness varying. The model accurately simulates the experimental data, corresponding to membrane 2 and membrane 3, for a cavity layer thickness of $\sim 201\text{nm}$ and 213nm respectively, as visible in Figure 3.22 (a and b) subsequently. Taking into account the actual thickness of the membrane, according to design, which is $\sim 203.2\text{nm}$, the cavity lengths for which the model is run corresponding to different membranes seem reasonable, thereby confirming the accuracy of the estimated coupling constants as well as the Rabi splitting of the system.

3.3.5 Determination of Q-factor

In order to determine the Q-factor precisely, the linewidth of the LPB at around a certain k_{\parallel} , is simulated using transfer matrix method (described in detail in appendix B), which actually takes into consideration the real structure of the full microcavity system. Initially the parameters of the model i.e. the oscillator strength corresponding to spacer GaN ($A_{GaN} + B_{GaN}$) and GaN QW ($A_{QW} + B_{QW}$) excitonic peaks, and the cavity length of the membranes are determined by fitting the room temperature, angle dependent PL experimental data corresponding to membranes 1, 2 and 3 respectively. For a constant oscillator strength of $4.6 \times 10^{21}/\text{cm}^3$ and $4.3 \times 10^{17}/\text{cm}^2$, corresponding to spacer GaN and QW excitonic peaks, the simulation returns a cavity length of 206nm , 201nm

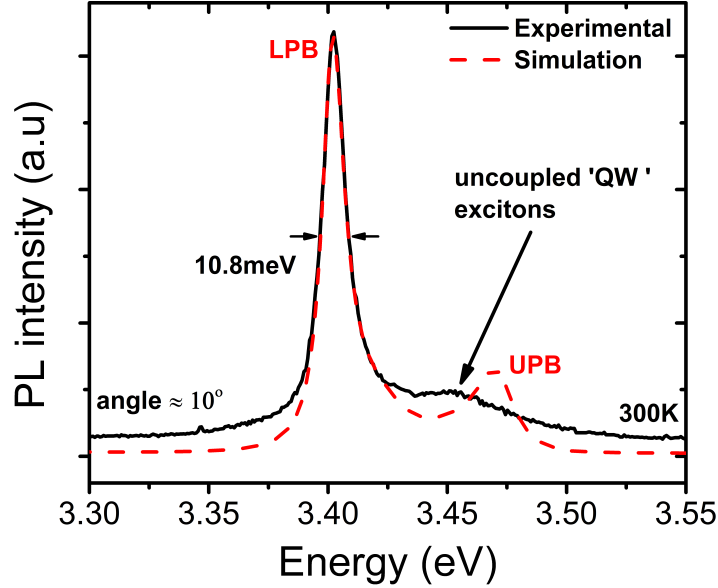


Figure 3.23: PL experimental data (black line) from membrane 1, at around $k_{\parallel} = 10^{\circ}$, at RT, where the narrow LPB is visible having a linewidth of $\sim 10.8\text{meV}$ and the uncoupled ‘QW’ excitons are seen as a weak shoulder. The dashed red line corresponds to simulated data, precisely following the experimental LPB curve and revealing the UPB as well, at a much higher energy.

and 213nm, for membranes 1, 2 and 3 respectively, very similar to the values estimated in the previous subsection 3.3.4, thereby confirming the accuracy of the model.

The room temperature PL experimental data (black line) at around $k_{\parallel}=10^{\circ}$, from membrane 1 is visible in Figure 3.23, which is measured by operating the setup in spectroscopy mode. The angles which are probed and averaged to give a single spectrum are $\sim 10^{\circ}$, due to a slight deviation of the collection path from the centre of the spectrometer. The very narrow line, having a linewidth of $\sim 10.8\text{meV}$ peaking at 3.402eV, corresponds to LPB whereas the weak shoulder $\sim 3.453\text{eV}$ represents the uncoupled QW excitons, once again confirming the energy position of QW excitons used in the models (see subsection 3.3.3). The model accurately simulates (red line) the linewidth of the LPB, as visible in Figure 3.23, for a homogeneous cavity linewidth of $\sim 1.93\text{meV}$, at 3.4154eV ($k_{\parallel}=10^{\circ}$), giving

a Q-factor of ~ 1770 using equation 3.5, taking into account the losses in the DBR mirrors and active region, which corresponds to 50cm^{-1} and 100cm^{-1} respectively. It should be noted that the losses included are quite minimal, especially for the active region, considering the fact that the negative detuning of the cavity mode from the GaN excitonic peak is just $\sim 6.6\text{meV}$. Taking into account the theoretical prediction as well, which is ~ 2350 , without including any losses in the structure, the estimated Q-factor thus corresponds to an extremely high quality full-microcavity structure. The profile of the cavity mode is depicted in Figure 3.15, and further discussion on Q-factor and finesse, aided by modelling, can be found under subsection 3.2.5.2.

3.4 Conclusion

A GaN membrane (GaN / AlGaIn QW's) based full microcavity structure is realised, which demonstrates strong coupling. The DBR mirrors (top and bottom) are of extremely high quality, confirmed by optical characterisation, and moreover the specifications like stopband width and position, and overall reflectivity response, are very close to the initial design. The etched out ultra-smooth membranes, using PEC lateral etching, have an RMS roughness of $\sim 0.65\text{nm}$, approximately one order of magnitude lower than the previously reported values, where they used a very similar technique [23]. The half-microcavity structure shows very sharp excitonic features, giving a further insight into the quality of the etched membranes, where the Q-factor is estimated to be ~ 85 . The full-microcavity structure has been carefully studied under the strong coupling regime, understanding the contribution of both spacer GaN as well as GaN QW excitons,

with the aid of modelling. The estimated Q-factor of the system is ~ 1770 , very close to the theoretical prediction, whereas the Rabi splitting is $\sim 64\text{meV}$.

Bibliography

- [1] H. Benisty, H. De Neve, and C. Weisbuch. “Impact of planar microcavity effects on light extraction - Part I: Basic concepts and analytical trends”, *IEEE Journal of Quantum Electronics* 34.9 (1998), pp. 1612–1631.
- [2] R. L. Kelly. “Program of the 1972 Annual Meeting of the Optical Society of America”. EN, *JOSA* 62.11 (Nov. 1972), p. 1336.
- [3] M. J. Weber. “Handbook of Optical Materials”. CRC Press, 2002, p. 536.
- [4] L. Gao, F. Lemarchand, and M. Lequime. “Exploitation of multiple incidences spectrometric measurements for thin film reverse engineering.” EN, *Optics express* 20.14 (July 2012), pp. 15734–51.
- [5] J. Piprek. “Electron Energy Bands”, *Semiconductor Optoelectronic Devices*. Elsevier, 2003, pp. 13–48.
- [6] R. A. Beach and T. C. McGill. “Piezoelectric fields in nitride devices”, *Journal of Vacuum Science & Technology B: Microelectronics and Nanometer Structures* 17.4 (1999), p. 1753.
- [7] C. F. Li, Y. S. Huang, L. Malikova, and F. H. Pollak. “Temperature dependence of the energies and broadening parameters of the interband excitonic transitions in wurtzite GaN”, *Physical Review B* 55.15 (Apr. 1997), pp. 9251–9254.
- [8] G. Christmann, D. Simeonov, R. Butté, E. Feltn, J. F. Carlin, and N. Grandjean. “Impact of disorder on high quality factor III-V nitride microcavities”, *Applied Physics Letters* 89.26 (2006), pp. 10–13.
- [9] S. Sonderegger, E. Feltn, M. Merano, A. Crottini, J. F. Carlin, R. Sachot, B. Deveaud, N. Grandjean, and J. D. Ganière. “High spatial resolution picosecond cathodoluminescence of InGaN quantum wells”, *Applied Physics Letters* 89.23 (Dec. 2006), p. 232109.
- [10] A. S. Barker and M. Ilegems. “Infrared lattice vibrations and free-electron dispersion in GaN”, *Physical Review B* 7.2 (1973), pp. 743–750.
- [11] G. M. Laws, E. C. Larkins, I. Harrison, C. Molloy, and D. Somerford. “Improved refractive index formulas for the $\text{Al}_x\text{Ga}_{1-x}\text{N}$ and $\text{In}_y\text{Ga}_{1-y}\text{N}$ alloys”, *Journal of Applied Physics* 89.2 (2001), p. 1108.

- [12] G. Christmann. “III-nitride Based Microcavities: Towards Polariton Condensation at Room Temperature”. PhD thesis. EPFL, 2009.
- [13] M. S. Skolnick, A. I. Tartakovskii, R. Butté, D. M. Whittaker, and R. M. Stevenson. “High-occupancy effects and stimulation phenomena in semiconductor microcavities”, *IEEE Journal on Selected Topics in Quantum Electronics* 8.5 (2002), pp. 1060–1071.
- [14] J. Levrat, R. Butté, E. Feltin, J. F. Carlin, N. Grandjean, D. Solnyshkov, and G. Malpuech. “Condensation phase diagram of cavity polaritons in GaN-based microcavities: Experiment and theory”, *Physical Review B - Condensed Matter and Materials Physics* 81 (2010), pp. 1–11.
- [15] V. Savona, L. Andreani, P. Schwendimann, and A. Quattropani. “Quantum well excitons in semiconductor microcavities: Unified treatment of weak and strong coupling regimes”, *Solid State Communications* 93.9 (1995), pp. 733–739.
- [16] R. Houdré, R. P. Stanley, U. Oesterle, M. Ilegems, and C. Weisbuch. “Room temperature exciton-photon Rabi splitting in a semiconductor microcavity”, *Le Journal de Physique IV* 03.C5 (Oct. 1993), pp. 51–58.
- [17] R. Houdré, R. P. Stanley, and M. Ilegems. “Vacuum-field Rabi splitting in the presence of inhomogeneous broadening: Resolution of a homogeneous linewidth in an inhomogeneously broadened system”, *Physical Review A* 53.4 (1996), pp. 2711–2715.
- [18] N. Antoine-Vincent, F. Natali, D. Byrne, A. Vasson, P. Disseix, J. Leymarie, M. Leroux, F. Semond, and J. Massies. “Observation of Rabi splitting in a bulk GaN microcavity grown on silicon”, *Physical Review B* 68.15 (Oct. 2003), p. 153313.
- [19] A. Kavokin and B. Gil. “GaN microcavities: Giant Rabi splitting and optical anisotropy”, *Applied Physics Letters* 72.22 (June 1998), p. 2880.
- [20] G. Christmann, R. Butté, E. Feltin, J.-F. Carlin, and N. Grandjean. “Room temperature polariton lasing in a GaN/AlGaIn multiple quantum well microcavity”, *Applied Physics Letters* 93.5 (2008), p. 051102.

- [21] S. Christopoulos, G. von Högersthal, A. Grundy, P. Lagoudakis, A. Kavokin, J. Baumberg, G. Christmann, R. Butté, E. Feltin, J.-F. Carlin, and N. Grandjean. “Room-Temperature Polariton Lasing in Semiconductor Microcavities”, *Physical Review Letters* 98.12 (Mar. 2007), pp. 1–4.
- [22] R. Jayaprakash, D. Ajagunna, S. Germanis, M. Androulidaki, K. Tsagaraki, A. Georgakilas, and N. T. Pelekanos. “Extraction of absorption coefficients from as-grown GaN nanowires on opaque substrates using all-optical method”, *Optics Express* 22.16 (2014), p. 19555.
- [23] E. Trichas, N. T. Pelekanos, E. Iliopoulos, E. Monroy, K. Tsagaraki, A. Kostopoulos, and P. G. Savvidis. “Bragg polariton luminescence from a GaN membrane embedded in all dielectric microcavity”, *Applied Physics Letters* 98.22 (2011), p. 221101.



This page is intentionally left blank

A GaN membrane based polariton laser

4.1 Introduction

The non-linear properties of a GaN membrane (GaN / AlGaN QW's) based full-microcavity structure, under non-resonant quasi-continuous excitation conditions, at room temperature, are discussed. The chapter begins with a brief theoretical description about the mechanisms that eventually lead to non-linearities like polariton condensation / lasing, which is followed by experimental verification, aided by modelling. The results clearly confirm polariton lasing, under the strong coupling regime, where the average power density at threshold is extremely low, of the order of $4.5\text{W} / \text{cm}^2$ ($\sim 594\mu\text{J} / \text{cm}^2$), the lowest ever reported for 2D-GaN based systems [1]. Above threshold, a beautiful condensation pattern is observed in the k-space, which is explained on the basis of polaritons getting trapped in a site specific, square-like pocket. Taking into account this picture, the non-linear properties are further analysed.

4.2 Theory

The basics of polariton condensation under non-resonant excitation [2, 3] is discussed with the help of a schematic as visible in Figure 4.1, where the cavity is negatively detuned $\sim 10\text{meV}$, from the excitonic energy. A pulsed laser $\sim 4.66\text{eV}$, is used as a source of excitation, well above the un-

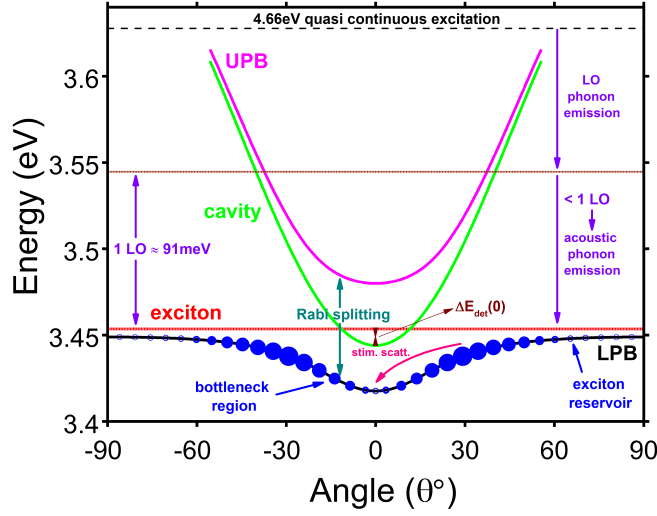


Figure 4.1: A schematic for understanding polariton condensation under non-resonant excitation, for a system where the cavity is negatively detuned $\sim 10\text{meV}$, from the excitonic energy.

coupled excitonic energy, creating electron-hole pairs which quickly bind to form excitons. These excitons initially undergo a quick thermalisation to an effective temperature by LO phonon emission, as a result of exciton-exciton and exciton-phonon scattering. As the kinetic energy of the excitons fall below 91meV , which corresponds to one LO phonon energy, the excitons continue to interact with the lattice through acoustic phonon emission, helping the excitons to reach a temperature close to the lattice, as depicted in Figure 4.1. The cavity mode interacts with the excitons under strong coupling regime, resulting in an anti-crossing of the exciton and cavity mode dispersions, forming new polariton branches corresponding to LPB and UPB, as depicted in Figure 4.1. The new quasi-particle formed as a result of the interaction can be referred to as cavity polaritons. The energy splitting between the LPB and UPB at the anti-crossing point, is referred to as the Rabi splitting of the system, as visible in Figure 4.1. The LPB (UPB) follows a more cavity (exciton) like dispersion at low k_{\parallel} 's, whereas a more exciton (cavity) like

dispersion at higher k_{\parallel} 's. Due to this dispersive nature of the LPB, in addition to the lower polaritons at $\sim k_{\parallel} = 0$, the polaritons at larger k_{\parallel} 's undergo polariton-polariton as well as polariton-phonon scattering, in order to reach the polariton trap at the centre of the Brillouin zone. Before discussing further about the distribution of polaritons in the dispersion curve, it is very important to know how the lifetimes affect this distribution. The lifetime of the polaritons in LPB and UPB, denoted as τ_{pol}^{LP} and τ_{pol}^{UP} respectively, are given by the following relations:

$$\frac{1}{\tau_{pol}^{LP}} = \frac{|C_{k_{\parallel}}|^2}{\tau_{cav}} + \frac{|X_{k_{\parallel}}|^2}{\tau_{exc}} \quad (4.1)$$

$$\frac{1}{\tau_{pol}^{UP}} = \frac{|C_{k_{\parallel}}|^2}{\tau_{exc}} + \frac{|X_{k_{\parallel}}|^2}{\tau_{cav}} \quad (4.2)$$

where $|X_{k_{\parallel}}|^2$ and $|C_{k_{\parallel}}|^2$ are indicative of the corresponding exciton (photon) and photon (exciton) fractions, of the lower (upper) polaritons respectively, for a given in-plane wavevector k_{\parallel} , τ_{cav} is the cavity lifetime and τ_{exc} is the excitonic lifetime. $|X_{k_{\parallel}}|^2$ and $|C_{k_{\parallel}}|^2$ can be determined from equations C.9 and C.10 respectively, based on the corresponding detuning ($\sim 10\text{meV}$), which are discussed in detail in appendix C. For a small negative detuning as discussed here, at $\sim k_{\parallel} = 0$, the lower polaritons have a more cavity like nature, resulting in very low lifetimes as compared to larger k_{\parallel} 's. Nevertheless a dominant part of the lower polariton dispersion curve, as visible in Figure 4.1, has states corresponding to wavevectors, larger than that of cavity photons, where the excitons do not couple to light forming an excitonic reservoir, whose lifetime is then determined by τ_{exc} . The low lifetimes at $\sim k_{\parallel} = 0$ along with the steep dispersion, results in a quick decay of the lower polaritons posing a serious competition to

the scattering mechanisms trying to populate the polariton trap. This is reflected by a lack of polaritons in the trap as opposed to the reservoir region, which is often referred to as the relaxation bottleneck effect.

The electron-hole components of the excitons usually have a fermionic nature, whereas the excitons exhibit bosonic properties. Taking into account the bosonic nature of photons as well, exciton-photon quasiparticles (polaritons) also behave as bosons. Unlike the fermions, bosons are particles with integer spin that do not follow Pauli exclusion principle, and hence they are allowed to occupy individual states in large numbers. The rate of any quantum mechanical transition is proportional to $1 + N_{final}$, where 1 represents spontaneous processes, and N_{final} corresponds to a stimulation of transition accompanied by a macroscopic occupation of the final state. In a conventional laser like VCSEL, photon emission is stimulated, accompanied by a macroscopic occupation of the photon modes of the cavity. However, a stimulation of scattering accompanied by a macroscopic occupation of the polariton trap, can be referred to as polariton condensation / lasing.

Polariton condensates can be formed either in the thermodynamic equilibrium regime ($\tau_{pol}^{LP} \gg \tau_{rel}$), also called as Bose-Einstein condensation (BEC), or in the kinetic regime ($\tau_{rel} \gg \tau_{pol}^{LP}$), where τ_{rel} is the time required for the lower polaritons to cool down from an initial temperature to the lattice temperature. One of the most important factors that govern the formation of condensates is the LP critical density (n_{crit}) at $k_{\parallel} = 0^{\circ}$, which is the minimum polariton density required to initiate polariton lasing for a certain temperature, and detuning. It should be noted that the LP critical density (n_{crit}), should be lower than the exciton saturation density (n_{exc}^{sat}), so as to ensure that the system is in the strong coupling re-

gime. The LP critical density (n_{crit}) can be related to the phase transition temperature (T_{crit}), for an ideal BEC, and the lower polariton effective mass (m_{pol}^{LP}) by the following relation:

$$T_{crit} = \left(\frac{n_{crit}}{\zeta(\frac{3}{2})} \right)^{\frac{2}{3}} \frac{h^2}{2\pi m_{pol}^{LP} k_B} \quad (4.3)$$

where ζ is the Riemann zeta function and k_B is the Boltzmann constant. It is very clear from equation 4.3, that n_{crit} increases as T_c increases. However for a given temperature, the lower polariton critical density (n_{crit}) can be reduced by decreasing the lower polariton effective mass (m_{pol}^{LP}). The lower and upper polariton effective masses denoted as m_{pol}^{LP} and m_{pol}^{UP} respectively, are given by the following relations:

$$\frac{1}{m_{pol}^{LP}} = \frac{|C_{k_{\parallel}}|^2}{m_{cav}^*} + \frac{|X_{k_{\parallel}}|^2}{M} \quad (4.4)$$

$$\frac{1}{m_{pol}^{UP}} = \frac{|X_{k_{\parallel}}|^2}{m_{cav}^*} + \frac{|C_{k_{\parallel}}|^2}{M} \quad (4.5)$$

where m_{cav}^* is the effective mass of the cavity photon and M is the total effective mass of the exciton ($M = m_e^* + m_h^*$, where $m_e^* = 0.2m_o$ and $m_h^* = m_o$ are the approximate electron and hole effective masses, for a GaN based system). Considering that the mass of the cavity photon $\sim 10^{-5}m_o$, which is very less than M , equation 4.4 clearly states that the lower polariton effective mass can be reduced by increasing the cavity fraction, which in turn can be achieved by increasing the negative detuning, based on equations C.9 and C.10, described in detail in appendix C. Thus from a thermodynamic point of view, n_{crit} can be reduced by increasing the negative detuning. However at large negative detunings, the reduced

excitonic nature of the lower polaritons decreases the polariton scattering rates i.e. it increases τ_{rel} . Moreover it also reduces the lifetimes at $\sim k_{\parallel} = 0$, based on equation 3.18, which results in a quick decay of the polaritons reaching the trap, eventually leading to a relaxation bottleneck effect, similar to the scenario described by the schematic in Figure 4.1. In such systems where $\tau_{rel} \gg \tau_{pol}^{LP}$, the polariton distribution completely depends on the relaxation dynamics of the particles. The polariton condensation occurs at a critical density (n_{crit}), mainly influenced by the lifetime (τ_{pol}^{LP}) of the lower polaritons, which is usually very low, and moreover should satisfy the condition of $n_{crit} < n_{exc}^{sat}$. However in the case of very low excitonic lifetimes i.e. when the excitonic lifetimes are comparable to the lower polariton lifetimes (τ_{pol}^{LP}), the scenario could be more complex.

A suppression of this bottleneck effect or a reduction in τ_{rel} is possible by decreasing the negative detuning or in other words going towards positive detuning. This in fact increases the excitonic nature of the lower polaritons according to equations C.9 and C.10, which in turn enhances the polariton scattering rates. Moreover it also increases the lifetime of the lower polaritons at $\sim k_{\parallel} = 0$, based on equation 4.1. Thus from a kinetic point of view, positive detunings are favourable, although it increases the polariton critical density (n_{crit}). As a trade off between n_{crit} and τ_{rel} , very small negative detunings are usually favourable for BEC, which then satisfies the condition of $\tau_{pol}^{LP} \gg \tau_{rel}$, where the polaritons acquire a reasonable equilibrium with the lattice. The polariton BEC then occurs at a critical density (n_{crit}), very close to the value predicted from the thermodynamic theory, such that $n_{crit} < n_{exc}^{sat}$. It should be noted that in either cases of polariton condensation, an initiation of lasing enhances the polariton scattering rates due to stimulated scattering mechanisms.

This is in particular important for systems characterised by a bottleneck effect, as depicted in Figure 4.1.

4.3 Experimental conditions and models used

All the discussions in this section are based on a full microcavity structure, where a membrane having two regions of varying thickness: 205.4nm and 201.8nm respectively, is embedded between DBR mirrors. The thicknesses corresponding to the two regions of the membrane are estimated by fitting their respective polariton dispersion curves, which will be discussed below. Hereby the membrane may be referred to as ‘membrane 4’, however depending on the usage, ‘membrane 4’ may also refer to the full microcavity structure based on the membrane. The PL measurements are performed using the setup described under subsection A.2.6, at RT. A Nd-YAG frequency-quadrupled, pulsed laser, at 266nm, with a pulse repetition rate of 7.58 kHz and a pulse-width of 0.51ns (see subsection A.1.1), is used as a source for all PL measurements including k-space imaging. In line with the discussion before (see subsection 3.3.2), since the whole setup is aligned for the emission wavelength $\sim 360\text{nm}$, the laser can be focused down only to a spot size of $\sim 60\mu\text{m} \times 10\mu\text{m}$, where the unequal dimensions are related to its elliptical profile. The spectrometer grating used is 600 grooves/mm (see subsection A.1.4). Here again the setup can be operated in two modes: the spectroscopy mode which captures the spectral data around $k_{\parallel} = 0$, and the imaging mode which extracts the k-space images (see subsection 3.3.2 for more details).

The linear Hamiltonian model, as discussed in detail in appendix C, is used for simulating all the experimental angular dispersion data, con-

firmed by the transfer matrix model (see appendix B). The initial parameters defined in the models are as follows: (1) two excitonic peaks are defined around $\sim 3.422\text{eV}$ and $\sim 3.453\text{eV}$, corresponding to spacer GaN ($A_{\text{GaN}} + B_{\text{GaN}}$) and GaN QW ($A_{\text{QW}} + B_{\text{QW}}$) excitons respectively, (2) the linewidth of both excitonic peaks are considered to be homogeneous and is fixed at 28meV , (3) the coupling constants (oscillator strengths) corresponding to spacer GaN and GaN QW excitonic peaks are 10meV ($4.6 \times 10^{21}/\text{cm}^3$) and 31.6meV ($4.3 \times 10^{17}/\text{cm}^2$) respectively, as estimated from subsection 3.3.4 (3.3.5), which are kept constant, and (4) the cavity length is kept varying in order to fit different regions of membrane 4, corresponding to contrasting thicknesses. Further information on modelling, and how the initial parameters are chosen, can be found under subsections 3.2.4.3 and 3.3.3.

4.4 Experimental verification of polariton condensation aided by modelling

A power dependent study is made on membrane 4, as shown in the images of Figure 4.2 and the corresponding spectral data in Figure 4.3 (a), in order to confirm polariton lasing / condensation. At low powers $\sim 0.39P_{th}$, a dispersion similar to Figure 3.21 can be seen, revealing the LPB and MPB contributions, which are fitted using the linear Hamiltonian model, returning a thickness of $\sim 205.4\text{nm}$. The respective lower polariton branch is named as LPB_1 , which is also evident in the spectral data. With increasing power, as visible in Figure 4.3 (a), the LPB_1 peak undergoes broadening towards the higher energy side, giving an impression of a blue-shift. However at around $0.81P_{th}$, we start seeing a

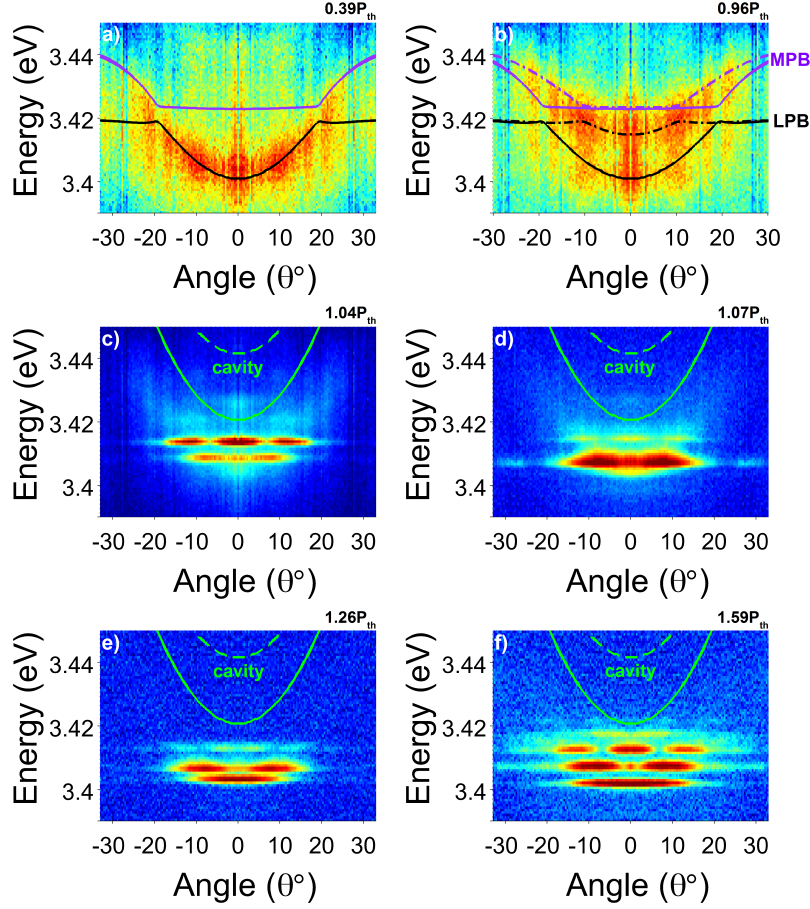


Figure 4.2: PL imaging data from membrane 4, at RT, for the following pump power densities: (a) $0.39P_{th}$ - only LPB₁ is visible, (b) $0.96P_{th}$ - just below threshold where LPB₁ and LPB₂ are visible, and (c) - (f) - polariton condensation above threshold with a k-space pattern, far below the cavity mode energies corresponding to LPB₁ and LPB₂.

second peak, at a higher energy, which becomes clearly visible just below threshold, at $\sim 0.96P_{th}$, while the LPB₁ line reappears at more or less the same position as at low powers. The second peak is also observable in the corresponding imaging data of Figure 4.2 (b), showing a dispersive behaviour, which is named as LPB₂. Two dot dashed lines in the spectroscopic data (Figure 4.3 (a)) is a guide to the eye showing the evolution of the two LPB's with power. Since the energy position of LPB₁,

hardly changes with excitation power, the exciton-exciton interaction in the coupled QWs is assumed to be negligible, which allows the use of the linear Hamiltonian model to fit LPB₂, as visible in Figure 4.2 (b) (dot dashed line), returning a cavity layer thickness of $\sim 201.8\text{nm}$ along with the fitting for LPB₁ (solid line). Figure 4.3 (b) shows the evolution of the spectrally integrated intensity (left) as well as linewidths (right) with pump power. The integrated intensity is estimated for the region around LPB₁ and LPB₂ at all powers, whereas the linewidth is estimated from LPB₁ below threshold, and level ‘1’ above threshold, where the origin of level ‘1’ is discussed below. A clear onset of lasing is visible at extremely low average power densities of $\sim 4.5\text{W} / \text{cm}^2$ (P_{th}), marked with a brown dashed line in Figure 4.3 (b). The corresponding energy density is $\sim 594\mu\text{J} / \text{cm}^2$. Above threshold, a quick narrowing of lines is observed with an increase in intensity of ~ 50 times, revealing at least three peaks within the energy range of LPB₁ and LPB₂, as depicted in Figure 4.3 (c), marked as ‘1’, ‘2’ and ‘3’. Level ‘3’ has the highest intensity at threshold, followed by ‘2’ and finally ‘1’. The corresponding image in Figure 4.2 (c), at $1.04P_{th}$, shows a spectacular pattern formed in the k-space corresponding to levels ‘2’ and ‘3’, while level ‘1’ remains relatively less visible. The system is clearly in strong coupling regime as visible from the dispersion, which at around $k_{\parallel} = 0$, is far below the cavity modes corresponding to LPB₁ and LPB₂ (solid and dashed green lines). Moreover at large angles, the dispersion seems to flatten out as opposed to the cavity modes, confirming polariton lasing vs. photonic lasing. The different levels follow an interesting power dependent behaviour as seen in the images of Figure 4.2 (c - f) and in Figure 4.3 (c). Level ‘3’, first blue-shifts and then follows a red-shift with pump power, whereas ‘1’ and ‘2’ red-shift, with ‘2’ gaining

maximum intensity already at $1.07P_{th}$. At higher powers maximum lasing occurs from level ‘1’ followed by ‘2’ and ‘3’, a behaviour that will be explained later. Above threshold, the integrated intensity and linewidths follow a linear law with pump power. The overall shape of the integrated intensity follows an S-like behaviour as a function of pump power (Figure 4.3 (b)), corresponding to $\frac{1}{\beta} \sim 50$, comparing favourably to previous works, that used dielectric DBR stacks just on one side [4].

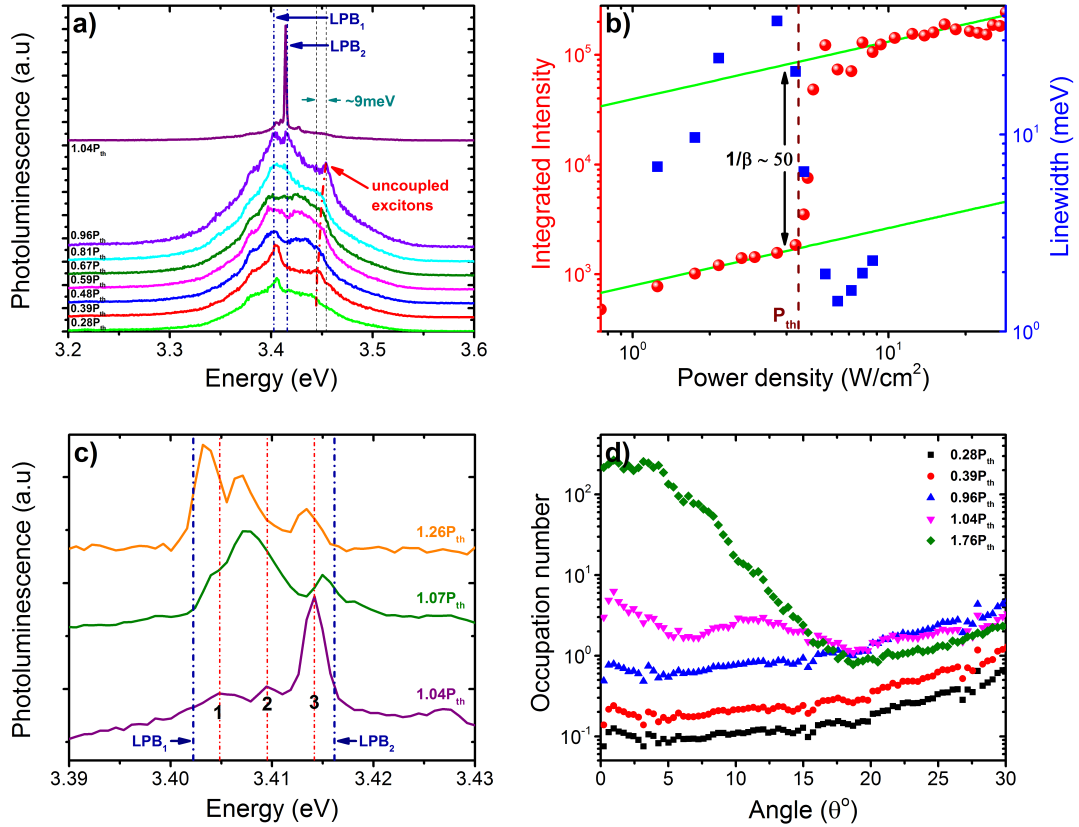


Figure 4.3: A PL power dependent study is made on membrane 4 at RT, using spectroscopy mode, discussing the following results: (a) spectral data from $0.28P_{th}$ - $1.04P_{th}$, clearly depicting LPB_1 and LPB_2 below threshold, and polariton condensation above threshold, (b) the integrated intensity (red) for the region around LPB_1 and LPB_2 , and the linewidth (blue), estimated from LPB_1 peak below threshold and level ‘1’ peak above threshold, as a function of pump power density, (c) the spectral data above threshold, from $1.04P_{th}$ - $1.26P_{th}$ revealing the three levels within the energy range of LPB_1 and LPB_2 , and (d) occupation number as a function of pump power density, from $0.28P_{th}$ - $1.76P_{th}$, where the occupation shoots up far beyond unity above threshold.

The above discussion clearly confirms polariton lasing / condensation,

although it is not obvious whether the condensation occurs in the thermodynamic regime or the kinetic regime. In order to have a better understanding about this, the occupation number as a function of angle, is estimated for different pump powers, as depicted in Figure 4.3 (d). The integrated PL intensity at different angles is normalised by the cavity fraction of both LPB's, in order to determine a joint occupation number. The cavity / exciton fraction of LPB₁ and LPB₂, is visible in Figure 4.4 (a) and Figure 4.4 (b) respectively, which are estimated using equations C.9 and C.10, discussed in detail in appendix C. The plot is normalised to unity for the power just below threshold ($0.96P_{th}$) [5]. At lower powers below threshold, the occupation numbers follow a similar slope, increasing linearly with pump power, with higher occupations at large angles, attributed to relaxation bottleneck effects [2, 6]. In line with the discussion under section 4.2, the presence of a characteristic bottleneck effect, confirms the system to be in the kinetic regime i.e. $\tau_{rel} \gg \tau_{pol}^{LP}$. In this regime, it is the cavity like nature of the lower polaritons at $\sim k_{\parallel} = 0$, as visible from Figure 4.4 (a) and Figure 4.4 (b), that reduces the efficiency of the polariton scattering mechanisms in efficiently populating the polariton trap. However, below threshold, this tendency seems to persist even with increasing pump power, as suggested from the unchanged slopes, in agreement with reduced polariton-polariton scattering, due to the low polariton densities in the system. Just above threshold, in the polariton lasing regime, the occupation at larger angles subside with a tremendous increase around $k_{\parallel} = 0$, pushing the occupation numbers far above unity, quite characteristic of polariton condensation in the kinetic regime [1, 2, 4–6].

4.4.1 Estimation of exciton density / QW at threshold

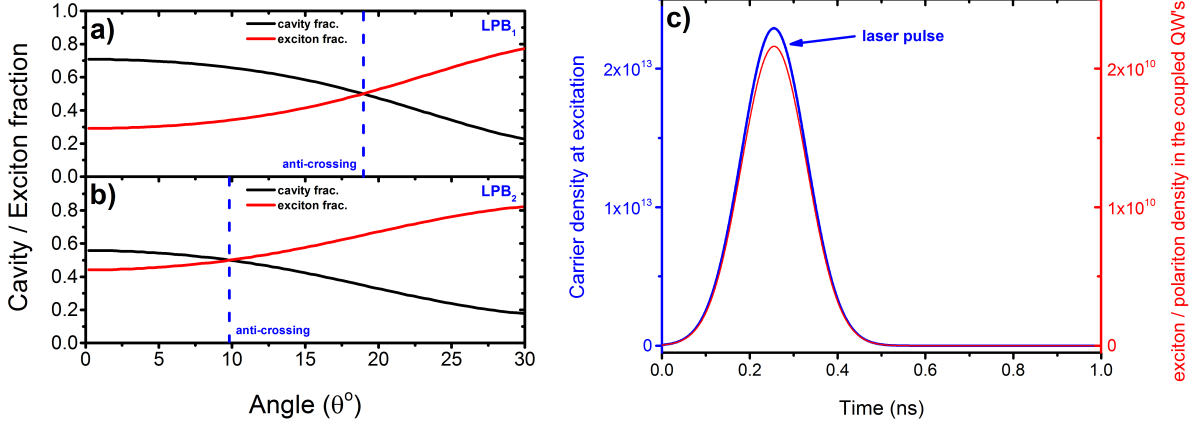


Figure 4.4: The exciton / cavity fraction corresponding to: (a) LPB₁, and (b) LPB₂. (c) A plot showing the carrier density at excitation (blue) and the exciton / polariton density (red), per QW per laser pulse, at threshold.

Polariton lasing can further be confirmed by estimating the exciton density per QW (coupled) at threshold. Usually by following the blue-shift (ΔE_{pol}^{LP}) of the LPB at around $k_{\parallel} = 0$, with pump power, up to threshold, an estimate for the exciton density / QW (N_{exc}^{2D}), at around $k_{\parallel} = 0$, at threshold, can be made using the following relation [7, 8]:

$$\Delta E_{pol}^{LP} = V_{pol} N_{exc}^{2D} \quad (4.6)$$

where V_{pol} is the matrix element of polariton-polariton interaction given by $V_{pol} = 6 |X_o|^2 E_x^B a_B^{*2} |X_o|^2$ being the exciton fraction at $k_{\parallel} = 0$, E_x^B the exciton binding energy and a_B^* the exciton Bohr radius. However in the case of membrane 4, as visible in Figure 4.3 (a), a blue-shift is hardly observable in LPB₁ up to threshold, underlining the ultra-low exciton densities in the coupled QW's of the microcavity system discussed here, compared to previous works. Alternatively, in order to estimate exciton densities in the coupled QW's, at around $k_{\parallel} = 0$, at threshold, a simple

system of equations is used as follows:

$$\frac{dN_2}{dt} = G - \frac{N_2}{\tau_{pol,2}^{LP}} - \frac{N_2}{\tau_{rel}} \quad (4.7)$$

where G is the carrier generation rate per QW per laser pulse at threshold, N_2 is the exciton density per QW per laser pulse at threshold in the reservoir, τ_{rel} is the time required for the lower polaritons to cool down from an initial temperature to the lattice temperature, and $\tau_{pol,2}^{LP}$ is the lifetime of polaritons in the reservoir, which should very much be influenced by $\tau_{exc} \sim 275$ ps. As per the discussion under subsection A.2.2, τ_{exc} is the estimated QW exciton lifetime at RT, for sample 2, very similar to the lifetime extracted from membrane 4, measuring independently. Since $\tau_{rel} \ll \tau_{pol,2}^{LP}$, at steady state, equation 4.7 can be written as following:

$$G = \frac{N_2}{\tau_{rel}} \quad (4.8)$$

The polariton density per QW per laser pulse (N_1), at around $k_{\parallel} = 0$, at threshold, can then be estimated using the following equation:

$$\frac{dN_1}{dt} = \frac{N_2}{\tau_{rel}} - \frac{N_1}{\tau_{pol,1}^{LP}} \quad (4.9)$$

where $\tau_{pol,1}^{LP}$ is the lifetime of the polaritons at around $k_{\parallel} = 0$. Substituting equation 4.8 into equation 4.9, gives the following equation:

$$\frac{dN_1}{dt} = G - \frac{N_1}{\tau_{pol,1}^{LP}} \quad (4.10)$$

Now G can be easily estimated from the energy density enumerated from the average threshold power density of ~ 4.5 W / cm², depicted in Figure 4.4 (c), taking into account the 5% loss from the top DBR mirror,

as directly determined from transmission measurements. $\tau_{pol,1}^{LP}$ for LPB₁, at $\sim k_{\parallel} = 0$, is estimated to be ~ 0.481 ps, using equation 4.1, where $\tau_{cav} \sim 0.34$ ps, estimated from the Q-factor of the microcavity system studied here (see subsection 3.3.5), using equation 3.14, and the exciton / cavity fractions for LPB₁ are determined from Figure 4.4 (a). Substituting these values into equation 4.10, gives a precise upper estimate of the steady state polariton density per laser pulse per QW (N_1 / n_{crit}), at threshold, at $\sim k_{\parallel} = 0^{\circ}$, for LPB₁, which is $\sim 2.1 \times 10^{10} / \text{cm}^2$, as depicted in Figure 4.4 (c). Now taking into account the exciton fraction ($|X_0|^2$) for LPB₁, at $\sim k_{\parallel} = 0^{\circ}$, the steady state exciton density per laser pulse per QW (N_{2D}^{exc}), at threshold, $\sim k_{\parallel} = 0^{\circ}$, for LPB₁, is given by:

$$N_{exc}^{2D} = N_1 |X_0|^2 \quad (4.11)$$

Substituting for N_1 and $|X_0|^2$ (determined from Figure 4.4 (a)), N_{exc}^{2D} is estimated to be around $6 \times 10^9 / \text{cm}^2$, more than two orders of magnitude below the exciton saturation density (n_{exc}^{sat}), which is $\sim 2 \times 10^{12} / \text{cm}^2$ [9]. The exciton saturation density is also independently estimated as described in [9, 10], using a QW exciton binding energy (E_x^B) of ~ 30 meV [9, 11] and an exciton Bohr radius (a_B^*) of ~ 2.7 nm, which in turn is enumerated from the binding energy. The corresponding threshold power density of ~ 4 W / cm^2 , is the lowest ever reported value for a 2D GaN-based microcavity system. Since at threshold, most of the lasing comes from level ‘3’, as opposed to level ‘1’, as visible in Figure 4.3 (c), an estimate for the steady state exciton density per laser pulse per QW (N_{2D}^{exc}), at threshold, $\sim k_{\parallel} = 0$, is also made for LPB₂, having an energy slightly greater than level ‘3’, which is not very different from the above estimated value in spite of the smaller detuning. Now based on the steady

state polariton density per laser pulse per QW (N_1 / n_{crit}), at threshold, $\sim k_{\parallel} = 0^\circ$, the possible blue-shift of LPB₁ with pump power is enumerated from equation 4.6, which turns out to be $\sim 0.06\text{meV}$, which is far below the maximum resolution of the system $\sim 0.2\text{meV}$.

To further confirm the validity of the estimates, the exciton density in the uncoupled QW's is determined based on the following equation:

$$\frac{dN_{exc}^{2D,uncoupled}}{dt} = G - \frac{N_{exc}^{2D,uncoupled}}{\tau_{exc}} \quad (4.12)$$

G is depicted from Figure 4.4 (c) and $\tau_{exc} \sim 275\text{ps}$, as per the discussion previously, thereby giving an estimate for the quasi steady state exciton density ($N_{exc}^{2D,uncoupled}$) per laser pulse per uncoupled QW, which is $\sim 10^{12} / \text{cm}^2$. Alternatively the exciton density is also estimated based on the blue-shift ($\Delta E_{exc,o}$) of the uncoupled QW excitons, up to threshold, as visible in Figure 4.3 (a), which is $\sim 9\text{meV}$, using equation 4.6, subjected to slight modification as follows:

$$\Delta E_{exc,o} = V_{exc} N_{exc}^{2D,uncoupled} \quad (4.13)$$

where V_{exc} is the matrix element of exciton-exciton interaction given by $V_{exc} = 6E_x^B a_B^{*2}$. The estimated exciton density per uncoupled QW $\sim 7 \times 10^{11} / \text{cm}^2$, which is very close to the density derived from the rate equation model.

4.5 The k-space pattern

Having confirmed ultra-low threshold polariton lasing, the spectacular pattern formed in k-space as visible in Figure 4.2 (c - f), corresponding to different energy levels, can be attributed to polaritons trapped in

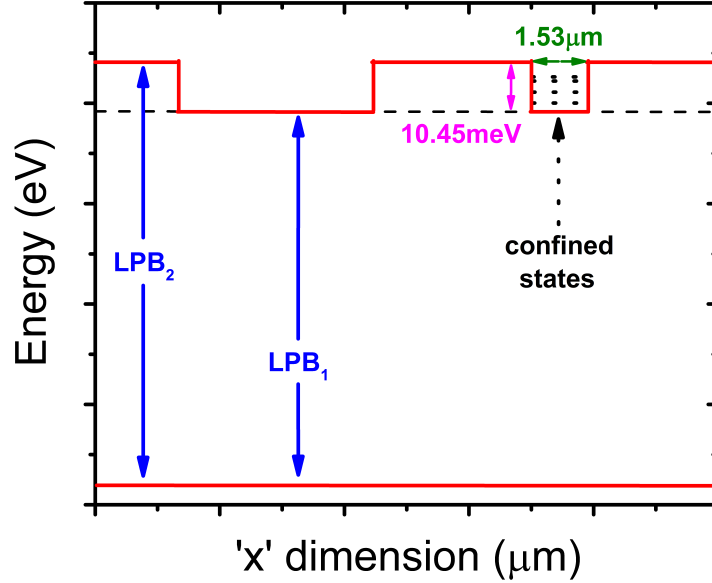


Figure 4.5: An energetic picture of membrane 4, depicting the two regions corresponding to LPB_1 and LPB_2 , and moreover highlighting the square-like pocket trap

‘in-plane’ natural pits [12, 13], arising from thickness variations on the membrane surface due to various reasons, which are discussed in detail under subsection 3.2.4.1. Such polaritons usually have a random pattern in k -space due to the multitude of confinement sites over the entire region being probed. However, only a single site-trapping, within the probed region can lead to such ordered condensation pattern, like in the case discussed over here, quite similar to the k -space imprint formed in the case of engineered polariton landscapes [14, 15]. It should be noted that the characteristic presence of such non-equilibrium condensate pattern within the k -space, further confirms the system to be in the kinetic regime i.e. $\tau_{rel} \gg \tau_{pol}^{LP}$. Moreover polaritons trapped in ‘in-plane’ natural pits, usually at the critical polariton density (n_{crit}), undergoes a Bosonic phase transition towards Anderson glass, before turning into superfluid at larger densities.

However to explain the scenario of the k -space pattern observed here,

different regions on the membrane corresponding to at least two different thicknesses are assumed, having a difference of $\sim 3.6\text{nm}$, (equivalent to 20.9meV , energy difference of the cavity modes corresponding to the two LPB's, as depicted in Figure 4.2 (c - f)), in the region of probing. Uniformly etched flat regions, which form the major part, correspond to LPB₁, while flat valleys correspond to LPB₂, with a relatively small LPB₁ hump (hereby referred to as a square-like pocket) acting as the site of confinement. Energetically this picture of the membrane surface can be transformed, as depicted in Figure 4.5. In order to verify this picture of polaritons getting confined in a site-specific trap (square-like pocket), Schrodinger's equation for particle in a 2D box is used, which is given by:

$$\left(\frac{-\hbar^2}{2m_{pol}^{LP}} (\delta_x^2 + \delta_y^2) + V(x, y) \right) \psi_{pol}^{LP}(x, y) = E\psi_{pol}^{LP}(x, y) \quad (4.14)$$

where $V(x, y) = V(x) + V(y)$, is the in-plane square-like pocket having an overall depth of $\sim 20.9\text{meV}$ (10.45meV in each direction), $\psi_{pol}^{LP}(x, y)$ is the polariton wavefunction and m_{pol}^{LP} is the polariton effective mass ($6.619 \times 10^{-5}m_o$, estimated using 4.1, for LPB₁, at $\sim k_{\parallel} = 0$). The model is used to simulate the discrete energy levels ('1', '2', '3'), just above threshold ($1.04P_{th}$), as depicted in Figure 4.6 (a), which returns four discrete energy levels 'a', 'b', 'c' and 'd', for a pocket width of $\sim 1.53\mu\text{m}$. The simulated levels, corresponding to different states, marked by a different colour, are visible in Figure 4.6 (a), where the degenerate states have the same energy. The real-space wavefunctions corresponding to the three levels ('1', '2', '3'), are plotted in Figure 4.6 (b - d), where the strip within the white dashed lines gives rise to the respective k-space profiles, in Figure 4.6 (a).

Level ‘a’ accurately simulates level ‘1’, which is relatively less visible in the image, although spectrally resolved, as depicted in Figure 4.6 (a). The corresponding wavefunction is $\psi_{pol}^{LP}(1, 1)$, as shown in Figure 4.6 (b). Level ‘b’ precisely matches the energy position of the two modes corresponding to level ‘2’, as visible in Figure 4.6 (a), with the respective wavefunction in Figure 4.6 (c), correlating to a superposition of degenerate states, $\psi_{pol}^{LP}(1, 2)$ and $\psi_{pol}^{LP}(2, 1)$, clearly showing two distinct maxima along the strip, within white dashed lines. Level ‘3’ corresponds to an average of the simulated levels, ‘c’ and ‘d’, with the respective wavefunctions being degenerate states [$\psi_{pol}^{LP}(1, 3)$ and $\psi_{pol}^{LP}(3, 1)$], and [$\psi_{pol}^{LP}(2, 2)$] subsequently. A superposition of the wavefunctions of degenerate states $\psi_{pol}^{LP}(1, 3)$ and $\psi_{pol}^{LP}(3, 1)$ or the independent wavefunction $\psi_{pol}^{LP}(2, 2)$ does not reproduce the k-space modes corresponding to level ‘3’, but a superposition of all three states, $\psi_{pol}^{LP}(1, 3)$, $\psi_{pol}^{LP}(3, 1)$ and $\psi_{pol}^{LP}(2, 2)$ are required, as shown in Figure 4.6 (d), where 3 distinct maxima are visible in the strip within white dashed lines, similar to the k-space modes of level ‘3’, as visible in Figure 4.6 (a). This confirms the contribution of simulated level’s ‘c’ and ‘d’ to level ‘3’. The discrepancy of the model, giving two resolved levels ‘c’ and ‘d’, instead of a single level, might be due to our assumption of the polariton trap being a perfect square-like pocket, a speculation made to simplify calculation complexities. However to verify this deviation, the levels in Figure 4.6 (a), are simulated, considering the trap to be an infinite supercircle [16], defined by a deformation parameter equal to 1.85, from reference [16], returning the first four energy lines defined by $E(m, n)$, where m is the azimuthal quantum number and n is the radial quantum number. $E(0, 1)$ and $E(1, 1)$ correspond to levels ‘1’ and ‘2’ with good precision, whereas the next two energy lines $E(2, 1)$ and

$E(0, 2)$ have exactly the same energies corresponding to level ‘3’, in Figure 4.6 (a), justifying the simulation of Level ‘3’ based on contributions from simulated levels ‘c’ and ‘d’, in the square well approach.

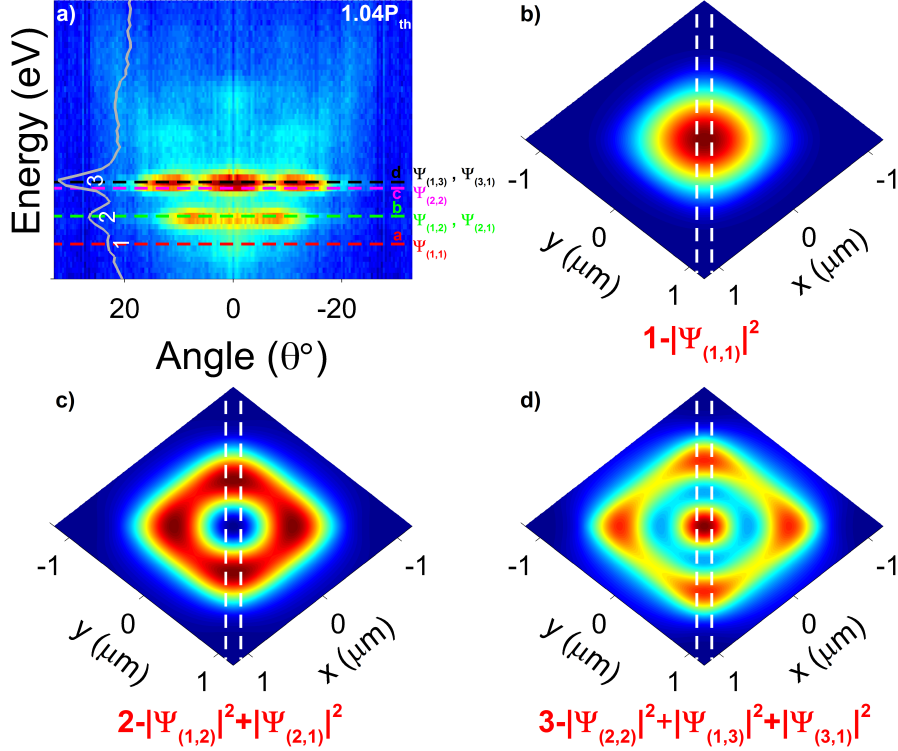


Figure 4.6: (a) PL imaging data from membrane 4 at RT, where the power density is $1.04P_{th}$. The corresponding spectral data is plotted within the image, marking the levels ‘1’, ‘2’ and ‘3’. The levels ‘a’, ‘b’, ‘c’ and ‘d’ are the respective simulated levels. A plot of the real space wavefunctions corresponding to: (b) level ‘1’, (c) level ‘2’, and (d) level ‘3’. The strip within white dashed lines gives rise to the respective k-space profiles.

4.5.1 Analysis of non-linear properties based on site-specific polariton trapping

The power dependent data in Figure 4.3 (a), is reanalysed based on the model, for polaritons trapped in a natural square-like pocket. At really low powers, most of the polariton emission comes from LPB_1 , although there could be simultaneous occupation of the lower confined states, in-

side the square-like pocket, which remains unresolved. The polaritons corresponding to LPB_2 , either fall into the flat humps of LPB_1 having an overall energy depth of around 20.9meV or into the square-like pocket, from a potentially flat landscape, minimising its visibility at low pump powers. With an increase in power, the polariton density increases, occupying higher states inside the pocket trap, which is seen as a broadening of the LPB_1 peak, towards higher energies. At higher powers (just before threshold), there is a subsequent filling up of the flat humps as well as the square-like pocket trap, corresponding to a more broadened LPB_1 peak, and thereby also results in a significant increase of the polariton density corresponding to LPB_2 , visible as a second peak, exhibiting a dispersive behaviour. It should be noted that just below threshold, LPB_2 peak is resolved while the confined states within the square-like pocket remain unresolved, which can be attributed to the energy proximity in the case of the latter, reflected by an unusual increase in the linewidth of LPB_1 towards the higher energy side, with pump power, as depicted in Figure 4.3 (a), whereas the former can be attributed to its 13meV blue-shifted position, as opposed to LPB_1 . Just above threshold, at $1.04P_{th}$, level ‘3’ (see Figure 4.3 (c)) has the maximum intensity, followed by level ‘2’ and finally the lowest energy level ‘1’. This can be attributed to the higher polariton lifetime of level ‘3’, closer to the excitonic reservoir, as compared to lower levels, in line with the discussion under section 4.2. In other words, it is easier for the polariton population to build-up in level ‘3’, followed by level ‘2’ and finally level ‘1’. This explanation holds only up to threshold, or maybe a bit above threshold, but beyond that, stimulated scattering [2, 6] takes over, efficiently scattering more polaritons into the lower states, as visible in Figure 4.3 (c). In par with the dis-

cussion, at $1.26P_{th}$, level ‘1’ has the highest intensity, followed by levels ‘2’ and ‘3’. This behaviour can also be confirmed from the occupation numbers, above threshold, as depicted in Figure 4.3 (d). Another factor contributing to the high intensity of level ‘3’, just above threshold, is the high occupation due to three degenerate states followed by level ‘2’ having two degenerate states and finally level ‘1’ having just a single state [12].

The non-linear properties of polaritons getting trapped in a site-specific square-like pocket is demonstrated in GaN based systems for the first time, offering significant advantages over conventional systems, where ‘in-plane’ natural pits do play their role unfavourably. In the case of the microcavity system discussed here, the relaxation dynamics as well as lifetimes of polaritons from at least two different sources, LPB_1 and LPB_2 , both having its own advantages and disadvantages, derived from a more photonic behaviour of the former as compared to the latter, are used to pump a square-like pocket, helping to escalate the polariton density locally, resulting in an ultra-low threshold, as low as $4W / cm^2$ for the system studied here. The overall efficiency of the trapping mechanism lies in easily triggering-off lasing, at the highest level inside the square-like pocket, where the build-up of polariton density is relatively easy, as discussed earlier, acting as an avalanche for the lower levels, with the aid of stimulated scattering.

4.6 Conclusion

To conclude, an ultra-low average threshold of $\sim 4.5W / cm^2$ ($\sim 594\mu J / cm^2$), polariton laser in the kinetic regime, has been realised at room temperature, based on GaN membranes containing GaN / AlGaN quantum

wells, under non-resonant quasi-continuous excitation. The threshold reported is the lowest ever for 2D GaN based systems [1]. Above threshold, the system can be confirmed to be in the strong coupling regime due to the following reasons: (1) a dispersive behaviour, indicative of polariton dispersion, observed in the k-space images, (2) the estimated exciton density per coupled QW, at threshold, is at least more than two orders below the exciton saturation density. Moreover analysing the beautiful k-space condensation pattern above threshold, based on polaritons getting trapped in a site-specific square-like pocket, has revealed that the mechanism could lead to the escalation of polariton density locally, resulting in an ultra-low threshold. The high quality of the all-dielectric microcavity also contributes to the ultra-low threshold, reported here.

Bibliography

- [1] G. Christmann, R. Butté, E. Feltin, J.-F. Carlin, and N. Grandjean. “Room temperature polariton lasing in a GaNAlGaN multiple quantum well microcavity”, *Applied Physics Letters* 93.5 (2008), p. 051102.
- [2] M. S. Skolnick, A. I. Tartakovskii, R. Butté, D. M. Whittaker, and R. M. Stevenson. “High-occupancy effects and stimulation phenomena in semiconductor microcavities”, *IEEE Journal on Selected Topics in Quantum Electronics* 8.5 (2002), pp. 1060–1071.
- [3] J. Levrat, R. Butté, E. Feltin, J. F. Carlin, N. Grandjean, D. Solnyshkov, and G. Malpuech. “Condensation phase diagram of cavity polaritons in GaN-based microcavities: Experiment and theory”, *Physical Review B - Condensed Matter and Materials Physics* 81 (2010), pp. 1–11.
- [4] S. Christopoulos, G. von Högersthal, A. Grundy, P. Lagoudakis, A. Kavokin, J. Baumberg, G. Christmann, R. Butté, E. Feltin, J.-F. Carlin, and N. Grandjean. “Room-Temperature Polariton Lasing in Semiconductor Microcavities”, *Physical Review Letters* 98.12 (Mar. 2007), pp. 1–4.
- [5] J. Kasprzak, M. Richard, S. Kundermann, A. Baas, P. Jeambrun, J. M. J. Keeling, F. M. Marchetti, M. H. Szymańska, R. André, J. L. Staehli, V. Savona, P. B. Littlewood, B. Deveaud, and L. S. Dang. “Bose-Einstein condensation of exciton polaritons.”, *Nature* 443.7110 (2006), pp. 409–414.
- [6] R. Butté, G. Delalleau, A. Tartakovskii, M. Skolnick, V. Astratov, J. Baumberg, G. Malpuech, A. Di Carlo, A. Kavokin, and J. Roberts. “Transition from strong to weak coupling and the onset of lasing in semiconductor microcavities”, 65 (2002), pp. 2–10.
- [7] F. Tassone and Y. Yamamoto. “Exciton-exciton scattering dynamics in a semiconductor microcavity and stimulated scattering into polaritons”, *Physical Review B* 59.16 (1999), pp. 10830–10842.
- [8] C. Ciuti, P. Schwendimann, B. Deveaud, and A. Quattropani. *Theory of the angle-resonant polariton amplifier*. 2000.

- [9] G. Rossbach, J. Levrat, G. Jacopin, M. Shahmohammadi, J.-F. Carlin, J.-D. Ganière, R. Butté, B. Deveaud, and N. Grandjean. “High-temperature Mott transition in wide-band-gap semiconductor quantum wells”, *Physical Review B* 90.20 (Nov. 2014), p. 201308.
- [10] G. Christmann, R. Butté, E. Feltin, A. Mouti, P. Stadelmann, A. Castiglia, J.-F. Carlin, and N. Grandjean. “Large vacuum Rabi splitting in a multiple quantum well GaN-based microcavity in the strong-coupling regime”, *Physical Review B* 77.8 (Feb. 2008), pp. 1–9.
- [11] P. Shields, R. Nicholas, N. Grandjean, and J. Massies. “Magnetophotoluminescence of GaN/Al_xGa_{1-x}N quantum wells: Valence band reordering and excitonic binding energies”, (2001), pp. 1–9. arXiv: 0101069v1 [arXiv:cond-mat].
- [12] D. Sanvitto, A. Amo, L. Viña, R. André, D. Solnyshkov, and G. Malpuech. “Exciton-polariton condensation in a natural two-dimensional trap”, *Physical Review B - Condensed Matter and Materials Physics* 80 (2009), pp. 1–6. arXiv: 0903.2723.
- [13] F. Li, L. Orosz, O. Kamoun, S. Bouchoule, C. Brimont, P. Disseix, T. Guillet, X. Lafosse, M. Leroux, J. Leymarie, M. Mexis, M. Mihailovic, G. Patriarche, F. Réveret, D. Solnyshkov, J. Zuniga-Perez, and G. Malpuech. “From excitonic to photonic polariton condensate in a ZnO-based microcavity”, *Physical Review Letters* 110.May (2013), pp. 1–5. arXiv: 1207.7172.
- [14] K. Winkler, J. Fischer, A. Schade, M. Amthor, R. Dall, J. Geßler, M. Emmerling, E. A. Ostrovskaya, M. Kamp, C. Schneider, and S. Höfling. “A polariton condensate in a photonic crystal potential landscape”, *New Journal of Physics* 17.2 (Jan. 2015), p. 023001.
- [15] C. W. Lai, N. Y. Kim, S. Utsunomiya, G. Roumpos, H. Deng, M. D. Fraser, T. Byrnes, P. Recher, N. Kumada, T. Fujisawa, and Y. Yamamoto. “Coherent zero-state and pi-state in an exciton-polariton condensate array.”, *Nature* 450.November (2007), pp. 529–532.
- [16] N. Bera, J. K. Bhattacharjee, S. Mitra, and S. P. Khastgir. “Energy levels of a particle confined in a super-circular box”, *European Physical Journal D* 46.1 (2008), pp. 41–50.



This page is intentionally left blank

Study of GaN nanowires as a potential candidate for polaritonic applications

5.1 Introduction

It is widely accepted that semiconductor nanowires (NWs) have a potential for low cost solar cell applications based on two main reasons: first, their relaxed lattice matching requirements due to strain accommodation at the NW free surface, providing flexibility in substrate selection and band-gap engineering, and second, the possibility for lesser material utilisation due to enhanced light absorption in NW arrays. On the latter very important issue, there has been extensive literature in recent years reporting on enhanced absorption characteristics of NW arrays, as a consequence of several physical effects such as their anti-reflective (AR) properties due to natural refractive index matching and grading [1–3], increased light trapping inside the NW array [3–5], and the excitation of resonant modes [6–10]. This enhanced absorption along with the high quality of strain free nanowires can find immense applications not only in the field of solar cells but also polaritonics. Recently Das et al. have shown a very large Rabi splitting value and an ultra-low threshold for their GaN nanowire based polariton lasers, where a single nanowire is positioned at the antinode of the field distribution within the microcavity structure [11, 12]. Towards this direction, a better understanding about the basic optical properties as well as absorption coefficients of GaN nanowires, considering the fact

that they are directly proportional to the oscillator strength of the excitons, could bring into light a new generation of extremely efficient GaN polaritonic devices.

However, in spite of the important role played by absorption coefficients in NW systems, most of the literature regarding nanowire absorption coefficients mentioned above, refers to theoretical predictions based on solving wave propagation models of increasing sophistication inside the NW array, whereas the corresponding experimental works claiming increased absorption in nanowire systems have been relatively few, and rely mostly on indirect experiments, such as photocurrent measurements. More specifically, increased absorption has been observed in direct optical transmission experiments on etched-down vertical Si nanowires, positioned on transparent [2] or semitransparent [3, 5] substrates, and was attributed to reduced reflectance and enhanced light trapping effects in the NW array. The effect of light trapping was also used to interpret the enhanced I-V characteristics of Si nanowire solar cells [4]. Regarding resonant effects, Cao et al. [6] observed distinct resonances in the spectral response of single Ge nanowire photodetectors, that they attributed to the excitation of leaky mode resonances formed at the nanowire/air dielectric system. The excitation of resonant modes as a means to increase the absorption of NW arrays was discussed in several theoretical works [7–10] and was used to interpret the improved performance of single Si nanowire photovoltaic devices [13], the very high 13.8% efficiency of InP-based NW solar cells [14] as well as the single GaAs NW photovoltaic device with $\eta \sim 40\%$ [15]. Although the above indirect measurements clearly suggest a serious enhancement in the absorption process, nevertheless, direct absorption measurements in the same as-grown NW systems

were not possible, mainly due to the fact that the substrates used were opaque. In this work, a new direct method is demonstrated, to extract absorption coefficients from as-grown GaN NWs grown on Si<111> substrates, using an all-optical method, merely by analysing the reflectivity spectra. This method can be extended to any family of NWs, provided they are grown on a substrate having considerable difference in permittivity with the nanowire-air matrix. Moreover the basic optical properties of the GaN NW system are carefully studied.

5.2 Samples studied and experimental methods

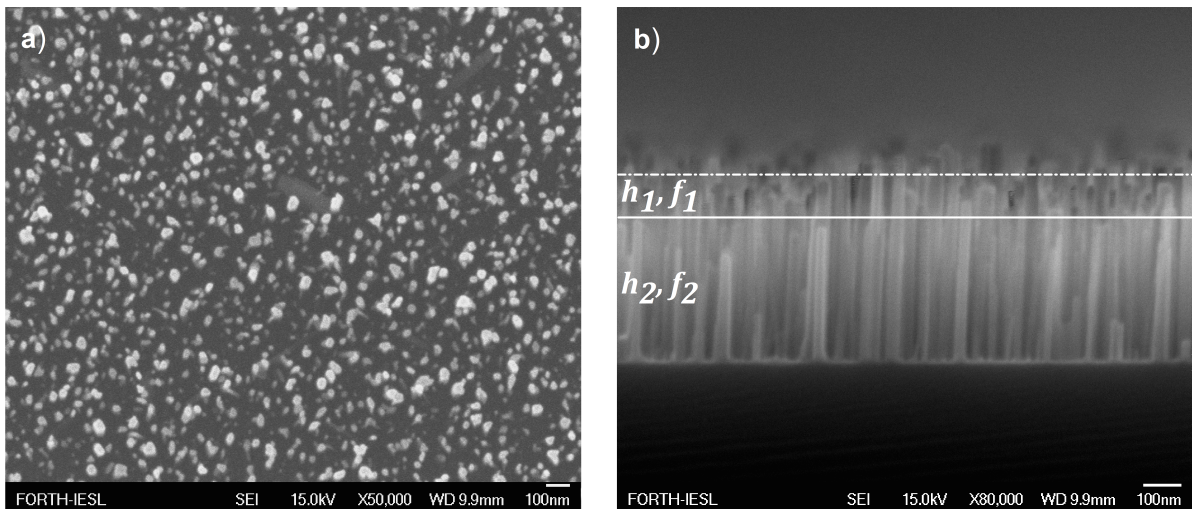


Figure 5.1: (a) Top, and (b) lateral SEM view, of GaN (0001) nanowires on Si (111).

The GaN NWs studied here are grown along the [0001] direction on a Si (111)-oriented substrate, by plasma-assisted molecular beam epitaxy (PAMBE), at nitrogen rich conditions. Several samples are grown at variable conditions, all however having similar diameters, heights and densities, typical of high quality GaN NWs grown on un-patterned substrates. The Scanning Electron Microscopy (SEM) top and lateral view for one

of the samples (G1643) are shown in Figure 5.1 (a) and Figure 5.1 (b) respectively. The GaN NWs are upright and uniform, having average heights (h) of $\sim 450\text{nm}$, diameters (d) of $\sim 24\text{nm}$, and a density of about 10^{10}cm^{-2} . A good fraction of the NWs possess on the top pitted tips or step-like surfaces, while the rest have flat top surfaces. More information regarding the possible morphologies of the top of GaN nanowires can be found in [16], supported by high quality TEM images. The pitted tip of nanowires is attributed to inversion domain boundaries while the step-like surface is due to prismatic stacking faults or planar defects [16]. A separate two-dimensional (2D) GaN thin film used for modelling is grown using the same technique along the [0001] direction on a Si substrate (111). The thickness of the 2D film is $\sim 810\text{nm}$ and possesses good crystalline quality. Most of the experimental results presented in this chapter are based on sample G1643, although very similar results are observed on the other available samples as well.

All basic PL / Reflectivity measurements are made using the setup described in subsection A.2.1. A He-Cd laser, at 325nm is used as a source of excitation for PL measurements whereas a Xenon lamp is used for reflectivity measurements. See section A.1 for more information. All high-resolution PL / reflectivity spectra are taken using a $2400\text{grooves} / \text{mm}$ grating, while the lower resolution spectra are taken using a $600\text{grooves} / \text{mm}$ grating (see subsection A.1.4 for more details). The absorption coefficients reported in the paper depend strongly on a precise estimate of the filling factor of the NW array. This is determined accurately by simulating the Fabry Perot region, of the total reflectivity spectrum, (i.e. specular + diffuse), acquired with a 150mm integrating sphere, equipped on a Perkin Elmer LAMBDA 950 UV / Vis / NIR Spectrophotometer,

as described in detail in subsection A.2.7. In this setup, apart from the total reflectivity, the diffuse reflectivity is separately recorded.

5.3 Basic optical characterisation

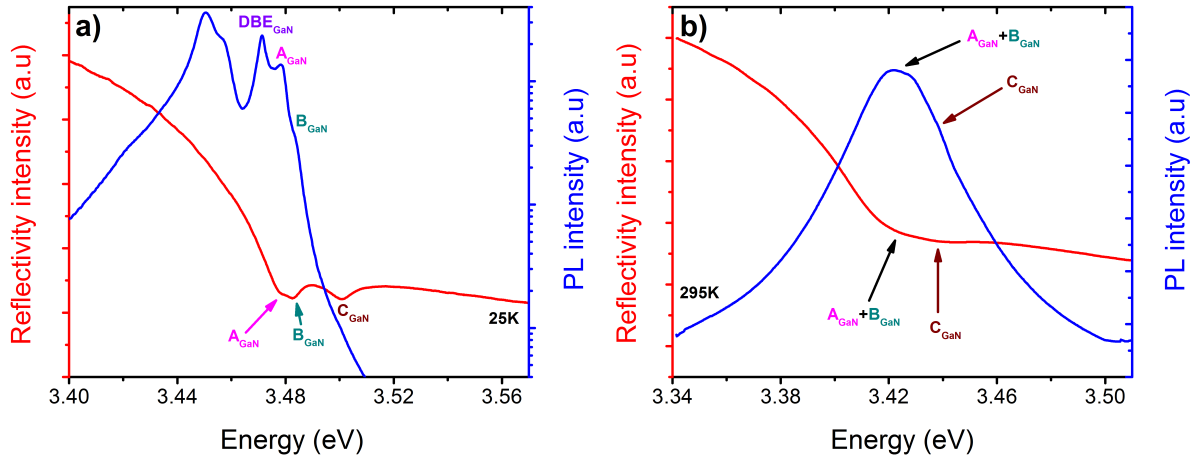


Figure 5.2: Comparison of PL (blue) and reflectivity (red) from GaN NWs: (a) at LT, and (b) at RT, showing pronounced excitonic features.

All measurements in this section are made using the setup described in A.2.1, where the initial experimental conditions are detailed in 5.2. The GaN NWs are of high optical quality, as testified by comparing the PL and reflectivity spectra, at LT and RT respectively, as depicted in 5.2. At LT, the A and B free excitons are clearly visible at ~ 3.4782 eV and ~ 3.4825 eV respectively, denoted as A_{GaN} and B_{GaN} subsequently, with the Donor Bound Exciton (DBE_{GaN}) emission placed approximately 7 meV below A_{GaN} excitons, at ~ 3.4713 eV. These positions are in excellent agreement with those reported for GaN films grown on bulk GaN substrates [17, 18], underlining the absence of any residual strain in the nanowires. The linewidth of DBE_{GaN} peak is ~ 4.4 meV, comparing closely to the DBE emission linewidth from strain free bulk GaN films. The PL spectrum highlights a double structure peak ~ 3.45 eV, which is typical

in N-polar GaN films, GaN samples with columnar structure, as well as in self-induced GaN nanowires. Its origin has been a topic of debate, as discussed by several groups [19–23]. A relatively weak peak ~ 3.42 eV can be attributed to excitons bound to surface defects [19] or to stacking faults [19, 20]. With increasing temperature, the excitons are seen to red-shift and broaden, in line with excitonic behavior, as shown in Figure 5.3 (a). Both the DBE_{GaN} emission as well as the doublet structure peak at ~ 3.45 eV “die” off quickly, becoming weaker than the free exciton lines, already at ~ 80 K. Above 80 K, the PL spectrum is dominated by free exciton emission all the way up to room temperature, a clear sign of high optical quality. A_{GaN} and B_{GaN} excitons start merging around 100 K, and a weak shoulder appears on the higher energy side, ~ 23 meV from A_{GaN} excitonic position, as depicted in Figure 5.3 (b). It is an energy position reported for C excitons in bulk GaN films [17, 18], hereby being denoted as C_{GaN} . At around 180 K, A_{GaN} and B_{GaN} excitons completely merge with each other, whose evolution can then be followed up to RT, as visible in Figure 5.3 (a). However the behaviour of C_{GaN} excitons with temperature is rather difficult to follow, due to its very weak signature in the PL. At RT, $A_{\text{GaN}} + B_{\text{GaN}}$ peak is centred ~ 3.422 eV, very similar to bulk GaN films, as visible in Figure 5.2 (b).

In order to confirm the excitonic positions and probe their oscillator strengths, specular reflectivity measurements are undergone, at an angle of incidence $\sim 15^\circ$, as shown in Figure 5.2. At low temperature, A_{GaN} and B_{GaN} excitons are clearly visible, perfectly corresponding to their PL positions. A third peak is also observed at ~ 3.5007 eV, matching very well with the position of C_{GaN} excitons reported in bulk GaN films [17, 18]. The A_{GaN} and B_{GaN} excitons appear to have very similar oscillator strengths,

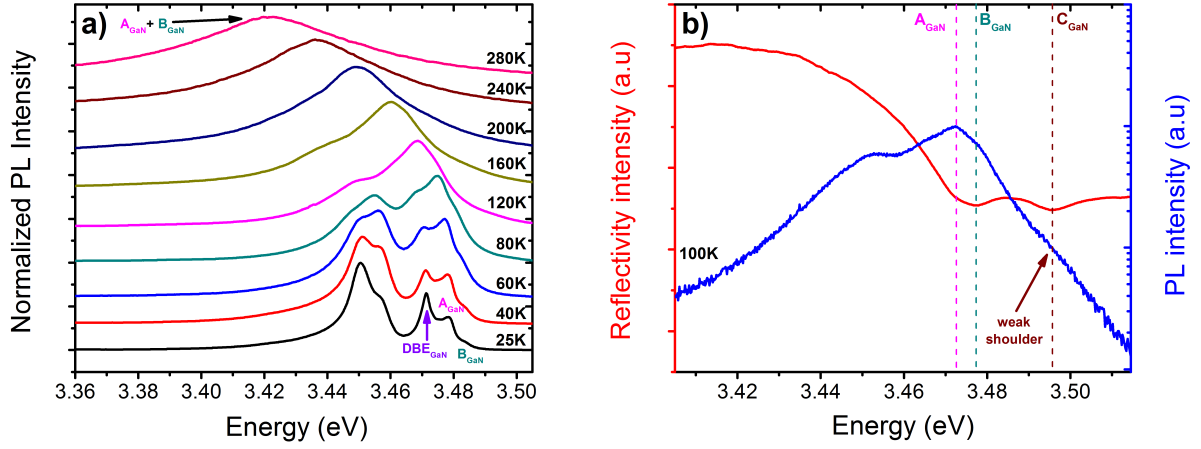


Figure 5.3: (a) Evolution of GaN NW excitons with temperature, based on PL. (b) Comparison of PL (blue) and reflectivity (red) from GaN NWs at 100K, where the weak shoulder corresponds to C_{GaN} excitons.

which is consistent with the picture of strain-free nanowires, considering that in strained GaN films, the B_{GaN} excitons tend to be stronger than the A_{GaN} ones [24, 25]. Interestingly, the oscillator strength of the C_{GaN} exciton is comparable to that of A_{GaN} and B_{GaN} excitons. This is somewhat puzzling, considering that in small angle reflectivity experiments on c -axis oriented GaN films, the C_{GaN} excitons are strongly suppressed [17, 18] in accordance with the well-known polarisation selection rules for GaN [26], favouring the A_{GaN} and B_{GaN} excitons for polarisation perpendicular to the c -axis, and the C_{GaN} excitons for polarisation parallel to it. Possible explanation for this is that, although the majority of NWs seem upright in Figure 5.1 (b), there is a scarce population of tilted NWs, or small deviations from verticality, relaxing the selection rule and enhancing the C_{GaN} exciton signature, in conjunction with the well-known anisotropy of the nanowires amplifying the absorption cross section for polarisation parallel to the c -axis [27]. In order to ensure that the 3.5eV peak behaves indeed as a C_{GaN} exciton, a polarisation-dependent reflectivity experiment is carried out at large incidence angles ($\sim 65^\circ$), using a Glan Thomson po-

lariser. Unlike the small angles, where all polarisation components are essentially perpendicular to the c-axis, the large angles serve the purpose of creating significant parallel and perpendicular to the c-axis polarisation components depending on the polariser angle. The results are as shown in Figure 5.4 (a). The angle 0° corresponds to p-polarisation whereas the angle 90° to s-polarisation. As expected, the C_{GaN} exciton line is much stronger at angle 0° , where a significant polarisation component parallel to the c-axis exists, whereas is significantly reduced at angle 90° , where all polarisation components are perpendicular to c-axis. With increasing temperature, the excitons start red shifting accompanied by broadening, where A_{GaN} and B_{GaN} excitonic features merge together forming a single peak at RT, whereas the C_{GaN} excitons can be uniquely identified at RT, by carefully following its evolution with temperature. The two peaks are depicted in Figure 5.2 (b), corresponding very well to its respective PL positions as well.

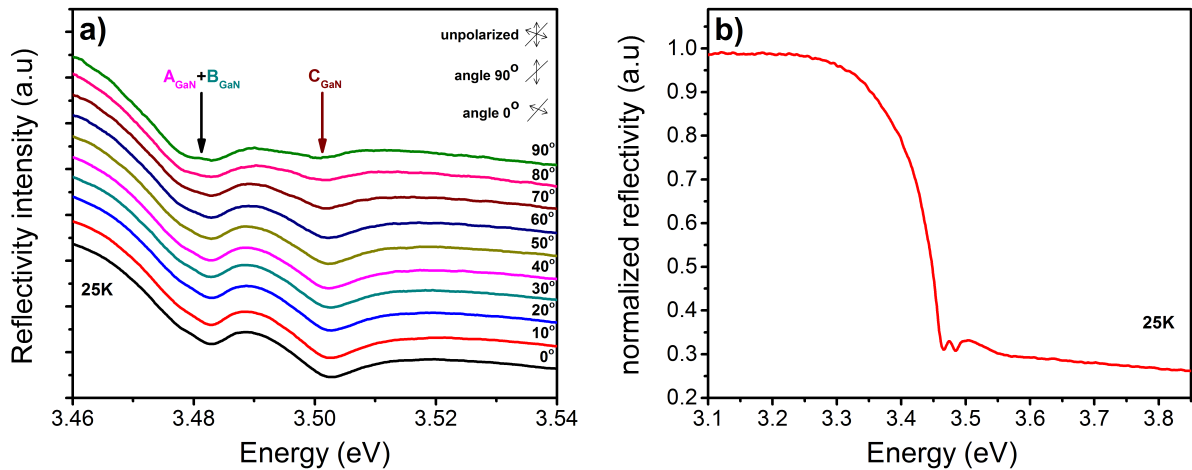


Figure 5.4: (a) Polarisation-resolved reflectivity measurements, at a large angle of incidence of $\sim 65^\circ$, where the polariser angle is varied from 0° to 90° , demonstrating the polarisation dependence of the excitons. (b) Wide range reflectivity spectrum of GaN NWs showing transmission-like characteristics.

However, what is most interesting in the optical characterisation of the NW samples is that the reflectivity spectrum looks very much like

transmission. This is quite evident in the wide range reflectivity spectrum of Figure 5.4 (b), where the characteristics of a transmission spectrum can be clearly distinguished, with the low absorption region below gap and the presence of exciton absorption peaks at A_{GaN} , B_{GaN} and C_{GaN} excitonic positions respectively [26]. Please note that the A_{GaN} and B_{GaN} excitons appear to be merged into a single peak due to the lower resolution grating used. The “transmission-like” characteristics of the reflectivity spectrum can be understood by considering a very simple scenario. If negligible reflectivity is assumed at the top GaN NW / air interface, then the specularly reflected spectrum of Figure 5.4 (b) derives from the light reflected at the bottom GaN NW / Si interface, after having traversed twice the GaN NW array, containing thus important information about the absorption characteristics of the NW array. In the rest of the chapter, this simple picture is validated, which in turn is used to extract for the first time, useful absorption coefficients for a NW system, grown on an opaque substrate. The estimation of absorption coefficients can provide an insight into the oscillator strength of the respective GaN NW excitons, which then can be harnessed for robust polaritonic applications.

5.4 Total reflectivity measurements and modelling

A key observation, strongly suggesting the anti-reflective character of the GaN NW/air interface, is the lack of any pronounced Fabry-Perot oscillation in the transparent region of GaN, at RT, as shown in Figure 5.5. By contrast, very intense Fabry-Perot oscillations are observed in the total reflectivity spectrum of the reference GaN/Si thin film, at RT, as shown in Figure 5.6 (a), consistent with having two optically-flat

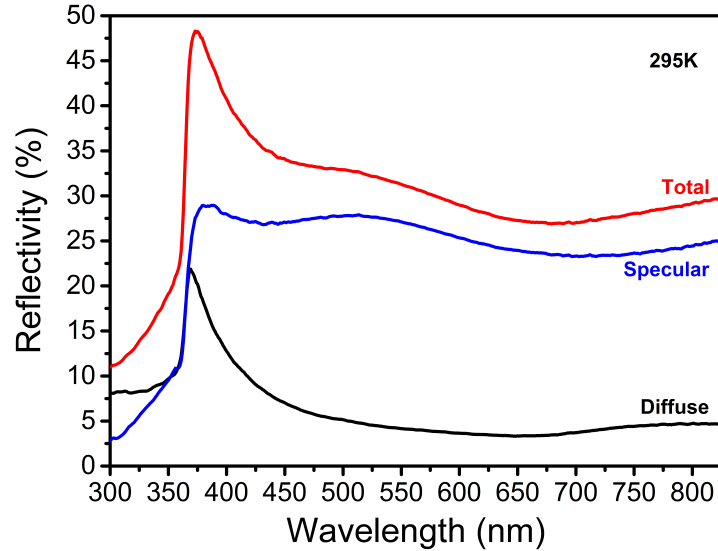


Figure 5.5: Total (red), specular (blue) and diffuse (black) reflectivity spectra obtained from the GaN NW sample, at RT.

top and bottom interfaces. By simulating the Fabry-Perot region of the total reflectivity spectrum for the two types of samples, quantitative information can be extracted, and moreover allows for the demonstration of very low reflectivity values, for the top GaN NW surface. Towards this end, it is necessary to perform some high precision total reflectivity measurements, taking into account the possible contribution of diffuse reflectivity. Thus, all measurements essential for modelling are taken with the help of the setup described in detail in A.2.7, which is operated in two configurations: 1) with specular white plate, 2) with specular light trap, corresponding to total and diffuse reflectivity measurements, as depicted in Figure 5.5. Subtraction of the diffuse from the total reflectivity gives the specular reflectivity, whose shape is in close similarity with the one, returned by measurements made with the setup described in A.2.1. In addition, the diffuse reflectivity of the nanowires appears to be significant even in the long wavelength region where it amounts to 5%. With decreasing wavelength, the NW diameter to wavelength ratio increases

[28] and the diffuse reflectivity becomes more prominent, reaching values over 20% near the GaN gap. Above the gap, the diffuse signal drops down sharply, due to the abrupt onset of absorption, limiting the volume for diffuse scattering to the very top part of the NW array. The 8.5% plateau at short wavelengths can thus be interpreted as due to surface diffuse scattering. Overall, however, it is clear from Figure 5.5 that the diffuse reflectivity cannot be neglected, making it essential to compare the modelling results with total reflectivity spectra, rather than specular alone.

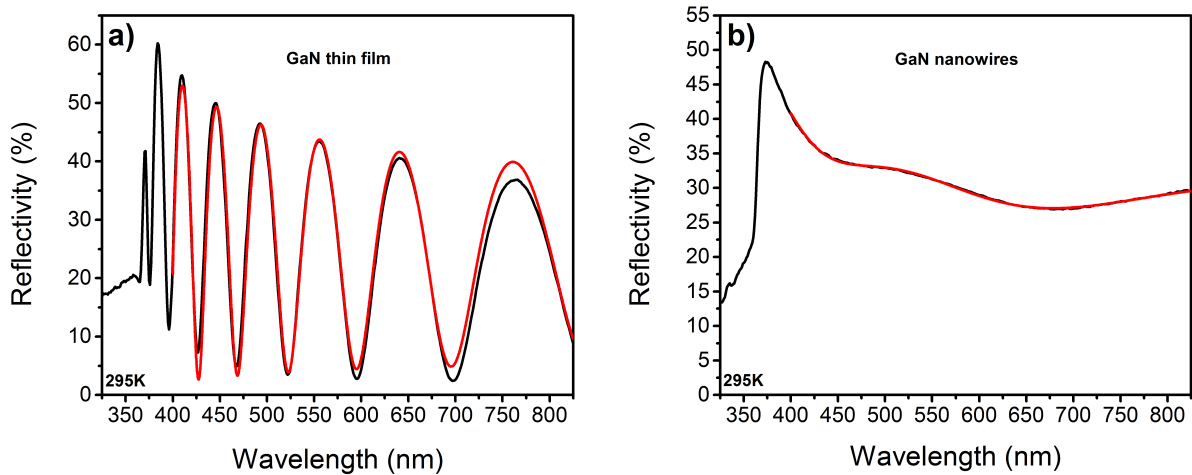


Figure 5.6: Simulation of the total reflectivity spectrum from: (a) GaN / Si thin film, and (b) GaN NWs grown on Si, where the black and red lines correspond to experimental and simulated data respectively.

In order to simulate the reflectivity in the transparent region for the two types of structures, a transfer matrix model, described in detail in appendix B is utilised. Several assumptions go along with the model: (1) the film and substrate are optically isotropic and homogeneous, (2) the surface of the film is flat and smooth, (3) there is no residual absorption in the Fabry-Perot region, and (4) the back reflection from the substrate / air bottom interface can be neglected, which applies in the case of the

samples discussed here since the Si substrate is strongly absorbing in the wavelength range under consideration. In order to ensure the accuracy of the model, initially the simulation is run for the reflectivity spectrum from GaN / Si thin film, whose nominal thickness is $\sim 810\text{nm}$. All the initial assumptions made for the model are applicable here. The Sellmeier coefficients for GaN as well as Si as a function of incident wavelength, at RT, are taken from [29, 30] respectively. The angle of incidence is set to $\sim 8^\circ$, similar to the incident angle used in the integrating sphere setup (see subsection A.2.7). The thickness of the GaN layer is the only adjustable parameter. The model precisely simulates the experimental data, as depicted in Figure 5.6 (a), for a thickness of $\sim 808.4\text{nm}$, very close to the nominal thickness of the film.

The transfer matrix model is now used to simulate the total reflectivity spectrum from GaN nanowires on Si, as visible in Figure 5.6 (b), where the nominal average height of the nanowires is $\sim 450\text{nm}$ (from SEM lateral view). However, the NW array does not meet the first two assumptions of the model, i.e. they are not optically isotropic and homogeneous, nor do they have a flat and smooth surface. Instead, the nanowires can be compared to a set of anisotropic scatterers dispersed in a medium of air forming a dielectric matrix that is not homogeneous [27]. In order to turn the NW array into a homogeneous medium, with a flat and smooth surface, an effective medium theory (EMT) [27, 31, 32] has to be applied. EMT calculates an effective permittivity for the dielectric matrix provided the individual permittivities $\varepsilon(\lambda) = n(\lambda)^2$, hereafter denoted as ε , and the volume fractions of the constituents are known [32]. However, a prerequisite for the validity of EMT is that the wavelength of incident light must be much larger than the nanowire average diameters and inter-

spacings (long-wavelength limit). This holds in the case of the nanowires described here, since the wavelength range of interest is between 400 nm and 845 nm, which is much larger than the nanowire average diameter ($d = 24\text{nm}$) as well as the inter-spacing between them, which is around 50 nm in this sample.

5.4.1 Homogenising an anisotropic medium

If the nanowires are considered to be inherently anisotropic scatterers [27], in the sense that light polarised parallel to the NW long axis is scattered more efficiently than light polarised perpendicular to it, then any effective medium theory homogenising the NW array, should take into account this anisotropy by using an effective permittivity tensor [27]. If the scatterers are aligned along a given crystallographic direction, the tensor can take the following form:

$$\varepsilon = \begin{pmatrix} \varepsilon_1 & 0 & 0 \\ 0 & \varepsilon_2 & 0 \\ 0 & 0 & \varepsilon_3 \end{pmatrix} \quad (5.1)$$

where ε_1 , ε_2 and ε_3 are the effective permittivities along the three principal axes. Such a medium is called birefringent and here it can be referred to as form birefringence [13], in order to differentiate it from the birefringence usually seen in certain types of crystals. For instance, if the nanowires are grown along the c-axis, all directions perpendicular to the growth direction can be expected to behave the same way i.e. $\varepsilon_1 = \varepsilon_2 \neq \varepsilon_3$. The tensor thus becomes that of a standard uniaxial birefringent material, where ε_1 and ε_2 correspond to effective ordinary permittivity (polarisation perpendicular to long axis) and ε_3 to effective extra-ordinary permittivity

(polarisation parallel to long axis) [13]. In the case of the nanowires discussed here, such complex homogenising procedures are not required, since the NWs are oriented along the c-axis, and the angle of incidence is near to normal, implying that both s and p polarisation of the incident light are practically perpendicular to the nanowire axis. As such, the medium's response is expected to be isotropic and can be described by a single effective ordinary permittivity.

5.4.2 Estimation of effective ordinary permittivity using effective medium theory (EMT)

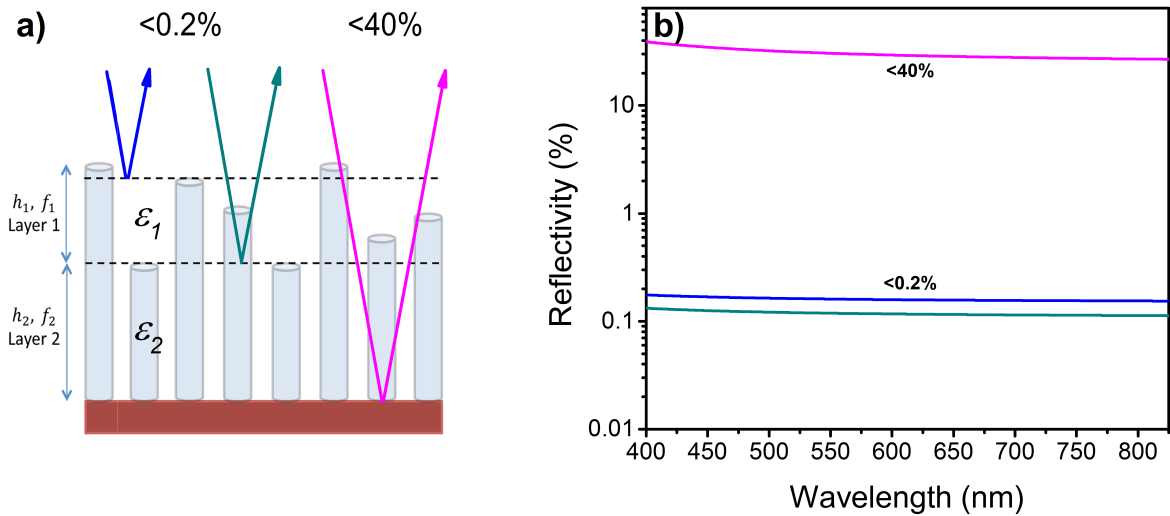


Figure 5.7: (a) An illustrative diagram showing how the nanowires are divided into two layers, introducing four parameters: h_1 - height of top layer, f_1 - volume fraction of top layer, h_2 - height of bottom layer and f_2 - volume fraction of bottom layer. (b) Deduced power reflectivities from the simulation, at different interfaces of the GaN NW array, such as top (blue), middle (dark cyan) and bottom (magenta) interfaces.

There are two well-known effective medium theories for calculating the effective ordinary permittivity of a dielectric matrix, based on Lorentz-Lorentz Clausius-Mossotti equation [32]: (1) the Maxwell Garnett theory (MGT), and the (2) Bruggeman effective medium approximation (EMA)

[31, 32]. Between the two, the MGT is less adapted to describe a GaN NW system, due to the large refractive index contrast between air and GaN, condition for which MGT fails. Therefore, hereafter, the Bruggeman EMA theory is applied, for which it is essential to know the permittivities of air and GaN, as well as the volume fraction of the nanowires in the dielectric matrix. To get an idea about the NW volume fraction, the SEM images are carefully observed, where one can easily realise that although most of the nanowires are upright, they have different heights, and as mentioned earlier, a fraction of them have stepped surfaces while some are pitted towards the top. In other words, the SEM images suggest that the effective ordinary permittivity should be graded along the height of the dielectric matrix. Accordingly, the dielectric matrix is divided into two layers for simplicity, as depicted in Figure 5.7 (a), introducing four parameters: h_1 - height of top layer, f_1 - volume fraction of top layer, h_2 - height of bottom layer and f_2 - volume fraction of bottom layer. The minimum height of most of the nanowires is determined by SEM lateral view to be $\sim 345.5\text{nm}$ and is assigned to h_2 . In order to estimate volume fractions, a magnified version of the grey scale, top view SEM image, of the nanowires, as visible in Figure 5.1 (a), is carefully analysed. Each pixel on the image has a relative intensity corresponding to the height of the nanowire in that particular spot. Next, an edge enhancement technique is applied to the image, using an image processing software, so as to highlight the nanowire boundaries, followed by the conversion of grey scale into negative black and white (B/W) image using 2 different thresholds: (1) by keeping the threshold high, such that the B/W image contains information only about the tallest nanowires, and (2) by keeping the threshold low, such that the B/W image contains information about

all nanowires having the minimum height of 345.5nm. The dark regions of the B/W image correspond to the boundaries confining the nanowires, whereas the bright regions outside correspond to air. The ratio of area confined by the nanowire boundaries to the total area, gives the volume fraction of the nanowires. The high threshold and low threshold B/W image, gives an estimate of ~ 0.108 and 0.1919 respectively, corresponding to f_1 and f_2 subsequently. In the Bruggeman EMA [32], the effective permittivity ε of the dielectric matrix is given by:

$$f \left(\frac{\varepsilon_n - \varepsilon}{\varepsilon_n + K\varepsilon} \right) + (1 - f) \left(\frac{\varepsilon_m - \varepsilon}{\varepsilon_m + K\varepsilon} \right) = 0 \quad (5.2)$$

where ε_n is the permittivity of the nanostructure, ε_m the permittivity of the surrounding matrix, f the volume fraction of the nanostructures, and $K=1$ for an array of cylinders arranged such that the incident beam is collinear to their long axis. Substituting for f in equation 5.2, with f_1 and f_2 respectively, and by using GaN and air permittivities, the effective ordinary permittivity (ε) for either layers, corresponding to ε_1 and ε_2 are determined.

5.4.3 Specular reflectivity to absorption

The transfer matrix model, as described in detail in appendix B, is used to simulate the total reflectivity spectrum from the GaN nanowire system, as visible in Figure 5.6 (b). The estimated values of ε_1 , h_2 and ε_2 are used in the simulation, where the height (h_1) of the top layer is kept as a sole adjustable parameter, in order to account for the irregular heights, stepped surface and pitted nature of the NW array towards the top. The simulation precisely follows the experimental data, for $h_1=120.1\text{nm}$, thus

returning an overall average height of $\sim h = (h_1 + h_2) = 465.6\text{nm}$, very close to the nominal average height of the nanowires which is $\sim 450\text{nm}$, estimated from SEM lateral view.

Now using $n = \sqrt{\varepsilon}$, as well as the basic relation for power reflectivity(R) at a given interface,

$$R = \left(\frac{n - n'}{n + n'} \right)^2 \quad (5.3)$$

with n and n' being the refractive indices above and below the interface, an additional plot is made in Figure 5.7 (b) for the top, middle and bottom power reflectivities of the GaN NW / air matrix, demonstrating that the top and middle reflectivities are negligible ($< 0.2\%$), while on the other hand the bottom reflectivity at the interface with Si is as high as 35% . These numbers strongly support the speculation that light incident on the NW / air matrix hardly gets reflected from the nanowires, but instead most of it gets transmitted through them, suffers reflection at the bottom interface with Si, and gets transmitted back again, thereby travelling a distance equivalent to twice the average height of the nanowires, i.e. $\sim 931.2\text{nm}$ for the sample discussed here. Thus, a modified Beer-Lambert's law can be applied for the specular reflectivity:

$$I = I_o (1 - D_s)^2 R_o e^{-(\alpha + D_v)d} \quad (5.4)$$

where I_o is the intensity of incident light, D_s and D_v correspond to diffuse scattering losses at the surface and volume of the NW array respectively, R_o is the reflectivity at the NW array / Si interface, α the absorption coefficient of the NW array, and d is the path length ($= 2h$). Neglecting the spectral dependence of diffuse scattering ($D_s = 0$ and $D_v = 0$), and

by considering a spectrally flat R_o ($R_o=1$), equation 5.4 gets reduced to:

$$I = I_o e^{-\alpha d} \quad (5.5)$$

By substituting for I_o , which is easily estimated from the reflectivity signal just below the bandgap of GaN, and for $d = 2h$, which is $\sim 931.2\text{nm}$ for the sample discussed here, the corresponding specular reflectivity spectra discussed in Figure 5.2, Figure 5.3 (b) and Figure 5.4 can be easily transformed into their respective absorption spectra.

5.5 Determination of absorption coefficients

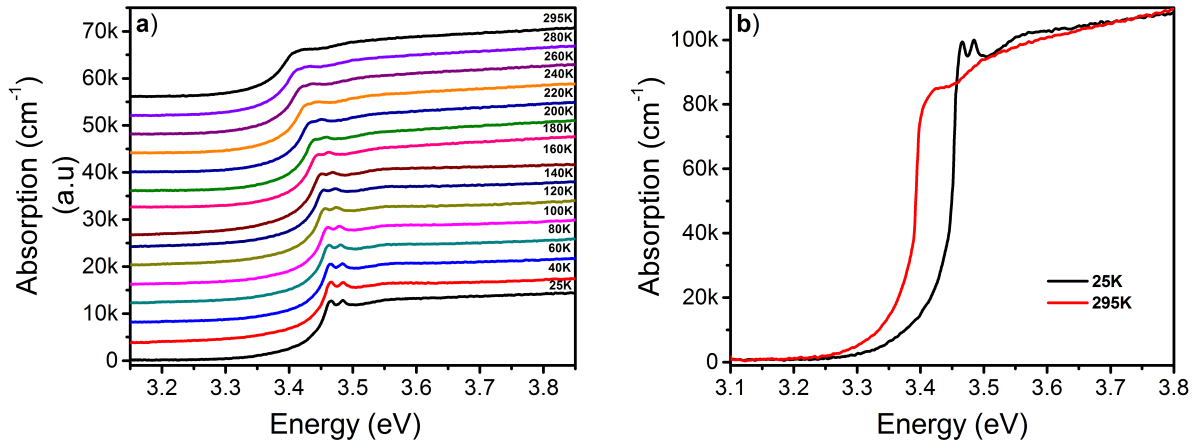


Figure 5.8: (a) Absorption spectra from GaN NWs, as a function of temperature, from 25K to 295K. (b) LT and RT absorption spectra, emphasising the exciton absorption lines, along with the phonon assisted absorption peak.

Figure 5.8 (a) shows a set of temperature-dependent absorption coefficient spectra, obtained as described previously, from specular reflectivity spectra between 25K and 295K, measured using the setup described in detail in subsection A.2.1, where the initial experimental conditions are described in 5.2. The spectra are upshifted between them by $4,000\text{cm}^{-1}$, for clarity. At low temperatures, we observe the prominent A_{GaN} , B_{GaN}

and C_{GaN} excitonic features as two separate peaks, one for the A_{GaN} and B_{GaN} excitons merged together, and one for the C_{GaN} exciton. With increasing temperature, the two peaks progressively merge into a single excitonic peak containing contributions from all A_{GaN} , B_{GaN} and C_{GaN} excitons. However the C_{GaN} exciton can be uniquely identified at RT, using the high resolution grating (see subsection 5.2). About 100meV above the A_{GaN} excitons, a characteristic bump-like feature can be distinguished, which is attributed to exciton-LO phonon bound states, as previously reported for bulk GaN [33, 34]. This bump is more visible in Figure 5.8 (b), where a closer look at the 25K and 295K absorption spectra, confirms its assignment further supported by the fact that with increasing temperature it follows the trails of the other excitonic peaks, thus justifying its excitonic character.

Next a discussion is made on the amplitude of the absorption coefficients α extracted as a function of temperature between 25K and 295K. At low temperature, the α -values refer to the maximum of the merged A_{GaN} and B_{GaN} excitonic peak, while at high temperature to the single merged A_{GaN} , B_{GaN} and C_{GaN} excitonic peak. From Figure 5.8 (a), α is equal to $13,000\text{cm}^{-1}$ at 25K, and to about $10,500\text{cm}^{-1}$ at 295K. These values can be corrected to about $17,000\text{cm}^{-1}$ at 25K and $14,500\text{cm}^{-1}$ at 295K, by considering the spectral dependence of diffuse scattering. This correction is achieved as follows. As discussed in the context of Figure 5.5, surface diffuse scattering seems to remain relatively constant in the range 300-400nm, i.e. above and below the gap, while volume diffuse scattering has a strong spectral dependence, reaching a maximum just beneath the gap and dropping down sharply above the gap due to absorption by the NW array. This implies that the observed specular reflectivity signal below the

gap, which serves as the base line of absorption, is in actuality diminished by the percentage of volume diffused photons. According to Figure 5.5, this correction is about 14%, raising the base line level from around 28% to about 42%. To compare now with the respective α -values reported in the literature, which are about $140,000\text{cm}^{-1}$ at 77K and $95,000\text{cm}^{-1}$ at 295K for bulk GaN films [33], the deficit amount of material available for absorption in the NW array compared to a thin film, has to be further taken into account. Accordingly, an estimate is made for the film factor, which is the volume fraction of available GaN material in the NW array, given by:

$$F = \frac{h_1 + h_2}{h_1 f_1 + h_2 f_2} \quad (5.6)$$

Substituting in equation 5.7, the value of h_1 returned by the simulation, and the values of h_2 , f_1 and f_2 determined by SEM image analysis, an estimate for the film factor (F) is made, which is ~ 5.88 . Thus the corrected absorption coefficient is given by:

$$\alpha_{corrected} = \alpha_{experimental} F \quad (5.7)$$

Using equation 5.7, the corrected α -values are estimated to be $\sim 100,000\text{cm}^{-1}$ at 25K and $\sim 85,000\text{cm}^{-1}$ at 295K, as depicted in Figure 5.8 (b).

The corrected absorption coefficients are still smaller than the values reported by Muth et al. [33] for GaN thin films, in spite of prior claims in the literature for enhanced absorption of NW arrays, due to AR property, light trapping effects, and excitation of resonant guided modes. The AR property of the GaN NWs is confirmed in this work by the very low reflectivity values ($< 0.2\%$), estimated for the top NW / air interface fol-

lowing the discussion of Figure 5.7. However, this AR property should not contribute to the deduced absorption coefficients, as it has been explicitly taken into account in the analysis leading to them. In addition, light trapping effects are not favoured in the rather short ($\sim 450\text{nm}$) and dense ($3 \times 10^{10}\text{cm}^{-2}$) NW arrays of this work. Similarly, resonant mode effects should be negligible in the case of the very thin ($\sim 24\text{nm}$) nanowires studied here. In other words, not much of an enhancement is expected for the NW array at hand, anyway. On the other hand, the smaller, compared to bulk, α -values could be possibly attributed to the large surface to volume ratio of nanowires and the presence of surface defects. In GaN NWs, surface states are formed by Ga or N dangling bonds, binding impurities on the surface [35]. These surface states have been reported to cause Fermi level pinning [35–38], drastically affecting the optical and electrical properties. Pfuller et al. [21] showed an enhancement in PL by continuous UV exposure for a certain time, that they attributed to a photo-induced desorption of oxygen from the NW sidewalls, unpinning the Fermi level and enhancing the PL efficiency. Tuoc et al. [37] showed that core shell nanowires perform better than bulk nanowires alone, again confirming the adverse influence of surface defects in GaN nanowires. Evidence for surface defects in the nanowires discussed here, is brought about by the PL peak at 3.42eV, which is typically attributed to excitons bound at surface defects [19]. Based on the above, it is quite reasonable to suggest that 1-2 nm from the GaN surface, do not contribute to the absorption process. Assuming just 1 nm of “dead” shell is sufficient to modify the film factor from 5.88 to 7, and increase the α -values to $120,000\text{cm}^{-1}$ at 25K and to $100,000\text{cm}^{-1}$ at 295K, i.e. quite similar to the values reported by Muth et al. [33] for bulk GaN.

5.6 Conclusion

In summary, a new all-optical method to extract absorption coefficients is introduced, from as-grown nanowire arrays, on opaque substrates. The method is based on simple reflectivity measurements on the as-grown samples, and can be extended to any family of nanowires, provided they are grown on substrates with sufficient permittivity difference compared to the nanowire-air matrix. The nanowires studied in this chapter are strain free, with high optical quality, confirmed by the strong excitonic features observed, both in the emission as well as absorption coefficient spectra, right from low temperature all the way up to room temperature, quite adhering to the prerequisites of a polaritonic system. However, evidence of enhancement in the amplitude of absorption coefficients are not observed, at least compared to bulk GaN [33]. This can be attributed to the particular structural characteristics of the studied nanowire arrays, not favouring light trapping effects, nor the excitation of resonant modes. As of now, the GaN nanowires discussed here are already suitable for polaritonic studies. Nevertheless, ongoing experiments focus on nanowire samples, prone to show absorption enhancement effects, which could then lead to the realisation of more robust GaN nanowire based polaritonic systems.

Bibliography

- [1] L. Hu and G. Chen. “Analysis of optical absorption in silicon nanowire arrays for photovoltaic applications.”, *Nano letters* 7.11 (Nov. 2007), pp. 3249–52.
- [2] J. Zhu, Z. Yu, G. F. Burkhard, C.-M. Hsu, S. T. Connor, Y. Xu, Q. Wang, M. McGehee, S. Fan, and Y. Cui. “Optical absorption enhancement in amorphous silicon nanowire and nanocone arrays.”, *Nano letters* 9.1 (Jan. 2009), pp. 279–82.
- [3] L. Tsakalacos, J. Balch, J. Fronheiser, M.-Y. Shih, S. F. LeBoeuf, M. Pietrzykowski, P. J. Codella, B. A. Korevaar, O. V. Sulima, J. Rand, A. Davuluru, and U. Rapol. “Strong broadband optical absorption in silicon nanowire films”, *Journal of Nanophotonics* 1.1 (2007), p. 013552.
- [4] E. Garnett and P. Yang. “Light trapping in silicon nanowire solar cells.”, *Nano letters* 10.3 (Mar. 2010), pp. 1082–7.
- [5] Y. Lu and A. Lal. “High-Efficiency Ordered Silicon Nano-Conical-Frustum Array Solar Cells by Self-Powered Parallel Electron Lithography”, *Nano Letters* 10.11 (Nov. 2010), pp. 4651–4656.
- [6] L. Cao, J. S. White, J.-S. Park, J. A. Schuller, B. M. Clemens, and M. L. Brongersma. “Engineering light absorption in semiconductor nanowire devices.”, *Nature materials* 8.8 (Aug. 2009), pp. 643–7.
- [7] C. Lin and M. L. Povinelli. “Optical absorption enhancement in silicon nanowire arrays with a large lattice constant for photovoltaic applications”, *Optics Express* 17.22 (Oct. 2009), p. 19371.
- [8] J. Kupec, R. L. Stoop, and B. Witzigmann. “Light absorption and emission in nanowire array solar cells.”, *Optics Express* 18 (2010), pp. 27589–27605.
- [9] P. Kailuweit, M. Peters, J. Leene, K. Mergenthaler, F. Dimroth, and A. W. Bett. “Numerical simulations of absorption properties of InP nanowires for solar cell applications”, *Progress in Photovoltaics: Research and Applications* 20.8 (Dec. 2012), pp. 945–953.
- [10] H. Guo, L. Wen, X. Li, Z. Zhao, and Y. Wang. “Analysis of optical absorption in GaAs nanowire arrays.”, *Nanoscale research letters* 6.1 (Jan. 2011), p. 617.

- [11] A. Das, J. Heo, M. Jankowski, W. Guo, L. Zhang, H. Deng, and P. Bhattacharya. “Room temperature ultralow threshold GaN nanowire polariton laser”, *Physical Review Letters* 107.6 (2011), pp. 1–5.
- [12] A. Das, P. Bhattacharya, J. Heo, A. Banerjee, and W. Guo. “Polariton Bose-Einstein condensate at room temperature in an Al(Ga)N nanowire-dielectric microcavity with a spatial potential trap.”, *Proceedings of the National Academy of Sciences of the United States of America* 110.8 (2013), pp. 2735–40.
- [13] T. J. Kempa, J. F. Cahoon, S.-K. Kim, R. W. Day, D. C. Bell, H.-G. Park, and C. M. Lieber. “Coaxial multishell nanowires with high-quality electronic interfaces and tunable optical cavities for ultrathin photovoltaics.”, *Proceedings of the National Academy of Sciences of the United States of America* 109.5 (Jan. 2012), pp. 1407–12.
- [14] J. Wallentin, N. Anttu, D. Asoli, M. Huffman, I. Aberg, M. H. Magnusson, G. Siefert, P. Fuss-Kailuweit, F. Dimroth, B. Witzigmann, H. Q. Xu, L. Samuelson, K. Deppert, and M. T. Borgström. “InP nanowire array solar cells achieving 13.8% efficiency by exceeding the ray optics limit.”, *Science (New York, N.Y.)* 339.6123 (Mar. 2013), pp. 1057–60.
- [15] P. Krogstrup, H. I. Jørgensen, M. Heiss, O. Demichel, J. V. Holm, M. Aagesen, J. Nygard, and A. Fontcuberta i Morral. “Single-nanowire solar cells beyond the Shockley-Queisser limit”, *Nature Photonics* 7.April (2013), p. 306.
- [16] D. Cherns, L. Meshi, I. Griffiths, S. Khongphetsak, S. V. Novikov, N. R. S. Farley, R. P. Champion, and C. T. Foxon. “Defect-controlled growth of GaN nanorods on (0001)sapphire by molecular beam epitaxy”, *Applied Physics Letters* 93.11 (2008), p. 111911.
- [17] K. Kornitzer, T. Ebner, M. Grehl, K. Thonke, R. Sauer, C. Kirchner, V. Schwegler, M. Kamp, M. Leszczynski, I. Grzegory, and S. Porowski. “High-Resolution Photoluminescence and Reflectance Spectra of Homoepitaxial GaN Layers”, *physica status solidi (b)* 216.1 (Nov. 1999), pp. 5–9.
- [18] B. Monemar. “Bound excitons in GaN”, *Journal of Physics: Condensed Matter* 13.32 (Aug. 2001), pp. 7011–7026.

- [19] M. A. Reshchikov, D. Huang, F. Yun, P. Visconti, L. He, H. Morkoç, J. Jasinski, Z. Liliental-Weber, R. J. Molnar, S. S. Park, and K. Y. Lee. “Unusual luminescence lines in GaN”, *Journal of Applied Physics* 94.9 (2003), pp. 5623–5632.
- [20] L. Geelhaar, C. Chèze, B. Jenichen, O. Brandt, C. Pfüller, S. Münch, R. Rothemund, S. Reitzenstein, A. Forchel, T. Kehagias, P. Komninou, G. P. Dimitrakopoulos, T. Karakostas, L. Lari, P. R. Chalker, M. H. Gass, and H. Riechert. “Properties of GaN Nanowires Grown by Molecular Beam Epitaxy”, *IEEE Journal of Selected Topics in Quantum Electronics* 17.4 (July 2011), pp. 878–888.
- [21] C. Pfüller, O. Brandt, F. Grosse, T. Flissikowski, C. Chèze, V. Consonni, L. Geelhaar, H. Grahn, and H. Riechert. “Unpinning the Fermi level of GaN nanowires by ultraviolet radiation”, *Physical Review B* 82.4 (2010), pp. 1–5.
- [22] P. J. Schuck, M. D. Mason, R. D. Grober, O. Ambacher, A. P. Lima, C. Miskys, R. Dimitrov, and M. Stutzmann. “Spatially resolved photoluminescence of inversion domain boundaries in GaN-based lateral polarity heterostructures”, *Applied Physics Letters* 79.7 (2001), p. 952.
- [23] P. Corfdir, P. Lefebvre, J. Ristić, P. Valvin, E. Calleja, A. Trampert, J.-D. Ganière, and B. Deveaud-Plédran. “Time-resolved spectroscopy on GaN nanocolumns grown by plasma assisted molecular beam epitaxy on Si substrates”, *Journal of Applied Physics* 105.1 (2009), p. 013113.
- [24] W. Shan, A. J. Fischer, S. J. Hwang, B. D. Little, R. J. Hauenstein, X. C. Xie, J. J. Song, D. S. Kim, B. Goldenberg, R. Horning, S. Krishnankutty, W. G. Perry, M. D. Bremser, and R. F. Davis. “Intrinsic exciton transitions in GaN”, *Journal of Applied Physics* 83.1 (1998), pp. 455–461.
- [25] A. J. Fischer, W. Shan, J. J. Song, Y. C. Chang, R. Horning, and B. Goldenberg. “Temperature-dependent absorption measurements of excitons in GaN epilayers”, *Applied Physics Letters* 71.14 (1997), p. 1981.
- [26] B. Gil. “Modulation spectroscopy of the Group III nitrides”, *Group III nitride semiconductor compounds: physics and applications*. Clarendon Press, 1998, pp. 158–181.
- [27] J. G. Rivas, O. L. Muskens, M. T. Borgström, S. L. Diedenhofen, and E. P. A. M. Bakkers. “Optical Anisotropy of Semiconductor Nanowires”, *One-Dimensional Nanostructures*. New York, NY: Springer New York, 2008, pp. 127–145.

- [28] O. L. Muskens, J. G. Rivas, R. E. Algra, E. P. A. M. Bakkers, and A. Lagendijk. “Design of Light Scattering in Nanowire Materials for Photovoltaic Applications”, *Nano Letters* 8.9 (Sept. 2008), pp. 2638–2642.
- [29] A. S. Barker and M. Ilegems. “Infrared lattice vibrations and free-electron dispersion in GaN”, *Physical Review B* 7.2 (1973), pp. 743–750.
- [30] I. Avrutsky and R. Soref. “Phase-matched sum frequency generation in strained silicon waveguides using their second-order nonlinear optical susceptibility”, *Optics Express* 19.22 (Oct. 2011), p. 21707.
- [31] A. H. Sihvola and O. P. M. Pekonen. “Effective medium formulae for bi-anisotropic mixtures”, *Journal of Physics D: Applied Physics* 29.3 (Mar. 1996), pp. 514–521.
- [32] J. B. Baxter and C. A. Schmuttenmaer. “Conductivity of ZnO nanowires, nanoparticles, and thin films using time-resolved terahertz spectroscopy.”, *The journal of physical chemistry. B* 110.50 (Dec. 2006), pp. 25229–39.
- [33] J. F. Muth, J. H. Lee, I. K. Shmagin, R. M. Kolbas, H. C. Casey, B. P. Keller, U. K. Mishra, and S. P. DenBaars. “Absorption coefficient, energy gap, exciton binding energy, and recombination lifetime of GaN obtained from transmission measurements”, *Applied Physics Letters* 71.18 (1997), p. 2572.
- [34] B. Gil. “Optical Properties and Lasing in GaN”, *Group III nitride semiconductor compounds: physics and applications*. Clarendon Press, 1998, pp. 182–241.
- [35] A. Armstrong, Q. Li, Y. Lin, A. A. Talin, and G. T. Wang. “GaN nanowire surface state observed using deep level optical spectroscopy”, *Applied Physics Letters* 96.16 (2010), p. 163106.
- [36] R. Calarco, M. Marso, T. Richter, A. I. Aykanat, R. Meijers, A. V D Hart, T. Stoica, and H. Lüth. “Size-dependent photoconductivity in MBE-grown GaN-nanowires.”, *Nano letters* 5.5 (May 2005), pp. 981–4.
- [37] V. N. Tuoc, T. D. Huan, and L. T. H. Lien. “Modeling study on the properties of GaN/AlN core/shell nanowires by surface effect suppression”, *Physica Status Solidi (B)* 9 (Feb. 2012), pp. 1–9.
- [38] K. A. Bertness, N. A. Sanford, and A. V. Davydov. “GaN Nanowires Grown by Molecular Beam Epitaxy”, *IEEE Journal of Selected Topics in Quantum Electronics* 17.4 (July 2011), pp. 847–858.



This page is intentionally left blank



This page is intentionally left blank

Conclusion

Most of the works on GaN based polariton lasers that rely on optical pumping, reported until now, mainly use bulk GaN [1], GaN QW's [2] or GaN nanowires [3], as the active layer. In the latter approach, individual nanowires positioned in a microcavity show remarkable polariton characteristics, however the feasibility of electrical injection is not obvious. The former two are currently compromised by the quality of the active region, due to structural disorders introduced by the bottom GaN based DBR mirror. The primary objective of this work was to improve the quality of the GaN based active region, and thereby perform polaritonic studies on them, eventually leading to the development of a GaN polariton laser. In this context, strain and structural disorder free ultra-smooth GaN membranes have been fabricated using PEC lateral etching, which are then embedded between dielectric mirrors, forming full microcavity structures, investigated for polaritonic as well as non-linear properties.

Prior to etching, focus has been given on enhancing the optical properties of the active region, by incorporating GaN / AlGaIn QW's, where the aluminium content ($\sim 5\%$) of the barriers is carefully selected, resulting in state of the art QW emission at RT, returning a homogeneous linewidth of $\sim 28\text{meV}$. The delocalisation of QW excitons is investigated as a function of temperature, where most of the delocalisation occurs below 100K, in line with the low linewidth of the dominant QW peak, at RT. Moreover the lifetime of the respective peak is estimated to be $\sim 275\text{ps}$. In short, the optical characteristics are found to be adhering to the requirements of a polaritonic system. Having optimised the act-

ive region, PEC lateral etching parameters are precisely fixed, so as to produce high quality freestanding GaN membranes, by ‘eating’ away the InGaN sacrificial layer. Extremely smooth membranes are produced by using very low concentration of KOH, as low as 0.0004M, along with constant excitation power and a constant / pulsed dc bias voltage. The AFM rms roughness of the membranes on the etched face, is estimated to be $\sim 0.65\text{nm}$, over an area of $100\ \mu\text{m}^2$, approximately one order of magnitude lower than the previously reported values, where they used a very similar technique [4]. In order to have an understanding about the oscillator strength of the excitons involved, which is crucial to a polaritonic system, absorption coefficients have been deduced from low temperature transmission experiments, performed on these amazingly planate membranes transferred to a sapphire substrate. The oscillator strength of the GaN excitons, turned out to be at least 30% higher, compared to previous reports in the literature [5].

The half-microcavity structure, formed by transferring the ultra-smooth membranes to a high quality dielectric based DBR mirror, exhibited very sharp excitonic features, giving a further insight into the quality of the etched membranes. The cavity mode observed is relatively broad, where the estimated Q-factor is ~ 85 . Optical characterisation of the full-microcavity structure, formed by the deposition of the top DBR mirror on to the half-microcavity structure, clearly demonstrated strong coupling, where two polariton branches mainly LPB and MPB are observed experimentally, whereas the UPB is determined with the aid of modelling. The contribution of the two excitonic peaks: spacer GaN and GaN QW, to the different polariton states are precisely analysed and the Rabi splitting of the system is estimated to be $\sim 64\text{meV}$. The Q-factor of the system is

determined to be ~ 1770 , very close to the theoretical prediction. The investigation of non-linear properties at RT, as a function of pump power density, has unveiled a highly efficient polariton laser in the kinetic regime, with an ultra-low average threshold of $\sim 4.5\text{W} / \text{cm}^2$ ($\sim 594\mu\text{J} / \text{cm}^2$), under non-resonant quasi-continuous excitation. The threshold reported is the lowest ever for 2D GaN based systems [2]. Above threshold, the system has been confirmed to be in the strong coupling regime by analysing the dispersive behaviour, as well as by determining the exciton density per coupled QW, at threshold, which turned out to be at least more than two orders below the exciton saturation density. The beautiful k-space condensation pattern above threshold, has been interpreted as polaritons getting trapped in a site-specific square-like pocket. Such a mechanism has been found to escalate the polariton density locally, resulting in an ultra-low threshold. The high quality of the all-dielectric microcavity further contributes to the ultra-low threshold, reported here. Thus to conclude, the primary objective of the project has been successfully implemented.

Additionally, GaN nanowires have been studied as a potential candidate for polaritonic studies, taking into account the very large Rabi splitting value [6] and an ultra-low threshold [3, 6], reported by Das et al., for their GaN nanowire based system. In this context, strain free GaN nanowires are studied, whose optical quality has been confirmed by strong excitonic features, observed in PL and reflectivity measurements, right from low temperature all the way up to room temperature, quite well adhering to the prerequisites of a polaritonic system. Moreover, a new all-optical method has been formulated, to extract absorption coefficients, from as-grown nanowires, on opaque substrates. The method is based on

simple reflectivity measurements on the as-grown samples, and can be extended to any family of nanowires, provided they are grown on substrates with sufficient permittivity difference compared to the nanowire-air matrix. Based on this method, absorption coefficients have been derived, as a function of temperature. However at RT, the derived absorption coefficients are comparable to bulk GaN [5], as opposed to an expected enhancement, which has been attributed to the particular structural characteristics of the studied nanowire arrays, not favouring light trapping effects, nor the excitation of resonant guided modes. Nevertheless, taking into account the superior optical properties of the GaN nanowires discussed in this work, they can already be considered optimal for polaritonic studies.

Future perspectives

The physics of polaritons in inorganic materials like GaAs [7, 8] and CdTe [9, 10], have been deeply investigated in the last decade [11]. GaN on the other hand, being a more promising material, in terms of high binding energy and oscillator strength, has been hardly studied for hard-core polariton physics, being limited by the quality of the active layer and processing difficulties. The use of strain free, structural disorder free, ultra-smooth GaN membranes, as the active region, unravels a new material system for profound polaritonic investigation. In this context, firstly it would be very fascinating to study the polariton lasing threshold as a function of detuning, for which membranes of different thicknesses can be employed. This would eventually lead to polariton lasing / condensation in the thermodynamic regime (BEC), which requires membranes with very

small negative detunings, that favours adequate polariton scattering rates and lifetimes. Another interesting experiment, would be through resonant excitation, which would unravel the prospects for directly investigating non-linear processes like parametric amplification [10, 11]. Moreover, it would also lead to even lower polariton lasing threshold, than what would have been possible by non-resonant excitation. Polaritons getting confined in a site-specific trap, has been shown to escalate the polariton density locally in this work. A further study in this direction, could open up possible ways of reducing the polariton lasing threshold. A feasible way of creating patterns or mesas on relatively large membranes, could lead to studies based on engineered polariton landscapes, simulating complex many-body phenomena [12, 13]. The ultra-smooth membranes, prior to top DBR deposition, can also be spin-coated with adequate organic polymers, which will unveil a whole new area of polaritonic research in the visible region, based on organic exciton polaritons [14]. The last and most important direction of research would be to create electrically injected GaN membrane based polariton lasers and light emitting diodes (LED's). Towards this objective, GaN membranes are highly preferable as contacts can be made directly on the membranes, eliminating issues related to resistance of the DBR mirrors, a common problem faced in GaAs based systems [8], that make use of DBR mirrors fabricated from the GaAs family. Such an approach will lead to the development of highly efficient, electrically injected, ultra-smooth GaN membrane-based polaritonic devices.



Bibliography

- [1] S. Christopoulos, G. von Högersthal, A. Grundy, P. Lagoudakis, A. Kavokin, J. Baumberg, G. Christmann, R. Butté, E. Feltin, J.-F. Carlin, and N. Grandjean. “Room-Temperature Polariton Lasing in Semiconductor Microcavities”, *Physical Review Letters* 98.12 (Mar. 2007), pp. 1–4.
- [2] G. Christmann, R. Butté, E. Feltin, J.-F. Carlin, and N. Grandjean. “Room temperature polariton lasing in a GaNAlGaN multiple quantum well microcavity”, *Applied Physics Letters* 93.5 (2008), p. 051102.
- [3] A. Das, J. Heo, M. Jankowski, W. Guo, L. Zhang, H. Deng, and P. Bhattacharya. “Room temperature ultralow threshold GaN nanowire polariton laser”, *Physical Review Letters* 107.6 (2011), pp. 1–5.
- [4] E. Trichas, N. T. Pelekanos, E. Iliopoulos, E. Monroy, K. Tsagaraki, A. Kostopoulos, and P. G. Savvidis. “Bragg polariton luminescence from a GaN membrane embedded in all dielectric microcavity”, *Applied Physics Letters* 98.22 (2011), p. 221101.
- [5] J. F. Muth, J. H. Lee, I. K. Shmagin, R. M. Kolbas, H. C. Casey, B. P. Keller, U. K. Mishra, and S. P. DenBaars. “Absorption coefficient, energy gap, exciton binding energy, and recombination lifetime of GaN obtained from transmission measurements”, *Applied Physics Letters* 71.18 (1997), p. 2572.
- [6] A. Das, P. Bhattacharya, J. Heo, A. Banerjee, and W. Guo. “Polariton Bose-Einstein condensate at room temperature in an Al(Ga)N nanowire-dielectric microcavity with a spatial potential trap.”, *Proceedings of the National Academy of Sciences of the United States of America* 110.8 (2013), pp. 2735–40.
- [7] H. Deng, G. Weihs, D. Snoke, J. Bloch, and Y. Yamamoto. “Polariton lasing vs. photon lasing in a semiconductor microcavity”, *Proceedings of the National Academy of Sciences* 100.26 (Dec. 2003), pp. 15318–15323.
- [8] S. I. Tsintzos, N. T. Pelekanos, G. Konstantinidis, Z. Hatzopoulos, and P. G. Savvidis. “A GaAs polariton light-emitting diode operating near room temperature.”, *Nature* 453.7193 (May 2008), pp. 372–5.

-
- [9] R. Huang, Y. Yamamoto, R. Andre, J. Bleuse, M. Muller, and H. Ulmer-Tuffigo. “Exciton-polariton amplification based on exciton-exciton scattering in a CdTe quantum well”, *Technical Digest. Summaries of papers presented at the Quantum Electronics and Laser Science Conference. Postconference Technical Digest (IEEE Cat. No.01CH37172)* 65 (2001), pp. 1–7.
- [10] E. Guillotel, M. Ravaro, F. Ghiglieno, C. Langlois, C. Ricolleau, S. Ducci, I. Favero, and G. Leo. “Parametric amplification in GaAs/AlOx waveguide”, *Applied Physics Letters* 94.17 (Apr. 2009), p. 171110.
- [11] M. Saba, C. Ciuti, J. Bloch, V. Thierry-Mieg, R. André, I. S. Dang, S. Kundermann, A. Mura, G. Bongiovanni, J. L. Staehli, and B. Deveaud. “High-temperature ultrafast polariton parametric amplification in semiconductor microcavities”. en, *Nature* 414.6865 (Dec. 2001), pp. 731–735.
- [12] K. Winkler, J. Fischer, A. Schade, M. Amthor, R. Dall, J. Geßler, M. Emmerling, E. A. Ostrovskaya, M. Kamp, C. Schneider, and S. Höfling. “A polariton condensate in a photonic crystal potential landscape”, *New Journal of Physics* 17.2 (Jan. 2015), p. 023001.
- [13] C. W. Lai, N. Y. Kim, S. Utsunomiya, G. Roumpos, H. Deng, M. D. Fraser, T. Byrnes, P. Recher, N. Kumada, T. Fujisawa, and Y. Yamamoto. “Coherent zero-state and pi-state in an exciton-polariton condensate array.”, *Nature* 450.November (2007), pp. 529–532.
- [14] J. Wenus, R. Parashkov, S. Ceccarelli, A. Brehier, J.-S. Lauret, M. Skolnick, E. Deleporte, and D. Lidzey. “Hybrid organic-inorganic exciton-polaritons in a strongly coupled microcavity”, *Physical Review B* 74.23 (Dec. 2006), pp. 1–6.



This page is intentionally left blank

Experimental equipments and setups

A.1 Building blocks

A.1.1 Laser's

1. Kimmon IK series, continuous wave, He-Cd laser, at 325 nm, with a maximum power output of 32mW and a beam divergence of 0.92mrad, used as a source of excitation in PL experiments.
2. Nanolase, pulsed, frequency quadrupled, Nd-YAG (neodymium-doped yttrium aluminium garnet; $\text{Nd:Y}_3\text{Al}_5\text{O}_{12}$) laser at 266nm, with a pulse-width of 0.51ns and a repetition rate of 7.58kHz. A quartz prism is used to separate the laser components after which, the average power at 266nm \sim 0.4mW. It is used as a source of excitation in PL experiments.
3. Mira-900 series, pulsed, tunable Ti:Sapphire laser, with a tuning range of 700 - 1000nm and a pulsewidth $<$ 2ps, where the repetition rate is 76MHz. It is used as a source of excitation in TRPL measurements.
4. A 405nm diode laser, used as a source of excitation in PEC etching.

A.1.2 White light source's

1. A 150W Xenon lamp, in a high precision Hamamatsu lamp housing, used as a source for reflectivity (RFL) and transmission measurements.
2. A fibre coupled, collimated Mikropack light source, equipped with a deuterium (for UV region) and halogen lamp (for visible and IR region), is used as a source for reflectivity measurements.

A.1.3 Sample placement and temperature dependent measurements

The sample is placed in an APD helium closed-circuit cryostat, equipped with a Scientific Instruments, series 5,500 temperature controller, which enables the variation of sample temperature right from 20K to 310K.

A.1.4 Spectrometer

All PL, RFL and transmission measurements are made on an Acton SpectraPro, 0.5 meter focal length, triple grating and imaging spectrograph, with a resolution of 0.02nm at 435.8nm and an accuracy of ± 0.02 nm. The three gratings are the following: (1) 150grooves/mm, blazed at 300nm (2) 600 grooves/mm, blazed at 300nm and (3) 2400 grooves/mm, blazed at HUV (holographic UV). Moreover it is equipped with a liquid nitrogen cooled charge-coupled device (CCD), having a width of 1024 pixels and a height of 256 pixels.

A.1.5 Streak camera

All TRPL measurements are made on a Hamamatsu M5675 streak camera, equipped with four different time range options, based on the sweep voltage used to deflect the light. Time range ‘1’ corresponds to the highest resolution whereas time range ‘4’ to the lowest one. Based on the MIRA (see subsection A.1.1) used with the streak the temporal resolution is estimated to be ~ 2 ps. Further information on the working of streak camera can be found in the following link.

A.2 Optical setups

A.2.1 Basic PL / Reflectivity setup

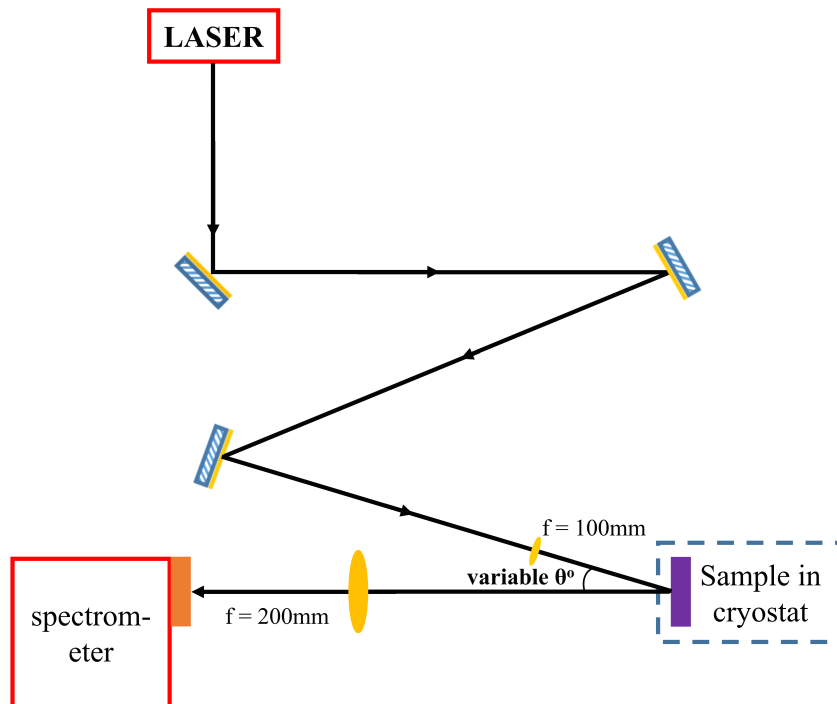


Figure A.1: Basic PL setup.

The schematic of the PL and Reflectivity setup are as visible in Fig-

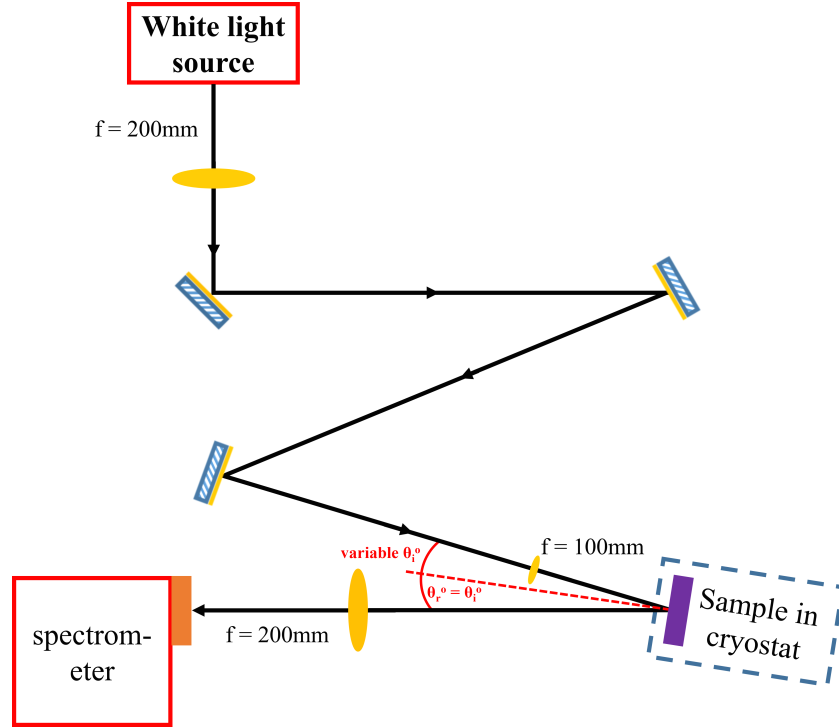


Figure A.2: Basic Reflectivity setup.

ure A.1 and Figure A.2 respectively. Both setups are very identical except for two instances: (1) A collimating lens is used just after the source, in the reflectivity setup, which is absent in the PL setup due to the minimal divergence of the laser beam (2) In the PL setup, the collection involves a large number of angles around $k_{\parallel} = 0^{\circ}$, limited by the NA of the collection lens, whereas in the reflectivity setup the collection angle is identical to the incidence angle, which in turn depends on the requirement of the experiments. However taking into consideration the size of the optics used, the angle of incidence is limited to a minimum of at least 10° in both setups, where the incident beam is focused onto the sample placed in the cryostat, and the response from the sample is focused onto the spectrometer using a collection lens. It should be noted that in the case of reflectivity measurements, in order to correct for the lamp's spectral

response, a Newport 5108 UV-Vis mirror is used as a reference, which has a nearly flat response and the reflectivity is $\sim 90\%$, in the range of 300 - 600nm.

A.2.2 Time resolved photoluminescence (TRPL) setup

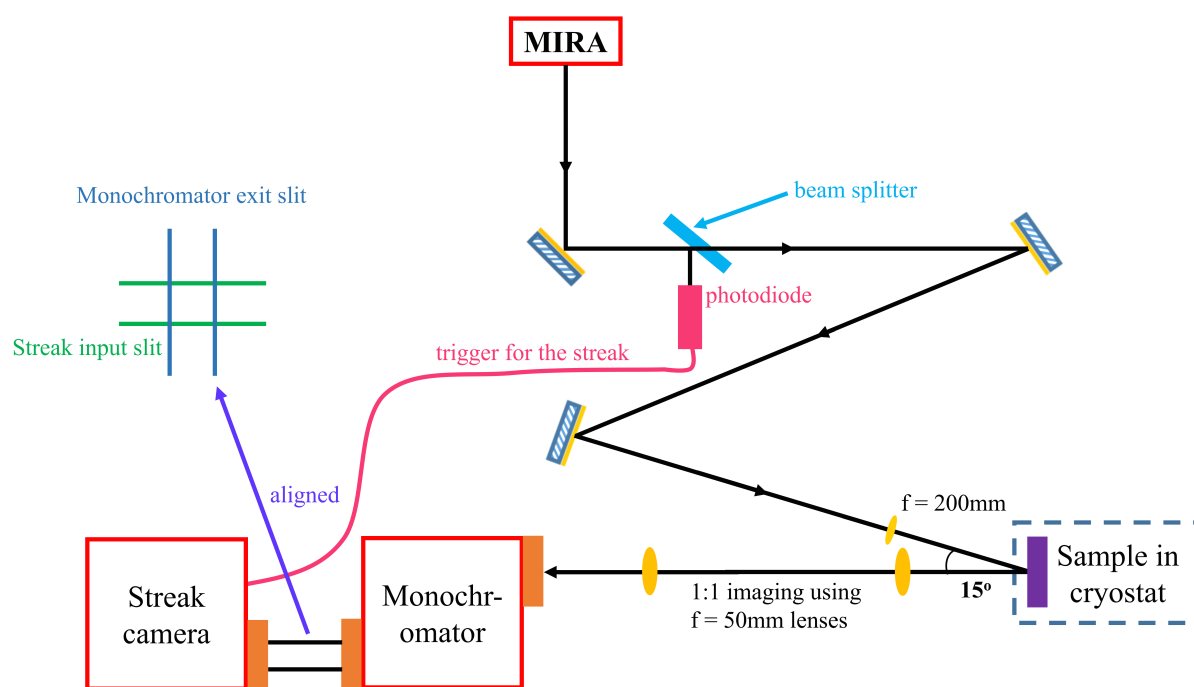


Figure A.3: Time resolved photoluminescence setup.

The schematic of the TRPL setup is as shown in Figure A.3. The source used is always a pulsed laser due to the nature of experiments, which is a MIRA over here (see subsection A.1.1 for more details). A small portion of the laser beam is fed to the photodiode using a beam splitter, which acts as a trigger to the streak camera. The pulse from the laser marks the beginning of the time resolved measurements, which in fact is the same instance at which the sample is excited as well. The incident beam is focussed on to the sample placed in the cryostat, where the angle of incidence is $\sim 15^\circ$. The PL signal is collected from the sample

in such a way that a large number of angles around $k_{\parallel} = 0^{\circ}$ is captured (limited by the NA of the first collection lens), using a (1:1) two lens imaging system, which in turn focuses the beam into the monochromator on the other end. The spatial resolution of the TRPL image depends on the grating used, which is equipped within the monochromator (see subsection A.1.4 for more details). The collected beam that undergoes wavelength dispersion within the spectrometer, exits through a slit on the back side of the monochromator, which is then aligned into the streak camera, that decides the temporal resolution of the TRPL image, based on the time range chosen. It should be noted that the input slit to the streak camera is horizontal, as depicted in the inset of Figure A.3, whereas the exit slit of the monochromator is vertical. In other words, the intersection of the two slits creates a very small window that allows the light to enter the streak camera. Thus great care should be taken while aligning the collected PL signal into the monochromator, ensuring that it is exactly at the centre of the vertical slit.

A.2.3 Simultaneous PL and Transmission setup relying on the principle of magnification

The schematic of the setup is as shown in Figure A.4, which allows simultaneous measurement of transmission and PL, although PL is collected from the back side of the sample. A collimating lens is used in combination with the white light source whereas the laser source does not require it due to minimal divergence of the laser beam. The beam from either sources is aligned into the same path using a beam splitter in such a way that the laser beam, having a smaller diameter is positioned exactly at the centre of the white light beam. In order to allow magnification in the

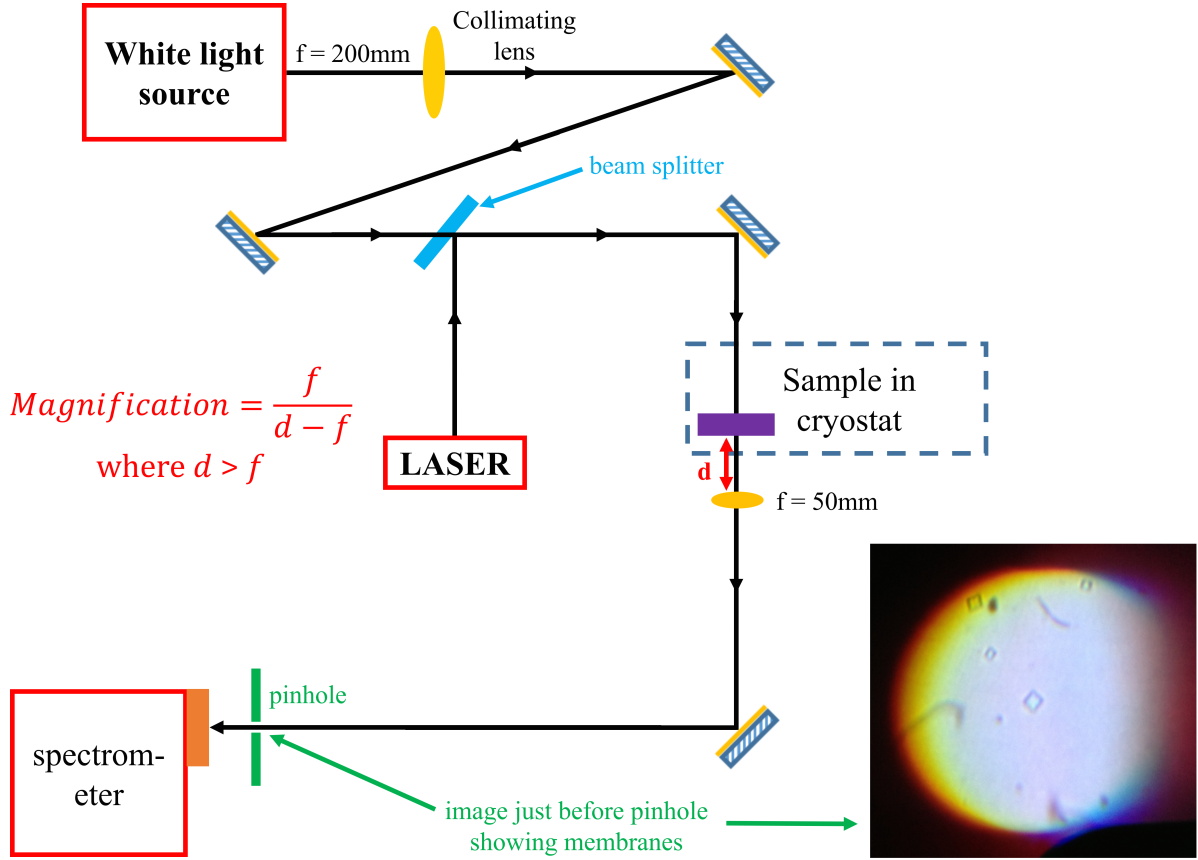


Figure A.4: Simultaneous PL and Transmission setup relying on the principle of magnification.

collection path from a large area of the sample, a focusing lens is not used in the incident path, where the angle of incidence is $\sim 0^\circ$. The collection lens having a focal length (f) of 50mm, is positioned at a distance d from the sample such that the magnification (M) that can be achieved by the single lens system is as follows:

$$M = \frac{f}{d - f} \quad (\text{A.1})$$

where $d > f$ and the image is formed at the spectrometer slit. It should be noted that, the use of a single lens system allows for a large magnification in a relatively simple way, as opposed to the two lens system. The inset of Figure A.4 shows the magnified image just before the pinhole, from a

sample containing GaN membranes on sapphire. The white region corresponds to white light transmission, whereas the blue spot, visible at the centre of white light transmission, on the membrane, corresponds to PL from the membrane. This particular membrane can be isolated using a 100 μ m pinhole, which is then aligned into the spectrometer, allowing the extraction of PL / Transmission from the single membrane. In the case of transmission measurements, in order to correct for the lamp's spectral response, a bare piece of sapphire is used as a reference, which has a nearly flat response and the transmission is $\sim 85 - 90\%$, in the range of 0.3 - 4 μ m.

A.2.4 Reflectivity setup relying on the principle of magnification

The schematic of the setup is as shown in Figure A.5, where the basic working principle is very similar to the previous setup (A.2.3), the only differences being the following: (1) the angle of incidence is not fixed at $\sim 0^\circ$, but instead should be greater than at least 10° (limited by the size of the optics), whose value is finally decided by the requirements of the experiment (2) the collection is the reflected beam path rather than the transmitted path. Here again in order to allow magnification in the collection path from a large area of the sample, a focusing lens is not used in the incident path. The collection lens (lens 'a'), having a focal length (f_a) of 50mm, is positioned at a distance (d_a) from the sample in such a way that the magnification that can be achieved by the single lens system is given by equation A.1 and the image is formed at the spectrometer slit. The spatial selection of individual features in the image is made possible with the help of a 100 μ m pinhole, which is then aligned into the spectrometer. In a scenario that requires further magnification, a second

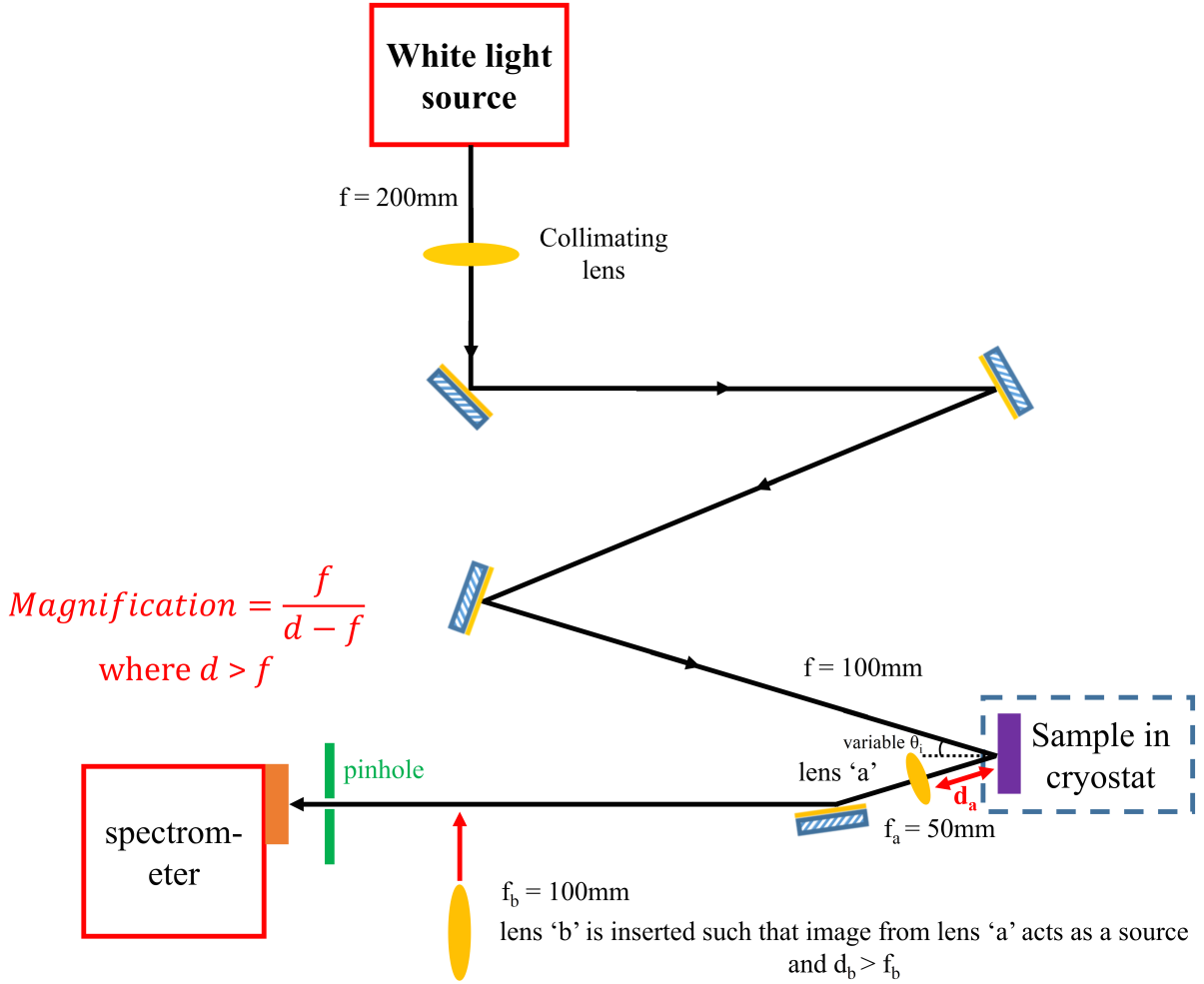


Figure A.5: Reflectivity setup relying on the principle of magnification.

lens (lens 'b') is used in the collection path as visible in Figure A.5. It should be noted that the system used here is not a usual two lens system for magnification, but instead lens 'a' is positioned at a distance (d_a) from the sample in such a way that an image is formed in the collection path, where the distance (d_b) between this image and lens 'b' is greater than the corresponding focal length ($f_b \sim 100\text{mm}$) of lens 'b', which then provides further magnification of the image formed by lens 'a' alone, given by the equation A.1. Moreover the distance d_b should be in such way, that the final image is formed at the spectrometer slit. In order to correct for

the lamp's spectral response, a Newport 5108 UV-Vis mirror is used as a reference, which has a nearly flat response and the reflectivity is $\sim 90\%$, in the range of 300 - 600nm.

A.2.5 Simple Reflectivity setup using optical fibres

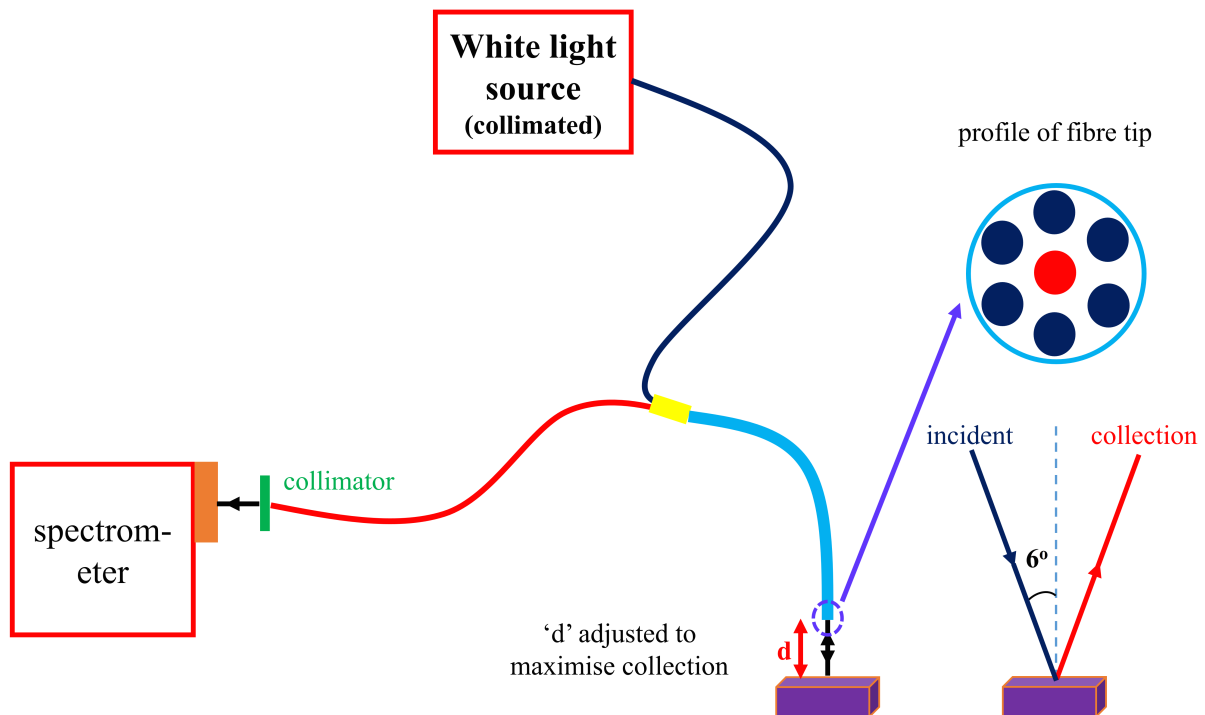


Figure A.6: Simple Reflectivity setup using optical fibres.

The schematic of the setup is shown in Figure A.6, which is a relatively very simple setup for quick reflectivity measurements. The core of the setup is a multicore fibre from Ocean optics (QR400-7-SR-BX), where the fibre diameter is 400 μm designed for a wavelength range from 200-1100nm. The fibre tip aligned normally with the sample is depicted in the inset of Figure A.6, which basically consists of 6 fibre bundles around 1. The outer fibre bundles are used for excitation whereas the one in the middle is used for the collection of the reflectivity response from the

sample. On the other end, the fibre is divided into two: (1) the outer fibre bundles form one arm which is attached to the collimated white light source and (2) the central fibre bundle forms the other arm which is aligned with the spectrometer using a collimator. Light is incident on the sample at various angles, however only a small portion of light at an angle of incidence $\sim 6^\circ$, gets collected by the central fibre bundle, as visible in the inset of Figure A.6. The distance d between the sample and the fibre tip, just above the sample, is positioned in such a way that the reflectivity response is maximised. It should be noted that in order to correct for the lamp's spectral response, a Newport 5108 UV-Vis mirror is used as a reference, which has a nearly flat response and the reflectivity is $\sim 90\%$, in the range of 300 - 600nm.

A.2.6 PL Imaging setup

The schematic of the setup is shown in Figure A.7, which allows PL imaging. The incident beam is focused on to the sample at normal incidence, using an objective having a numerical aperture (NA) of ~ 0.63 . In other words the range of the objective is from -39° to $+39^\circ$. The collection path is same as the incident path, which is made possible by using a beam splitter. The whole setup is aligned for $\sim 360\text{nm}$, which is close to the emission wavelength of the samples studied in this thesis. In the absence of the imaging lens, the PL collected from the sample is collimated by the objective, which is focused into the spectrometer by the final collection lens. In order to facilitate imaging, the Fourier plane of the sample which is formed at a distance of f_o from the objective, where $f_o \sim 8\text{mm}$ is the focal length of the objective, has to be imaged into the spectrometer, which is achieved by using an imaging lens at a distance d from the ima-

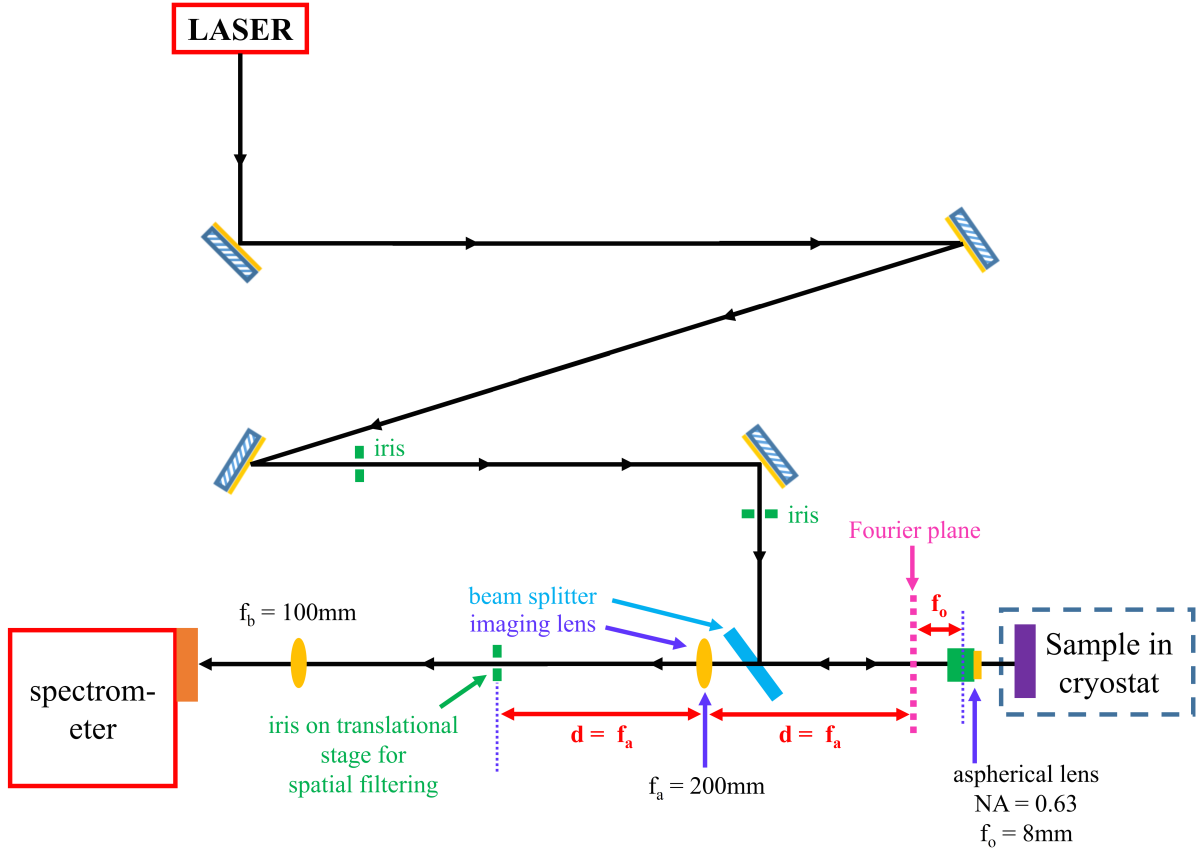


Figure A.7: PL Imaging setup.

ging plane. The distance d is actually equal to the focal length (f_a) of the imaging lens which is around 200mm. The setup further allows spatial filtering, which is made possible by installing an iris on a translational stage at a distance $d = f_a$ from the imaging lens, which in theory is the region where the Fourier plane would be focused by the imaging lens, as visible in Figure A.7. It should be noted that the focal length ($f_b \sim 100\text{mm}$) of the final collection lens solely depends on the final magnification required in order to utilise the CCD dimensions completely. Figure A.8, shows the imaging setup on a breadboard, which allows the measurement of PL / Reflectivity, made possible by the use of a flipping mirror.

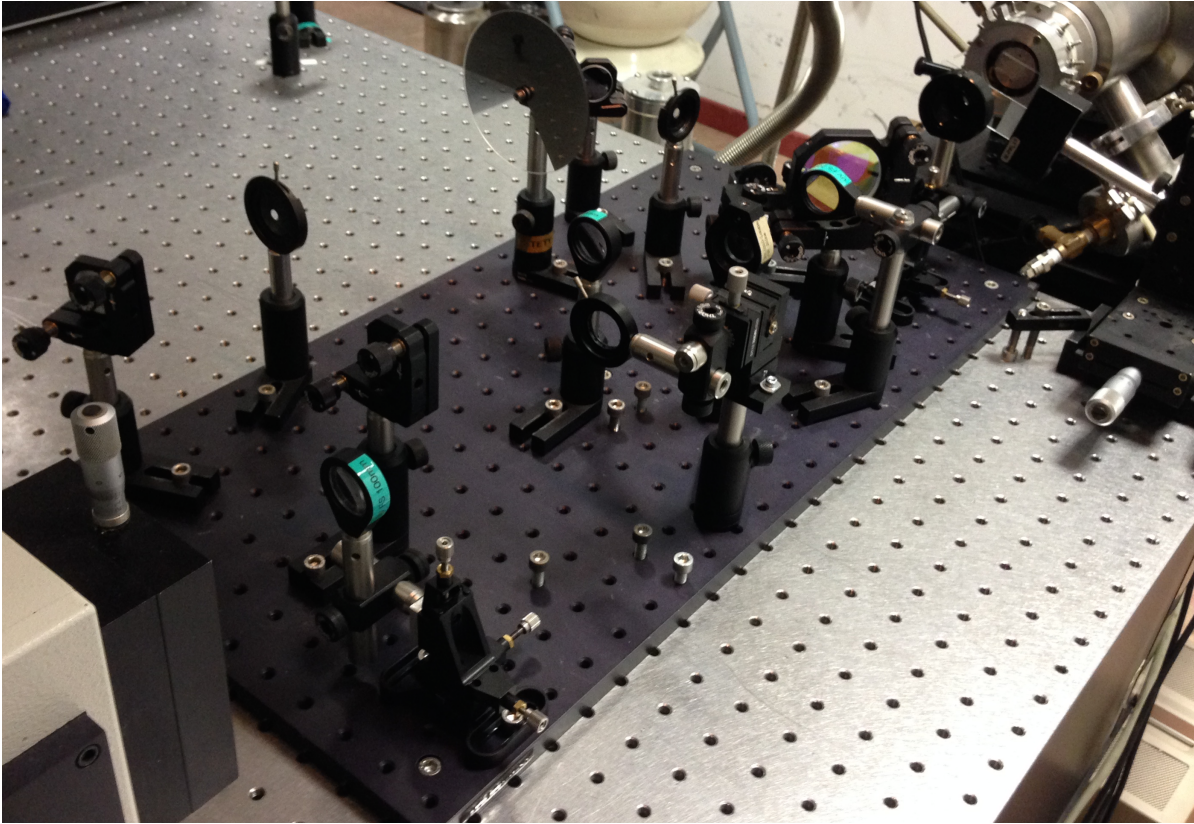


Figure A.8: An imaging setup on a breadboard, which allows the measurement of PL / Reflectivity, by the use of a flipping mirror.

A.2.7 Reflectivity measurements using integrating sphere

A Perkin Elmer LAMBDA 950 UV/Vis/NIR spectrophotometer, equipped with an integrating sphere is used for measuring the total reflectivity (specular + diffuse) spectrum from the sample, at RT. The setup can be operated in two configurations: 1) with specular white plate, 2) with specular light trap, as depicted by the schematic of Figure A.9, where the angle of incidence is $\sim 8^\circ$. With the first configuration, the total reflectivity response from the sample can be measured, whereas with the second, the specular reflection is trapped providing an accurate estimate of the diffuse reflectivity. The subtraction of the diffuse from the total reflectivity gives the specular reflectivity response of the sample. A detailed

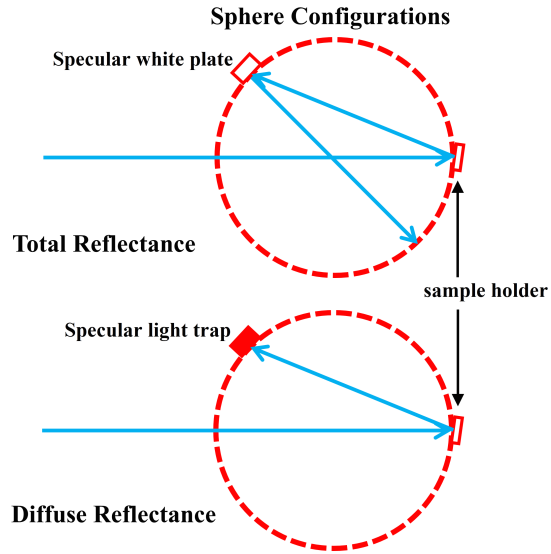


Figure A.9: Different integrating sphere configurations, used for measuring total and diffuse reflectivity.

description of the entire setup can be found in the following link.



This page is intentionally left blank



This page is intentionally left blank

Transfer matrix model

The matrix calculating method as described by F. Abeles (1950), is used to calculate the effective characteristic matrix of a multilayer system, which is then linked to its respective spectral coefficients using a transfer matrix. The model is described in detail, in [1].

B.1 Matrix calculating method

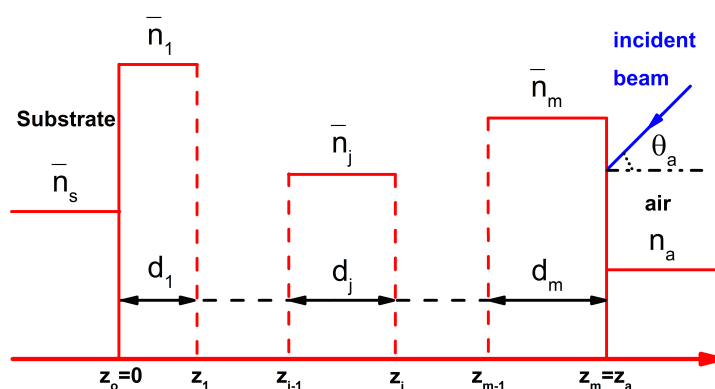


Figure B.1: A multilayer system consisting of homogeneous, isotropic layers, where the number of layers are assumed to be m , numbered from the substrate to air.

A multilayer system consisting of homogeneous, isotropic layers, is considered as shown in Figure B.1. The total number of layers are assumed to be m , numbered from the substrate to air, such that the right boundaries of each layer is denoted by z_1, z_2, \dots, z_m where $z_m=z_a$. z_a represents the coordinate of the outer boundary of the system, as well as the overall thickness of the multilayer system. The individual thickness of the layers are denoted by d_1, d_2, \dots, d_m and their complex respective refractive

index are given by $\tilde{n}_1, \tilde{n}_2, \dots, \tilde{n}_m$. The refractive index of the substrate is denoted by n_s (can be absorbing as well, then can be replaced by \tilde{n}_s) and that of air by n_a . The complex refractive index of any given layer is as follows:

$$\tilde{n} = n - ik \quad (\text{B.1})$$

where n is the real part of the refractive index and k is the imaginary part, also called as extinction coefficient, related to absorption coefficient (α) of the layer by the following equation:

$$k = \alpha \frac{\hbar c}{2\hbar\omega} \quad (\text{B.2})$$

where \hbar is the planck's constant, c is the velocity of light in air and ω is the angular frequency. The real part of the refractive index as a function of wavelength $n(\lambda)$ can be calculated using Sellmeier equation given by:

$$n(\lambda)^2 = 1 + \frac{B_1\lambda^2}{\lambda^2 - C_1} + \frac{B_2\lambda^2}{\lambda^2 - C_2} + \frac{B_3\lambda^2}{\lambda^2 - C_3} \quad (\text{B.3})$$

where B_1, B_2, B_3, C_1, C_2 and C_3 are the Sellmeier coefficients for the material under consideration and λ is the wavelength of incident light.

According to this method, the incident beam is assumed to be propagating from the air towards the substrate as shown in Figure B.1, at an angle of incidence θ_a , suffering multiple reflections/transmissions at each interface, interfering either constructively or destructively at the output, which can be either be at the reflected side or the transmitted side. The tangential components of the electric and magnetic vectors of the field, at some arbitrary point of the j_{th} layer are given by:

$$u(z) = u(z_{j-1}) \cos [k\tilde{n}_j \cos\theta_j (z - z_{j-1})] + \left(\frac{i}{q_j} \right) v(z_{j-1}) \sin [k\tilde{n}_j \cos\theta_j (z - z_{j-1})] \quad (\text{B.4})$$

$$v(z) = iq_j u(z_{j-1}) \sin [k\tilde{n}_j \cos\theta_j (z - z_{j-1})] + v(z_{j-1}) \cos [k\tilde{n}_j \cos\theta_j (z - z_{j-1})] \quad (\text{B.5})$$

Assuming $z = z_j$ in equations B.4 and B.5, the following equations are obtained:

$$u(z_j) = u(z_{j-1}) \cos\beta_j + \left(\frac{i}{q_j} \right) v(z_{j-1}) \sin\beta_j \quad (\text{B.6})$$

$$u(z_j) = iq_j u(z_{j-1}) \sin\beta_j + v(z_{j-1}) \cos\beta_j \quad (\text{B.7})$$

where β_j is the angular phase thickness inside the j^{th} layer given by:

$$\beta_j = \frac{2}{\lambda} \tilde{n}_j d_j \cos\theta_j \quad (\text{B.8})$$

where \tilde{n}_j is the complex refractive index of the j^{th} layer, d_j is the thickness of the j^{th} layer given by $d_j = z_j - z_{j-1}$, and θ_j is the angle of incidence to the j^{th} layer, which can be estimated from Snell's law as follows:

$$\tilde{n}_j \sin\theta_j = n_a \sin\theta_a \quad (\text{B.9})$$

where θ_a is the external angle of incidence from air, as shown in Figure B.1.

$$q_j = \tilde{n}_j \cos\theta_j \quad (\text{B.10})$$

for S-case and

$$q_j = \frac{\tilde{n}_j}{\cos\theta_j} \quad (\text{B.11})$$

for P-case, being the only difference in the extraction of spectral coefficients for the two respective cases. The equations B.6 and B.7 can also be written in the matrix form as following:

$$\begin{pmatrix} u \\ v \end{pmatrix}_{z=z_j} = \begin{pmatrix} \cos\beta_j & \left(\frac{i}{q_j}\right) \sin\beta_j \\ iq_j \sin\beta_j & \cos\beta_j \end{pmatrix} \begin{pmatrix} u \\ v \end{pmatrix}_{z=z_{j-1}} \quad (\text{B.12})$$

The matrix introduced can be defined as the characteristic matrix of the j_{th} layer given by:

$$M_j = \begin{pmatrix} \cos\beta_j & \left(\frac{i}{q_j}\right) \sin\beta_j \\ iq_j \sin\beta_j & \cos\beta_j \end{pmatrix} \quad (\text{B.13})$$

The tangential components of the electric and magnetic field of the incident wave are continuous at the individual boundaries due to which the effective characteristic matrix of the multilayer system (M) is a product of the characteristic matrix (M_j) of each individual layer, numbered from $j = 1 \dots n$, given by:

$$M = M_n \cdot M_{n-1} \dots M_1 \quad (\text{B.14})$$

where $j = 1$, corresponds to the layer adjacent to the substrate and $j = n$, adjacent to air.

B.2 Relation between transfer matrix and effective characteristic matrix

The amplitude transmittance and reflectance of the multilayer system, in the forward (air to substrate) and reverse (substrate to air) direction can be related to the effective characteristic matrix of the system using a transfer matrix denoted by C . The reflection, transmission and absorption amplitudes in the forward direction are denoted by r , t and a , and in the reverse direction by r' , t' and a' , as shown in Figure B.2.

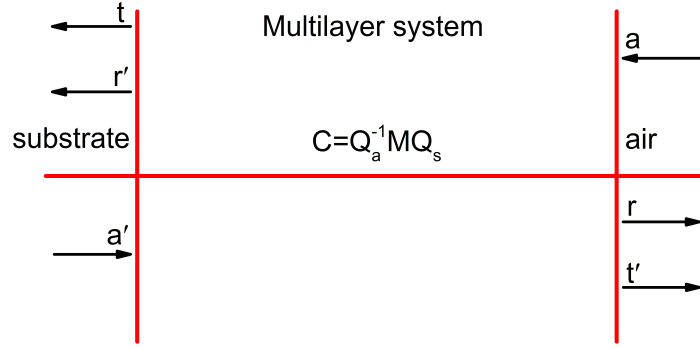


Figure B.2: Relation between effective characteristic matrix (M) and the different spectral amplitudes such as reflection, transmission and absorption, which in turn are represented by the transfer matrix (C).

$$C = Q_a^{-1} M Q_s \quad (\text{B.15})$$

where $C = \begin{bmatrix} \frac{1}{t} & \frac{-r}{t} \\ \frac{r}{t} & \frac{1}{t^+} \end{bmatrix}$, $t^+ = \frac{t}{tt-rr}$,

$$Q_a = \begin{bmatrix} 1 & 1 \\ q_a & -q_a \end{bmatrix}, \quad q_a = n_a \cos \theta_a \text{ (S-case) and } q_a = \frac{n_a}{\cos \theta_a} \text{ (P-case)}$$

$$Q_s = \begin{bmatrix} 1 & 1 \\ q_s & -q_s \end{bmatrix}, \quad q_s = n_s \cos \theta_s \text{ (S-case) and } q_s = \frac{n_s}{\cos \theta_s} \text{ (P-case)}$$

Considering the incident beam to be propagating in the forward direction i.e. from air to substrate, equation (1.10) can be solved for the

reflectance amplitude r and transmittance amplitude t . Therefore for the S-case, with $q = \tilde{n} \cos \theta$, the spectral coefficients are as following:

$$R_s = |r|^2 \quad (\text{B.16})$$

$$T_s = \frac{q_s}{q_a} |t|^2 \quad (\text{B.17})$$

Similarly for P-case, with $q = \frac{\tilde{n}}{\cos \theta}$, the reflectance is denoted by R_p and transmittance by T_p . The overall reflectance and transmittance of the multilayer system is given by:

$$R = \frac{R_s + R_p}{2} \quad (\text{B.18})$$

Now the absorption of the system can be calculated from:

$$A = 1 - R - T \quad (\text{B.19})$$

B.3 Application of the model to a microcavity system

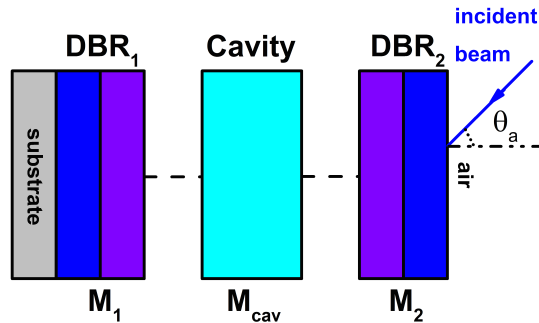


Figure B.3: A multilayer system divided into three regions: (1) bottom DBR₁, (2) cavity layer, and finally (3) top DBR₂, collectively forming a microcavity system, where the effective characteristic matrix of the corresponding regions are M_1 , M_{cav} and M_2 respectively.

Consider a microcavity system as shown in Figure B.3. It is very similar to the multilayer system defined in subsection B.1, with substrate at the bottom and light incident from air, except that the system is divided into three regions: 1) bottom DBR₁ 2) cavity layer and finally 3) top DBR₂. The effective characteristic matrix of the corresponding regions are given by M_1 , M_{cav} and M_2 . According to equation B.14, the effective characteristic matrix of the entire system is then as follows:

$$M = M_2 \cdot M_{cav} \cdot M_1 \quad (\text{B.20})$$

Now M can be related to the spectral coefficients using equation B.15, which thereby can be solved for the reflectance, transmission and absorption response of the system.

Moreover the equations B.4 and B.5 can be used to estimate the field distribution within the microcavity structure, by expressing $u(z_{j-1})$ and $v(z_{j-1})$ through the amplitude of the incident wave. If E is considered as the electric vector of the incident wave, then $u(0) = tE$ and $v(0) = q_s u(0) = q_s tE$. Applying these boundary conditions to equations B.4 and B.5, gives the respective electric and magnetic field distributions within the structure. It has to be noted that the solution is valid for both S-case and P-case, the only difference being $q = \tilde{n} \cos \theta$ for S-case and $q = \frac{\tilde{n}}{\cos \theta}$ for P-case.

Bibliography

- [1] S. A. Furman and A. V. Tikhonravov. “Spectral Characteristics of Multi-Layer Coatings: Theory”, *Basics of optics of multilayer systems*. Atlantica Séguier Frontières, 1992, pp. 1–102.



This page is intentionally left blank



This page is intentionally left blank

Linear Hamiltonian model

The linear Hamiltonian of a system using rotating wave approximation, in the low density regime, where exciton-exciton interaction can be ignored, can be written in the second quantisation form as following:

$$H = \sum_{k_{\parallel}} H_{k_{\parallel}} = \sum_{k_{\parallel}} E_{exc,o}(k_{\parallel}) b_{k_{\parallel}}^{\dagger} b_{k_{\parallel}} + E_o(k_{\parallel}) a_{k_{\parallel}}^{\dagger} a_{k_{\parallel}} + g b_{k_{\parallel}}^{\dagger} a_{k_{\parallel}} + g a_{k_{\parallel}}^{\dagger} b_{k_{\parallel}} \quad (C.1)$$

where $a_{k_{\parallel}}$, $b_{k_{\parallel}}$ are the annihilation, and $a_{k_{\parallel}}^{\dagger}$, $b_{k_{\parallel}}^{\dagger}$ are the creation operators, of the cavity photon and an exciton respectively, for a given in-plane wavevector k_{\parallel} , E_o and $E_{exc,o}$ are the corresponding cavity photon and exciton energies and g is the coupling constant given by:

$$g = \hbar \sqrt{\frac{2\Gamma_o c N_{QW}}{n_{cav} d_{cav}^*}} \quad (C.2)$$

where c is the velocity of light in air, N_{QW} is the number of QW's, n_{cav} is the effective refractive index of the cavity layer, d_{cav}^* is the effective cavity length including the penetration into the mirrors and finally $\hbar\Gamma_o$ is given by:

$$\hbar\Gamma_o = \frac{\pi e^2 \hbar}{4\pi \varepsilon_o n_{cav} m c} \frac{f_{osc}^{QW}}{S} \quad (C.3)$$

where e is the charge of an electron, ε_o is the vacuum dielectric constant, m is the mass of an electron and $\frac{f_{osc}^{QW}}{S}$ is the QW oscillator strength per

unit area. It should be noted that the expression for coupling constant (g) is an approximate formula, derived under the following assumptions: (1) the cavity layer has a higher refractive index as opposed to its DBR constituents and (2) the QW's are placed exactly at the antinodes of the field distribution within the cavity layer, estimated for a resonant cavity photon energy (E_o). $H_{k_{\parallel}}$ of equation C.1, can be represented in the form of a matrix as following:

$$\begin{pmatrix} E_{exc,o}(k_{\parallel}) & g \\ g & E_o(k_{\parallel}) \end{pmatrix} \quad (\text{C.4})$$

For a given in-plane wavevector k_{\parallel} , the matrix can be diagonalised to determine the eigen energies, corresponding to the eigen states of the coupled excitons and photons, given by:

$$E_{LPB}(k_{\parallel}) = \frac{1}{2} \left(E_{exc,o}(k_{\parallel}) + E_o(k_{\parallel}) - \sqrt{(E_{exc,o}(k_{\parallel}) - E_o(k_{\parallel}))^2 + 4g^2} \right) \quad (\text{C.5})$$

$$E_{UPB}(k_{\parallel}) = \frac{1}{2} \left(E_{exc,o}(k_{\parallel}) + E_o(k_{\parallel}) + \sqrt{(E_{exc,o}(k_{\parallel}) - E_o(k_{\parallel}))^2 + 4g^2} \right) \quad (\text{C.6})$$

$E_{LPB}(k_{\parallel})$ and $E_{UPB}(k_{\parallel})$, can be referred to as the energies, corresponding to the lower and upper polariton states, for a given in-plane wavevector k_{\parallel} . The corresponding normalised eigen vectors are as following:

$$\begin{pmatrix} X_{k_{\parallel}} \\ C_{k_{\parallel}} \end{pmatrix} \quad (\text{C.7})$$

and

$$\begin{pmatrix} C_{k_{\parallel}} \\ -X_{k_{\parallel}} \end{pmatrix} \quad (\text{C.8})$$

where $X_{k_{\parallel}}$ and $C_{k_{\parallel}}$ are the Hopfield coefficients, given by:

$$|X_{k_{\parallel}}|^2 = \frac{1}{2} \left(1 + \frac{\Delta E_{det}(k_{\parallel})}{\sqrt{\Delta E_{det}(k_{\parallel})^2 + 4g^2}} \right) \quad (\text{C.9})$$

$$|C_{k_{\parallel}}|^2 = \frac{1}{2} \left(1 - \frac{\Delta E_{det}(k_{\parallel})}{\sqrt{\Delta E_{det}(k_{\parallel})^2 + 4g^2}} \right) \quad (\text{C.10})$$

where $|X_{k_{\parallel}}|^2$ and $|C_{k_{\parallel}}|^2$ are indicative of the corresponding exciton (photon) and photon (exciton) fractions, of the lower (upper) polaritons respectively, for a given in-plane wavevector k_{\parallel} , $\Delta E_{det}(k_{\parallel})$ is the detuning, for a given in-plane wavevector k_{\parallel} , given by $\Delta E_{det}(k_{\parallel}) = E_{exc,o}(k_{\parallel}) - E_o(k_{\parallel})$. The Hopfield coefficients satisfy the following relation:

$$|X_{k_{\parallel}}|^2 + |C_{k_{\parallel}}|^2 = 1 \quad (\text{C.11})$$

So when the detuning is 0, $|X_{k_{\parallel}}|^2$ and $|C_{k_{\parallel}}|^2$ equals 0.5 i.e. the lower polaritons (LPB) and the upper polaritons (UPB) are 50% photon like and 50% exciton like. The corresponding energy splitting ($\hbar\Omega_{VRS}$) is called vacuum field Rabi splitting, given by:

$$\hbar\Omega_{VRS} = 2g \quad (\text{C.12})$$

The interaction of the excitons with phonons or the presence of absorption / interface losses in the microcavity structure, leads to homogeneous broadening of the excitons and cavity photons respectively. This ho-

mogeneous broadening can be included in the model, by modifying the matrix in equation C.4 slightly, as follows:

$$\begin{pmatrix} E_{exc,o}(k_{\parallel}) - i\gamma & g \\ g & E_o(k_{\parallel}) - i\gamma_{cav} \end{pmatrix} \quad (C.13)$$

where γ and γ_{cav} are the linewidths (FWHM) of the exciton and cavity photon respectively. The eigen energies thereby gets modified as following:

$$E_{LPB}(k_{\parallel}) = E_{avg}(k_{\parallel}) - i\gamma_{avg} - \sqrt{g^2 + \frac{1}{4}(\Delta E_{det}(k_{\parallel}) - i\Delta\gamma)^2} \quad (C.14)$$

$$E_{UPB}(k_{\parallel}) = E_{avg}(k_{\parallel}) - i\gamma_{avg} + \sqrt{g^2 + \frac{1}{4}(\Delta E_{det}(k_{\parallel}) - i\Delta\gamma)^2} \quad (C.15)$$

where $E_{avg}(k_{\parallel}) = \frac{E_{exc,o}(k_{\parallel}) + E_o(k_{\parallel})}{2}$, $\gamma_{avg} = \frac{\gamma + \gamma_{cav}}{2}$ and $\Delta\gamma = \gamma - \gamma_{cav}$. At zero detuning i.e. when $\Delta E_{det}(k_{\parallel}) = 0$, equations C.14 and C.15, gets reduced to the following:

$$E_{LPB}(k_{\parallel}) = E_{avg}(k_{\parallel}) - i\gamma_{avg} - \sqrt{g^2 + \frac{1}{4}\Delta\gamma^2} \quad (C.16)$$

$$E_{UPB}(k_{\parallel}) = E_{avg}(k_{\parallel}) - i\gamma_{avg} + \sqrt{g^2 + \frac{1}{4}\Delta\gamma^2} \quad (C.17)$$

The vacuum field Rabi splitting from equation C.12 thus gets modified as:

$$\hbar\Omega_{VRS} = 2\sqrt{g^2 - \frac{1}{4}\Delta\gamma^2} \quad (C.18)$$

The polariton linewidth (γ_{pol}) is thus given by the relation:

$$\gamma_{pol} = \frac{\gamma + \gamma_{cav}}{2} \quad (\text{C.19})$$

Thus it can be concluded from equation C.18 that $4g^2 > \Delta\gamma^2$, in order for the system to be in the strong coupling regime.

In order to include more than one excitons in the model, the matrix in equation C.13, can be modified as follows:

$$\left(\begin{array}{cccccc} E_{exc1,o}(k_{\parallel}) - i\gamma_1 & 0 & \cdots & \cdots & 0 & g_1 \\ 0 & E_{exc2,o}(k_{\parallel}) - i\gamma_2 & 0 & \cdots & \vdots & g_2 \\ \vdots & 0 & \ddots & 0 & \vdots & \vdots \\ \vdots & \vdots & 0 & \ddots & 0 & \vdots \\ 0 & \cdots & \cdots & 0 & E_{exc n,o}(k_{\parallel}) - i\gamma_n & g_n \\ g_1 & g_2 & \cdots & \cdots & g_n & E_o(k_{\parallel}) - i\gamma_{cav} \end{array} \right) \quad (\text{C.20})$$

The matrix includes n excitons, defined by a matrix of dimension $(n + 1) \times (n + 1)$. The matrix can be diagonalised, as described before in order to calculate $n + 1$ eigen energies, corresponding to different polariton states. Further discussion about the model can be found in the following references [1, 2].

Bibliography

- [1] H. Deng, H. Haug, and Y. Yamamoto. “Exciton-polariton Bose-Einstein condensation”, *Reviews of Modern Physics* 82.June (2010), pp. 1489–1537.
- [2] G. Christmann. “III-nitride Based Microcavities: Towards Polariton Condensation at Room Temperature”. PhD thesis. EPFL, 2009.